

**Untersuchungen zur Gassorption und Protonenleitung
synthetisch und postsynthetisch modifizierter poröser
organischer Polymere**

Dissertation

Zur Erlangung des akademischen Grades

Doktor der Naturwissenschaften

(Dr. rer. Nat)

An der Fakultät für

Chemie, Biologie und Geowissenschaften

der Universität Bayreuth

Christoph Klumpen

geboren in Viersen

Bayreuth 2018

Die vorliegende Arbeit wurde an der Universität Bayreuth am Lehrstuhl für Anorganische Chemie III unter Betreuung von Prof. Dr. Jürgen Senker im Zeitraum vom Januar 2015 bis März 2018 angefertigt

Vollständiger Abdruck der von der Fakultät für Biologie, Chemie und Geowissenschaften der Universität Bayreuth genehmigten Dissertation zur Erlangung des akademischen Grades eines Doktors der Naturwissenschaften (Dr. rer.nat)..

Dissertation eingereicht am: 28.03.2018

Zulassung durch die Promotionskommission am: 02.05.2018

Wissenschaftliches Kolloquium: 18.09.2018

Amtierender Dekan: Prof. Dr. Stefan Peiffer

Prüfungsausschuss:

Prof. Dr. Jürgen Senker (Gutachter)

Prof. Dr. Bettina Lotsch (Gutachterin)

Prof. Dr. Peter Strohriegel (Vorsitz)

Prof. Dr. Josef Breu

„Chancen multiplizieren sich, wenn man sie ergreift“

(Sun Tsu)

Danksagung

Mein Dank gebührt an erster Stelle Prof. Dr. Jürgen Senker für die Aufnahme in den Arbeitskreis, das spannende Forschungsfeld und die vielen Diskussionen. Danke für die Möglichkeit einer freien Forschungs- und Projektwahl, welche die Zeit wie im Flug haben vergehen lassen. Danke für eine schöne Zeit an deinem Arbeitskreis.

Für das angenehme Arbeitsklima und viele Interessante Gespräche danke ich den Mitgliedern der Arbeitsgruppen AC-I und AC-III. Danke für die vielen schönen Kaffeepausen, Konferenzen und Festlichkeiten.

Besonderer Dank gilt den alten und aktuellen Mitgliedern sowie regelmäßigen Besuchern des Syntheselabors. Danke an Paul, Nadine, Marko, Dominik, Marion, Tobi, Helen, Renée, Beate, Robert, Simon, Thomas und Carina für eine schöne Zeit, die Einführung in fränkisches Brauchtum, Sprache und Gepflogenheiten und die vielen anregenden Gespräche und Diskussionen, ob fachbezogen, politisch oder einfach nur Quatsch. Danke an Jürgen, Marion, Thomas sowie meine Mutter und Caro für die Hilfe bei Korrektur und Formatierung. Danke an Dr. Renée Siegel und Beate Bojer für die vielen NMR Messungen und die Unterstützung.

Danke an meine Familie, welche mich zu jeder Zeit unterstützt hat. Sara danke ich besonders für die permanente seelische Unterstützung und das Verständnis der von mir gesetzten Prioritäten.

Inhaltsverzeichnis

Abkürzungsverzeichnis	X
Zusammenfassung	XIII
Abstract	XV
1. Einleitung	1
1.1 Poröse Materialien.....	1
1.2 Gassorption und Separation.....	2
1.3 Brennstoffzellen	3
1.4 Darstellung poröser organischer Polymere.....	5
1.5 Physisorptionsanalyse.....	10
1.6 Impedanzspektroskopie	13
2. Synopsis	16
2.1 Microporous Organic Polyimides for CO ₂ and H ₂ O Capture and Separation from CH ₄ and N ₂ Mixtures: Interplay between Porosity and Chemical Function	17
2.2 BILP-19 – An Ultramicroporous Organic Network with Exceptional Carbon Dioxide Uptake	19
2.3 Water mediated Proton Conduction in a Sulfonated Porous Polymer Network.....	22
2.4 Anhydrous Proton Conduction in Porous Organic Networks.....	25
2.5 Ausblick.....	28
3. Literaturverzeichnis	29
4. Publikationsverzeichnis	39
5. Publikationen	40
5.1 Microporous Organic Polyimides for CO ₂ and H ₂ O Capture and Separation from CH ₄ and N ₂ Mixtures: Interplay between Porosity and Chemical Function	40
5.2 BILP-19 – An Ultramicroporous Organic Network with Exceptional Carbon Dioxide Uptake	79
5.3 Water mediated Proton Conduction in a Sulfonated Microporous Organic Polymer	109
5.4 Anhydrous Proton Conduction in Porous Organic Networks.....	145
6. Anhang	195
6.1 Frequenzabhängigkeit von Ionenleitern	195
6.2 Ersatzschaltkreise	196
6.3 Spezielle elektronische Elemente	198

Abkürzungsverzeichnis

Abkürzung	Bedeutung
Abb.	Abbildung
AFM	<i>Atomic force microscopy</i>
BET	Brunauer Emmett Teller
CCS	<i>Carbon dioxide capture and storage</i>
CMP	<i>Covalent microporous polymer</i>
COF	<i>Covalent organic framework</i>
CP	<i>Cross polarization</i>
CTF	<i>Covalent triazine framework</i>
DCM	Dichlormethan
DMFC	<i>Direct methanol fuel cell</i>
EDX	<i>Energy dispersive x-ray spectroscopy</i>
EIS	<i>Electrochemical impedance spectroscopy</i>
EOF	<i>Element organic framework</i>
HCP	<i>Hypercrosslinked polymer</i>
HFC	<i>Hydrogen fuel cell</i>
IAST	<i>Ideal adsorbed solution theory</i>
IR	<i>Infrared spectroscopy</i>
MCFC	<i>Molten carbonate fuel cell</i>
MOF	<i>Metal organic framework</i>
MOPI	<i>Microporous organic polyimide</i>
NLDFT	<i>Non local density functional theory</i>
NMR	<i>Nuclear magnetic resonance</i>
OP	<i>Onepulse</i>
PAF	<i>Porous aromatic framework</i>
PEM	Polymerelektrolytmembran

PFG	<i>Pulse field gradient</i>
PGSE	<i>pulsed magnetic field gradient spin echo</i>
PIM	<i>Polymer with intrinsic microporosity</i>
PON	<i>Porous organic network</i>
PSA	<i>Pressure swing adsorption</i>
PSM	<i>Post synthetic modification</i>
PXRD	<i>Powder x-ray spectroscopy</i>
QSDFT	<i>Quenched solid state density functional theory</i>
REM	Rasterelektronenmikroskopie
rH	<i>Relative humidity</i>
SOFC	<i>Solid oxide fuel cell</i>
SPAF	<i>Sulfonated porous aromatic framework</i>
TGA	<i>Thermogravimetric analysis</i>
VSA	<i>Vacuum swing adsorption</i>

Zusammenfassung

Ziel dieser Arbeit war die Synthese und postsynthetische Modifizierung poröser organischer Polymere sowie deren Untersuchung hinsichtlich prominenter Anwendungsgebiete in der Gassorption und Protonenleitung. Im Fokus standen hier vor allem die Einflüsse von Porosität und Funktionalisierung auf die spezifischen Netzwerkeigenschaften. Anhand einer systematischen Studie auf Basis von fünf neuartigen Polyimiden konnte die Präsenz von Ultramikroporen als dominierender Faktor für die Aufnahmekapazität von Kohlenstoffdioxid und Wasser dargestellt werden. Des Weiteren konnte gezeigt werden, dass für die selektive Aufnahme von Kohlenstoffdioxid gegenüber Stickstoff und Methan, neben der Porosität, die funktionellen Seitengruppen des Polymerrückgrats entscheidenden Einfluss nehmen. Hier haben sich polare Seitengruppen, welche spezifische Wirt-Gast Wechselwirkungen generieren als potent erwiesen. In einer weiterführenden Arbeit wurde das erarbeitete Konzept auf die Strukturklasse der Polybenzimidazole übertragen. Durch die Wahl kleiner Linkermoleküle wurde sowohl die Ausbildung von Ultramikroporen als auch eine dichte Verteilung funktioneller Gruppen im Netzwerk BILP-19 realisiert. Infolgedessen zeigte das Netzwerk hohe Aufnahmekapazitäten für Kohlenstoffdioxid und Wasser von $6 \text{ mmol}\cdot\text{g}^{-1}$ und $18 \text{ mmol}\cdot\text{g}^{-1}$ mit hohen Selektivitäten gegenüber Stickstoff und Methan. Des Weiteren wurde ein Mechanismus für die selektive Aufnahme von CO_2 und H_2O postuliert, demzufolge eine größenselektive Ausdehnung des Netzwerks stattfindet, welche sukzessiv weiteren Porenraum und somit Aufnahmekapazität freigibt.

Anders als für die Gassorption, haben sich im Rahmen dieser Arbeit für die Darstellung protonenleitender Netzwerke vor allem mesoporöse Netzwerke als zielführend erwiesen. So konnte durch die postsynthetische Sulfonierung des Polymers PAF-1 das protonenleitende SPAF-1 generiert werden. In einer systematischen Studie wurden ferner der Einfluss von Sulfonierungsgrad, relativer Luftfeuchtigkeit und Temperatur näher beleuchtet und eine starke Abhängigkeit von Temperatur und Feuchtigkeitsgrad (Ladungsträger-konzentration) festgestellt. Es konnte gezeigt werden, dass anders als bei *state of the art* Materialien, wie beispielsweise Nafion, die Leitfähigkeit nicht auf einer Mikrophasenseparation des Netzwerks, sondern auf einer Wanderung der Protonen durch die Systemkavitäten beruht. Die Folge ist eine hohe Leitfähigkeit von bis zu $10^{-1} \text{ S}\cdot\text{cm}^{-1}$ bei 95 % rH und 80 °C.

Um der starken Abhängigkeit der Leitfähigkeit vom Feuchtigkeitsgrad zu begegnen, wurde in einer weiteren Arbeit der Austausch von Wasser mit amphoteren Molekülen untersucht. Auf Basis von sechs strukturell unterschiedlichen porösen Polymeren wurden die Einflüsse von Struktur, Porosität, Funktionalität und Gastbeladung auf die wasserfreie Protonenleitung herausgearbeitet. Hier konnten Werte von bis zu $10^{-4} \text{ S}\cdot\text{cm}^{-1}$ bei 130 °C

Zusammenfassung

unter N₂ Atmosphäre festgestellt werden. Als ausschlaggebend für die Leitfähigkeit hat sich vor allem eine hohe Imidazolbeladung (Ladungsträgerkonzentration) sowie Mesoporosität des Gastnetzwerks gezeigt. Diese sichert eine homogene Verteilung der eingelagerten Moleküle und somit die Ausbildung durchgängiger Protonenleitungswege.

Abstract

The scope of this work was the synthesis and postsynthetic modification of porous organic polymers, as well as their investigation towards prominent areas of application in gas sorption and proton conduction. Among others, the focus was set on the influences of porosity and functionality on the specific network properties. With the help of a systematic study, based on five novel polyimides, the presence of ultra-micropores as dominating factor for the uptake capacity for carbon dioxide and water was presented. Furthermore, it has been shown, that for the selective uptake of carbon dioxide over nitrogen and methane, besides porosity, the functional side groups of the polymer backbone take significant influence. Here, polar side groups, which generate specific host-guest-interactions, showed to be potent. In a pursuing work, the compiled concept has been transferred to the structure class of polybenzimidazoles. Due to the choice of small linker molecules, the formation of ultra-micropores as well as a dense distribution of functional groups in the network BILP-19 has been realized. As a result, the network showed high uptake capacities for carbon dioxide and water of $6 \text{ mmol}\cdot\text{g}^{-1}$ and $18 \text{ mmol}\cdot\text{g}^{-1}$ with high selectivities over nitrogen and methane. Additionally, a mechanism for the selective uptake of CO_2 and H_2O has been postulated, which states a size selective expansion of the network, which successively provides further pore space and thus uptake capacity.

In contrast to gas sorption, for the synthesis of proton conducting networks mesoporous networks showed to be expedient, within this work. Thus, through post synthetic sulfonation of the polymer PAF-1, the proton conducting SPAF-1 could be generated. In a systematic study, the influence of sulfonation degree, relative humidity and temperature has been further investigated, determining a strong dependence on temperature and humidification degree (charge carrier concentration). It could be pointed out, that in contrast to state of the art materials, like nafion, the conductivity doesn't rely on microphase separation, but on a migration of protons through the system cavities. The result was a high conductivity up to $10^{-1} \text{ S}\cdot\text{cm}^{-1}$ at 95 % rH and $80 \text{ }^\circ\text{C}$.

To face the strong dependence of the conductivity on humidification, in a further work, the exchange of water with amphoteric molecules has been investigated. Based on six structural varying porous polymers, the influence of structure, porosity, functionality and guest incorporation on water free proton conduction has been investigated. Here, values up to $10^{-4} \text{ S}\cdot\text{cm}^{-1}$ at $130 \text{ }^\circ\text{C}$ under N_2 atmosphere were determined. As crucial for a high conductivity showed to be a high loading of imidazole (charge carrier concentration) as well as the mesoporosity of the host networks. This ensures a homogeneous distribution of incorporated molecules and therefore die formation of continuous proton conducting pathways.

1. Einleitung

1.1 Poröse Materialien

Die natürliche Verwendung von Kavitäten als Nutz- bzw. Speicherraum oder Struktur- und Stabilitätsgeber ist hinlänglich bekannt.¹ So sind als prominente Beispiele poröser Strukturen die Waben des Bienenstocks oder die Spongiosa des Knochens (lat.: *substantia spongiosa*) zu nennen, bei denen die permanenten Hohlräume, gestützt durch stabile Wandstrukturen, jeweils spezifische Funktionen erfüllen.^{1,2} Bei der Übertragung dieses Konzepts auf die Nanoskala, liegt die Ausbildung permanenter Hohlräume (Poren) in sterisch gehemmten Packungsmustern von Atomen begründet, welche sich als geordnet wie im Fall der Honigwaben oder ungeordnet wie im Fall der Spongiosa repräsentieren können.² Die Unterteilung der Porosität erfolgt hierbei durch die IUPAC nach der jeweiligen Größe der Kavität in Makroporen (>50 nm), Mesoporen (<50 nm, >2 nm) und Mikroporen (<2 nm) sowie der Porenform in offene, halboffene und geschlossene Poren.³ Hierbei ist die Porosität von der Rauigkeit (Textur) eines Festkörpers abzugrenzen.⁴ Die Folge einer nanoskaligen, porösen Struktur ist oft eine hohe innere Oberfläche, welche vor allem aus materialchemischer und -technischer Sicht ein großes Potential birgt.⁵ Die Entwicklung poröser Materialien für die Speicherung⁶, Filtration⁷ oder Katalyse⁸ ist somit ein wichtiger Bestandteil der heutigen Industrie und Forschung.

Bei der Darstellung hochporöser Materialien lassen sich im Allgemeinen drei verschiedene Klassen nach Art ihrer Beschaffenheit herauskristallisieren. Rein anorganische Materialien, wie Schichtsilikate⁹ (Tonminerale) oder Zeolithe¹⁰ (Alumosilikate) beispielsweise, setzen sich aus Zusammenschlüssen anorganischer Untergruppen zusammen und bilden so poröse Strukturen aus. Der Zugang zu diesen Substanzklassen bilden beispielsweise Templatsynthesen durch organische Agglomerate, wodurch wohlgeordnete und thermisch hochstabile Strukturen entstehen.¹⁰ Die Klasse der anorganisch-organischen Hybridmaterialien hingegen setzt auf dativ-kovalente Verknüpfungen anorganischer Metalloxidcluster mit organischen Linkermolekülen.¹¹ Auf diese Weise lassen sich beliebige, hochgeordnete Porenstrukturen durch solvothermale oder Mikrowellen gestützte Syntheserouten realisieren.¹¹ Durch die organische Einheit dieser metall-organischen Gerüstverbindungen (engl.: *metal organic frameworks* (MOFs)) ist ferner eine hohe Vielfalt hinsichtlich synthetischer Funktionalisierung und postsynthetischer Modifikation gegeben.¹²⁻¹⁴ Als Dritte, und im Rahmen dieser Arbeit besonders hervorzuhebende, Klasse sind die porösen organischen Netzwerke (PONs) zu nennen.² Anders als bei den vorangegangenen Materialien bestehen PONs ausschließlich aus organischen, leichten Elementen.² Ihre Darstellung erfolgt durch Methoden der klassischen organischen bzw. metallorganischen Chemie, wobei stets kovalente Bindungen geknüpft werden.²

Die Vielzahl möglicher Monomere in Kombination mit unterschiedlichsten Reaktionsbedingungen ermöglichen eine hohe Variabilität in der Darstellung geordneter und ungeordneter Systeme. Die daraus resultierende Diversität poröser organischer Netzwerke hinsichtlich ihrer Morphologie und Funktionalität eröffnen verschiedenste Applikationsmöglichkeiten.^{15,16} Neben traditionellen Gebieten wie der Filtration und Speicherung technisch-ökologisch relevanter Gase¹⁷ und der Reaktionskatalyse¹⁸ wurden viele weitere Anwendungsgebiete wie die Wasserspaltung¹⁹, organische Photovoltaik²⁰, Protonenleitung²¹, Biomedizin²², Pharmazie²³ und Sensorik²⁴ erschlossen. Im Folgenden werden die für diese Arbeit relevanten Themengebiete der Gassorption sowie Protonenleitung näher ausgeführt.

1.2 Gassorption und Separation

Die Reduktion des Treibhausgases Kohlenstoffdioxid, als Hauptverursacher der globalen Erwärmung, ist eine der Kernherausforderungen der globalen Forschung, Politik und Wirtschaft.²⁵ Neben der Entwicklung alternativer, emissionsfreier Technologien ist die Senkung der Kohlenstoffdioxidfreisetzung aktueller, technischer Anlagen hierfür von zentraler Bedeutung für das Erreichen festgesetzter Klimaziele.²⁶ Die bekannteste CCS-Methode (engl.: *carbon dioxide capture and storage*; CCS), unterteilt sich hierbei in die selektive Filtration von Kohlenstoffdioxid, dessen transportfähige Speicherung und eine finale Lagerung in unterirdische bzw. unterseeische Lagerstätten.²⁷ Als Kernbereiche der Filtration sind Verbrennungsprozesse²⁸ (engl.: *post combustion*), Treibstoffreinigung²⁹ (engl.: *pre combustion*) sowie die Naturgasveredelung³⁰ (engl.: *natural (sour) gas sweetening*) zu nennen, welche jeweils besondere Bedingungen hinsichtlich Einsatztemperatur und Umgebungsdruck an Filtrationsprozesse stellen. In Kombination mit unterschiedlichsten Gasmischungen aus CO₂, N₂, H₂O, CO, NO_x und SO_x ergibt sich ein komplexes Anforderungsprofil für die Entwicklung passender Filtermaterialien. Um sowohl Aufwand als auch Kosten der Regeneration Rechnung zu tragen, ist ein selektiver Filtrationsmechanismus auf Basis physisorptiver Wechselwirkungen dem der chemisorptiven Gast Anbindung vorzuziehen. So stellen beispielsweise parallel geschaltete Druckwechsel- (engl.: *pressure swing adsorber*; PSA) respektive Vakuumwechselanlagen (engl.: *vacuum swing adsorber*; VSA) eine sowohl effektive als auch effiziente Alternative zu herkömmlichen, chemisorptiven Systemen auf Basis von Alkanolaminen dar.³¹

Ihrer hohen strukturellen Flexibilität und physikochemischen Stabilität entsprechend, sind poröse organische Polymere in den Fokus der Forschungsbemühungen gerückt. So wurden in zahlreichen Arbeiten der besondere Einfluss von Oberfläche, Porengröße, Adsorptionswärme, Funktionalität und Netzwerkmorphologie auf die selektive Adsorption von Kohlenstoffdioxid untersucht und die erlangten Erkenntnisse erfolgreich umgesetzt.¹⁷

So konnten durch die Kombination hoher innerer Oberflächen ($600\text{-}1300\text{ m}^2\cdot\text{g}^{-1}$) mit der chemischen Funktionalisierung des Polymerrückgrates (ALP-1³² ($5,4\text{ mmol}\cdot\text{g}^{-1}$), BILP-4³³ ($5,3\text{ mmol}\cdot\text{g}^{-1}$)) bzw. der Einbringung funktioneller Seitengruppen (PPN-6-SO₃NH₄³⁴ ($7,5\text{ mmol}\cdot\text{g}^{-1}$), HAT-CTF 459/600³⁵ ($6,3\text{ mmol}\cdot\text{g}^{-1}$)) exzellente Aufnahmekapazitäten für Kohlenstoffdioxid bei 273 K und 1 bar erzielt werden. Die Vielzahl der Möglichkeiten auf Basis des bereits erlangten Wissens im Bereich der Synthese und postsynthetischen Funktionalisierung poröser organischer Polymere ist bei Weitem noch nicht ausgeschöpft und wird auch weiterhin mit dem Ausbau der Konkurrenzfähigkeit zu anderen CO₂ affinen Materialien wie Zeolithen oder MOFs aufwarten.³⁶

1.3 Brennstoffzellen

Neben den Bemühungen zur Reduktion der anthropogenen Kohlenstoffdioxidemission durch Einbau potenter Filteranlagen in neue und bereits bestehende Kraftwerke ist die Suche nach alternativen umweltfreundlichen Energieträgern eine der primären Bestrebungen aktueller Forschung und Entwicklung. Neben dem begrenzten Potential der „erneuerbaren Energien“ wie Wind-, Wasserkraft sowie Erdwärme bieten Applikationen auf Basis chemischer Reaktionsmechanismen einen vielversprechenden Ansatz für die Sicherung zukünftiger Energieversorgung. Als prominentester Vertreter sei an dieser Stelle die Brennstoffzellentechnologie zu nennen, welche bereits 1839 von William Grove entdeckt worden ist (Abb. 1).³⁷

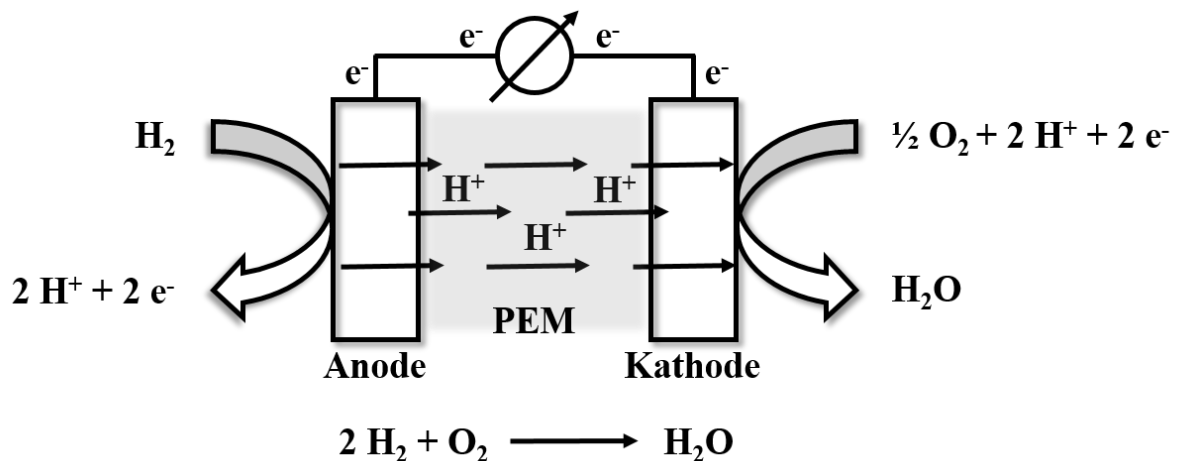
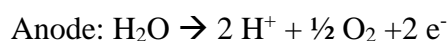
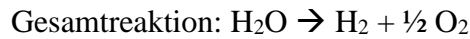


Abbildung 1: Schematische Darstellung eines Membran-Elektroden-Aufbaus als Kern der Brennstoffzelle.

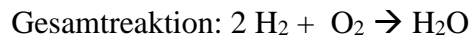
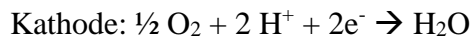
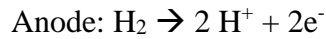
Durch das Eintauchen zweier Platin Elektroden in eine schwefelsaure Lösung konnte dieser nach Anlegen einer Spannung die Elektrolysereaktion von Wasser beobachten.



Einleitung



Ferner konnte durch die Messung eines schwachen Stroms, welcher aus der katalytischen Wasserstoffspaltung an der Platinanode resultiert, die Rückreaktion beobachtet werden.



Die Möglichkeit der Nutzung der bei dieser Reaktion freiwerdenden Elektronen hat im Laufe der Zeit die Weiterentwicklung der Brennstoffzelltechnologie vorangetrieben und erlebte Mitte des 20. Jahrhunderts durch die Applikation in die Apollo und Gemini Raumfahrtprogramme eine Hochzeit.³⁸ Der Preis und die Applikationsbedingungen der damaligen Systeme schlossen eine massentaugliche Verwendung jedoch aus. Der Durchbruch gelang mit dem 1960 von DuPont entwickelten sulfonierten Polyfluorethylen Nafion®, welches als Polymerelektrolytmembran das Kernstück der meisten Wasserstoffbrennstoffzellen darstellt, da sie sowohl als Protonenleiter als auch Elektrodenseparator dient.^{39,40}

Die jedoch immer noch hohen Kosten, die eingeschränkten Arbeitsbedingungen sowie die Umweltunverträglichkeit polyfluorierter Kohlenstoffe erfordern die Entwicklung alternativer Materialien, um die breite Anwendung dieser alternativen Energietechnologie zu ermöglichen. Neben Hochtemperatursystemen wie Kohlenstoffbrennstoffzellen⁴¹ (*Molten Carbonate Fuel Cells; MCFCs*), Metalloxid Brennstoffzellen⁴² (*Solid Oxide Fuel Cells; SOFCs*) sind vor allem Niedrigtemperatursysteme (25 °C – 200 °C) wie Polymerelektrolyt Membran Brennstoffzellen⁴³ (engl.: *polymer electrolyte membrane fuel cells; PEMFCs*) mit ihren prominenten Vertretern der Methanol-⁴⁴ (engl.: *direct methanol fuel cells; DMFCs*) respektive Wasserstoffbrennstoffzelle⁴⁵ (engl.: *hydrogen fuel cell; HFC*) in den Fokus wissenschaftlichen und industriellen Interesses gerückt. Bei der Erforschung und Entwicklung neuer Polymerelektrolytmembranen sind dabei verschiedene Parameter zu beachten, welche sich unter dem Schlagwort „*iron triangle*“ aus Leistungsfähigkeit, Beständigkeit und Kosteneffizienz zusammenfassen lassen (Abb. 2).^{46,47}

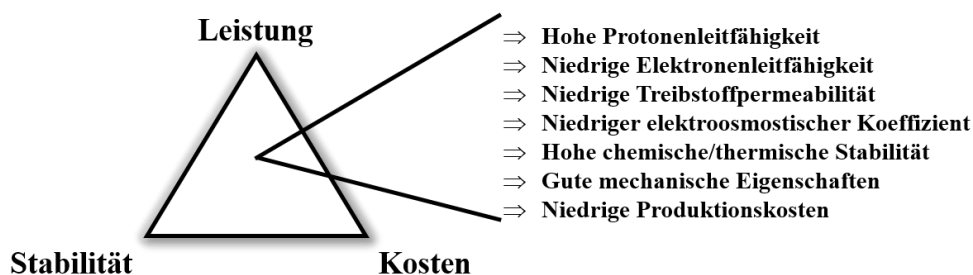


Abbildung 2: Darstellung der bei der Entwicklung neuer Elektrolytmaterialien zu beachtenden Hauptparameter als „Iron Triangle“.^{46,47}

Durch ihre strukturelle Vielfalt und außerordentliche chemische wie auch physikalische Robustheit stellen poröse organische Netzwerke eine interessante Alternative zu bisher verwendeten Materialklassen dar. Ferner bietet die Kombination aus funktionalisierbarem Polymergerüst und intrinsischer Porosität interessante Ausgangspunkte für die Optimierung bisheriger Protonenleitungssysteme. So kann die Eigenschaft zur Protonenleitung sowohl durch die kovalente Anbindung saurer Gruppen als auch durch Einlagerung geeigneter Verbindungen in die Poren eines Netzwerks realisiert werden. Oft geschieht dies in Abhängigkeit des angestrebten Einsatzbereichs.⁴⁸ Für PONs mit wassermediertem Protonenleitung, also einem Einsatzbereich bis ~80 °C, hat sich die synthetische respektive postsynthetische Anbindung von Sulfon- und Phosphorsäuregruppen an das Polymerrückgrat in Kombination mit der Einlagerung von Wasser in das Porensystem als zielführend erwiesen.^{21,49–54} Für die wasserfreie Protonenleitung fand bislang die Einlagerung azidischer (Phosphorsäure) oder amphoterer (Imidazol, Triazol) Moleküle in die Porenstruktur sowie auch der Weg über eine intrinsische Protonenleitung ohne Gastmoleküle Anwendung.^{21,55–58}

1.4 Darstellung poröser organischer Polymere

Die systematische Einteilung poröser organischer Polymere ist nicht eindeutig und erfolgt meist nach Art der organischen Verknüpfung, der Morphologie oder Porosität. Auf Grund der Vielzahl möglicher Bindungsknüpfungen und organischer Linker haben sich daher im Laufe der Jahre Untergruppen wie beispielsweise COFs¹⁵ (engl.: *covalent organic frameworks*), PIMs⁵⁹ (engl.: *polymers with intrinsic microporosity*), HCPs⁶⁰ (engl.: *hypercrosslinked polymers*), CTFs⁶¹ (engl.: *covalent triazine linked frameworks*), PAFs⁶² (engl.: *porous aromatic frameworks*), CMPs⁶³ (engl.: *conjugated microporous polymers*), EOFs⁶⁴ (engl.: *element organic frameworks*) und viele andere gebildet, welche eine näherungsweise Klassifizierung ermöglichen.

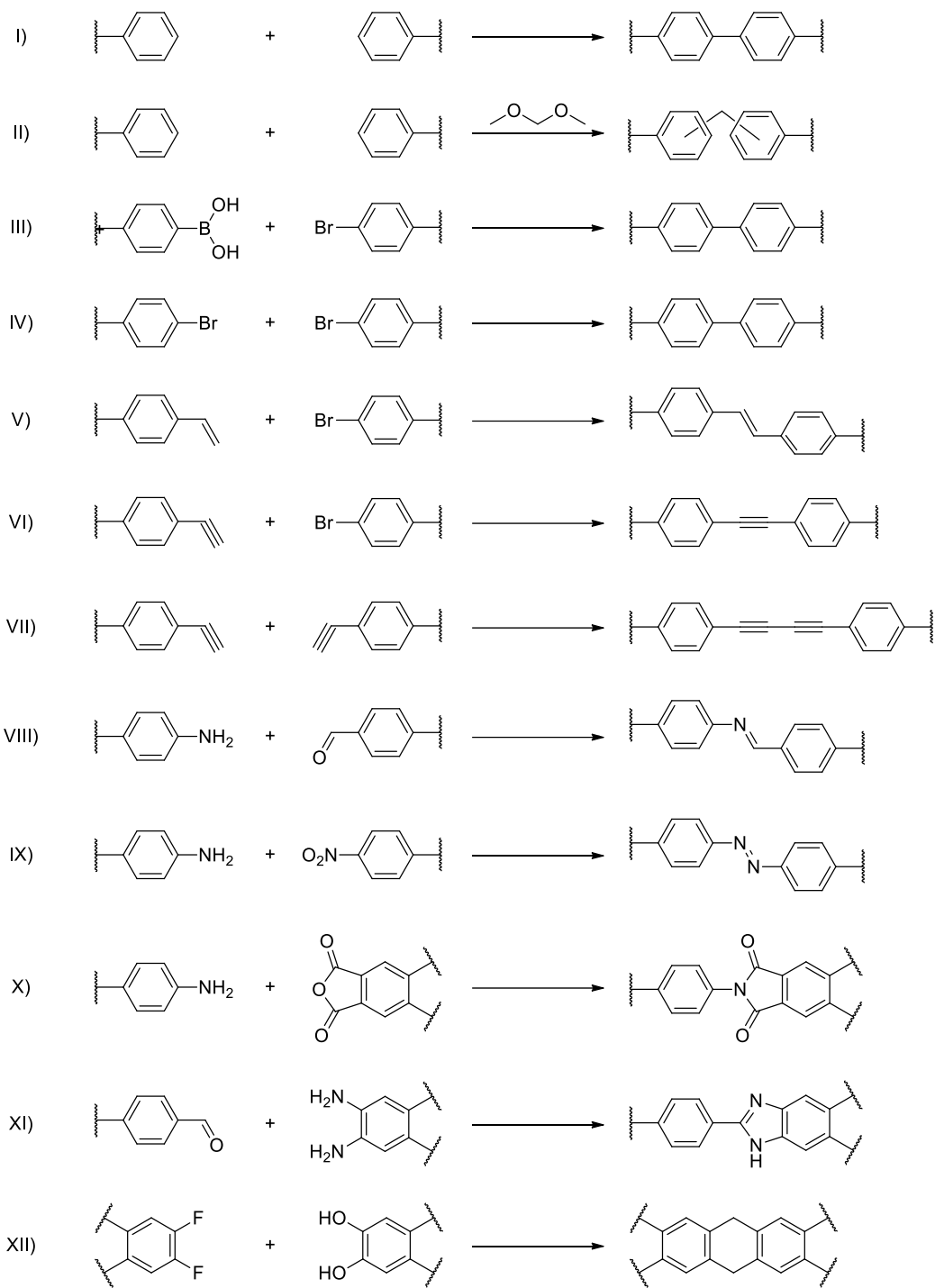
Ein weiterer richtungsweisender Unterschied ist die Darstellung mittels kinetisch oder thermodynamisch kontrollierter Reaktionen. Ein thermodynamisch kontrollierter Prozess ermöglicht gleichzeitig die Assemblierung von Monomeren und deren Polymerisation zu

strukturierten Netzwerken.⁶⁵ Die Kombination mit einer dynamisch, reversiblen Bindungsbildung ermöglicht dem System die Fähigkeit zur „Selbstheilung“, also der Korrektur thermodynamisch unvorteilhafter Bindungen.^{65,66} Die Folge sind kristalline, kovalent verknüpfte, organische Netzwerke mit hoher innerer Oberfläche. Eines der ersten kovalent organischen Netzwerke COF-1 wurde von der Arbeitsgruppe um Omar Yaghi 2005 auf Basis einer molekularen Dehydrierung von Borsäurelinkern zu einer zyklischen Boroxin Einheit synthetisiert (Abb. 3).⁶⁷ Die resultierende zweidimensionale Gerüststruktur zeigt ein π - π induziertes Stapelverhalten, welches in der Ausbildung molekularer Kristallite resultiert. Trotz weiterer Untersuchungen auf Basis von Boroxinen oder Boronatestern, welche ebenfalls kristalline und poröse Netzwerke hervorbrachten, stand die hohe Wasserempfindlichkeit, welche in einer Degradation der kovalent organischen Netzwerke resultierte, der weiteren Entwicklung für technische Aspekte entgegen.⁶⁸ Als eine weitere Klasse der COFs sind die kovalenten Triazin-Netzwerke (CTFs) zu nennen, welche erstmals von der Arbeitsgruppe um Arne Thomas 2013 auf Basis der Trimerisierung von Karbonitrilen in einer Salzsäuremelze synthetisiert wurden.⁶¹ Neben einer exzellenten physikochemischen Stabilität zeigten CTFs eine hohe Affinität für CO₂ sowie katalytische Aktivität, was zu weiterführenden Studien mit einer Vielzahl neuer auf Triazinen basierender Netzwerke geführt hat.^{35,69,70} So sei an dieser Stelle erwähnt, dass unter anderem die extremen Reaktionsbedingungen, welche zu einer Einschränkung in Bezug auf die verwandten Monomere führten, durch einen solvothermalen Reaktionsprozess umgangen und somit die Diversität der CTF Netzwerkmorphologien erhöht werden konnte.⁷¹ Die vielfältigen Applikationsmöglichkeiten in Kombination mit einem durch die kristalline Struktur erleichterten analytischen Zugang haben die Weiterentwicklung von kovalent organischen Netzwerken in den letzten Jahren stark vorangetrieben. Durch entsprechende Synthesebedingungen sind neben den klassisch zweidimensionalen Bor und Triazin basierten Netzwerken auch Imin, Imid und Hydrazon verbrückte kristalline COFs mit zwei- und dreidimensionaler Ausdehnung zugänglich.⁷² Die Gruppe um Rahul Banerjee präsentierte jüngst die Darstellung kovalent organischer Netzwerke im technischen Maßstab über einen mechanochemischen Zugang.⁷³ Dieser Prozess überwindet nun vollends die komplexen Hürden der COF-Synthese und wird das ohnehin schon hohe Interesse an dieser Materialklasse noch weiter steigern.

Die Synthese auf Basis kinetisch gesteuerter Reaktionen führt zu einer Vororganisation der Linkermoleküle in Oligomere und anschließender Polymerisation über meist irreversible Reaktionen.⁶⁵ So führen auch bei reversiblen Bindungsknüpfungen, wie beispielsweise der Iminbindung, die vermeintlichen Reparaturmechanismen auf Grund der Synthesebedingungen nicht zu einer höheren Ordnung des Systems. Dagegen ist der Zugang zu amorphen porösen organischen Netzwerken ausschließlich durch die Vielfalt der organischen und metallorganischen Bindungsknüpfungen begrenzt und wird durch die

Vielzahl an Kombinationsmöglichkeiten der organischen Linker noch erweitert (Abb. 3). Durch die Wahl geeigneter Linkermoleküle lassen sich hochporöse ein-, zwei- und dreidimensionale Netzwerke realisieren, welche durch ausschließlich kovalente Bindungsbildung hohe physikalische und chemische Stabilität aufweisen. Durch gezielte Modifikationen der Linker lassen sich die Netzwerke auf verschiedenste Applikationen anpassen. Ihre strukturelle Integrität ermöglicht ferner die weitere Modifikation über postsynthetische Prozesse durch gezielte Weiterreaktion implementierter funktioneller Gruppen oder aromatischer Ringe, auch unter Anwendung extremer Synthesebedingungen.⁷⁴⁻⁷⁸

Einleitung



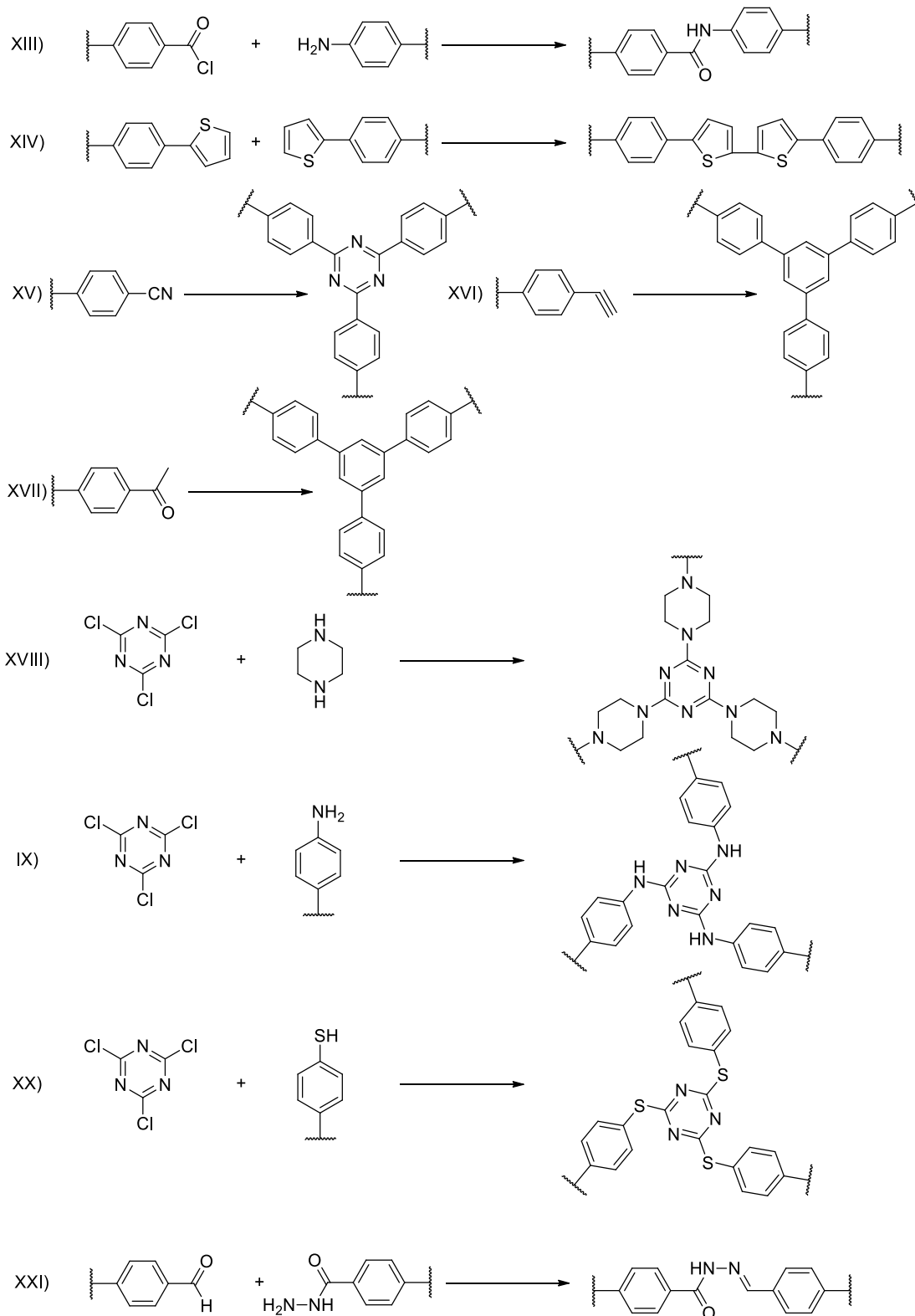


Abbildung 3: Darstellung bei der Synthese von porösen organischen Netzwerken verwendeter Bindungsmechanismen. Als Standardverknüpfungsmuster sind zu nennen I) Scholl-Reaktion⁷⁹, II) Friedel-Craft-Alkylierung⁸⁰, III) Suzuki-Kupplung⁶⁴, IV) Yamamoto-Kupplung⁸¹, V) Heck-Kupplung⁸², VI) Sonogashira-Hagihara-Kupplung⁸³, VII) Ethylanyl-Homokupplung⁸⁴, VIII) Imine⁸⁵, IX) Azo-Kupplung³², X) Imide⁸⁶, XI) Benzimidazole³³, XII) Aromatische nukleophile Substitution⁸⁷, XIII) Amide⁸⁸, XIV) Thiophenyle⁸⁹, XV) Triazine⁶¹, XVI) Ethylanyl-Cyclotrimerisierung⁹⁰, XVII) Benzophenon-Cyclotrimerisierung⁹¹, XVIII) Nucleophile Substitution⁹², IX) Nucleophile Substitution⁹³, XX) Thioether⁹⁴, XXI) Hydrazone¹⁹.

1.5 Physisorptionsanalyse

Die Arbeit mit porösen organischen Materialien im Allgemeinen und auf dem Gebiet der CCS im Besonderen, ob nun organischer, hybrider oder anorganischer Natur, erfordert Kennzahlen, um dem Vergleich der Materialien Genüge zu tun und die Steigerung des wissenschaftlichen Mehrwerts zu gewährleisten. So sind, gemäß der durch die IUPAC vorgeschlagenen Herangehensweise, neben grundsätzlichen Eigenschaften wie der inneren Oberfläche und Porosität vor allem die Aufnahmekapazität, die Adsorptionswärme und die Selektivität poröser Netzwerke für ein spezifisches Gas miteinander zu vergleichen.³ Die Abschätzung der inneren Oberfläche erfolgt hierbei über die Aufnahme von Stickstoff oder Argon Isothermen bei 77 K resp. 87 K bis zu einem relativen Druck $p \cdot p_0^{-1}$ von 1. Aus der Form der Isotherme lässt sich neben ersten Erkenntnissen hinsichtlich des Porengrößenbereichs mithilfe der BET-Gleichung (1) (Mesoporen) bzw. Roquerol-BET-Gleichung (Mikroporen) die innere Oberfläche berechnen.³

$$\frac{1}{W \left[\frac{p}{p_0} - 1 \right]} = \frac{1}{W_m C} + \frac{C - 1}{W_m C} \left(\frac{p}{p_0} \right) \quad (1)$$

Aus der Auftragung von $1/W[(p_0/p)-1]$ als Funktion des relativen Drucks p/p_0 ergibt sich üblicherweise im (Mesoporen) Bereich $0.05 < p/p_0 < 0.35$ ein Linearbereich, aus welchem sich die Werte für die adsorbierte Menge W_m und die BET-Konstante C aus der Steigung s und Achsenabschnitt i über die Gleichungen (2) und (3) ableiten lassen.

$$s = \frac{C - 1}{C W_m} \quad (2)$$

$$i = \frac{1}{W_m C} \quad (3)$$

Aus diesen lässt sich somit mit dem räumlichen Bedarf des Adsorbivmoleküls A_x , dem entsprechenden Molekulargewicht M und der Avogadro Konstante N die absolute Oberfläche des Adsorbens berechnen (4).

$$S_A = \frac{W_m N A_x}{M} \quad (4)$$

Um einen besseren Vergleich zwischen Materialien zu gewährleisten, wird diese in Form der spezifischen Oberfläche, bezogen auf das Probengewicht ($\text{m}^2 \cdot \text{g}^{-1}$) angegeben.

Für Materialien mit Porengrößen, bei denen eine kinetische Hemmung bei Adsorption der oben genannten Analyse-gase zu erwarten ist, wird Kohlenstoffdioxid verwandt.³ Die auf diese Weise beleuchtete Ultramikroporosität ($d_{\text{pore}} < 0.7 \text{ nm}$) wird auf Basis von NLDFT (engl.: *non linear density functional theory*) Berechnung abgeschätzt und ist zusätzlich zu

den durch N₂ oder Ar ermittelten Oberflächen in die Charakterisierung miteinzubeziehen. Auch für Stickstoff und Argon sind entsprechende NLDFT bzw. QSDFT (engl.: *quenched solid state desity functional theory*) Methoden vorhanden, welche die Abschätzung der Porengröße bzw. Volumina ermöglichen.⁹⁵ Bei Betrachtung amorpher poröser organischer Netzwerke sei jedoch zu beachten, dass diese Methoden auf Materialien mit uniformen Poren und nichtfunktionalisierten Porenwänden basieren, bei Abweichungen also die Akkuratessse auf NLDFT resp. QSDFT basierter Berechnungen nicht gewährleistet ist.

Die Untersuchung der Aufnahmekapazität meist technisch relevanter Gase erfolgt ebenfalls über Adsorptionsisothermen von CO₂, CH₄, N₂, H₂O oder H₂. Ein Vergleich verschiedener Materialien erfolgt hierbei meist über die gravimetrische (g·g⁻¹, mmol·g⁻¹, wt%) bzw. volumetrische (cm³·cm⁻³) Aufnahmekapazität des Reingases bei einem Druck von 1 bar bei 273 K.³⁶ An dieser Stelle sei erwähnt, dass für die Aufnahme von CO₂ nach Verbrennungsprozessen Umgebungsbedingungen von min. 40 °C bei einem Druck von 1 bar vorherrschen und somit bei Vergleich verschiedener Aufnahmekapazitäten zu beachten sind.³⁶ In direktem Zusammenhang mit der Aufnahmekapazität der zu untersuchenden Materialien für ein spezifisches Gas steht die isostere Adsorptionswärme als Maß der Stärke der Wechselwirkung zwischen Adsorbiv (Gastmolekül) und Adsorbens (Oberflächendonor).⁹⁶ Dabei wird die beim Übergang des Adsorbivs aus der dreidimensionalen Gasphase in das an der Materialoberfläche gebundene zweidimensionale Adsorbent freiwerdende Energie aus dem Vergleich gleicher Oberflächenbenetzungsgrade bei unterschiedlichen Temperaturen betrachtet.⁹⁷ Neben Clausius Clapeyron oder Langmuir basierter Berechnung der Adsorptionswärme Q_{st} eignet sich vor allem die *zero-coverage isosteric heat of adsorption* Methodik zur Abschätzung der stärksten Wechselwirkungen im Material. Es wird hierbei angenommen, dass die Adsorptionswärme mit steigender Oberflächenbenetzung abnimmt. Die Berechnung von Q_{st} erfolgt nach Gleichung (5).⁹⁷

$$Q_{st} = -m \cdot R \quad (5)$$

In diesem Zusammenhang bezeichnet R die allgemeine Gaskonstante ($R = 8.314 \text{ J} \cdot \text{mol}^{-1} \cdot \text{K}^{-1}$) und m mit $\text{dln}(p)/\text{d}(1/T)$ die Steigung aus dem im Arrhenius Diagramm aufgetragenen Druck (p) gleicher Oberflächenbenetzung als Funktion der reziproken Temperatur (T).⁹⁷

Für eine anwendungsbezogene Betrachtung poröser Materialien im Bereich der Gassorption und Separation ist spezifische Selektivität für eine Gasspezies im Gasgemisch von entscheidender Bedeutung. In Anlehnung an potentielle Applikationsbereiche stehen hierbei vor allem Gemische aus CO₂/N₂ (Verbrennungsprozesse), CO₂/H₂O (Verbrennungsprozesse), CO₂/H₂ (Treibstoffreinigung) und CO₂/CH₄ (Naturgasveredelung) im Fokus des wissenschaftlichen Interesses.⁷ Für eine nähere Untersuchung der Selektivität haben sich verschiedene direkte Methoden, wie die

Einleitung

gravimetrische Bestimmung von Gasgemischen, dynamische Sorptionsverfahren und Durchbruchsexperimente, sowie indirekte Methoden, wie die Berechnung von Zweikomponentengemischen auf Basis von Reingasisothermen mittels *Henry* und *IAST* (engl.: *ideal adsorbed solution theory*) Methoden, etabliert. Im Weiteren sollen, mit Hinblick auf die in dieser Arbeit verwandten Methoden, jedoch nur letztere näher erläutert werden.

Bei der Bestimmung der spezifischen Selektivität für ein Gas $S(A)_{IS}$ auf Basis zweier unabhängiger Reingasisothermen mittels der *Initial Slope Henry* Methode ($Henry_{IS}$) wird der jeweilige Niedrigdruckbereich bis 0.1 bar über eine lineare Funktion „angepasst“ und die entsprechenden Steigungen nach Gleichung (6) zueinander ins Verhältnis gesetzt.

$$S(A)_{IS} = \frac{m(A)}{m(B)} \quad (6)$$

Es sei an dieser Stelle darauf hingewiesen, dass es sich bei der $Henry_{IS}$ Methode um ein Modell zur Abschätzung der Selektivität auf Basis direkter Netzwerkwechselwirkung ähnlich zur *zero coverage isosteric heat adsorption* handelt. Bei der ursprünglichen Henry Methode dagegen wird die gesamte Isotherme und somit die Gasaufnahme über den gesamten Druckbereich nach Gleichung (7) beschrieben.³⁶

$$\ln(P) = \ln(N) + \frac{1}{T} \sum_{i=1}^m a_0 N^i + \frac{1}{T} \sum_{j=1}^n b_0 N^j \quad (7)$$

Hierbei entsprechen a_0 und b_0 den Virialkoeffizienten der Isothermen, P dem Druck und N der Menge adsorbierter Moleküle. Die Henry-Konstante K_H errechnet sich nunmehr aus den Werten der Virialkoeffizienten (7) nach (8)

$$K_H = e^{(-b_0)} * e^{\left(\frac{-a_0}{T}\right)} \quad (8)$$

, woraus sich durch anschließendes Einsetzen in (9)

$$S_{ij} = \frac{K_{Hi}}{K_{Hj}} \quad (9)$$

die entsprechenden Henry-Selektivitäten für ein Zweikomponentengasgemisch (i, j) ergeben.

Eine Methode für die spezifischere Abschätzung der Selektivitäten für Gasgemische bestimmter Zusammensetzung ist die *ideal adsorbed solution theory* (IAST-Methode). Diese beruht auf den Annahmen idealen Gasverhaltens der Adsorptive, deren thermodynamischer Inertheit sowie einer Temperaturinvarianz der untersuchten Materialoberfläche. Durch die Beschreibung der Reingasisothermen mittels (*single-site* respektive *dual-site*) Langmuir-Freundlich-Methodik (10)

$$q_i = \sum_{i=1}^n q_{i,sat.} \frac{b_i p^{v_i}}{1 + b_i p^{v_i}} \quad (10)$$

lässt sich die molare Kapazität q_i der jeweiligen Einzelgaskomponenten berechnen. Hierbei entspricht $q_{i,sat.}$ der Sättigungskapazität der Gasspezies i bei der jeweiligen Langmuir-Freundlich-Konstante und p^{v_i} dem jeweiligen Gasphasendruck von i . Über die molare Kapazität q_i lässt sich nunmehr die Selektivität für ein Zweikomponentengemisch beliebiger Zusammensetzung nach (11) berechnen.³⁶

$$S = \frac{\left(\frac{q_1}{q_2}\right)}{\left(\frac{p_1}{p_2}\right)} \quad (11)$$

Wobei $p_{1,2}$ dem jeweiligen Gasdruck der Einzelgaskomponenten entspricht. Ein prominentes Beispiels ist hier die Simulation eines Verbrennungsgasgemischs von CO_2/N_2 mit der Zusammensetzung 0,15 : 0,85.⁷

1.6 Impedanzspektroskopie

Entgegen ihrem hohen Potential steht die Investigation poröser organischer Polymere als alternative Festkörperelektrolytmaterialien noch in den Anfängen und vor allem hinsichtlich des Verständnisses der zugrundeliegenden Leitungsmechanismen. Es sei erwähnt, dass hier vor allem das analytische Potential bislang noch kaum ausgeschöpft worden ist. Bei der Charakterisierung potentieller Festkörperelektrolyte fällt der Bestimmung der Protonenleitfähigkeit des Materials eine tragende Rolle zu. Durch die vielen Einflüsse auf die spezifische Leitfähigkeit wie Materialstruktur, Funktionalität, Morphologie, Ionenart etc. ist diese nicht als Standardprozedur, sondern vor dem Hintergrund des Wissens um das zu untersuchende Material zu betrachten, da sich nur so Artefakte wie Oberflächenleitung, Korngrenzen, Symmetriebrüche, Dislokationen oder Fremdphasen ausschließen lassen.⁹⁸ Als aussagekräftigste Methoden zur Messung des Ladungstransports sind an dieser Stelle die elektrochemische Impedanzspektroskopie (engl.: *electrochemical impedance spectroscopy*; *EIS*) sowie die Feldgradienten NMR Spektroskopie (engl.: *pulsed magnetic field gradient spin echo NMR*; *PGSE*- respektive *PFM-NMR*) zu nennen.⁹⁸ Vor dem Hintergrund dieser Arbeit sei im Folgenden jedoch nur auf erstere näher einzugehen.

Die elektrochemische Natur der zu beobachtenden Prozesse erlaubt ihre Untersuchung mittels elektrotechnischer Methoden, was Vorteile hinsichtlich kurzer Messzeiten, hoher Messgenauigkeit und die Möglichkeit kontinuierlicher Messungen birgt.⁹⁹ Die wohl bekannteste Methode zur Messung von Ionenbewegung ist hier die elektrochemische Impedanzspektroskopie, bei der durch Anlegen eines Wechselstrompotentials U an die

Einleitung

Probe das induzierte Wechselstromsignal I gemessen und somit der daraus resultierende komplexe Wechselstromwiderstand Z (Impedanz) ermittelt wird. Hierzu wird eine schwache, sinusoidale Wechselspannung (12) (ca. 1-10 mV)

$$U = U_0 \sin(\omega t) \quad (12)$$

mit einer Amplitude U_0 und der Kreisfrequenz ω angelegt, um ein pseudolineares und somit ebenfalls sinusoidales Strom-Antwortsignal I (13) zu erhalten, welches jedoch in der Phase φ verschoben ist.

$$I = I_0 \sin(\omega t + \varphi_I) \quad (13)$$

Auf Basis der Ohm'schen Regel (14) lässt sich die Impedanz Z somit als Funktion der Magnitude Z_0 und der Phasenverschiebung φ darstellen.

$$Z = \frac{U}{I} = \frac{U_0 \sin(\omega t)}{I_0 \sin(\omega t + \varphi_I)} = Z_0 \frac{\sin(\omega t)}{\sin(\omega t + \varphi_I)} \quad (14)$$

Um eine einfachere mathematische Behandlung der zeitabhängigen Größen zu gewährleisten, erfolgt die Darstellung der Impedanz häufig im Komplexen. Gemäß der Eulerschen Formel (15) lässt sich die Impedanz nach der Transformation somit in Real- und Imaginärteil aufspalten (16).

$$e^{(i\varphi)} = \cos\varphi + i\sin\varphi \quad (15)$$

$$Z = \frac{U}{I} = Z_0 e^{(i\varphi)} = Z_0 (\cos\varphi + i\sin\varphi) \quad (16)$$

Die Auftragung des Realteils der Impedanz auf der x-Achse und des Imaginärteils auf der y-Achse resultiert in der Nyquist (bzw. Argand)¹⁰⁰ Darstellung, wobei jeder Messpunkt des Halbkreises die Impedanz bei einer bestimmten Frequenz ω repräsentiert (Abb. 4, links). Hierbei sei zu beachten, dass der hochfrequente Bereich ($\omega \rightarrow \infty$) im Realteil Richtung niedrige Impedanz und der niederfrequente Bereich ($\omega \rightarrow 0$) gegen hohe Impedanzen läuft (Abb. 4, links). Für die direkte Abbildung des frequenzabhängigen Widerstands eignet sich dagegen die Bode-Auftragung (Abb. 4, rechts), welche die Impedanz als Funktion der Frequenz zeigt.¹⁰⁰ Es sei an dieser Stelle erwähnt, dass bei der Auswertung von Impedanzdaten stets beide Darstellungsformen zu berücksichtigen sind.

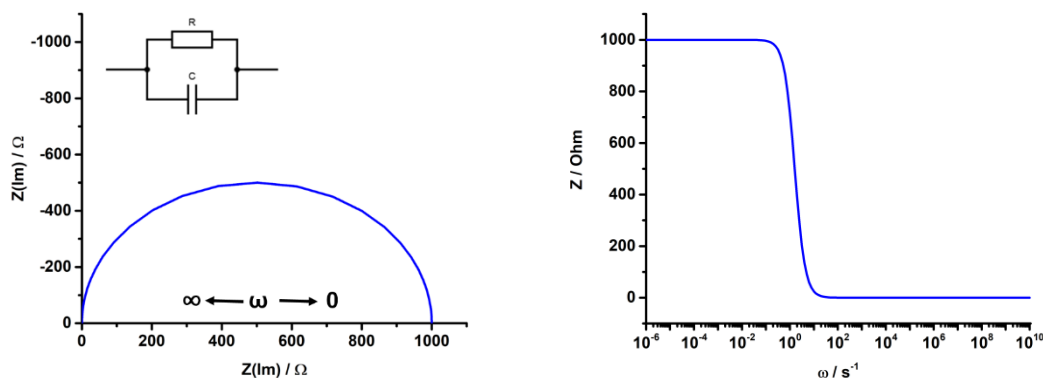


Abbildung 4: Nyquist-(links) und Bode-(rechts) Auftragungen des abgebildeten Ersatzschaltkreises mit einem Widerstand von 1000 Ohm und einer Kapazität von 0.0001 F.

Wie in Abbildung 4 ersichtlich, lassen sich Impedanzdaten durch elektrische Ersatzschaltkreise beschreiben. Durch entsprechende Programme lassen sich somit aufgenommene Datensätze durch elektrische Elemente wie beispielsweise Widerstände ($Z = R$), Kapazitäten ($Z = (i\omega C)^{-1}$) oder Induktoren ($Z = i\omega L$) wiedergeben, was die Zuordnung komplexer elektrochemischer Zusammenhänge ermöglicht. So lässt sich der Verlauf des in Abbildung 4 dargestellten Halbkreises mit dem Kurzschluss der Kapazität bei hohen Frequenzen, und der daraus resultierenden abfallenden Impedanz, und dem Fließen des Stroms ausschließlich über den Widerstand bei niedrigen Frequenzen erklären. Es sei an dieser Stelle darauf verwiesen, dass sich der Kurvenverlauf oft komplexer als hier dargestellt gestaltet und somit die Wahl komplizierter Ersatzschaltkreise und elektrischer Elemente erfordert (s. Anhang).

Ist der komplexe Widerstand der Ionenbewegung ermittelt, wird dieser für die Charakterisierung eines Materials meist in die spezifische Ionenleitfähigkeit κ umgerechnet. Hierzu werden die Parameter der zu messenden Probe in (17) mit einbezogen, wobei l der Länge

$$\kappa = \frac{l}{R \cdot A} \quad (17)$$

der Probe (cm) und A der Fläche (cm²) entspricht. Die spezifische Leitfähigkeit ist in S·cm⁻¹ anzugeben.

2. Synopsis

Den Kernpunkt der Dissertation bilden die im Folgenden aufgeführten drei Publikationen sowie ein Manuskript. Vor dem Themenschwerpunkt der Porosität werden hier organische Polymere in den potentiellen Anwendungsgebieten der Gassorption und -separation sowie der Protonenleitung betrachtet. Das Hauptinteresse gilt dabei der Untersuchung des Einflusses von Porosität und Funktionalität auf die spezifischen Eigenschaften der Netzwerke.

In der Publikation „*Microporous Organic Polyimides for CO₂ and H₂O Capture and Separation from CH₄ and N₂ Mixtures: Interplay between Porosity and Chemical Function*“ wird anhand von fünf neuartigen Polyimidnetzwerken systematisch der Einfluss der Porosität gegenüber intrinsischer Funktionalität auf die selektive Aufnahmekapazität von technisch relevanten Gasen herausgearbeitet. Im Fokus der Arbeit standen neben der Synthese von fünf neuartigen Polyimiden, die Investigation des Physisorptionsverhaltens gegenüber Kohlenstoffdioxid, Methan und Wasserdampf. Hier konnte eine Korrelation der Aufnahmekapazität für Kohlenstoffdioxid und Wasser mit der Ultramikroporosität der Polymere beobachtet werden, während die Selektivität gegenüber Methan und Stickstoff zusätzlich von der Art der funktionellen Gruppen dominiert wird.

In der fortführenden Arbeit „*BILP-19 – An Ultramicroporous Organic Network with Exceptional Carbon Dioxide Uptake*“ konnten die vorherigen Erkenntnisse bezüglich der Einflüsse von Porosität und Funktionalität auf ein selektives Sorptionsverhalten aufgegriffen und umgesetzt werden. Das Ergebnis stellt ein ultramikroporöses Polymer aus der Klasse der Benzimidazole dar, welches durch eine feine Porenstruktur in Kombination mit einer außerordentlich hohen Dichte funktioneller Gruppen eine erstklassige Kapazität für Kohlenstoffdioxid aufweist. Neben der Darstellung eines neuartigen Polybenzimidazols stand hier vor allem die Untersuchung und Aufklärung der Sorptionsdynamik im Vordergrund.

Ein, hinsichtlich einer potentiellen Applikation, thematischer Wechsel wird mit der Veröffentlichung „*Water mediated Proton Conduction in a Sulfonated Microporous Organic Polymer*“ eingeleitet. Kernthema ist die postsynthetische Funktionalisierung eines bekannten, mesoporösen Materials mit sowohl etablierter als auch neuartiger Sulfonierungsmethodik und eine anschließende Untersuchung hinsichtlich wasservermittelter Protonenleitung. Im Fokus standen hier vor allem die Einflüsse der Porosität sowie der Grad der funktionalisierten Porenumgebung auf die Leitfähigkeit. Neben einer hohen Protonenleitfähigkeit für das dargestellte Polymer, wurde zudem die Wanderung der Ionen durch die Porenstruktur als vorherrschender Mechanismus herausgearbeitet.

Eine Fortsetzung der Thematik bildet das Manuskript „*Anhydrous Proton Conduction in Porous Organic Networks*“. Die Möglichkeit der Wanderung von Protonen durch die Systemkavitäten in Form von Leitungspfaden bildete hierbei den Ausgangspunkt weiterführender Investigationen. Vor dem Hintergrund der wasserfreien Protonenleitung werden hier systematisch die Einflüsse von Struktur, Porosität, Funktionalität und Gastbeladung auf die Protonenleitfähigkeit diskutiert. Den Ausgangspunkt bilden sechs strukturell unterschiedliche Netzwerke, welche postsynthetisch mit dem amphoteren Heterozyklus Imidazol beladen wurden.

2.1 Microporous Organic Polyimides for CO₂ and H₂O Capture and Separation from CH₄ and N₂ Mixtures: Interplay between Porosity and Chemical Function

Thematisch ist diese Publikation der Investigation poröser organischer Netzwerke auf ihre Gassorptions- und Separationseigenschaften hinsichtlich der Aufbereitung industriell relevanter Gasgemische vor und nach Verbrennungsprozessen zuzuordnen. Im Fokus steht hier der Einfluss von Struktur und Funktionalität auf das Sorptions- und Selektionsverhalten gegenüber Kohlenstoffdioxid, Methan, Stickstoff und Wasserdampf. Den Ausgangspunkt der systematischen Studie, bildet die Synthese von fünf neuartigen mikroporösen organischen Polyimiden (MOPIs), welche sich hinsichtlich ihrer Porosität sowie funktioneller Seitengruppen unterscheiden (Abb. 5).

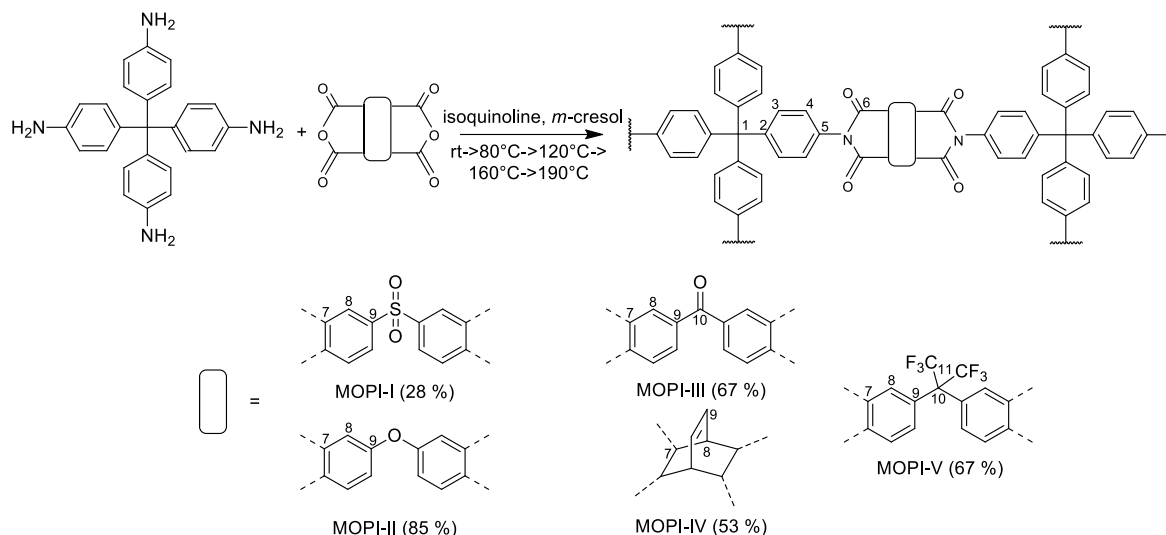


Abbildung 5: Schema der synthetischen Darstellung mikroporöser organischer Polyimide sowie die Wahl der in dieser Arbeit verwandten funktionellen Gruppen.

Die strukturelle Charakterisierung der Netzwerke erfolgte durch Methoden der ¹³C und ¹⁵N NMR Spektroskopie, Infrarotspektroskopie, PXRD-, TG- sowie der CHN-Analyse, welche für alle Polymere sowohl eine strukturelle Integrität als auch einen hohen Vernetzungsgrad bestätigte. Im Fokus stand jedoch vor allem die Untersuchung der inneren Oberfläche, der Porosität sowie der Porengrößenverteilung der Netzwerke durch BET- (Brunauer, Emmet,

Teller) und DFT- (Dichtefunktionaltheorie) Methoden, basierend auf Argon und CO₂ Physisorptionsisothermen. Die Netzwerke zeigten BET-Oberflächen von 220 m²·g⁻¹ (MOPI-I) bis 930 m²·g⁻¹ (MOPI-V) (Abb. 6) sowie Porengrößen im Mikro- wie auch im kleinen Mesoporenbereich. Zusätzlich zeigten die Polymere ultramikroporösen Charakter, welcher mittels CO₂ isothermen aufgelöster Oberflächen im Bereich von 676 m²·g⁻¹ (MOPI-II) bis 896 m²·g⁻¹ (MOPI-IV) erschlossen werden konnte (Abb. 6).

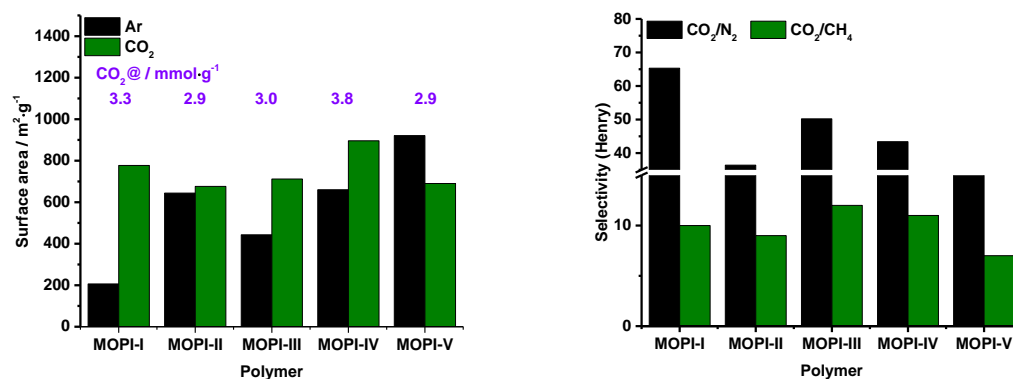


Abbildung 6: Vergleich von Ar und CO₂ Oberflächen der Polymere mit Bezug auf ihre CO₂-Aufnahmekapazität bei 273 K und 1 bar (links). Vergleich der Kohlenstoffdioxid-Selektivität gegenüber Stickstoff und Methan bei 273 K, basierend auf der Henry Methode (rechts).

Durch Reingasisothermen bis zu einem Maximaldruck von 1 bar wurde die jeweilige Aufnahmekapazität der einzelnen Polymere ermittelt. Die CO₂ Aufnahme der hier betrachteten Netzwerke wurde auf Werte zwischen 2,9 mmol·g⁻¹ (MOPI-II, -V) und 3,8 mmol·g⁻¹ (MOPI-IV) bei 273 K und 1 bar bestimmt (Abb. 6). Es wurde festgestellt, dass diese direkt mit der Ultramikroporosität des Netzwerks korreliert, während die Höhe der durch Ar bestimmten Oberfläche keinen direkten Zusammenhang aufweist (Abb. 6). Auch der Einfluss der funktionellen Seitengruppen scheint für die Einlagerung von Kohlenstoffdioxid nur marginal zu sein, da das nicht funktionalisierte MOPI-IV die höchste Aufnahme zeigt. Die Aufnahmekapazitäten Methan und Stickstoff fallen mit Maximalwerten von 0,83 mmol·g⁻¹ (MOPI-IV) bzw. 0,11 mmol·g⁻¹ (MOPI-I) bei 273 K und 1 bar im Vergleich zu Kohlenstoffdioxid nur gering aus.

Die selektive Aufnahme von Kohlenstoffdioxid gegenüber Methan und Stickstoff wurde auf Basis von Reingasisothermen der entsprechenden Komponente für verschiedene industriell relevante Mischungsverhältnisse (Verbrennungsprozesse, Natur- und Deponiegasveredelung) berechnet.⁷ Die durch die Henry-Methode¹⁰¹, also dem Vergleich des Anstiegs der Niedrigdruckisothermen, errechneten Selektivität für Gasgemische aus sowohl CO₂/N₂ als auch CO₂/CH₄ zeigen die besten Werte für MOPI-I (CO₂/N₂ = 66; 273 K) und MOPI-III (CO₂/CH₄ = 12, 273 K) und somit für Netzwerke mit sehr polaren Seitengruppen, während die schwächsten spezifischen Wechselwirkungen jeweils bei MOPI-V (CO₂/N₂ = 26; CO₂/CH₄ = 7; 273 K) verblieben (Abb. 6). Im Gegensatz zur reinen

Aufnahmekapazität, zeigte somit die Wahl der funktionellen Seitengruppe entscheidenden Einfluss für die Selektivität eines Netzwerks.

Eine Sonderstellung dieser Arbeit nimmt die Wasserdampfadsorption ein. Neben der Rolle als potentiell Coadsorbens zu Kohlenstoffdioxid wurde die Wasseraufnahme auch vor dem Hintergrund der potentiellen Applikation der dargestellten Netzwerke als Wasserspeicher betrachtet.

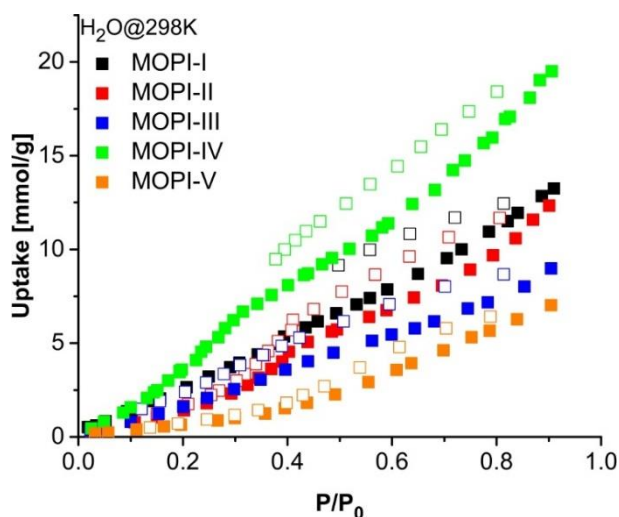


Abbildung 7: Wasserdampfadsorptionsisothermen der hier dargestellten MOPIs, aufgenommen bei 298 K.

In Kooperation mit der Arbeitsgruppe um N. Stock (Christian-Albrechts-Universität zu Kiel) wurde die Wasseraufnahmekapazität der Polymere bei Raumtemperatur auf bis zu $19,5 \text{ mmol}\cdot\text{g}^{-1}$ (MOPI-IV) bei 1 bar bestimmt (Abb. 7). Ähnlich der Aufnahme von Kohlenstoffdioxid korreliert die Wasseraufnahme mit der Ultramikroporosität des Netzwerks. Bemerkenswert ist hier die vergleichsweise stark reduzierte Aufnahme von MOPI-V ($7 \text{ mmol}\cdot\text{g}^{-1}$).

Die Berechnung der spezifischen Wechselwirkung, in Form der $\text{H}_2\text{O}/\text{CO}_2$ - Selektivität, weist auf einen signifikanten Einfluss der $\text{R}(\text{CF}_3)_2$ Funktionalität auf ebendiese hin. Sie wurde für MOPI-V auf einen Wert von 36 errechnet, während dem nicht funktionalisierten MOPI-IV mit 105 die höchste Affinität für Wasser zuzuordnen ist.

Als Fazit der Veröffentlichung sei somit der Trend zur Korrelation der Aufnahmekapazität mit der Ultramikroporosität eines Netzwerks zu nennen. Der Funktionalität kommt hier eine eher untergeordnete Rolle zu, während sie bei der spezifischen Wechselwirkung der Polymere im Gasgemisch zu dominieren scheint.

2.2 BILP-19 – An Ultramicroporous Organic Network with Exceptional Carbon Dioxide Uptake

Die Kombination einer ultramikroporösen Netzwerkstruktur mit einem hohen Funktionalisierungsgrad sollte sich auf Basis der vorangegangenen Arbeit als zielführend für die Darstellung CO_2 affiner Systeme herausstellen. Basierend auf den Erfolgen der auf Benzimidazol basierenden Polymere von El-Kaderi^{33,102,103}, wurde dies durch die Wahl sterisch kleiner Wiederholungseinheiten sowie einer zweidimensionalen Netzwerkstruktur realisiert (Abb. 8).

Synopsis

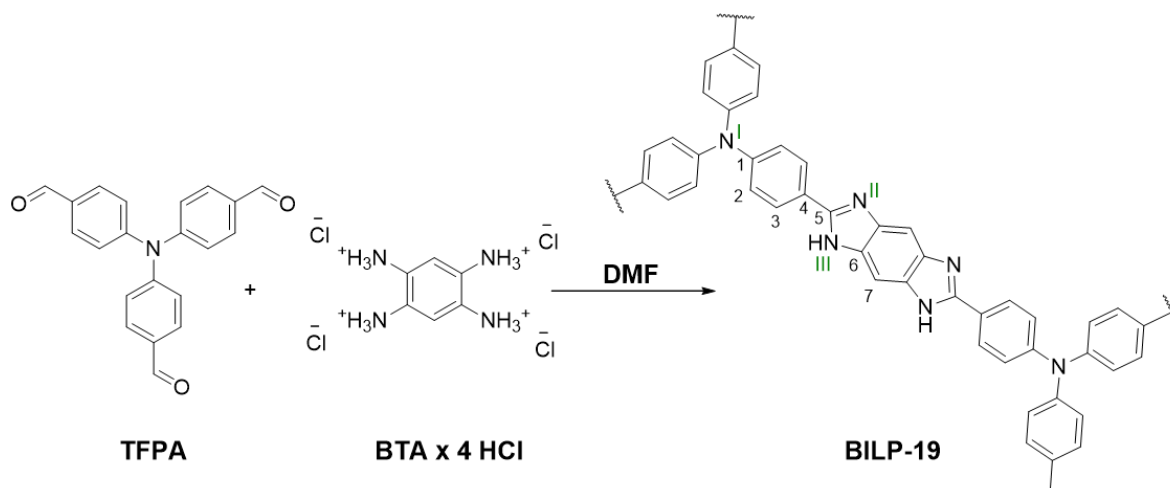


Abbildung 8: Schematische Darstellung der Synthese von BILP-19.

Gestützt durch IR-Spektroskopie und CHN Analyse bestätigt die Zuordnung der Signale aus ^{13}C und ^{15}N NMR CP Spektroskopie eine nahezu komplette Vernetzung der Linker. Die kovalente Bindung zwischen Kohlenstoff und Stickstoff führt zu einer hohen thermischen Stabilität des Netzwerks, welche mittels thermogravimetrischer Analyse auf $500\text{ }^\circ\text{C}$ bestimmt wurde. Die durch die planaren Linker dirigierte zweidimensionale Struktur des Netzwerks wurde durch die Rasterelektronenmikroskopie abgebildet (Abb. 9).

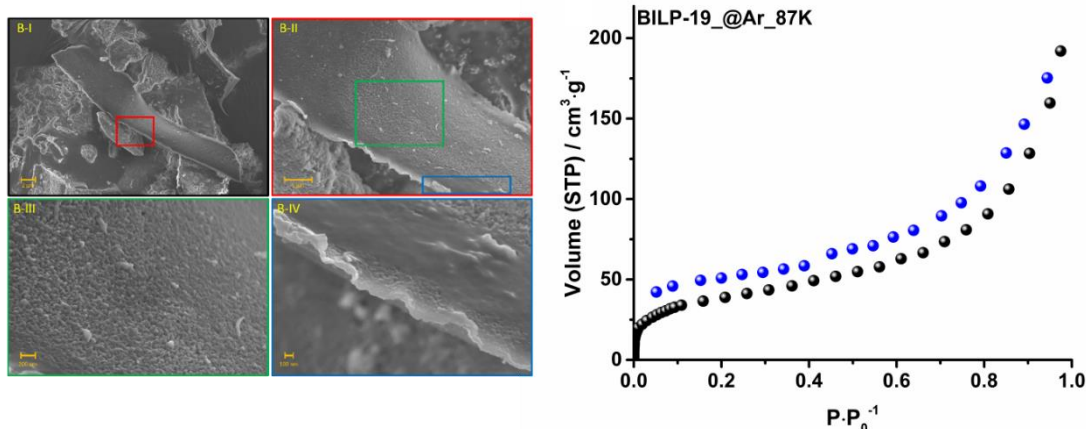


Abbildung 9: Rasterelektronische Aufnahmen eines BILP-19 Plättchens (links). Argon Isotherme, gemessen bei 87 K (rechts).

Die Charakterisierung der inneren Oberfläche und Porosität erfolgte durch Argon und Stickstoffisothermen und ergaben BET- Oberflächen von $144\text{ m}^2\cdot\text{g}^{-1}$ bzw. $252\text{ m}^2\cdot\text{g}^{-1}$. Die Typ II Form der Isothermen in Kombination mit einer Typ III Hysterese deutete hier auf nicht- bzw. makroporöse Plättchen hin (Abb. 9).³ Die Abschätzung der Ultramikroporosität ($d_{\text{Pore}} < 0,7\text{ nm}$), basierend auf bei 273 K gemessenen CO_2 Isothermen, erbrachte indessen eine innere Oberfläche von $1325\text{ m}^2\cdot\text{g}^{-1}$. Somit ist von einem nur für CO_2 , nicht aber für N_2 oder Ar zugänglichen Porenvolumen auszugehen. Das Netzwerk zeigte eine Aufnahmekapazität für Kohlenstoffdioxid von $6\text{ mmol}\cdot\text{g}^{-1}$ (Abb. 10). Bei steigender Temperatur nimmt diese zwar bis auf $4,5\text{ mmol}\cdot\text{g}^{-1}$ bei 313 K ab, übertrifft aber die meisten

literaturbekannten porösen Polymere und metallorganischen Netzwerke. Bemerkenswert sind die stark ausgeprägten, für Kohlenstoffdioxid eher untypischen, Hysteresen, welche auf Atmungseffekte hindeuten (Abb. 10).

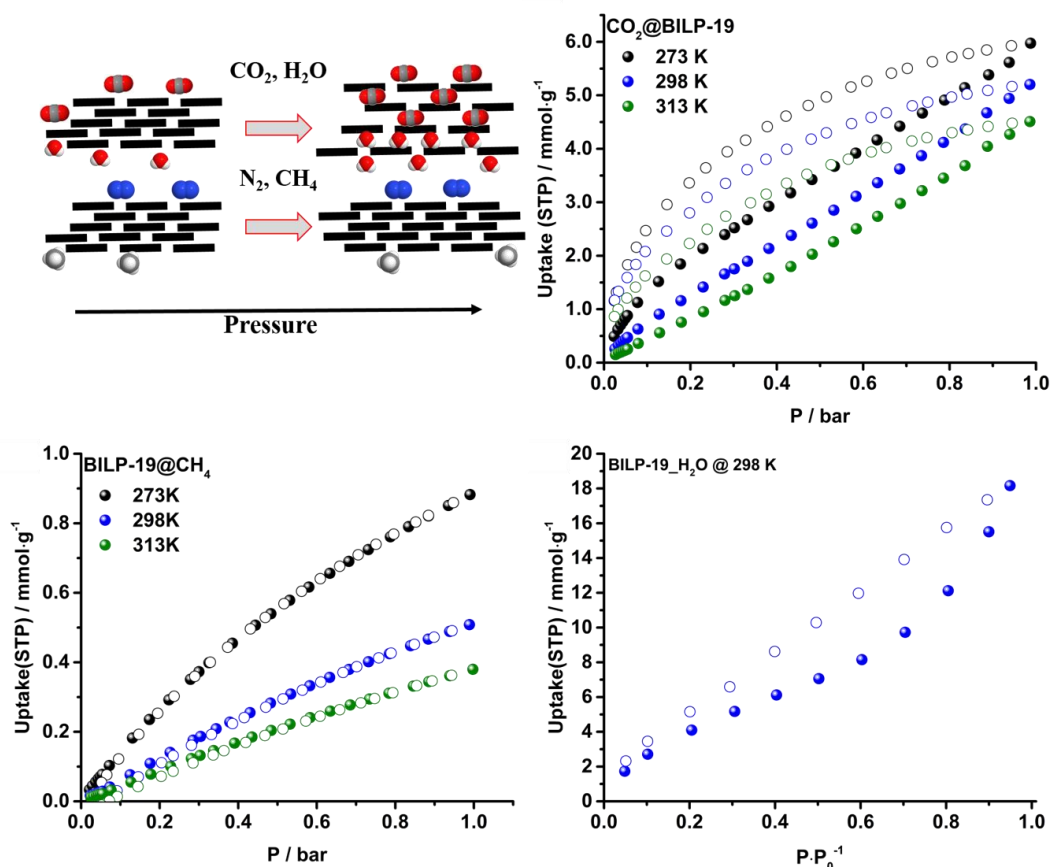


Abbildung 10: Schematische Darstellung des postulierten Mechanismus der selektiven Gasaufnahme von BILP-19 nebst zugrundeliegender Kohlenstoffdioxid, Methan und Wasseradsorptionsisothermen.

Ferner konnte mittels einer Wassersorptionsisotherme, gemessen bei 298 K, eine Wasser-einlagerung von 18 mmol·g⁻¹ beobachtet werden. Die im Gegensatz hierzu stehende niedrige Affinität für Stickstoff (0,11 mmol·g⁻¹, 298 K) und Methan (0,88 mmol·g⁻¹, 273 K) führt im Weiteren zu IAST Selektivität von 60 bzw. 12 für eine theoretische Gasgemischkomposition von 15/85 (CO₂/N₂(CH₄)). Die Ausbildung einer Hysterese bleibt sowohl bei Stickstoff als auch bei den Methanisothermen aus (Abb. 10).

Auf Grundlage des Sorptionsverhaltens sowie der zweidimensionalen Struktur wurde für den Aufnahmemechanismus ein selektives Schwellverhalten des Polymers postuliert. Hierbei ermöglicht die ultramikroporöse Struktur gröÙenselektiv ausschließlich die Penetration von Kohlenstoffdioxid und Wasser, worauf ein Aufquellen der Schichten folgt, was bis dato unzugänglichen Porenraum freigibt (Abb. 10). Dieser ist anhand der auftretenden Hysterese zu beobachten. Der hohe Anteil funktioneller Gruppen sorgt hierbei für die nötige Triebkraft. Bei Methan und Stickstoff hingegen bleibt dies auf Grund des

größenselektiven Ausschlusses aus (Abb. 10). Hier ist keine Hysterese zu beobachten. Zusammenfassend konnte im Zuge der Publikation erneut die tragende Rolle der Ultramikroporosität in Kombination mit einer dichten Verteilung polarer funktioneller Gruppen bei der selektiven Adsorption von Kohlenstoffdioxid aufgezeigt werden.

2.3 Water mediated Proton Conduction in a Sulfonated Porous Polymer Network

Während sich in den vorangegangenen Arbeiten die Synthese von Netzwerken mit einer möglichst hohen Ultramikroporosität als zielführend erwiesen hat, wurde für die Darstellung protonenleitender Systeme ein alternativer Ansatz verfolgt. In Anlehnung an das industriell erfolgreiche Fluoropolymer Nafion® sollte die Einbringung von Schwefelsäure in das Polymerrückgrat die Eigenschaft zu wasservermittelten Protonenleitung realisieren. Hierbei wurde vor allem im Bereich des Feuchtigkeitsmanagements, auf Grund von attraktiver Wechselwirkungen mit der Materialoberfläche, ein großer Einfluss der hochporösen Netzwerkstruktur erwartet. Um eine möglichst hohe Ladungsträgerkonzentration in Kombination mit in Porenkanälen eingelagertem Wasser zu erreichen, sollte das mesoporöse organische Polymer PAF-1 als Testsystem dienen (Abb. 11). Dies zeichnet sich sowohl durch eine ausgezeichnete Stabilität als auch durch eine hohe Porosität aus.

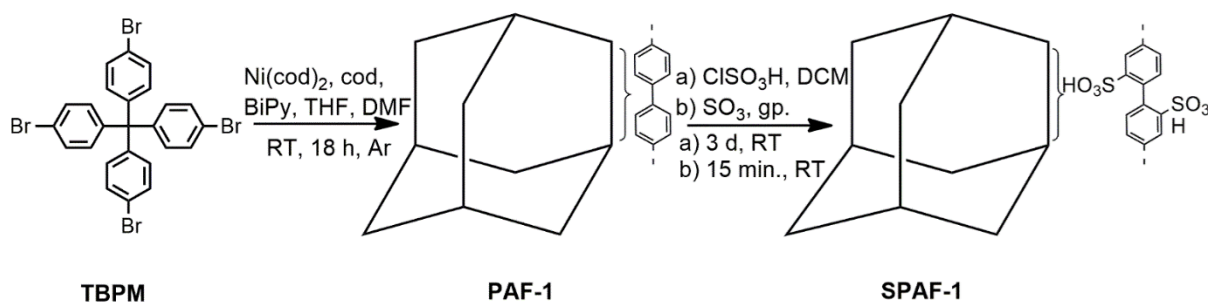


Abbildung 11: Schema der Synthese sowie postsynthetischen Modifizierung von PAF-1. Während "a)" die Bedingungen der lösemittelbasierten Sulfonierung beschreibt, zeigt "b)" die der Gasphasensulfonierung.

Für das in dieser Arbeit verwandte PAF-1 wurde, nach der Synthese durch die Yamamoto Homokupplung von Tetrakis(4-bromophenyl)methan, ein Vernetzungsgrad von ca. 80 % durch ein quantitatives ^{13}C OP NMR Experiment festgestellt. Mittels Physisorption mit

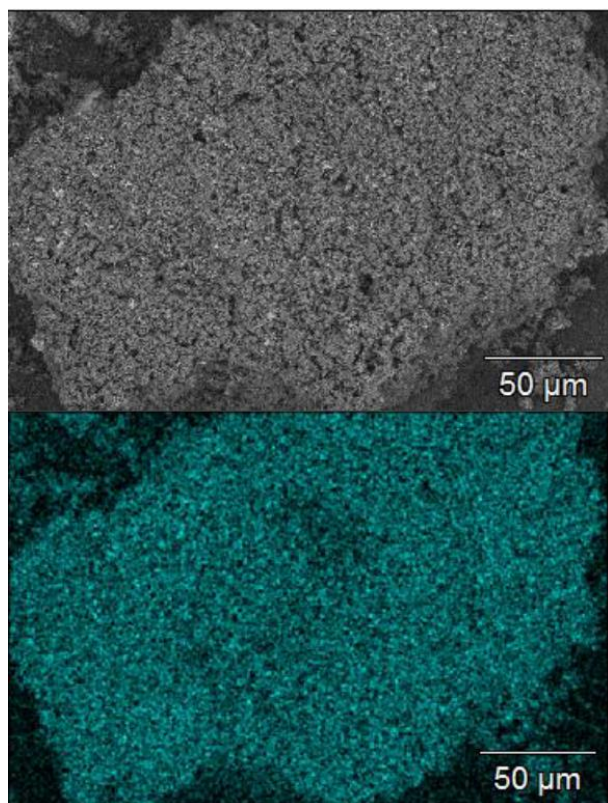


Abbildung 12: REM Aufnahme von SPAF-1(1.25) (oben) und durch EDX Mapping bestimmte Schwefelverteilung im Polymer (unten).

Argon wurde ferner eine innere Oberfläche von $2625 \text{ m}^2 \cdot \text{g}^{-1}$ mit überwiegend (77 %) mesoporöser Struktur berechnet. Um die postsynthetische, kovalente Anbindung der Sulfonsäuregruppen an die Netzwerkstruktur zu ermöglichen, wurde zunächst ein lösungsmittelbasierter Ansatz verfolgt. Durch den Einsatz von Chlorsulfonsäure in Dichlormethan (DCM) konnte somit ein Sulfonierungsgrad von ca. 50 % erreicht werden, was der Sulfonierung jedes zweiten Phenylrings pro Linkermolekül entspricht. Eine konsequente Weiterentwicklung der postsynthetischen Modifizierung ist der Einsatz von Oleum (H_2SO_4 mit 65 % SO_3), welches das poröse Polymer über die Gasphase kontaktiert und somit die Gleichgewichtsreaktion in der Flüssig-

phase umgeht. Das Ergebnis ist ein Sulfonierungsgrad von 125 %, was der Doppelsulfonierung jedes vierten Rings im Netzwerk entspricht.

In Folge der Sulfonierung ist eine deutliche Abnahme der Ar-Oberfläche beider Netzwerke auf $670 \text{ m}^2 \cdot \text{g}^{-1}$ (SPAF-1(0.5)) respektive $115 \text{ m}^2 \cdot \text{g}^{-1}$ (SPAF-1(1.25)) zu beobachten, während die CO_2 -Oberfläche nur bei SPAF-1(1.25) abnimmt ($392 \text{ m}^2 \cdot \text{g}^{-1}$), bei SPAF-1(0.5) jedoch unberührt scheint ($\text{m}^2 \cdot \text{g}^{-1}$). Dies liegt in dem durch die Größe der Ultramikroporen limitierten Zugang der Chlorsulfonsäure, welche somit nicht in diese Bereiche vordringen kann. Demnach ist durch Anwendung einer Gasphasensulfonierung mit SO_3 von einer vollständigeren und homogenen Funktionalisierung des Netzwerks auszugehen, da diese auch in die ultramikroporösen Bereiche des Netzwerks vordringen kann.

Da die Leitfähigkeit für Protonen in direkter Abhängigkeit zu den Ladungsträgern steht, ist die Wasseraufnahmekapazität λ (Wassermoleküle pro Sulfonsäuregruppe) der Netzwerke von zentraler Bedeutung. Durch TGA Experimente mit vorher bei 100 % rH equilibrierten Proben konnte diese auf 8 für SPAF-1(0.5) und 13 für SPAF-1(1.25) bestimmt werden. Durch ein DSC Experiment in Kombination mit EDX und AFM Untersuchungen konnte ferner die Einlagerung des Wassers primär in den Mikroporenbereichen der Netzwerke bestimmt werden (Abb. 13). Anders als zum Beispiel bei Nafion, kommt es also zu keiner

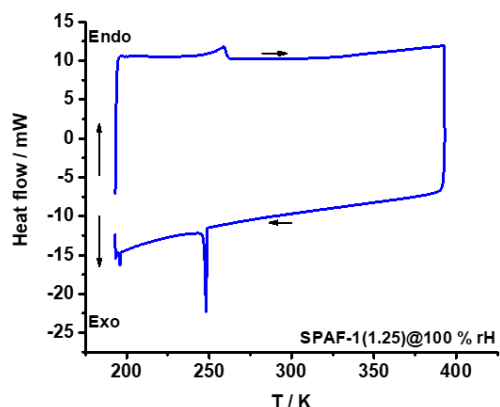


Abbildung 13: DSC Experiment zur Lokalisation des Wassers. Schmelz und Kristallisationspeak sind typisch für mesoporöse Umgebungen.

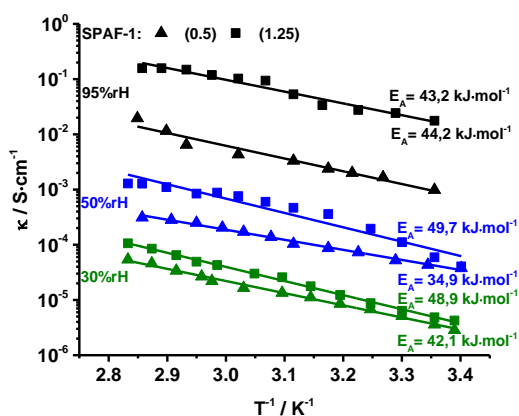
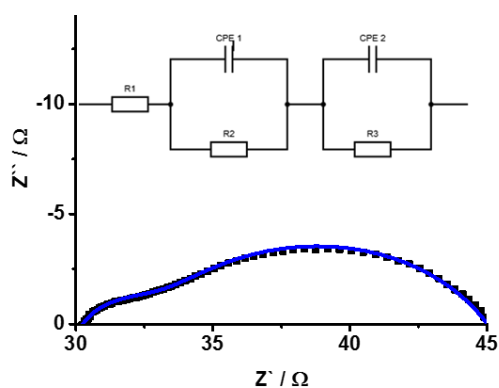


Abbildung 14: Nyquist Plot mit entsprechendem Ersatzschaltkreis (oben). Arrhenius Plots der SPAF-1 Netzwerke bei verschiedenen relativen Luftfeuchten (unten).

Mikrophasenseparation während der Hydratation. Vielmehr wird hier eine Reaktivierung der durch die PSM kollabierten Porenräume postuliert, um das ausnehmend starke Quellverhalten der schwammartigen Netzwerke zu erklären.

Die Protonenleitfähigkeit der Netzwerke wurde durch die elektrochemische Impedanzspektroskopie bei verschiedenen Temperaturen und Luftfeuchtigkeiten untersucht, wobei zwei Trends ermittelt werden konnten. Ersterer betrifft die starke Abhängigkeit der Leitfähigkeit von der relativen Luftfeuchte, wobei sich die Leitfähigkeit von SPAF-1(1.25) von $10^{-6} \text{ S}\cdot\text{cm}^{-1}$ bei 30 % rH auf $10^{-1} \text{ S}\cdot\text{cm}^{-1}$ bei 95 % rH verbessert (Abb. 16). Bemerkenswerterweise scheint die Leitfähigkeit der beiden Netzwerke bis zu einer relativen Luftfeuchte von 50 % ähnlich zu sein, während bei 95 % SPAF-1(1.25) sein Konterpart um ein Vielfaches übertrifft. Als Grund ist hier die durch den höheren Sulfonierungsgrad hervorgerufene, dichtere Ladungsträgerverteilung zu nennen, welche sich jedoch erst bei vollständiger Hydratation bemerkbar macht. Der zweite Trend ist die Temperaturabhängigkeit der Leitfähigkeit, welche bei beiden Netzwerken in einer Verdopplung der Leitfähigkeit

resultiert. Aus dieser konnte eine Aktivierungsbarriere für die Leitfähigkeit zwischen 35 und 50 $\text{kJ}\cdot\text{mol}^{-1}$ abgeleitet werden. Da bei einer Wanderung der Protonen durch uneingeschränkte Wasserpfade mittels Grotthuss Mechanismus eine deutlich niedrigere Aktivierungsbarriere zu erwarten ist, wird hier die Wanderung des Protons durch kleine Porenkanäle mittels Vehikel Mechanismus als limitierender Prozess angenommen. Die

Annahme wird durch die fehlende Mikrophasenseparation und die somit feststehende Leitung der Protonen durch die poröse Struktur gefestigt. Zusammenfassend wurde in dieser Arbeit die Protonenleitfähigkeit mikroporöser organischer Polymere aufgezeigt. Die Kombination poröser Strukturen mit entsprechend funktionalisierten Porenwänden hat sich ferner als zielführende Alternative zu bisherigen Systemen wie Nafion (Mikrophasenseparation) hinsichtlich der wasservermittelter Protonenleitung gezeigt.

2.4 Anhydrous Proton Conduction in Porous Organic Networks

Trotz ihres Erfolges ist die Abhängigkeit der Protonenleitfähigkeit von der Hydratation eine der Hauptnachteile bestehender Systeme, da sie ein komplexes Wassermanagement während des Betriebs nach sich zieht und eine Temperaturobergrenze von 80 °C setzt. Dabei ist gerade ein Temperaturbereich jenseits dieser Grenze interessant, kommt es doch bei höheren Temperaturen zu vorteilhaften kinetischen Effekten wie beispielsweise eine Erhöhung der Ionenmobilität und der Beschleunigung der Katalysatorleistung. Ein weiterer wichtiger Punkt ist die Herabsetzung der Katalysatorvergiftung durch Kohlenmonoxid, was eine Verlängerung der Lebenszeit des Systems sowie eine Erniedrigung der Aufbereitungskosten für H₂ zur Folge hat.

Eine Möglichkeit zu Verwirklichung wasserfreier Systeme ist die Substitution von Wasser durch amphotere Moleküle wie Imidazol, welche ein ähnliches Verhalten im Sinne von Wasserstoffbrückenbindungen und Autoprotolyse aufweisen. Das Ziel dieser Arbeit war daher, die Einlagerung von Imidazol in verschiedene poröse, organische Netzwerke (PON) sowie die systematische Untersuchung des Einflusses von Struktur, Porosität und Funktionalität auf die wasserfreie Protonenleitung (Abb. 15).

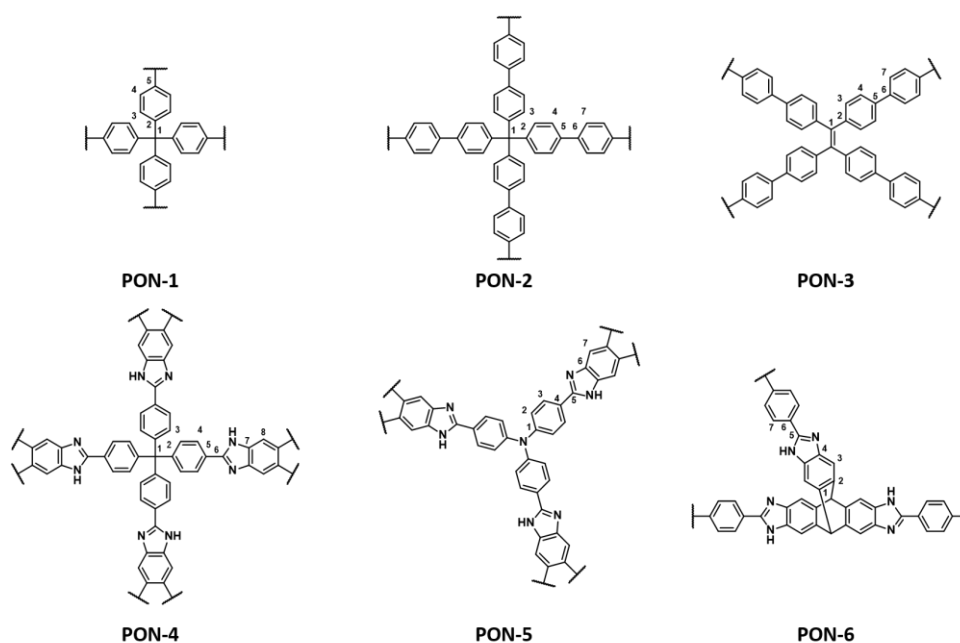


Abbildung 15: Schematische Darstellung der verwandten porösen organischen Netzwerke.

Die in Abbildung 15 dargestellten Netzwerke wurden mittels ^{13}C und ^{15}N NMR Spektroskopie nebst TGA und PXRD charakterisiert. Die Aufnahme von Argon Isothermen bei 87 K ermöglichte weitere Untersuchungen hinsichtlich innerer Oberfläche und Porosität. So konnten für die Netzwerke verschiedenste Oberflächen von $590 \text{ m}^2\cdot\text{g}^{-1}$ (PON-3) bis $5043 \text{ m}^2\cdot\text{g}^{-1}$ (PON-1) ermittelt sowie unterschiedliche Anteile von Mikro- als auch Mesoporen aufgezeigt werden. Die Einlagerung von Imidazol erfolgte postsynthetisch über die Gasphase. Dieser Prozess unterstützt eine effiziente Porenfüllung und verhindert gleichzeitig

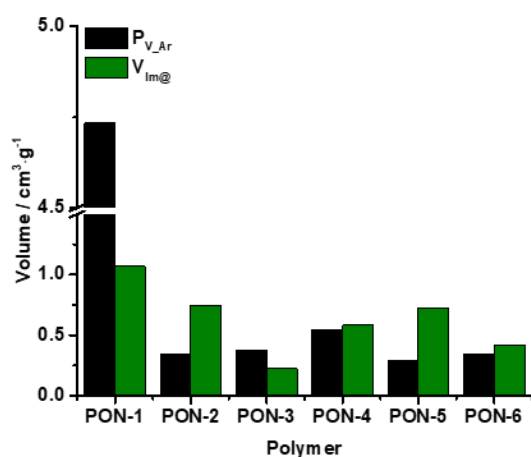


Abbildung 16: Aufnahme von Imidazol im Vergleich zu dem durch Argon bestimmten theoretischen Porenvolumens.

die Kondensation von Imidazolkristallen auf der Polymeroberfläche. Hier konnte die höchste Aufnahme von Imidazol für PON-1 mit $1,08 \text{ g}\cdot\text{g}^{-1}$ ermittelt werden, was sich aus der Kombination aus Porenvolumen und Mesoporosität ableitet (Abb. 16). Die unvollständige Porenfüllung ist auf die Blockierung kleinerer Poren zurückzuführen, welche eine weitere Einlagerung verhindern. Im Gegenzug steht das kaum poröse PON-3 mit einer Aufnahmekapazität von $0,23 \text{ g}\cdot\text{g}^{-1}$. Bemerkenswert an dieser Stelle sind der hohe Imidazolgehalt von PON-2 und PON-5 mit $0,77 \text{ g}\cdot\text{g}^{-1}$ und $0,75 \text{ g}\cdot\text{g}^{-1}$. Hier wird das theoretisch vorhandene Porenvolumen bei Weitem von der eingelagerten Menge übertroffen, was auf einen Atmungseffekt, ähnlich zu den bereits beobachteten Mechanismen aus BILP-19 und SPAF-1(1.25) der vorangegangenen Arbeiten, hindeutet.

Die Protonenleitfähigkeit der beladenen Polymere wurde mittels elektrochemischer Impedanzspektroskopie ermittelt. Aus den Ladungstransferwiderständen wurde unter Einbeziehen der spezifischen Probenparameter die Leitfähigkeit für die Netzwerke als Funktion der Temperatur gemessen. Der Vergleich der Netzwerke lässt, wie schon bei der wasservermittelten Protonenleitung, die primäre Abhängigkeit der Leitfähigkeit von der Ladungsträgerdichte, in diesem Fall Imidazol, erkennen. Während PON-3 bei einem Imidazolgehalt von $0,23 \text{ g}\cdot\text{g}^{-1}$ mit $2,1\cdot 10^{-7} \text{ S}\cdot\text{cm}^{-1}$ die niedrigste Leitfähigkeit bei $130 \text{ }^\circ\text{C}$ zeigt, ist diese bei PON-1 ($1,08 \text{ g}\cdot\text{g}^{-1}$) mit $5,2\cdot 10^{-4} \text{ S}\cdot\text{cm}^{-1}$ am höchsten (Abb. 17).

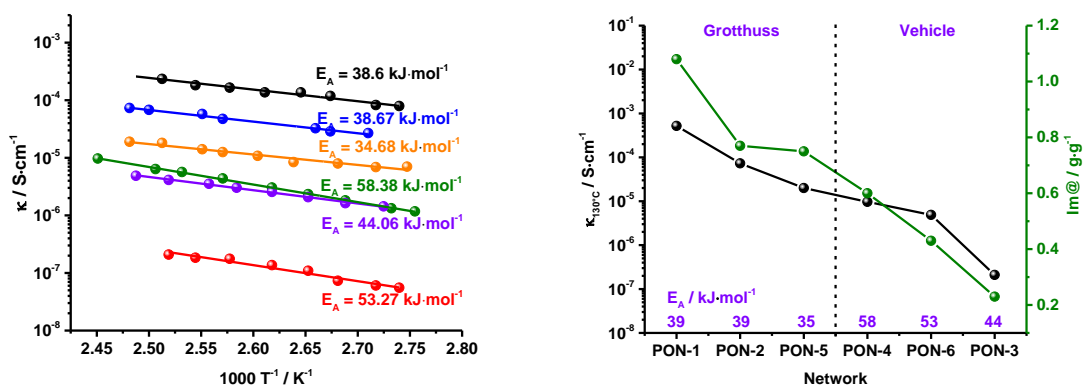


Abbildung 17: Arrheniusdiagramm für PON-1 - PON-6 in einem Temperaturbereich von 90 °C - 130 °C (links). Darstellung der Abhängigkeit der Leitfähigkeit vom Imidazolgehalt (rechts).

Die Beladung scheint ferner auch einen direkten Einfluss auf die Aktivierungsbarriere zu nehmen, welche mit fallendem Imidazolgehalt von 39 kJ·mol⁻¹ auf 58 kJ·mol⁻¹ stark ansteigt (Abb. 17). Während bei einer hohen Beladung Leitungspfade ausgebildet werden können, die den Langstreckentransport mittels eines Grotthuss typischen Mechanismus ermöglichen, erfordert ein niedriger Imidazolgehalt den Ladungstransport über die Diffusion von Ladungsträgern (Abb. 17). Auch scheint eine dreidimensionale Struktur der Netzwerke indirekt favorisiert, wobei diese wohl auf die homogene Einlagerung von Gastmolekülen zurückzuführen ist.

Die Implementierung von Benzimidazolgruppen in das Polymerrückgrat zeigt keine positiven Effekte auf das Ionenleitungsverhalten. Hier war zwar bei PON-5 eine ausnehmend hohe Leitfähigkeit von $2,0 \cdot 10^{-5} \text{ S}\cdot\text{cm}^{-1}$ bei einem Imidazol zu Benzimidazol Verhältnis von 1,8 festzustellen, diese kann jedoch auf den ausnehmend hohen Beladungsgrad zurückgeführt werden. PON-4 und PON-6 mit einem Verhältnis von 1.4 und 1.0, zeigen nur sehr geringe Leitfähigkeiten mit vergleichsweise hohen Aktivierungsenergien von 58 kJ·mol⁻¹ bzw. 53 kJ·mol⁻¹. Dies deutet auf eine Hemmung der Ionenleitung durch stärkere Anbindung, und damit Immobilisierung, des Imidazols an die Benzimidazoleinheiten. Zusammenfassend konnte ein Zugang zur wasserfreien Protonenleitung in porösen organischen Polymeren aufgezeigt werden. Die Beladung mit Imidazol in Kombination mit einer mesoporösen, dreidimensionalen Netzwerkstruktur hat sich hier als zielführend erwiesen und kann somit als Ausgangspunkt für weiterführende Untersuchungen dienen.

2.5 Ausblick

Die in dieser Arbeit gewonnenen Erkenntnisse liefern einige vielversprechende Ausgangspunkte für die Weiterentwicklung poröser organischer Polymere hinsichtlich potentieller Anwendung in Bereichen der Gassorption und Protonenleitung. So haben sich für die selektive Gassorption der Grad der Ultramikroporosität in Kombination mit einer dichten Verteilung funktioneller Gruppen als ausschlaggebende Eigenschaften potenter Materialien erwiesen. In nachfolgenden Projekten sollte daher speziell die Weiterentwicklung dieser Eigenschaften gezielt angestrebt werden. So könnte durch die Verwendung kleiner, sterisch effizienter Linker der Grundstein zur Ultramikroporosität gesetzt werden. Durch Methoden der postsynthetischen Modifizierung, wie z.B. Quervernetzung oder kovalente Verknüpfung funktioneller Gruppen ist diese dann weiter auszubauen. Gleichzeitig kann auf diese Weise die Funktionalität des Netzwerks postsynthetisch verändert werden, wobei es weiter zu untersuchen gilt, inwieweit die Selektivität des Netzwerks durch eine Wahl der funktionellen Gruppen eingestellt werden kann. Ein interessanter Ansatzpunkt könnte beispielsweise die Wahl sogenannter *Hypercrosslinked Polymers* auf Basis stickstoffhaltiger Ringsysteme in Kombination mit einer anschließenden Gasphasensulfonierung, für eine hohen CO₂ und Wasseraffinität, oder Fluorierung, für eine erhöhte Hydrophobizität, sein.

Im Bereich der Protonenleitung konnte ferner die Ausbildung von Leitungspfaden durch die Kavitäten eines mikroporösen Polymers nachgewiesen werden. Dies eröffnet, vor allem für einen auf Feuchtigkeit basierenden Mechanismus vielversprechende Ansatzpunkte. Ausgehend von der Annahme, dass sich mit Reduktion der Porengröße die Wechselwirkungen eingelagerter Molekülen mit den Porenwänden erhöht, könnte durch den Einsatz entsprechend funktionalisierter Polymere eine erhöhte Unabhängigkeit von der relativen Luftfeuchte erreicht werden. Des Weiteren gilt es zu untersuchen, inwiefern eine daraus erfolgende Hemmung der Wasserevaporation Einfluss auf einen Einsatz des Materials bei höheren Temperaturen, jenseits der 80 °C, nimmt. Als Ausgangspunkt könnte hier ein bereits Mikroporöses Material dienen, dessen Porenräume durch anschließende Sulfonierung weiter verkleinert werden.

3. Literaturverzeichnis

- (1) Su, B. L.; Sanchez, C.; Yang, X. Y. *Hierarchically Structured Porous Materials: From Nanoscience to Catalysis, Separation, Optics, Energy, and Life Science*; Wiley-VCH, **2011**.
- (2) Zhu, G.; Ren, H. *Porous Organic Frameworks*; Springer Berlin Heidelberg: Berlin, Heidelberg, **2015**.
- (3) Thommes, M.; Kaneko, K.; Neimark, A. V.; Olivier, J. P.; Rodriguez-Reinoso, F.; Rouquerol, J.; Sing, K. S. W. Physisorption of Gases, with Special Reference to the Evaluation of Surface Area and Pore Size Distribution (IUPAC Technical Report). *Pure Appl. Chem.* **2015**, *87* (9), 1051.
- (4) Rouquerol, J.; Avnir, D.; Fairbridge, C. W.; Everett, D. H.; Haynes, J. H.; Pernicone, N.; Ramsay, J. D. F.; Sing, K. S. W.; Unger, K. K. Recommendations for the Characterization of Porous Solids. *Pure Appl. Chem.* **1994**, *66* (8), 1739.
- (5) Davis, M. E. Ordered Porous Materials for Emerging Applications. *Nature* **2002**, *417* (6891), 813.
- (6) Germain, J.; Fréchet, J. M. J.; Svec, F. Nanoporous Polymers for Hydrogen Storage. *Small* **2009**, *5* (10), 1098.
- (7) D'Alessandro, D. M.; Smit, B.; Long, J. R. Carbon Dioxide Capture: Prospects for New Materials. *Angew. Chemie - Int. Ed.* **2010**, *49* (35), 6058.
- (8) Zhang, Y.; Riduan, S. N. Functional Porous Organic Polymers for Heterogeneous Catalysis. *Chem. Soc. Rev.* **2012**, *41* (41), 2083.
- (9) Solin, S. A. Clays and Clay Intercalation Compounds: Properties and Physical Phenomena. *Annu. Rev. Mater. Sci.* **1997**, *27* (1), 89.
- (10) Cho, J.; Ishida, Y. Macroscopically Oriented Porous Materials with Periodic Ordered Structures: From Zeolites and Metal–Organic Frameworks to Liquid-Crystal-Templated Mesoporous Materials. *Adv. Mater.* **2017**, *29* (25) 1605974.
- (11) Lee, Y. R.; Kim, J.; Ahn, W. S. Synthesis of Metal–Organic Frameworks: A Mini Review. *Korean J. Chem. Eng.* **2013**, *30* (9), 1667.
- (12) Furukawa, H.; Cordova, K. E.; O’Keeffe, M.; Yaghi, O. M. The Chemistry and Applications of Metal–Organic Frameworks. *Science* **2013**, *341* (6149), 1230444.
- (13) Ramaswamy, P.; Wong, N. E.; Shimizu, G. K. H. MOFs as Proton Conductors—Challenges and Opportunities. *Chem Soc Rev* **2014**, *43* (16), 5913.

- (14) Wang, X.; Ye, N. Recent Advances in Metal-Organic Frameworks and Covalent Organic Frameworks for Sample Preparation and Chromatographic Analysis. *Electrophoresis* **2017**, *1*, 1.
- (15) Ding, S.-Y.; Wang, W. Covalent Organic Frameworks (COFs): From Design to Applications. *Chem. Soc. Rev.* **2013**, *42* (42), 548.
- (16) Wu, M. X.; Yang, Y. W. Applications of Covalent Organic Frameworks (COFs): From Gas Storage and Separation to Drug Delivery. *Chinese Chemical Letters* **2017**, *28* (6) 1135.
- (17) Chang, Z.; Zhang, D.-S.; Chen, Q.; Bu, X.-H. Microporous Organic Polymers for Gas Storage and Separation Applications. *Phys. Chem. Chem. Phys.* **2013**, *15* (15), 5430.
- (18) Kaur, P.; Hupp, J. T.; Nguyen, S. T. Porous Organic Polymers in Catalysis: Opportunities and Challenges. *ACS Catal.* **2011**, *1* (7), 819.
- (19) Stegbauer, L.; Schwinghammer, K.; Lotsch, B. V. A Hydrazone-Based Covalent Organic Framework for Photocatalytic Hydrogen Production. *Chem. Sci.* **2014**, *5*, 2789.
- (20) Bildirir, H.; Gregoriou, V. G.; Avgeropoulos, A.; Scherf, U.; Chochos, C. L. Porous Organic Polymers as Emerging New Materials for Organic Photovoltaic Applications: Current Status and Future Challenges. *Mater. Horizons* **2017**, *4* (4), 546.
- (21) Chandra, S.; Kundu, T.; Kandambeth, S.; Babarao, R.; Marathe, Y.; Kunjir, S. M.; Banerjee, R. Phosphoric Acid Loaded Azo (-N=N-) Based Covalent Organic Framework for Proton Conduction. *J. Am. Chem. Soc.* **2014**, *136* (18), 6570.
- (22) Lee, S.; Barin, G.; Ackerman, C. M.; Muchenditsi, A.; Xu, J.; Reimer, J. A.; Lutsenko, S.; Long, J. R.; Chang, C. J. Copper Capture in a Thioether-Functionalized Porous Polymer Applied to the Detection of Wilson's Disease. *J. Am. Chem. Soc.* **2016**, *138* (24), 7603.
- (23) Bai, L.; Phua, S. Z. F.; Lim, W. Q.; Jana, A.; Luo, Z.; Tham, H. P.; Zhao, L.; Gao, Q.; Zhao, Y. Nanoscale Covalent Organic Frameworks as Smart Carriers for Drug Delivery. *Chem. Commun.* **2016**, *52* (22), 4128.
- (24) Dong, J.; Tummanapelli, A. K.; Li, X.; Ying, S.; Hirao, H.; Zhao, D. Fluorescent Porous Organic Frameworks Containing Molecular Rotors for Size-Selective Recognition. *Chem. Mater.* **2016**, *28* (21), 7889.
- (25) World Meteorological Organization. The State of Greenhouse Gases in the Atmosphere Based on Global Observations through 2013. **2014**, *10*, 1.

- (26) UNFCCC. Conference of the Parties (COP). *Paris Climate Change Conference- November 2015, COP 21*; **2015**; Vol. 21932.
- (27) Haszeldine, R. S. Carbon Capture and Storage: How Green Can Black Be? *Science*. **2009**, 325 (5948), 1647.
- (28) Bhowan, A. S. Status and Analysis of Next Generation Post-Combustion CO₂ Capture Technologies. *Energy Procedia* **2014**, 63, 542.
- (29) Davidson, R. M. Pre-Combustion Capture of CO₂ in IGCC Plants. **2011**.
- (30) Muhammad, A.; Gadelhak, Y. Simulation Based Improvement Techniques for Acid Gases Sweetening by Chemical Absorption: A Review. *International Journal of Greenhouse Gas Control*. **2015**, 481.
- (31) Dawson, R.; Cooper, A. I.; Adams, D. J. Chemical Functionalization Strategies for Carbon Dioxide Capture in Microporous Organic Polymers. *Polym. Int.* **2013**, 62 (3), 345.
- (32) Arab, P.; Rabbani, M. G.; Sekizkardes, A. K.; İslamoğlu, T.; El-Kaderi, H. M. Copper(I)-Catalyzed Synthesis of Nanoporous Azo-Linked Polymers: Impact of Textural Properties on Gas Storage and Selective Carbon Dioxide Capture. *Chem. Mater.* **2014**, 26 (3), 1385.
- (33) Rabbani, M. G.; El-Kaderi, H. M. Synthesis and Characterization of Porous Benzimidazole-Linked Polymers and Their Performance in Small Gas Storage and Selective Uptake. *Chem. Mater.* **2012**, 24 (8), 1511.
- (34) Lu, W.; Verdegaal, W. M.; Yu, J.; Balbuena, P. B.; Jeong, H.-K.; Zhou, H.-C. Building Multiple Adsorption Sites in Porous Polymer Networks for Carbon Capture Applications. *Energy Environ. Sci.* **2013**, 6 (12), 3559.
- (35) Zhu, X.; Tian, C.; Veith, G. M.; Abney, C. W.; Dehaudt, J.; Dai, S. In Situ Doping Strategy for the Preparation of Conjugated Triazine Frameworks Displaying Efficient CO₂ Capture Performance. *J. Am. Chem. Soc.* **2016**, 138 (36), 11497.
- (36) Zou, L.; Sun, Y.; Che, S.; Yang, X.; Wang, X.; Bosch, M.; Wang, Q.; Li, H.; Smith, M.; Yuan, S.; et al. Porous Organic Polymers for Post-Combustion Carbon Capture. *Adv. Mater.* **2017**, 29 (37), 1.
- (37) Yuan, X.-Z.; Song, C.; Wang, H.; Zhang, J. *Electrochemical Impedance Spectroscopy in PEM Fuel Cells*; Springer London: London, **2010**.
- (38) Hickner M. A., Ghassemi, H.; Kim, Y. S.; Einsla B. R.; McGrath, J. Alternative Polymer Systems for Proton Exchange Membranes (PEMs). *Chem. Rev.* **2004**, 104 (10), 4587.

- (39) Moore, R. B.; Mauritz, K. A.; Moore, R. B. State of Understanding of Nafion. *Chem. Rev.* **2004**, *104* (10), 4535.
- (40) Napoli, L.; Franco, J.; Fasoli, H.; Sanguinetti, A. Conductivity of Nafion® 117 Membrane Used in Polymer Electrolyte Fuel Cells. *Int. J. Hydrogen Energy* **2014**, *39* (16), 8656.
- (41) Mehmeti, A.; Santoni, F.; Della Pietra, M.; McPhail, S. J. Life Cycle Assessment of Molten Carbonate Fuel Cells: State of the Art and Strategies for the Future. *J. Power Sources* **2016**, *308*, 97.
- (42) da Silva, F. S.; de Souza, T. M. Novel Materials for Solid Oxide Fuel Cell Technologies: A Literature Review. *Int. J. Hydrogen Energy* **2017**, *42* (41), 26020.
- (43) Li, G.; Xie, J.; Cai, H.; Qiao, J. New Highly Proton-Conducting Membrane Based on Sulfonated Poly(arylene Ether Sulfone)s Containing Fluorophenyl Pendant Groups, for Low-Temperature Polymer Electrolyte Membrane Fuel Cells. *Int. J. Hydrogen Energy* **2014**, *39* (6), 2639.
- (44) Ong, B. C.; Kamarudin, S. K.; Basri, S. Direct Liquid Fuel Cells: A Review. *Int. J. Hydrogen Energy* **2017**, *42* (15), 10142.
- (45) Sharaf, O. Z.; Orhan, M. F. An Overview of Fuel Cell Technology: Fundamentals and Applications. *Renew. Sustain. Energy Rev.* **2014**, *32*, 810.
- (46) Peighambaroust, S. J.; Rowshanzamir, S.; Amjadi, M. Review of the Proton Exchange Membranes for Fuel Cell Applications. *Int. J. Hydrogen Energy* **2010**, *9* (2), 3.
- (47) Cao, X.; Jing, L.; Liu, Y.; Hu, W.; Jiang, Z.; Liu, B. Immiscible Blends of Sulfonated Polyetheretherketone and Fluorinated Polyimide for Proton Exchange Membranes. *High Perform. Polym.* **2014**, *26* (5), 532.
- (48) Yoon, M.; Suh, K.; Natarajan, S.; Kim, K. Proton Conduction in Metal-Organic Frameworks and Related Modularly Built Porous Solids. *Angew. Chem. Int. Ed. Engl.* **2013**, *52* (10), 2688.
- (49) Kang, D. W.; Lim, K. S.; Lee, K. J.; Lee, J. H.; Lee, W. R.; Song, J. H.; Yeom, K. H.; Kim, J. Y.; Hong, C. S. Cost-Effective, High-Performance Porous-Organic-Polymer Conductors Functionalized with Sulfonic Acid Groups by Direct Postsynthetic Substitution. *Angew. Chemie Int. Ed.* **2016**, *55* (52), 16123.
- (50) Peng, Y.; Xu, G.; Hu, Z.; Cheng, Y.; Chi, C.; Yuan, D.; Cheng, H.; Zhao, D. Mechanoassisted Synthesis of Sulfonated Covalent Organic Frameworks with High Intrinsic Proton Conductivity. *ACS Appl. Mater. Interfaces* **2016**, *8* (28), 18505.

- (51) Karmakar, A.; Illathvalappil, R.; Anothumakkool, B.; Sen, A.; Samanta, P.; Desai, A. V.; Kurungot, S.; Ghosh, S. K. Hydrogen-Bonded Organic Frameworks (HOFs): A New Class of Porous Crystalline Proton-Conducting Materials. *Angew. Chemie Int. Ed.* **2016**, *55* (36), 10667.
- (52) Samanta, P.; Desai, A. V.; Anothumakkool, B.; Shirolkar, M. M.; Karmakar, A.; Kurungot, S.; Ghosh, S. K. Enhanced Proton Conduction by Post-Synthetic Covalent Modification in a Porous Covalent Framework. *J. Mater. Chem. A* **2017**, *5* (26), 13659.
- (53) Klumpen, C.; Gödrich, S.; Papastavrou, G.; Senker, J. Water Mediated Proton Conduction in a Sulfonated Microporous Organic Polymer. *Chem. Commun.* **2017**, *53* (54), 7592.
- (54) Kang, D. W.; Song, J. H.; Lee, K. J.; Lee, H. G. H. Y.; Kim, J. Y. J. E.; Lee, H. G. H. Y.; Kim, J. Y. J. E.; Hong, C. S. A Conductive Porous Organic Polymer with Superprotonic Conductivity of a Nafion-Type Electrolyte. *J. Mater. Chem. A* **2017**, *5* (33), 17492.
- (55) Ye, Y.; Zhang, L.; Peng, Q.; Wang, G.-E.; Shen, Y.; Li, Z.; Wang, L.; Ma, X.; Chen, Q.-H.; Zhang, Z.; et al. High Anhydrous Proton Conductivity of Imidazole-Loaded Mesoporous Polyimides over a Wide Range from Subzero to Moderate Temperature. *J. Am. Chem. Soc.* **2015**, *137* (2), 913.
- (56) Xu, H.; Tao, S.; Jiang, D. Proton Conduction in Crystalline and Porous Covalent Organic Frameworks. *Nat. Mater.* **2016**, *15* (7), 722.
- (57) Banerjee, R.; Shinde, D. B.; Aiyappa, H. B.; Bhadra, M.; Biswal, B. P.; Kandambeth, S.; Garai, B.; Kundu, T.; Wadge, P. N.; Kurungot, S.; et al. Mechanochemically Synthesized Covalent Organic Framework as Proton-Conducting Solid Electrolyte. *J. Mater. Chem. A* **2016**, *4* (7), 2682.
- (58) Chandra, S.; Kundu, T.; Dey, K.; Addicoat, M.; Heine, T.; Banerjee, R. Interplaying Intrinsic and Extrinsic Proton Conductivities in Covalent Organic Frameworks. *Chem. Mater.* **2016**, *28* (5), 1489.
- (59) Ramimoghadam, D.; Gray, E. M. A.; Webb, C. J. Review of Polymers of Intrinsic Microporosity for Hydrogen Storage Applications. *Int. J. Hydrogen Energy.* **2016**, *41* (38), 16944.
- (60) Xu, S.; Luo, Y.; Tan, B. Recent Development of Hypercrosslinked Microporous Organic Polymers. *Macromol. Rapid Commun.* **2013**, *34* (6), 471.
- (61) Katekomol, P.; Roeser, J.; Bojdys, M.; Weber, J.; Thomas, A. Covalent Triazine Frameworks Prepared from 1,3,5-Tricyanobenzene. *Chem. Mater.* **2013**, *25* (9),

- 1542.
- (62) Meng, S.; Ma, H.; Jiang, L.; Ren, H.; Zhu, G. A Facile Approach to Prepare Porphyrinic Porous Aromatic Frameworks for Small Hydrocarbon Separation. *J. Mater. Chem. A* **2014**, *2* (35), 14536.
- (63) Liu, Q.; Tang, Z.; Wu, M.; Zhou, Z. Design, Preparation and Application of Conjugated Microporous Polymers. *Polym. Int.* **2014**, *63* (3), 381.
- (64) Rose, M.; Klein, N.; Böhlmann, W.; Böhringer, B.; Fichtner, S.; Kaskel, S. New Element Organic Frameworks via Suzuki Coupling with High Adsorption Capacity for Hydrophobic Molecules. *Soft Matter* **2010**, *6* (16), 3918.
- (65) Colson, J. W.; Dichtel, W. R. Rationally Synthesized Two-Dimensional Polymers. *Nat. Chem.* **2013**, *5* (6), 453.
- (66) Rowan, S. J.; Cantrill, S. J.; Cousins, G. R. L.; Sanders, J. K. M.; Stoddart, J. F. Dynamic Covalent Chemistry. *Angew. Chemie Int. Ed.* **2002**, *41* (6), 898.
- (67) Côté, A. P.; Benin, A. I.; Ockwig, N. W.; O’Keeffe, M.; Matzger, A. J.; Yaghi, O. M. Porous, Crystalline, Covalent Organic Frameworks. *Science* **2005**, *310* (5751), 1166.
- (68) Feng, X.; Ding, X.; Jiang, D. Covalent Organic Frameworks. *Chem. Soc. Rev.* **2012**, *41* (18), 6010.
- (69) Tao, L.; Niu, F.; Wang, C.; Liu, J.; Wang, T.; Wang, Q. Benzimidazole Functionalized Covalent Triazine Frameworks for CO₂ Capture. *J. Mater. Chem. A* **2016**, *4* (30), 11812.
- (70) Bhunia, A.; Vasylyeva, V.; Janiak, C. From a Supramolecular Tetranitrile to a Porous Covalent Triazine-Based Framework with High Gas Uptake Capacities. *Chem. Commun.* **2013**, *49* (38), 3961.
- (71) Wang, K.; Yang, L.-M.; Wang, X.; Guo, L.; Cheng, G.; Zhang, C.; Jin, S.; Tan, B.; Cooper, A. Covalent Triazine Frameworks via a Low-Temperature Polycondensation Approach. *Angew. Chemie Int. Ed.* **2017**, *56* (45), 14149.
- (72) Das, S.; Heasman, P.; Ben, T.; Qiu, S. Porous Organic Materials: Strategic Design and Structure–Function Correlation. *Chem. Rev.* **2017**, *117* (3), 1515.
- (73) Karak, S.; Kandambeth, S.; Biswal, B. P.; Sasmal, H. S.; Kumar, S.; Pachfule, P.; Banerjee, R. Constructing Ultraporous Covalent Organic Frameworks in Seconds via an Organic Terracotta Process. *J. Am. Chem. Soc.* **2017**, *139* (5), 1856.
- (74) Nagai, A.; Guo, Z.; Feng, X.; Jin, S.; Chen, X.; Ding, X.; Jiang, D. Pore Surface Engineering in Covalent Organic Frameworks. *Nat. Commun.* **2011**, *2*, 536.

- (75) Bunck, D. N.; Dichtel, W. R. Postsynthetic Functionalization of 3D Covalent Organic Frameworks. *Chem. Commun.* **2013**, 49 (24), 2457.
- (76) Zhang, Q.; Zhang, S.; Li, S. Novel Functional Organic Network Containing Quaternary Phosphonium and Tertiary Phosphorus. *Macromolecules* **2012**, 45 (7), 2981.
- (77) Lu, W.; Yuan, D.; Sculley, J.; Zhao, D.; Krishna, R.; Zhou, H.-C. Sulfonate-Grafted Porous Polymer Networks for Preferential CO₂ Adsorption at Low Pressure. *J. Am. Chem. Soc.* **2011**, 133 (45), 18126.
- (78) Lu, W.; Sculley, J. P.; Yuan, D.; Krishna, R.; Wei, Z.; Zhou, H.-C. Polyamine-Tethered Porous Polymer Networks for Carbon Dioxide Capture from Flue Gas. *Angew. Chemie Int. Ed.* **2012**, 51 (30), 7480.
- (79) Li, B.; Guan, Z.; Yang, X.; Wang, W. D.; Wang, W.; Hussain, I.; Song, K.; Tan, B.; Li, T. Multifunctional Microporous Organic Polymers. *J. Mater. Chem. A* **2014**, 2 (30), 11930.
- (80) Tan, L.; Tan, B. Hypercrosslinked Porous Polymer Materials: Design, Synthesis, and Applications. *Chem. Soc. Rev.* **2017**, 46, 3322
- (81) Ben, T.; Ren, H.; Ma, S.; Cao, D.; Lan, J.; Jing, X.; Wang, W.; Xu, J.; Deng, F.; Simmons, J. M.; et al. Targeted Synthesis of a Porous Aromatic Framework with High Stability and Exceptionally High Surface Area. *Angew. Chemie Int. Ed.* **2009**, 48 (50), 9457.
- (82) Xu, W.; Xia, W.; Guan, Y.; Wang, Y.; Lu, C.; Yang, G.; Nie, J.; Chen, Z. DMAP-Based Flexible Polymer Networks Formed via Heck Coupling as Efficient Heterogeneous Organocatalysts. *React. Funct. Polym.* **2016**, 104, 15.
- (83) Trunk, M.; Herrmann, A.; Bildirir, H.; Yassin, A.; Schmidt, J.; Thomas, A. Copper-Free Sonogashira Coupling for High-Surface-Area Conjugated Microporous Poly(aryleneethynylene) Networks. *Chem. - A Eur. J.* **2016**, 22 (21), 7179.
- (84) Wang, J. L.; Wang, C.; Dekrafft, K. E.; Lin, W. Cross-Linked Polymers with Exceptionally High Ru(bipy)₃²⁺ Loadings for Efficient Heterogeneous Photocatalysis. *ACS Catal.* **2012**, 2 (3), 417.
- (85) Popp, N.; Homburg, T.; Stock, N.; Senker, J. Porous Imine-Based Networks with Protonated Imine Linkages for Carbon Dioxide Separation from Mixtures with Nitrogen and Methane. *J. Mater. Chem. A* **2015**, 3 (36), 18492.
- (86) Liebl, M. R.; Senker, J. Microporous Functionalized Triazine-Based Polyimides with High CO₂ Capture Capacity. *Chem. Mater.* **2013**, 25 (6), 970.

- (87) Taylor, R. G. D.; Bezzu, C. G.; Walker, J.; Msayib, J.; Mcdermott, A. G.; Runt, J.; Lauren, J.; Colina, C. M.; Maynard-atem, L.; Budd, P. M.; et al. Synthesis of Organic Molecules and Dendrimers of Intrinsic Microporosity (OMIMs and DIMs). *Proc. Publ. by Am. Chem. Soc.* **2011**, *1*, 1.
- (88) Khatioda, R.; Talukdar, D.; Saikia, B.; Bania, K. K.; Sarma, B. Constructing Two Dimensional Amide Porous Polymer to Promote Selective Oxidation Reactions. *Catal. Sci. Technol.* **2017**, *7* (14), 3143.
- (89) Palma-Cando, A.; Brunklaus, G.; Scherf, U. Thiophene-Based Microporous Polymer Networks via Chemical or Electrochemical Oxidative Coupling. *Macromolecules* **2015**, *48* (19), 6816.
- (90) Jing, Z. A Nanoporous Organic Polymer Constructed from a 1,3,5-Triazine Derivative via Ethynyl Cyclotrimerization Reaction: Synthesis and Carbon Dioxide Capture. *J. Chem. Pharm. Res.* **2014**, *6* (2), 322.
- (91) Rose, M.; Klein, N.; Senkovska, I.; Schrage, C.; Wollmann, P.; Böhlmann, W.; Böhringer, B.; Fichtner, S.; Kaskel, S. A New Route to Porous Monolithic Organic Frameworks via Cyclotrimerization. *J. Mater. Chem.* **2011**, *21* (3), 711.
- (92) Zhao, H.; Jin, Z.; Su, H.; Jing, X.; Sun, F.; Zhu, G. Targeted Synthesis of a 2D Ordered Porous Organic Framework for Drug Release. *Chem. Commun.* **2011**, *47* (47), 6389.
- (93) Kundu, S. K.; Bhaumik, A. A Triazine-Based Porous Organic Polymer: A Novel Heterogeneous Basic Organocatalyst for Facile One-Pot Synthesis of 2-Amino-4H-Chromenes. *RSC Adv.* **2015**, *5* (41), 32730.
- (94) Patel, H. A.; Karadas, F.; Byun, J.; Park, J.; Deniz, E.; Canlier, A.; Jung, Y.; Atilhan, M.; Yavuz, C. T. Highly Stable Nanoporous Sulfur-Bridged Covalent Organic Polymers for Carbon Dioxide Removal. *Adv. Funct. Mater.* **2013**, *23* (18), 2270.
- (95) Rouquerol, F.; Rouquerol, J.; Sing, K. S. W. *Adsorption by Powders and Porous Solids : Principles, Methodology, and Applications*; Academic Press, **1999**.
- (96) Mohr, R.; Rao, M. B. Isosteric Heat of Adsorption: Theory and Experiment. *J. Phys. Chem. B* **1999**, *103* (31), 6539.
- (97) Lowell, S.; Shields, J. E.; Thomas, M. A.; Thommes, M. *Characterization of Porous Solids and Powders: Surface Area, Pore Size and Density*; Particle Technology Series; Springer Netherlands: Dordrecht, **2004**; Vol. 16.
- (98) Colombari, P. *Proton Conductors : Solids, Membranes and Gels - Materials and Devices*; Cambridge University Press, **1992**.

- (99) Cogger, N. D.; Evans, N. J. An Introduction to Electrochemical Impedance Measurement. *Solartron Anal. Tech. Rep.* **1999**, 6, 11.
- (100) Lasia, A. Electrochemical Impedance Spectroscopy and Its Applications; Springer New York: New York, NY, **2014**.
- (101) Carroll, J. J. Henry's Law Revisited. *Chem. Eng. progress.* **1999**, 95 (1), 49.
- (102) Sekizkardes, A. K.; Culp, J. T.; Islamoglu, T.; Marti, A.; Hopkinson, D.; Myers, C.; El-Kaderi, H. M.; Nulwala, H. B. An Ultra-Microporous Organic Polymer for High Performance Carbon Dioxide Capture and Separation. *Chem. Commun. Chem. Commun* **2015**, 51 (51), 13393.
- (103) Sekizkardes, A. K.; Altarawneh, S.; Kahveci, Z.; Islamoğlu, T.; El-Kaderi, H. M. Highly Selective CO₂ Capture by Triazine-Based Benzimidazole-Linked Polymers. *Macromolecules* **2014**, 47 (23), 8328.
- (104) Barsoukov, E.; Macdonald, J. R. *Impedance Spectroscopy*; Wiley-Int. **2005**, 2.
- (105) Munch, W.; Kreuer, K.-D.; Silvestri, W.; Maier, J.; Seifert, G. The Diffusion Mechanism of an Excess Proton in Imidazole Molecule Chains: First Results of an Ab Initio Molecular Dynamics Study. *Solid State Ionics* **2001**, 145, 437.
- (106) Kreuer, K. D.; Weppner, W.; Rabenau, A. Proton Conduction in Zeolites. *Mater. Res. Bull.* **1982**, 17 (4), 501.
- (107) Kreuer, K. . On the Development of Proton Conducting Materials for Technological Applications. *Solid State Ionics* **1997**, 97 (1), 1.
- (108) Kreuer, K. D. D.; Fuchs, A.; Ise, M.; Spaeth, M.; Maier, J. Imidazole and Pyrazole-Based Proton Conducting Polymers and Liquids. *Electrochim. Acta* **1998**, 43 (10), 1281.
- (109) Kreuer, K.-D.; Paddison, S. J.; Spohr, E.; Schuster, M. Transport in Proton Conductors for Fuel-Cell Applications: Simulations, Elementary Reactions, and Phenomenology. *Chem. Rev.* **2004**, 104 (10).
- (110) Kreuer, K.-D. Proton Conductivity: Materials and Applications. *Chem. Mater.* **1996**, 8 (3), 610.
- (111) Schuster, M. F. H.; Meyer, W. H.; Schuster, M.; Kreuer, K. D. Toward a New Type of Anhydrous Organic Proton Conductor Based on Immobilized Imidazole. *Chem. Mater.* **2004**, 16 (2), 329.
- (112) Schuster, M. F. H.; Meyer, W. H. Anhydrous Proton-Conducting Polymers. *Annu. Rev. Mater. Res.* **2003**, 33 (1), 233.
- (113) Funke, K.; Banhatti, R. D.; Brückner, S.; Cramer, C.; Wilmer, D. Dynamics of

Literaturverzeichnis

Mobile Ions in Crystals, Glasses and Melts, Described by the Concept of Mismatch and Relaxation. *Solid State Ionics* **2002**, 154–155, 65.

- (114) MacDonald, J. R. Critical Examination of the Mismatch-and-Relaxation Frequency-Response Model for Dispersive Materials. *Solid State Ionics* **1999**, 124 (1), 1.

4. Publikationsverzeichnis

- I) Klumpen, C.; Breunig, M.; Homburg, T.; Stock, N.; Senker, J. Microporous Organic Polyimides for CO₂ and H₂O Capture and Separation from CH₄ and N₂ Mixtures: Interplay between Porosity and Chemical Function. *Chem. Mater.* **2016**, 28, 5461.
- II) Klumpen, C.; Radakovitsch, F.; Jess, A.; Senker, J. R. BILP-19 - An Ultramicroporous Organic Network with Exceptional Carbon Dioxide Uptake. *Molecules* **2017**, 22, 1343.
- III) Klumpen, C.; Gödrich, S.; Papastavrou, G.; Senker, J. Water Mediated Proton Conduction in a Sulfonated Microporous Organic Polymer. *Chem. Commun.* **2017**, 53, 7592.
- IV) Klumpen, C.; Winterstein, S.; Papastavrou, G.; Senker, J. Anhydrous Proton Conduction in Porous Organic Networks *accepted in J. Mater. Chem. A*, **2018**, DOI: 10.1039/C8TA07822J

5. Publikationen

5.1 Microporous Organic Polyimides for CO₂ and H₂O Capture and Separation from CH₄ and N₂ Mixtures: Interplay between Porosity and Chemical Function

Die Publikation wurde in Zusammenarbeit mit dem Lehrstuhl für Anorganische Chemie der Universität Kiel, Arbeitsgruppe Prof. Dr. N. Stock, durchgeführt. Die Beiträge der Autoren sind wie folgt:

Christoph Klumpen

- ⇒ Projektplanung und Durchführung
- ⇒ Synthesen und Charakterisierung der Verbindungen
- ⇒ Durchführung und Auswertung der Gassorptionsanalytik
- ⇒ Auswertung des Gesamtdatensatzes
- ⇒ Planung und Aufsetzen des Manuskripts

Marion Breunig

- ⇒ Synthese der Verbindungen

Thomas Homburg, Norbert Stock

- ⇒ Durchführung der Wassersorptionsmessungen
- ⇒ Design des Manuskripts

Jürgen Senker

- ⇒ Projektplanung und Supervision
- ⇒ Planung und Aufsetzen des Manuskripts

Microporous Organic Polyimides for CO₂ and H₂O Capture and Separation from CH₄ and N₂ Mixtures: Interplay between Porosity and Chemical Function

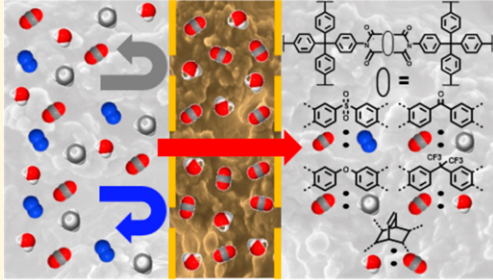
Christoph Klumpen,[†] Marion Breunig,[†] Thomas Homburg,^{†,‡} Norbert Stock,^{†,‡} and Juergen Senker^{*,†}

[†]University of Bayreuth, Inorganic Chemistry III, Universitaetsstraße 30, 95440 Bayreuth, Germany

[‡]Christian-Albrechts-University Kiel, Institute for Inorganic Chemistry, Max-Eyth-Straße 2, 24118 Kiel, Germany

Supporting Information

ABSTRACT: Porous polyimides have been considered to be a promising material class for gas capture and sequestration, leading to the synthesis of a substantial number of individual networks with noteworthy sorption properties. In spite of these efforts, the vision of a chemical control of adsorption and desorption of small molecules, in particular, for the competing uptake of technical relevant gas mixtures, is still hardly investigated. Here, we present a systematic study of five new polyimide networks based on a set of linkers with chemical functionalities covering the full range from hydrophobic to hydrophilic interactions. The corresponding microporous organic polyimides (MOPI-I to -V) were synthesized successfully based on a condensation reaction between amino and anhydride linker molecules in *m*-cresol at high temperatures, resulting in cross-linking degrees beyond 95% in all cases. Argon and carbon dioxide isotherms reveal surface areas up to 940 m²/g with ultramicroporosity, about 50% microporosity and high thermal stabilities under air with decomposition temperatures up to 480 °C. Sorption screening for variable temperatures revealed remarkable uptakes for carbon dioxide up to 3.8 mmol/g and water vapor up to 19.5 mmol/g combined with a smooth gate opening around 0.25 *p*/*p*₀ for MOPI-IV. In contrast, for MOPI-V the water vapor uptake decreases down to 7 mmol/g. Interestingly, the trend of the selectivities calculated by IAST and Henry does not correlate with the uptake behavior. For instance, MOPI-I and MOPI-III exhibit with 78 and 13 the highest CO₂ over N₂ and CH₄ Henry selectivities, although their CO₂ uptake is around 3.0 mmol/g. In total, we attribute the sorption properties for this class of materials mainly to the void size and shape within the ultramicroporous region. The chemical environment of the surfaces seems to have little influence on the uptake and a stronger effect on the separation behavior.



INTRODUCTION

To satisfy the energy requirements of modern society, the combustion of fossil fuels is still one of the most important energy sources nowadays.¹ This implicates the emission of large amounts of carbon dioxide rich gas mixtures, increasing the atmospheric carbon dioxide concentration and in turn intensifying global warming.² According to the World Meteorological Organization (WMO), CO₂ is the most important anthropogenic greenhouse gas, contributing 65% to radiative forcing. However, the atmospheric CO₂ level still rises now reaching 145% of the pre industrial status.³ Until environmentally more friendly techniques are developed, the capture and sequestration (CCS) of CO₂ is important to decrease the global carbon dioxide emission. In general, CCS techniques address two main fields, precombustion and postcombustion processes, which provide different demands on potential materials.⁴

The typical conditions for a postcombustional gas stream are nearly ambient pressures (~1 bar) and temperatures around

40–80 °C for typical coal-fired power plants.⁴ The high volume streams consist of 15–16% CO₂, 70–75% N₂, 5–7% water vapor, and other impurities like CO, N_xO_x and SO_x.^{2,5} Precombustion is usually further subdivided into natural gas sweetening and the purification of gas mixtures from gasification or water/gas-shift reactor processes.² The first one deals predominantly with CO₂ impurities (>40%), whereas in the second CO₂/H₂ separation is of major interest. In both cases, elevated temperatures above 40 °C and high pressures around 30 bar have to be taken into account.^{2,4} Natural gas and precombustional gas for coal fire plants are usually contaminated with 5–20% and 40–60% of CO₂, respectively. CO₂ as main contaminant is not only an initiator for global warming, but has also corroding effects on the transporting pipeline systems due to its acidity. Additionally, captured CO₂ could be

Received: May 18, 2016

Revised: July 10, 2016

Published: July 11, 2016

used as reactant for the synthesis of various chemical compounds.⁶ This makes the CO₂ capture and sequestration important for both environmental and industrial interests. Considering the gigantic amount of annual CO₂ release, any solution has to be based on reversible processes.

Since 1930, CCS systems were predominantly based on wet amine solutions (e.g., MEA), which use chemisorptive interactions with carbon dioxide as filtration mechanism.⁷ Because of severe drawbacks, like high cost regeneration, instabilities toward impurities, and equipment corrosion, this method is regarded to be highly inefficient.^{4,8–10} Some of the main drawbacks are a substantial parasitic load of CO₂ capture about 25–30% and a high energy demand for the regeneration step which amounts to 25–40% of the power plants energy output.^{2,4,9,11} A more elegant solution could be provided by solid-state materials with high surface areas, which interact with the adsorptives via physisorption and, in succession, the advantage to facilitate their regeneration by changing physical parameters to unload incorporated molecules like in pressure swing adsorption (PSA) or vacuum swing adsorption (VSA) techniques.⁴ Thus, the possibility to modify both adsorbent properties and process designs strongly influences the effectiveness of a separation method.¹⁰ Additionally, new materials should provide further properties like low cost synthesis, recyclability and high selectivity values.

In this respect, microporous organic polymers^{11–13} (MOPs) exhibit outstanding physicochemical properties combined with high surface areas as well as chemically modifiable structures and are thus in line with other porous solid materials like carbons,^{14–17} zeolites,^{18–21} and metal organic frameworks.^{22–24} In fact, many publications on MOPs have proven their high potential and established strategies for enhancing the CO₂ uptake like surface area modification, pore size engineering, or isosteric heat of adsorption tuning.^{4,12,13,25–27} Simulations have shown that CO₂ acting both as Lewis acid and Lewis base can bind to phenyl rings and polar functionalities inside of a porous network.¹³ Thus, the incorporation of such moieties is a promising start to tune the CO₂ sorption behavior.

Applying these strategies led to the synthesis of promising materials like BILP-4, PPN-6-deta, and ALP-1 with the remarkable CO₂ uptake values of 5.3, 4.3, and 5.4 mmol/g at 273 K and 1 bar, respectively, which are among the best porous polymer networks up to date.^{9,28,29} Focusing on microporous polyimides like PI-NO₂-1, uptakes up to 4.0 mmol/g at 273 K and 1 bar were reached.³⁰ Furthermore, excellent selectivities of CO₂ over N₂, like in TPI-2@IC³¹ (151) or STPI-2³² (107), and CH₄, for example, PI-NO₂-2³⁰ (21) or NPI-1³³ (13), have been reported.

Similar or even better sorption properties were obtained for microporous, crystalline materials like metal–organic-frameworks (MOFs). For example, mmen-Mg₂(dobpdc) adsorbs up to 6.4 mmol/g at 298 K and 1 bar in combination with a CO₂ over N₂ selectivity over 96%.^{34,35} The zeolitic imidazolate framework UTSA-49a shows a CO₂ uptake capacity of 4.8 mmol/g at 273 K and 1 bar in combination with a substantial CO₂ over CH₄ selectivity around 35.³⁶ Nevertheless, MOFs often suffer from a limited chemical and thermal stability underlining the competitiveness of MOPs.

Herein, we report the synthesis of five new microporous polyimides (MOPIs) via a polycondensation polymerization process of amine and anhydride linker molecules. Although the synthesis procedure is based on our previous work on TPIs,³⁷ here, we focus on 3D networks with a central tetrahedral core

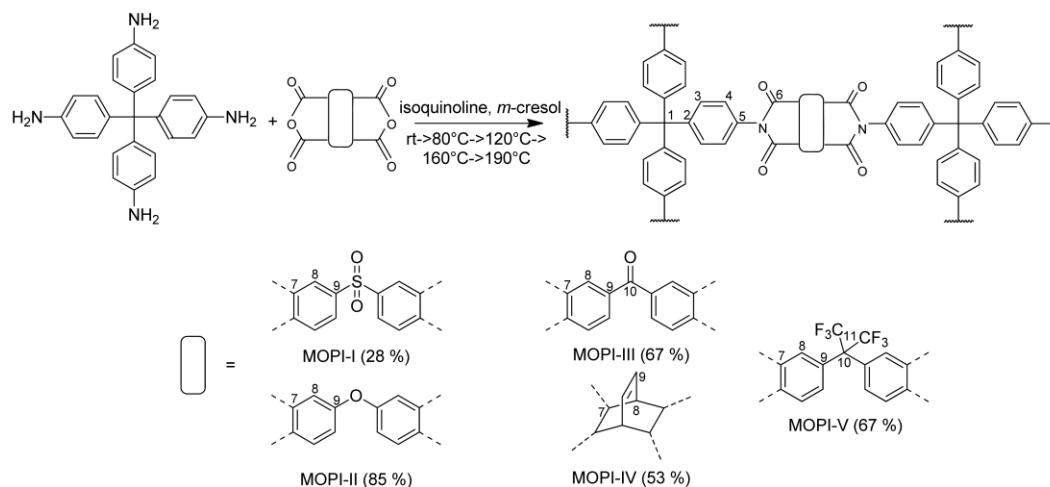
based on tetrakis(4-aminophenyl)methane for all five MOPIs. The corresponding anhydrides are chosen to favor a more or less linear expansion of the network. Their individual electronic properties, additionally, allow to vary the chemical nature of the void surfaces in a systematic fashion among other things from hydrophilic to hydrophobic. After a thorough characterization of the polymers by IR spectroscopy, ¹³C and ¹⁵N solid-state NMR spectroscopy, CHN analysis, and TG analysis as well as X-ray diffraction, the influence of surface areas, pore structures, and different side groups on their gas sorption behavior will be discussed. In addition, the gas uptake and selectivity for N₂, CO₂, and CH₄, as well as the water vapor uptake into the networks is considered. All these properties are discussed in the context of the chemical nature of the inner surfaces.

EXPERIMENTAL SECTION

General Information. Argon and nitrogen sorption measurements were carried out on a Quantachrome Autosorb-1 pore analyzer at 87 and 298 K, respectively. The data were analyzed using the ASIQ v 3.0 software package. Pore size distributions were calculated with methods of quasistationary density functional theory (QSDFT). The isosteric heat of adsorption was calculated using the CO₂ adsorption isotherms at 273, 298, and 313 K. CO₂ and CH₄ adsorption isotherms were measured on a Quantachrome Nova surface analyzer at 273, 298, and 313 K, respectively. Selectivities and adsorption parameters were calculated using IAST and Henry methods according to the literature.^{38,39} Calculations of the specific surface area, pore volumes and pore size distributions measured with CO₂ at 273 K were carried out using the nonlocal density functional theory (NLDF) slit-pore model for carbon materials. For the Ar-based isotherms, the choice of the QSDFT adsorption branch kernel for cylindrical pores in carbon based materials depended on the calculated fitting error. Water sorption isotherms were measured using a BEL JAPAN INC. Belsorpmax instrument. To avoid extremely long measuring times, the desorption branch was aborted when the pressure equilibration exceeded 24 h. Thus, for two networks (MOPI-I and MOPI-IV) the water isotherms are not fully closed. All polymers have been degassed under vacuum (10⁻² kPa) at 110 °C for 12 to 16 h before starting the adsorption experiments.

¹H and ¹³C liquid-NMR spectra of the linker molecules were carried out on a Bruker 500 MHz spectrometer using either CDCl₃ or DMSO as solvents. For infrared spectra (IR) a JASCO FT/IR-6100 Fourier transform infrared spectrometer with an attenuated total reflectance (ATR) unit was used. CHN analysis was carried out at a vario EL-III with acetanilide as standard (Measured: C [71.09], H [6.71], N [10.36]. Calcd: C [71.09], H [6.71], N [10.36]). Mass spectrometry (MS) was performed at a Finnigan MAT-8500-spectrometer with an ionization energy of 70 eV. Thermogravimetric analysis (TGA) was carried out on a Mettler Toledo TGA/SDTA851^e. Powder X-ray diffraction (PXRD) measurements were performed on a PANalytical X'Pert Pro diffractometer. Here, a region from 2 to 30° 2θ was measured with a 1/4 antiscatter slit and Cu Kα radiation (nickel filtered). All solid-state NMR spectra were acquired on a Bruker Avance-III HD spectrometer operating at a B₀ field of 9.4 T. ¹³C (δ = 100.6 MHz) and ¹⁵N (δ = 40.6 MHz) MAS spectra were obtained with ramped cross-polarization (CP) experiments where the nutation frequency ν_{nut} on the proton channel was varied linearly from 70–100%. The samples were spun at 12.5 kHz (¹³C) and 10.0 kHz (¹⁵N) in a 4 mm MAS double resonance probe (Bruker). The corresponding ν_{nut} on the ¹³C channel and the contact time were adjusted to 70 kHz and 3.0 ms, respectively. On the ¹⁵N channel, the corresponding ν_{nut} and the contact time were adjusted to 35 kHz and 5.0 ms, respectively. Proton broadband decoupling with spinal-64 and ν_{nut} = 12.5 kHz was applied during acquisition.⁴⁰ ¹³C spectra are referenced with respect to TMS (tetramethylsilane) using the secondary standard adamantane. ¹⁵N spectra are referenced with respect to CH₃NO₂ using the secondary standard glycine.

Scheme 1. General Polymerization Reaction and Simplified Structures of the Presented MOPI Networks



Synthesis. All chemicals were purchased at Sigma-Aldrich Chemistry GmbH, VWR Chemicals, TCI, or Grüssing GmbH and were, if not mentioned otherwise, used without further purification (Table S1). *m*-Cresol was freshly distilled over CaH_2 and stored under Ar over a molecular sieve M4 prior to use. All polymerizations were carried out under Ar atmosphere.

Synthesis of the Linker. Tetraphenylmethane.⁴¹ A total of 15 g of trityl chloride (0.054 mol, 1 equiv) and 14.05 mL of aniline (0.154 mol, 2.9 equiv) were heated up to 180°C in a round flask with magnetic stirrer and condenser, until the reaction mixture turned into a violet solid. The heating process was extended for 10 more minutes. The solid was cooled down, crushed and suspended in 75 mL of MeOH and 75 mL of 2 M HCl. The suspension was refluxed for 30 min, filtered, and washed with water. After suspending in ethanol, the reaction mixture was cooled down to -30°C and 15.75 mL of sulfuric acid and 9.44 g of isopentyl nitrite (0.081 mol, 1.5 equiv) were added under vigorous stirring. After stirring for 1 h at -10°C , 26.9 mL of phosphinic acid (0.609 mol, 11 equiv) were added slowly and the reaction mixture was refluxed for 1.5 h. After cooling down, the solid was filtered, washed with DMF, H_2O , and ethanol, and subsequently dried in vacuo to get a light brown powder. Yield: 16.1 g (0.05 mol, 93%). ^1H NMR (500 MHz, CDCl_3): δ [ppm] = 7.07–7.20 (m, 5H, Ar–H). ^{13}C NMR (500 MHz, CDCl_3): δ [ppm] = 146.8 (C-2), 131.2 (C-3), 127.5 (C-4), 125.9 (C-5), 65.0 (C-1). Anal. Found: C [91.73], H [6.91], N [0.24]. Calcd: C [93.71], H [6.29], N [0.00]. MS [m/z] = 320, 243, 165. IR (ATR): ν [cm^{-1}] = 3050, 1589, 1496, 1434, 1319, 1268, 1185, 1080, 1029, 987, 935, 899, 842, 749, 697, 635.

Tetrakis(4-nitrophenyl)methane.⁴² A total of 14 mL of fuming nitric acid in a flask equipped with a magnetic stirrer, a thermometer, and a gas funnel were cooled down to -10°C , followed by the portioned addition of 2.5 g of tetraphenylmethane ($7.8 \cdot 10^{-3}$ mol), 9 mL of acetic acid, and 4 mL of acetic anhydride. The mixture was stirred at -10°C for 1 h. The resulting yellow solid was filtered, washed with acetic acid and water, and dried in an oven at 100°C . Yield: 2.5 g (4.9×10^{-3} mol, 63%). ^1H NMR (500 MHz, CDCl_3): δ [ppm] = 8.2 (d, 2H, Ar–H), 7.3 (d, 2H, Ar–H). ^{13}C NMR (500 MHz, CDCl_3): δ [ppm] = 150.8 (C-2), 141.0 (C-5), 136.3 (C-3), 117.9 (C-4), 66.3 (C-1). Anal. Found: C [59.67], H [3.35], N [10.67]. Calcd: C [60.00], H [3.22], N [11.20]. MS [m/z] = 500, 278, 332, 302, 285, 239, 213, 163. IR (ATR): ν [cm^{-1}] = 3095, 1590, 1510, 1407, 1339, 1222, 1182, 1106, 1011, 962, 917, 836, 746, 706.

Tetrakis(4-aminophenyl)methane.⁴³ A total of 0.75 g of tetrakis(4-nitrophenyl)methane (1.5×10^{-3} mol, 1 equiv) were suspended in 50 mL THF. Then, 1 g of $\text{N}_2\text{H}_4 \cdot \text{H}_2\text{O}$ (20×10^{-3} mol, 13 equiv) and ~ 5 g

of Raney nickel were added and the mixture was refluxed for 3 h. After hot filtration and washing with THF, the solvent was evaporated and the residue washed with DCM to give a white solid. Yield: 0.358 g (9×10^{-4} mol, 63%). ^1H NMR (500 MHz, CDCl_3): δ [ppm] = 6.9 (d, 1H, Ar–H), 6.5 (d, 1H, Ar–H), 3.5 (s, 2H, NH_2). ^{13}C NMR (500 MHz, CDCl_3): δ [ppm] = 146.1 (C-5), 136.3 (C-2), 131.6 (C-3), 113.1 (C-4), 61.5 (C-1). Anal. Found: C [77.31], H [6.70], N [14.32]. Calcd: C [78.92], H [6.36], N [14.73]. MS [m/z] = 380, 288, 271, 195, 180. IR (ATR): ν [cm^{-1}] = 3391, 3162, 1609, 1501, 1425, 1268, 1177, 1191, 1101, 1011, 955, 859, 809.

General Polymerization Procedure. On the basis of a former publication in the field of porous polyimides, all polymerization reactions were carried out under argon atmosphere in dry three-necked flasks equipped with a magnetic stirrer and a thermometer.³⁷ For all polymers, *m*-cresol was used as solvent. The molar ratio of tetrakis(4-aminophenyl)methane to the corresponding anhydride was set to 1:2 to provide equimolar amounts of amine and anhydride groups. The following, more detailed synthesis of MOPI-I is given as reference protocol for all polymerization reactions.

Synthesis of MOPI-I. A total of 68.9 mg of tetrakis(4-aminophenyl)methane (0.181×10^{-3} mol, 1 equiv) and 130 mg 3,3',4,4'-diphenylsulfonetetracarboxyldianhydride (0.362×10^{-3} mol, 2 equiv) were added to 20 mL of *m*-cresol under Ar atmosphere. The mixture was stirred for 24 h at 0°C . Afterward, a catalytic amount (≈ 1 mg) of isoquinoline was added and the mixture was again stirred for 12 h at room temperature. The polymerization reaction was carried out at 80°C for 4 h, 120°C for 4 h, 160°C for 6 h, 190°C for 18 h. After cooling down to room temperature, the resulting solid was filtered and washed with toluene, dichloromethane, and methanol. Additional purification was achieved in a Soxhlet apparatus with tetrahydrofuran overnight. After drying in an oven at 100°C , MOPI-I was obtained as brown powder. Yield: 56 mg (0.055 mmol, 28%). ^{13}C NMR (CP-MAS, 12.5 kHz): δ [ppm] = 166 (C-6), 147 (C-2, C-9), 132 (C-3, C-7), 124 (C-4), 115 (C-8), 64 (C-1). Anal. Found: C [61.12], H [3.66], N [5.11]. Calcd: C [67.18], H [2.72], N [5.40]. IR (ATR): ν [cm^{-1}] = 1784, 1721, 1603, 1507, 1420, 1367, 1317, 1223, 1184, 1150, 1094, 1057, 1023, 916, 820, 740.

Synthesis of MOPI-II. A total of 81.9 mg of tetrakis(4-aminophenyl)methane (0.215×10^{-3} mol, 1 equiv) and 134 mg of 4,4'-oxidiphthalicdianhydride (0.43×10^{-3} mol, 2 equiv) were used as reactants. MOPI-II was obtained as light brown powder. Yield: 170 mg (0.183×10^{-3} mol, 85%). ^{13}C NMR (CP-MAS, 12.5 kHz): δ [ppm] = 166 (C-6), 159 (C-9), 146 (C-2), 134 (C-5, C-7), 130 (C-3), 126 (C-4), 117 (C-8), 108 (C-8), 64 (C-1). Anal. Found: C [70.45], H [3.43],

N [5.72]. Calcd: C [74.04], H [3.00], N [5.95]. IR(ATR): ν [cm^{-1}] = 1780, 1717, 1603, 1507, 1474, 1430, 1360, 1273, 1234, 1080, 1020, 956, 806, 744.

Synthesis of MOPI-III. A total of 100 mg of tetrakis(4-aminophenyl)methane (0.262×10^{-3} mol, 1 equiv) and 169 mg of 3,3',4,4'-benzophenonetetracarboxylic dianhydride (0.525×10^{-3} mol, 2 equiv) were used as reactants. MOPI-III was obtained as other colored solid. Yield: 168 mg (0.176×10^{-3} mol, 67%). ^{13}C NMR (CP-MAS, 12.5 kHz): δ [ppm] = 193 (C-10), 166 (C-6), 144 (C-2, C-9), 134 (C-5, C-3), 131 (C-4), 124 (C-8), 64 (C-1). Anal. Found: C [69.59], H [3.48], N [5.29]. Calcd: C [74.59], H [2.92], N [5.81]. IR(ATR): ν [cm^{-1}] = 1780, 1710, 1615, 1497, 1411, 1365, 1294, 1255, 1208, 1161, 1082, 1019, 972, 918, 854, 815, 714.

Synthesis of MOPI-IV. A total of 118 mg of tetrakis(4-aminophenyl)methane (0.311×10^{-3} mol, 1 equiv) and 0.154 mg of bicyclo[2,2,2]oct-7-en-2,3,5,6-tetracarboxylic dianhydride (0.621×10^{-3} mol, 2 equiv) were used as reactants. MOPI-IV was obtained as brown solid. Yield: 132 mg (0.164×10^{-3} mol, 53%). ^{13}C NMR (CP-MAS, 12.5 kHz): δ [ppm] = 177 (C-6), 147 (C-2, C-9), 131 (C-3, C-5), 127 (C-4), 65 (C-1), 42 (C-7), 35 (C-8). Anal. Found: C [69.61], H [4.20], N [6.26]. Calcd: C [73.52], H [3.95], N [6.86]. IR(ATR): ν [cm^{-1}] = 1782, 1714, 1663, 1679, 1495, 1444, 1368, 1334, 1241, 1182, 1123, 1022, 979, 819, 751.

Synthesis of MOPI-V. A total of 80 mg of tetrakis(4-aminophenyl)methane (0.209×10^{-3} mol, 1 equiv) and 186 mg of 4,4'-(hexafluoroisopropylidene)diphthalic anhydride (0.418×10^{-3} mol, 2 equiv) were used as reactants. MOPI-V was obtained as brown solid. Yield: 167 mg (0.140×10^{-3} mol, 67%). ^{13}C NMR (CP-MAS, 12.5 kHz): δ [ppm] = 166 (C-6), 146 (C-2), 139 (C-9), 132 (C-7, C-5), 124 (C-3, C-8), 117 (C-11), 64 (C-1), 61 (C-10). Anal. Found: C [62.02], H [2.93], N [4.65]. Calcd: C [63.59], H [2.33], N [4.63]. IR(ATR): ν [cm^{-1}] = 1785, 1729, 1617, 1503, 1435, 1366, 1298, 1252, 1206, 1145, 1092, 1023, 986, 916, 886, 856, 818, 741, 711.

RESULTS AND DISCUSSION

Synthesis. Tetrakis(4-aminophenyl)methane was synthesized by a well established procedure, starting with the coupling of triphenylchloromethane and aniline.⁴¹ After nitration of the resulting tetraphenylmethane the nitro group was reduced to tetrakis(4-aminophenyl)methane using Raney nickel and hydrazine in an overall yield of 37%.^{42,43} For the polymerization reaction, tetrakis(4-nitrophenyl)methane and the correspondent anhydride were used in a molar ratio of 1:2, following a procedure established by Liebl et al.³⁷ The choice of *m*-cresol as solvent is essential due to its high boiling point (202 °C), which turned out to be optimal for this kind of polymerization reactions.³⁷ After dissolving the reactants (Scheme 1), isoquinoline was added as catalyst due to its basic and hygroscopic properties.^{5,44} The reaction was carried out using a five step temperature program, starting at room temperature, followed by several heating periods including 80 °C for 4 h, 120 °C for 4 h, 160 °C for 6 h and 190 °C for 18 h. This induces a slow polymerization process and simultaneously circumvent an early precipitation of oligomers.^{37,45} At the final heating step, the precipitation of the polymer was observed. All polymers were obtained with good yields between 50 and 85%. Only for MOPI-I was the yield considerably lower (28%).

Characterization. The resulting polymers were characterized by combining solid-state NMR and IR spectroscopy as well as elemental analysis. Further information about physicochemical properties were derived from PXRD (Figure S16) and TG experiments (Figure S17) carried out in air. All five MOPIs share a tetrakis(phenyl)methane core and imide linkages as a result of the cross-linking. The most characteristic peaks in the ^{13}C and ^{15}N MAS spectra (Figure 1, Table S2) for both units are 64 ppm assigned to the tetrahedral carbon atoms

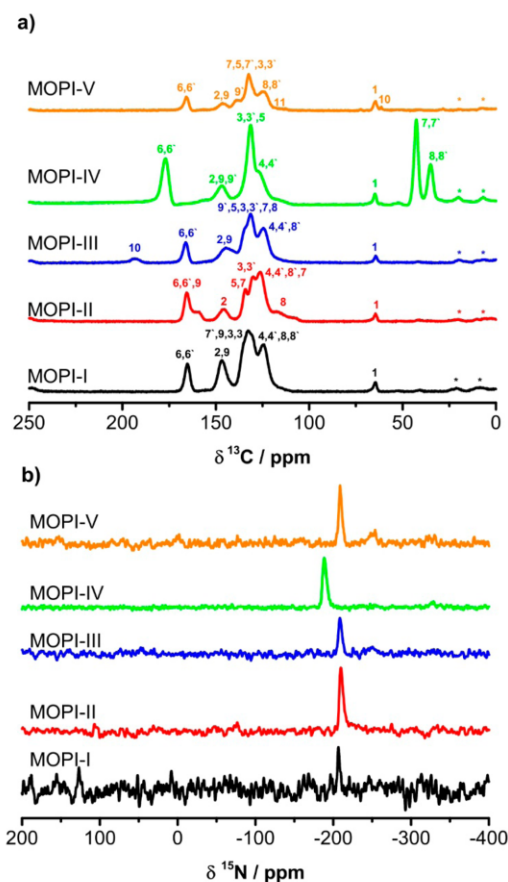


Figure 1. Solid-state ^{13}C (a) and ^{15}N (b) MAS NMR spectra of MOPI I–V, measured with cross-polarization and spinning speeds of 12.5 and 10 kHz, respectively. Assignment correlates with Scheme 1. The asterisks mark spinning side bands.

(1) as well as 165 ppm for the imide carbon atoms (6). The corresponding imide nitrogen atoms resonate at -209 ppm in the ^{15}N NMR spectra. Furthermore, the absence of the ^{15}N amine resonance around -315 ppm (Figure 1) as well as of the two characteristic anhydride bands around 1830 and 1750 cm^{-1} and of the NH_2 stretching vibration around 3500 cm^{-1} (Figure S4) ensure an almost complete cross-linking with an exception being MOPI-V, where a small amount of unreacted amine end groups remains.¹⁸

This is in agreement with the results of the CHN analysis which show only small deviations (<1% for H, N and <5% for C) from the calculated data (Table 1). In the case of MOPI-IV, the resonances for both the imide carbons (6) and nitrogens are low field shifted to 177 ppm and -188 ppm due to the aliphatic character of the corresponding core of the linker (Figure 1, Table S2). The imide functional groups were also observed in the infrared spectra of the polymers at 1778 cm^{-1} where the typical imide carbonyl band of cyclic five membered

Table 1. CHN Analysis^a of MOPIs and Decomposition Temperatures Measured under Air

CHN-Analysis	MOPI-I [%]	MOPI-II [%]	MOPI-III [%]	MOPI-IV [%]	MOPI-V [%]
C (exp./calc.) ^b	61.12 (66.12)	70.45 (73.71)	69.59 (74.37)	69.61 (73.14)	62.02 (63.22)
H (exp./calc.) ^b	3.66 (2.75)	3.43 (3.94)	3.48 (2.97)	4.20 (4.01)	2.92 (2.36)
N (exp./calc.) ^b	5.11 (6.26)	5.72 (6.03)	5.29 (5.88)	6.26 (6.96)	4.65 (5.62)
TGA Analysis ^c					
Decomposition [°C]	421	440	390	350	475

^aIn wt %. ^bRepeating units used to derive calculated weight percentages are given in Supporting Information Section 3.2. ^cFull decomposition curves are shown in Figure S17.

rings resonates at 740 cm⁻¹, which is due to N–H wagging (Figure S4).

Further distinct but individual ¹³C NMR and IR spectroscopic features are observed in the case of MOPI-I at 145 ppm, typical for the α -carbon of a sulfone group (9) (Figure 1). The IR bands of the sulfone group appear at 1177, 1320, and 1058 cm⁻¹ (Figure S7). For MOPI-II, the α -carbon of the ether group (9) resonates at 159 ppm. The corresponding CO stretching vibration for the aryl ether was found at 1273 cm⁻¹ (Figure 2, Figure S9). In the case of MOPI-III, the α -keto-carbon signal (10) appears at 194 ppm and the aryl ketone band was observed at 1211 cm⁻¹ (Figure S11). For MOPI-IV, the aliphatic β -carbon atom (7) next to the imide group is assigned to 42 ppm (Figure 1). The β -carbon atoms of the bicyclooctene group (8) resonate at 35 ppm. In the IR spectra the C=C stretching vibration of the bicyclooctene unit is prominent at 1663 cm⁻¹ (Figure S13). The structure of MOPI-V is, furthermore, validated by a signal at 61 ppm, assigned to the quaternary carbon atoms (10) next to the CF₃ moieties (11) expected around 113 ppm (Figure 1). Because of the strong ¹³C¹⁹F dipole interactions, the signal is broadened. The corresponding –CF₃ stretching vibration was observed at 1255 and 1191 cm⁻¹ (Figure S15).

TG measurements carried out in air reveal first indications for structural decomposition between 350 °C for MOPI-IV and 475 °C for MOPI-V reflecting the thermal persistence of the core units (Table 1, Figure S16). For MOPI-I additionally, a weight loss of about 10% was observed at 160 °C due to desorption of water. PXRD measurements as well as SEM micrographs confirm the amorphous nature of all polymers (Figures S15 and S35).

Surface Area and Porosity. The porosity of all MOPIs was determined from Ar adsorption isotherms measured at 87 K (Figure 2, Supporting Information (SI) Section 4.1). Ar, as monatomic gas, is engaged in fewer interactions with surfaces in comparison to the often used N₂, especially with polar compounds and due to its higher boiling point, and equilibrium processes are significantly shortened. The isotherms show high Ar uptakes at low relative pressures, typical for microporous materials. The shapes of the isotherms resemble IUPAC Type I(b) isotherms, indicating broader pore size distributions including wider micropores and narrow mesopores.⁴⁶ For all polymers, a hysteresis was observed, which is generally associated with capillary condensation, a phenomenon linked with mesoporosity.⁴⁶ The extension of the hysteresis into the low pressure region, nevertheless, favors swelling of the networks.

MOPI-I shows, the lowest BET and DFT surface areas around 220 m²/g, which is probably due to the high flexibility of the sulfone bridge leading to a more compact packing of the network. The highest surface area was observed for MOPI-V

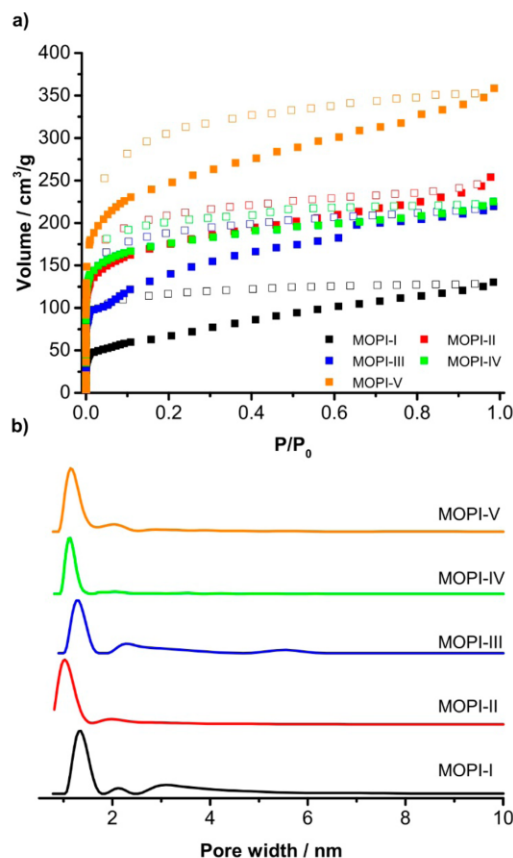


Figure 2. Ar isotherms measured at 87 K (a) and normalized pore size distributions (b) calculated by QSDFT adsorption branch kernel for cylindrical pores in carbon based materials. Full symbols characterize adsorption isotherms, hollow symbols the corresponding desorption curve.

with roughly 930 m²/g. For the other polyimides, specific surface areas in between (480 and 730 m²/g) are found.

For MOPI-I and -III the ratio V_{mic}/V_{tot} is around 30%, indicating a large percentage of mesopores, which correlates with their lower surface areas in comparison with the other polyimides (Table 2). This is in line with the pore size distributions given in Figure 2, revealing a broad distribution of mesopores up to 6 nm. MOPI-II and MOPI-V developed higher values of microporosity around 50% with only small

Table 2. Surface Areas Determined from Ar and CO₂ Isotherms and Calculated by BET and DFT Methods^{a,c}

polymer	Ar/87.3 K ^b [m ² /g]	Ar/87.3 K ^c [m ² /g]	CO ₂ /273 K ^d [m ² /g]	V _{tot,Ar,DFT} [cm ³ /g]	V _{mic,Ar,DFT} [cm ³ /g]	V _{mic} /V _{tot} Ar, DFT	V _{tot,CO₂,DFT} [cm ³ /g]
MOPI-I	206	231	777	0.16	0.05	0.31	0.24
MOPI-II	644	739	676	0.32	0.17	0.53	0.19
MOPI-III	443	468	712	0.27	0.09	0.33	0.22
MOPI-IV	660	735	896	0.28	0.19	0.68	0.27
MOPI-V	921	939	690	0.44	0.23	0.52	0.23

^aPore volumes calculated by DFT methods from Ar and CO₂ isotherms. ^bCalculated based on the BET equation. ^cCalculated using QSDFT for cylindrical pores in carbon based materials for the adsorption branch only. ^dCalculated based on NLDFT with a slit-pore model for carbon materials.

mesopores around 2 nm (Figure 2). The highest microporosity is observed for MOPI-IV (68%) (Table 2). All five polyimide networks exhibit a narrow pore size distribution in the microporous region with a center of gravity between 1.0 nm for MOPI-II and 1.4 nm for MOPI-I (Figure 2). To probe potential ultramicropores CO₂ isotherms at 273 K were measured (Figure 3, SI Section 4.2), which allows detection of pores between 0.3 and 1.5 nm.

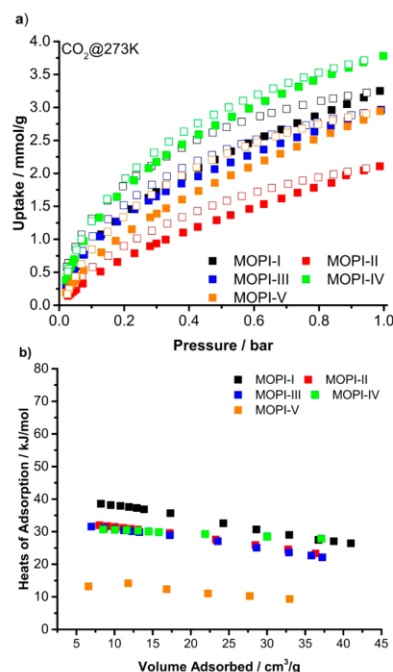


Figure 3. CO₂ uptake at 273 K (a) and isosteric heats of adsorption for CO₂ (b) calculated from adsorption isotherms at 273, 298, and 313 K. Full symbols characterize adsorption isotherms, hollow symbols the corresponding desorption curve.

The pore size distributions for all polymers (Figure S18), calculated from the CO₂ isotherms show a broad distribution of pore sizes between 0.3 to 1 nm, which indicates an undirected pore formation due to the amorphous character of the networks. For MOPI-I, -III, and -V the surface areas derived from the CO₂ isotherms are markedly higher compared to the Ar surfaces, in particular for MOPI-I (777 m²/g vs 231 m²/g), demonstrating a high degree of ultramicropores (Table 2). In

contrast, the surface areas of MOPI-II and MOPI-V decrease toward 676 m²/g and 690 m²/g in comparison to Ar surface areas of 739 m²/g and 939 m²/g, respectively. These values indicate a high amount of pore sizes beyond 1.5 nm for those networks (Table 2). In conclusion, MOPI-I, MOPI-III, and MOPI-IV possess a higher ratio of ultramicropores than their related polymers, which is discussed in more detail together with the sorption behavior toward CO₂ and CH₄.

CO₂, CH₄, and H₂O Adsorption. The high surface areas and microporous structures render all MOPIs as suitable candidates for applications such as gas storage and separation. As mentioned before, the interaction of those materials with industrial relevant gas mixtures is of vital relevance. In particular, industrial flue gas mixtures contain high amounts of water (up to 7%), which is a potential competitor for binding sites in filtering materials and would decrease the potential of an appropriate material. In return, super hydrophilic materials could be favorable for alternative applications like water absorber or heat transformation. In this context, the uptake of water vapor at low pressures in materials like covalent organic frameworks and porous carbons for the application in atmospheric water capture (AWC), heat pumps or electric dehumidifiers has gained some interest in the literature.^{47–49} Recently, Lotsch et al. synthesized the AB-COF for AWC application with a remarkable water uptake of 15 mmol/g at low relative pressure ($p/p_0 < 0.3$), which shows the high potential of porous polymer networks in this field of application.⁴⁹

With this in mind the behavior of the synthesized polymers toward CO₂, CH₄, N₂, and H₂O at various temperatures as well as their selectivity toward specific gas mixtures has been analyzed (Tables 3 and 4). CO₂ adsorption measurements at 273, 298, and 313 K, respectively, were performed to compare the uptake behavior of the polymers at 1 bar.

At 273 K MOPI-I, -II, -III, and -V show CO₂ uptakes around 3 mmol/g which are already extraordinary high compared to literature values.^{5,30,32,33,50–56} The best CO₂ uptake, however, was obtained for MOPI-IV with 3.8 mmol/g at 273 K, which is the second best value for microporous polyimides next to the previous mentioned PI-NO₂-1 and exceeds all other polyimide networks where the uptake is not higher than 3.5 mmol/g.^{30–32,52} In accordance to the literature, we attribute the CO₂ uptake to the ultramicroporosity of the networks,⁴ for which we use the CO₂ surface areas as indicator. MOPI-IV has by far the largest ultramicroporous surface area, followed by MOPI-I, -III, -V, and -II. This is in line with the CO₂ uptake given in Table 3 and explains, for example, why MOPI-V and -II exhibits lower CO₂ uptakes in spite of the comparably large microporous surfaces (determined with Ar). As expected, a decrease of the CO₂ uptake is observed with increasing temperature. Similar uptakes of around 1.5 mmol/g are found for all MOPIs at 313 K (Table 3).

Table 3. Uptakes Taken from Individual Isotherms^a

polymer	CO ₂ 273 K [mmol/g]	CO ₂ 298 K [mmol/g]	CO ₂ 313 K [mmol/g]	N ₂ 298 K [mmol/g]	CH ₄ 273 K [mmol/g]	CH ₄ 298 K [mmol/g]	CH ₄ 313 K [mmol/g]	H ₂ O 298 K [mmol/g]
MOPI-I	3.3	2.2	1.7	0.11	0.61	0.34	0.25	13.5
MOPI-II	2.9	1.9	1.4	0.09	0.61	0.35	0.24	12.3
MOPI-III	3.0	1.8	1.5	0.07	0.72	0.19	0.2	9.0
MOPI-IV	3.8	2.3	1.6	0.10	0.83	0.4	0.3	19.5
MOPI-V	2.9	1.6	1.3	0.04	0.49	0.5	0.17	7.0

^aThe values for CO₂ and CH₄ were determined at $p = 1$ bar and the ones for N₂ and H₂O were extracted at $p/p_0 = 0.9$.

Table 4. CO₂/N₂, CO₂/CH₄, and CO₂/H₂O Selectivities of All MOPIs Calculated from the Correspondent Isotherms and CO₂ Isothermic Heats of Adsorption

sample	CO ₂ /N ₂ ^{a,b} 298 K	CO ₂ /CH ₄ ^{c,d,e} 273 K	CO ₂ /CH ₄ ^{c,d,e} 298 K	CO ₂ /CH ₄ ^{c,d,e} 313 K	H ₂ O/CO ₂ ^e 298 K	Q _{st} ^f [kJ/mol]
MOPI-I	65.3 (78)	16/10 (11)	14/11 (9)	10/9 (7)	92	39
MOPI-II	36.4 (51)	18/9 (8)	9/9 (9)	10/12 (8)	63	32
MOPI-III	50.2 (50)	18/12 (13)	14/11 (10)	12/11 (10)	63	32
MOPI-IV	43.4 (52)	17/11 (10)	15/12 (9)	11/9 (10)	105	31
MOPI-V	26.4 (33)	9/7 (7)	10/9 (9)	4/4 (5)	36	13

^aCalculated by IAST for a mixture of 15% CO₂ and 85% N₂. ^bCalculated by initial slopes of pure-component sorption isotherms. ^cCalculated by IAST from a mixture of 5% CO₂ and 95% CH₄. ^dCalculated by IAST from a mixture of 15% CO₂ and 85% CH₄. ^eCalculated by initial slopes of pure-component sorption isotherms. ^fCalculated from CO₂ isotherms at 273, 298, and 313 K.

The isosteric heats of adsorption calculated from the CO₂ isotherms lead to values around 30 kJ/mol, which are typical for strong physisorptive interactions between guest molecules and the network (Figure 3). Here, we observe the lowest Q_{st} near zero coverage (13 kJ/mol) for MOPI-V, which is expected to have the weakest interactions with CO₂ due to the presence of CF₃ groups. The highest Q_{st} value (39 kJ/mol) is observed for MOPI-I, which is caused by the stronger interactions of the CO₂ molecule with the highly polar sulfone groups. The values for MOPI-II, -III, and -IV were found to be similar around 32 kJ/mol (Table 4). It is worth noting, that the trend for Q_{st} near zero coverage does not reflect the one for the CO₂ uptake. This suggests that the uptake at higher pressures is rather dominated by unselective interactions and not by preferred binding sites within the ultramicropores. The CH₄ uptake, determined from methane adsorption isotherms measured at 273, 298, and 313 K (SI Section 4.3), is remarkably low for all polymers (around 0.5 to 0.7 mmol/g at 273 K) and decreases strongly with increasing temperature, caused by only weak interactions between the unipolar methane molecules and the polar network structures.

Water adsorption measurements at 298 K provide information about the behavior of the polymers in humid environments (Table 3). MOPI-IV shows the highest water uptake with 6.3 mmol/g at 0.3 p/p_0 , which rises toward a total amount of 19.5 mmol/g at 0.9 p/p_0 (Figure 4). Recently published ultrahydrophilic covalent organic frameworks like AB-COF⁴⁹ (22.9 mmol/g), TpPA-1⁴⁸ (24.5 mmol/g) or porous carbons like PCC-1⁴⁷ (~22 mmol/g) give comparable results. This is surprising because for MOPI-IV, the only polar groups are the imide linkages and it is thus considered to be less polar than, for example, MOPI-I with its sulfone bridges, reaching only 13.5 mmol/g at 0.9 p/p_0 .

Thus, the high water vapor uptake of MOPI-IV is more likely to correlate with its high CO₂ surface area which we take as a measure for the amount of ultramicropores (Table 2). For MOPI-I, -II, -III, and -V the CO₂ surface areas are similar. Here, the uptake values of 13.5, 12.3, 9.0, and 7 mmol/g correlate with the polarity of the bridging groups. Additionally, unlike

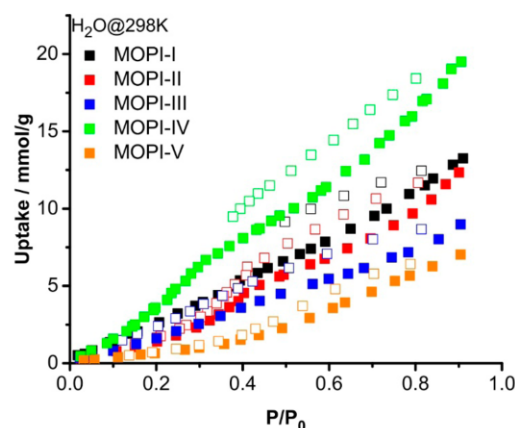


Figure 4. Water vapor adsorption isotherm measured at 298 K. Full symbols characterize adsorption isotherms, hollow symbols the corresponding desorption curve.

MOPI-IV the other networks do not show an enhanced water uptake below 0.3 p/p_0 .

The introduction of CF₃ units in MOPI-V allowed to reduce the water uptake roughly by a factor of 2 and 3 compared to MOPI-I and MOPI-IV, whereas the CO₂ uptake is reduced only by 15 to 30%, respectively. This trend was already reported for FPOP-2 by Han et al.,⁵⁷ which exhibits uptakes as low as 1.5 mmol/g. In the case of MOPI-V, the hydrophobicity of the CF₃ groups is probably counterbalanced by the imide linkages leading to significant higher values.

Selectivities toward CO₂, CH₄, N₂, and H₂O. Because flue gas is a complex mixture of diverse gases, potential filter materials should possess selective uptake proclivity toward specific molecules to ensure their effectiveness and efficiency. To estimate selectivities for the here presented networks, we applied ideal adsorbed solution theory (IAST) for the following industrial relevant gas mixtures CO₂/N₂ (15/85), CO₂/CH₄

(5/95 and 15/85) in comparison to initial slope calculations in the Henry's Law region (<0.1 bar) (SI Section 5.1).^{38,39}

The highest CO₂ over N₂ IAST selectivities calculated at 298 K are 65.3 and 50.2 obtained for MOPI-I and MOPI-III, respectively (Table 4). Especially, MOPI-I competes with materials in the top area of CO₂/N₂ selectivities, only surpassed by networks like modified PPN-6⁴ with values from 150 to 420 or IRMOF-1-4Li⁵⁸ with a selectivity of 395.

We attribute these high values to their pronounced ultramicroporosity and the presence of keto/sulfone and imide groups, which provide Lewis acidic and basic preferred adsorption sites for CO₂. For MOPI-IV, MOPI-II and MOPI-V a further decrease of the selectivity to 43.4, 36.4, and 26.4 is observed, respectively.

This trend does not correlate solely to the CO₂ uptake and thus the ultramicroporosity (CO₂ surface areas). For example, MOPI-IV exhibits the by far largest CO₂ surface area leading to a significant carbon dioxide uptake. Nevertheless, its CO₂/N₂ selectivity is with 43 markedly lower compared to MOPI-I (65) and -III (50). In contrast, the diene functionality of the corresponding linker within MOPI-IV is less polar compared to the sulfone and ketone groups for MOPI-I and -III and thus does not increase the affinity for CO₂ adsorption. Even lower but similar ultramicroporosities were obtained for MOPI-II and MOPI-V leading to a further decrease of the CO₂/N₂ selectivities. For this pair the CF₃ moieties within MOPI-V provide a much lower attraction for CO₂ (Table 4) compared to the ether units of MOPI-II, again accounting for the lower CO₂/N₂ selectivity of 26 in the case of MOPI-V. As consequence, in contrast to the CO₂ uptakes, the selectivities seem to be influenced by both the ultramicroporosity and the functionality of the networks in equal measures. Thus, at least to a certain degree preferred binding sites are important to influence the separation properties.

The IAST selectivities for the corresponding CO₂/CH₄ mixtures, reveal similar trends, indicating that the same influencing effects discussed above are relevant. For MOPI-III, -IV, -I, -II, and -V values of 12, 11, 10, 9, and 7 were found in order to their ultramicroporosity and decreasing affinity of their functional groups for CO₂ (Table 4, SI Section 5.2). Lowering the portion of CO₂ toward a ratio of 5:95 results in increasing selectivities for all networks with top values of 18 for MOPI-II and -III as well as toward 17 and 16 for MOPI-IV and -I, respectively. For MOPI-V only a minor CO₂ affinity improvement from 7 to 9 was observed (Table 4). The increase of the temperature leads toward significantly lowered CO₂ affinities toward 12, 11, 10, 10, and 4 for MOPI-III, -IV, -I, -II, and -V, respectively, for a 5:95 CO₂/CH₄ mixture. At higher CO₂ ratios (15:85) the temperature seems to have only a minor effect on the selectivities. Interestingly, in the case of MOPI-II even an increase from 9 to 12 was found hinting at a cooperative effect between CO₂ and CH₄ within the network (Table 4).

The calculation of H₂O/CO₂ selectivities by initial slopes of pure-component sorption isotherms, obtained high values of 105 and 92 for MOPI-IV and -I, respectively, indicating a major effect of the ultramicroporosity with respect to the chemical nature of the polymers. For MOPI-II and -III a lower selectivity of 63 was observed. Due to its hydrophobic —CF₃ moieties the selectivity for MOPI-V decreases to 36 (Table 4).

CONCLUSION

The condensation polymerization of amino- and anhydride-linker molecules in *m*-cresol leads to five new microporous organic polyimides, MOPI-I to -V. Compared to the recent literature, the compounds presented here are promising materials for gas capture and sequestration, as well as potential water vapor adsorber.^{9,28–32,55–57}

All polymers show high cross-linking degrees, confirmed by ¹³C and ¹⁵N MAS NMR spectroscopy and by elemental analysis. The polyimides exhibit moderate to high specific surface areas between 231 m²/g (MOPI-I) and 957 m²/g (MOPI-V) and a mainly micro- to ultramicroporous character. Their porosity in combination with different functional groups leads to remarkable CO₂ uptake values up to 3.8 mmol/g at 273 K and 1 bar in the case of MOPI-IV, which is among the highest values obtained for polyimides only surpassed by PI-NO₂-1 (4.03 mmol/g).³⁰ The polymers exhibit respectable IAST selectivity values toward N₂ (up to 65 for MOPI-I) and CH₄ (18 for MOPI-II, -III) and can compete with most polyimides (CO₂/N₂ < 150 and CO₂/CH₄ < 20).^{30,31,33,52} In addition, water sorption isotherms showed a surprisingly hydrophilic character for MOPI-IV, with uptakes of 6.3 mmol/g at 0.3 *p*/*p*₀ and 19.5 mmol/g at 0.9 *p*/*p*₀. For MOPI-I, -II, -III, and -V a decrease of the water uptake in correlation with the polarity of their functional group down to 7 mmol/g at 0.9 *p*/*p*₀ and 298 K for MOPI-V was observed.

Summarizing, the CO₂ and H₂O uptakes of all polyimides are dominated by the ultramicroporous character of the networks. Here, the chemical functionalities introduced by the individual linkers play only a secondary role indicating that size discrimination within the frameworks might be an essential part of the adsorption process. In contrast, for the selectivities both the porosity as well as the chemical functionality seem to be equally important. This, in turn, hints at the existence of preferred adsorption sites for CO₂ and H₂O.

ASSOCIATED CONTENT

Supporting Information

The Supporting Information is available free of charge on the ACS Publications website at DOI: 10.1021/acs.chemmater.6b01949.

Further spectra, isotherms, and selectivity plots are provided. (PDF)

AUTHOR INFORMATION

Corresponding Author

*E-mail: juergen.senker@uni-bayreuth.de.

Notes

The authors declare no competing financial interest.

ACKNOWLEDGMENTS

The authors thank Dr. Renée Siegel and Beate Bojer for performing solid-state NMR measurements, Lena Geiling for gas sorption measurements, Carina Bojer for taking SEM images, Dr. Ulrike Lacher for performing mass spectrometry experiments, and Nadine Popp for consultative support. We gratefully thank Prof. Josef Breu and Prof. Rhett Kempe for access to the respective instruments.

■ REFERENCES

- (1) Haszeldine, R. S. Carbon Capture and Storage: How Green Can Black Be? *Science* **2009**, *325*, 1647–1652.
- (2) D'Alessandro, D. M.; Smit, B.; Long, J. R. Carbon Dioxide Capture: Prospects for New Materials. *Angew. Chem., Int. Ed.* **2010**, *49*, 6058–6082.
- (3) *The State of Greenhouse Gases in the Atmosphere Based on Global Observations through 2013*; World Meteorological Organization: Geneva, Switzerland, 2014; No. 10, pp 1–8.
- (4) Dawson, R.; Cooper, A. I.; Adams, D. J. Chemical Functionalization Strategies for Carbon Dioxide Capture in Microporous Organic Polymers. *Polym. Int.* **2013**, *62*, 345–352.
- (5) Li, G.; Wang, Z. Microporous Polyimides with Uniform Pores for Adsorption and Separation of CO₂ Gas and Organic Vapors. *Macromolecules* **2013**, *46*, 3058–3066.
- (6) Grande, C. A.; Ribeiro, R. P. L.; Oliveira, E. L. G.; Rodrigues, A. E. Electric Swing Adsorption as Emerging CO₂ Capture Technique. *Energy Procedia* **2009**, *1*, 1219–1225.
- (7) Rochelle, G. T. Amine Scrubbing for CO₂ Capture. *Science* **2009**, *325*, 1652–1654.
- (8) Byun, J.; Je, S.-H.; Patel, H. A.; Coskun, A.; Yavuz, C. T. Nanoporous Covalent Organic Polymers Incorporating Tröger's Base Functionalities for Enhanced CO₂ Capture. *J. Mater. Chem. A* **2014**, *2*, 12507.
- (9) Lu, W.; Sculley, J. P.; Yuan, D.; Krishna, R.; Wei, Z.; Zhou, H.-C. Polyamine-Tethered Porous Polymer Networks for Carbon Dioxide Capture from Flue Gas. *Angew. Chem., Int. Ed.* **2012**, *51*, 7480–7484.
- (10) Bhowan, A. S. Status and Analysis of Next Generation Post-Combustion CO₂ Capture Technologies. *Energy Procedia* **2014**, *63*, 542–549.
- (11) Dawson, R.; Stöckel, E.; Holst, J. R.; Adams, D. J.; Cooper, A. I. Microporous Organic Polymers for Carbon Dioxide Capture. *Energy Environ. Sci.* **2011**, *4*, 4239.
- (12) Lu, A.-H.; Hao, G.-P. Porous Materials for Carbon Dioxide Capture. *Annu. Rep. Prog. Chem., Sect. A: Inorg. Chem.* **2013**, *109*, 484.
- (13) Chang, Z.; Zhang, D.-S.; Chen, Q.; Bu, X.-H. Microporous Organic Polymers for Gas Storage and Separation Applications. *Phys. Chem. Chem. Phys.* **2013**, *15* (15), 5430–5442.
- (14) Li, D.; Ma, T.; Zhang, R.; Tian, Y.; Qiao, Y. Preparation of Porous Carbons with High Low-Pressure CO₂ Uptake by KOH Activation of Rice Husk Char. *Fuel* **2015**, *139*, 68–70.
- (15) Seema, H.; Kemp, K. C.; Le, N. H.; Park, S.-W.; Chandra, V.; Lee, J. W.; Kim, K. S. Highly Selective CO₂ Capture by S-Doped Microporous Carbon Materials. *Carbon* **2014**, *66*, 320–326.
- (16) Ma, X.; Cao, M.; Hu, C. Bifunctional HNO₃ Catalytic Synthesis of N-Doped Porous Carbons for CO₂ Capture. *J. Mater. Chem. A* **2013**, *1*, 913–918.
- (17) Sevilla, M.; Valle-Vigón, P.; Fuertes, A. B. N-Doped Polypyrrole-Based Porous Carbons for CO₂ Capture. *Adv. Funct. Mater.* **2011**, *21*, 2781–2787.
- (18) Socrates, G. *Infrared and Raman Characteristic Group Frequencies: Tables and Charts*, 3rd ed., revised; Wiley: Chichester, U.K., 2010.
- (19) Fisher, J. C.; Siriwardane, R. V.; Stevens, R. W. Zeolite-Based Process for CO₂ Capture from High-Pressure, Moderate-Temperature Gas Streams. *Ind. Eng. Chem. Res.* **2011**, *50*, 13962–13968.
- (20) Yang, S.-T.; Kim, J.-Y.; Kim, J.; Ahn, W.-S. CO₂ Capture over Amine-Functionalized MCM-22, MCM-36 and ITQ-2. *Fuel* **2012**, *97*, 435–442.
- (21) Cheung, O.; Hedin, N. Zeolites and Related Sorbents with Narrow Pores for CO₂ Separation from Flue Gas. *RSC Adv.* **2014**, *4*, 14480.
- (22) Li, W.; Zhang, Y.; Li, Q.; Zhang, G. Metal-organic Framework Composite Membranes: Synthesis and Separation Applications. *Chem. Eng. Sci.* **2015**, *135*, 232–257.
- (23) Cabello, C. P.; Berlier, G.; Magnacca, G.; Rumori, P.; Palomino, G. T. Enhanced CO₂ Adsorption Capacity of Amine-Functionalized MIL-100(Cr) Metal-organic Frameworks. *CrystEngComm* **2015**, *17* (2), 430–437.
- (24) Sabouni, R.; Kazemian, H.; Rohani, S. Carbon Dioxide Capturing Technologies: A Review Focusing on Metal Organic Framework Materials (MOFs). *Environ. Sci. Pollut. Res.* **2014**, *21*, 5427–5449.
- (25) Zhu, G.; Ren, H. *Porous Organic Frameworks*; Springer: Berlin/Heidelberg, 2015.
- (26) Sakaushi, K.; Antonietti, M. Carbon- and Nitrogen-Based Organic Frameworks. *Acc. Chem. Res.* **2015**, *48*, 1591–1600.
- (27) Xu, S.; Luo, Y.; Tan, B. Recent Development of Hyper-crosslinked Microporous Organic Polymers. *Macromol. Rapid Commun.* **2013**, *34*, 471–484.
- (28) Arab, P.; Rabbani, M. G.; Sekizkardes, A. K.; İslamoğlu, T.; El-Kaderi, H. M. Copper(I)-Catalyzed Synthesis of Nanoporous Azo-Linked Polymers: Impact of Textural Properties on Gas Storage and Selective Carbon Dioxide Capture. *Chem. Mater.* **2014**, *26*, 1385–1392.
- (29) Rabbani, M. G.; El-Kaderi, H. M. Synthesis and Characterization of Porous Benzimidazole-Linked Polymers and Their Performance in Small Gas Storage and Selective Uptake. *Chem. Mater.* **2012**, *24*, 1511–1517.
- (30) Shen, C.; Wang, Z. Tetraphenyladamantane-Based Microporous Polyimide and Its Nitro-Functionalization for Highly Efficient CO₂ Capture. *J. Phys. Chem. C* **2014**, *118*, 17585–17593.
- (31) Wu, S.; Gu, S.; Zhang, A.; Yu, G.; Wang, Z.; Jian, J.; Pan, C. A Rational Construction of Microporous Imide-Bridged Covalent-organic Polytriazines for High-Enthalpy Small Gas Absorption. *J. Mater. Chem. A* **2015**, *3*, 878–885.
- (32) Zhang, C.; Zhai, T.-L.; Wang, J.-J.; Wang, Z.; Liu, J.-M.; Tan, B.; Yang, X.-L.; Xu, H.-B. Triptycene-Based Microporous Polyimides: Synthesis and Their High Selectivity for CO₂ Capture. *Polymer* **2014**, *55*, 3642–3647.
- (33) Neti, V. S. P. K.; Wang, J.; Deng, S.; Echegoyen, L. Synthesis of a Polyimide Porous Porphyrin Polymer for Selective CO₂ Capture. *J. Chem.* **2015**, *2015*, 1–7.
- (34) McDonald, T. M.; Lee, W. R.; Mason, J. A.; Wiers, B. M.; Hong, C. S.; Long, J. R. Capture of Carbon Dioxide from Air and Flue Gas in the Alkylamine-Appended Metal-Organic Framework Mmen-Mg₂(dobpdc). *J. Am. Chem. Soc.* **2012**, *134*, 7056–7065.
- (35) Zhang, Z.; Yao, Z.-Z.; Xiang, S.; Chen, B. Perspective of Microporous Metal-organic Frameworks for CO₂ Capture and Separation. *Energy Environ. Sci.* **2014**, *7*, 2868.
- (36) Xiong, S.; Gong, Y.; Wang, H.; Wang, H.; Liu, Q.; Gu, M.; Wang, X.; Chen, B.; Wang, Z. A New Tetrazolate Zeolite-like Framework for Highly Selective CO₂/CH₄ and CO₂/N₂ Separation. *Chem. Commun. (Cambridge, U. K.)* **2014**, *50*, 12101–12104.
- (37) Liebl, M. R.; Senker, J. Microporous Functionalized Triazine-Based Polyimides with High CO₂ Capture Capacity. *Chem. Mater.* **2013**, *25*, 970–980.
- (38) Landa, H. O. R.; Flockerzi, D.; Seidel-Morgenstern, A. A Method for Efficiently Solving the IAST Equations with an Application to Adsorber Dynamics. *AIChE J.* **2013**, *59*, 1263–1277.
- (39) Dawson, R.; Stevens, L. A.; Drage, T. C.; Snape, C. E.; Smith, M. W.; Adams, D. J.; Cooper, A. I. Impact of Water Coadsorption for Carbon Dioxide Capture in Microporous Polymer Sorbents. *J. Am. Chem. Soc.* **2012**, *134*, 10741–10744.
- (40) Fung, B. M.; Khitritin, A. K.; Ermolaev, K. An Improved Broadband Decoupling Sequence for Liquid Crystals and Solids. *J. Magn. Reson.* **2000**, *142*, 97–101.
- (41) Lu, W.; Yuan, D.; Zhao, D.; Schilling, C. I.; Plietzsch, O.; Müller, T.; Bräse, S.; Guenther, J.; Bliemel, J.; Krishna, R.; Li, Z.; Zhou, H.-C. Porous Polymer Networks: Synthesis, Porosity, and Applications in Gas Storage/Separation. *Chem. Mater.* **2010**, *22*, 5964–5972.
- (42) Lu, J.; Zhang, J. Facile Synthesis of Azo-Linked Porous Organic Frameworks via Reductive Homocoupling for Selective CO₂ Capture. *J. Mater. Chem. A* **2014**, *2*, 13831.
- (43) Ganesan, P.; Yang, X.; Loos, J.; Savenije, T. J.; Abellon, R. D.; Zuilhof, H.; Sudhölter, E. J. R. Tetrahedral N-Type Materials: Efficient Quenching of the Excitation of P-Type Polymers in Amorphous Films. *J. Am. Chem. Soc.* **2005**, *127*, 14530–14531.

- (44) Liu, X.; Yang, J.; Guo, L.; Gu, Y. Effects of Catalyst Isoquinoline in Polymerization Process on the Aggregation Structures of Polyimide in Solution. *Macromol. Rapid Commun.* **2005**, *26*, 1682–1686.
- (45) Popp, N.; Homburg, T.; Stock, N.; Senker, J. Porous Imine-Based Networks with Protonated Imine Linkages for Carbon Dioxide Separation from Mixtures with Nitrogen and Methane. *J. Mater. Chem. A* **2015**, *3*, 18492–18504.
- (46) Thommes, M.; Kaneko, K.; Neimark, A. V.; Olivier, J. P.; Rodriguez-Reinoso, F.; Rouquerol, J.; Sing, K. S. W. Physisorption of Gases, with Special Reference to the Evaluation of Surface Area and Pore Size Distribution (IUPAC Technical Report). *Pure Appl. Chem.* **2015**, *87*, 1051–1069.
- (47) Hao, G.-P.; Mondin, G.; Zheng, Z.; Biemelt, T.; Klosz, S.; Schubel, R.; Eychmüller, A.; Kaskel, S. Unusual Ultra-Hydrophilic, Porous Carbon Cuboids for Atmospheric-Water Capture. *Angew. Chem., Int. Ed.* **2015**, *54*, 1941–1945.
- (48) Biswal, B. P.; Kandambeth, S.; Chandra, S.; Shinde, D. B.; Bera, S.; Karak, S.; Garai, B.; Kharul, U. K.; Banerjee, R. Pore Surface Engineering in Porous, Chemically Stable Covalent Organic Frameworks for Water Adsorption. *J. Mater. Chem. A* **2015**, *3*, 23664–23669.
- (49) Stegbauer, L.; Hahn, M. W.; Jentys, A.; Savasci, G.; Ochsenfeld, C.; Lercher, J. A.; Lotsch, B. V. Tunable Water and CO₂ Sorption Properties in Isostructural Azine-Based Covalent Organic Frameworks through Polarity Engineering. *Chem. Mater.* **2015**, *27*, 7874–7881.
- (50) Yang, Y.; Zhang, Q.; Zhang, Z.; Zhang, S. Functional Microporous Polyimides Based on Sulfonated Binaphthalene Dianhydride for Uptake and Separation of Carbon Dioxide and Vapors. *J. Mater. Chem. A* **2013**, *1*, 10368.
- (51) Rao, K. V.; Haldar, R.; Maji, T. K.; George, S. J. Porous Polyimides from Polycyclic Aromatic Linkers: Selective CO₂ Capture and Hydrogen Storage. *Polymer* **2014**, *55*, 1452–1458.
- (52) Liao, Y.; Weber, J.; Faul, C. F. J. Fluorescent Microporous Polyimides Based on Perylene and Triazine for Highly CO₂-Selective Carbon Materials. *Macromolecules* **2015**, *48*, 2064–2073.
- (53) Farha, O. K.; Bae, Y.-S.; Hauser, B. G.; Spokoyny, A. M.; Snurr, R. Q.; Mirkin, C. A.; Hupp, J. T. Chemical Reduction of a Diimide Based Porous Polymer for Selective Uptake of Carbon Dioxide versus Methane. *Chem. Commun. (Cambridge, U. K.)* **2010**, *46*, 1056–1058.
- (54) Farha, O. K.; Spokoyny, A. M.; Hauser, B. G.; Bae, Y.-S.; Brown, S. E.; Snurr, R. Q.; Mirkin, C. A.; Hupp, J. T. Synthesis, Properties, and Gas Separation Studies of a Robust Diimide-Based Microporous Organic Polymer. *Chem. Mater.* **2009**, *21*, 3033–3035.
- (55) Li, G.; Wang, Z. Naphthalene-Based Microporous Polyimides: Adsorption Behavior of CO₂ and Toxic Organic Vapors and Their Separation from Other Gases. *J. Phys. Chem. C* **2013**, *117*, 24428–24437.
- (56) Rao, K. V.; Haldar, R.; Kulkarni, C.; Maji, T. K.; George, S. J. Perylene Based Porous Polyimides: Tunable, High Surface Area with Tetrahedral and Pyramidal Monomers. *Chem. Mater.* **2012**, *24*, 969–971.
- (57) Liu, D.-P.; Chen, Q.; Zhao, Y.-C.; Zhang, L.-M.; Qi, A.-D.; Han, B.-H. Fluorinated Porous Organic Polymers via Direct C–H Arylation Polycondensation. *ACS Macro Lett.* **2013**, *2*, 522–526.
- (58) Liu, J.; Thallapally, P. K.; McGrail, B. P.; Brown, D. R.; Liu, J. Progress in Adsorption-Based CO₂ Capture by Metal-Organic Frameworks. *Chem. Soc. Rev.* **2012**, *41*, 2308–2322.

Supporting Information towards:

**Microporous Organic Polyimides for CO₂ and H₂O Capture and
Separation from CH₄ and N₂ Mixtures – Interplay between Porosity
and Chemical Function**

Christoph Klumpen[†], Marion Breunig[†], Thomas Homburg^{††}, Norbert Stock^{††},
Juergen Senker^{†*}

[†]Bayreuth University, Inorg.Chem. III, Universitätsstraße 30, 95440 Bayreuth, Germany

^{††}Christian-Albrechts-University, Institut für Anorg. Chemie, Max-Eyth-Straße 2, 24118 Kiel,
Germany

Table of Content

1. Chemicals	3
2. Linker	4
2.1 Liquid NMR Spectra.....	4
2.1.1 ¹ H-NMR.....	4
2.1.2 ¹³ C-NMR.....	4
2.2 IR-Spectra	5
3. Polyimides	6
3.1 NMR/IR Spectra.....	6
3.1.1 MOPI-I.....	8
3.1.2 MOPI-II.....	9
3.1.3 MOPI-III.....	10
3.1.4 MOPI-IV	11
3.1.5 MOPI-V	12
3.2 CHN analysis	13
3.2.1 MOPI-I.....	13
3.2.2 MOPI-II.....	13
3.2.3 MOPI-III.....	13
3.2.4 MOPI-IV	13
3.2.5 MOPI-V	14
3.3 Powder x-ray diffractograms.....	14

1

3.4 TGA patterns.....	15
4. Isotherms	15
4.1 Ar isotherms and pore size distributions	15
4.2 CO ₂ isotherms and pore size distributions	17
4.3 CH ₄ isotherms	20
5. Selectivities	21
5.1 CO ₂ /N ₂	21
5.1.1 MOPI-I.....	21
5.1.2 MOPI-II.....	21
5.1.3 MOPI-III.....	22
5.1.4 MOPI-IV	23
5.1.5 MOPI-V	23
5.2 CO ₂ /CH ₄	24
5.2.1 MOPI-I.....	24
5.2.2 MOPI-II.....	25
5.2.3 MOPI-III.....	25
5.2.4 MOPI-IV	26
6. SEM images	28

1. Chemicals

Table S1: List of used chemicals, their purities and distributor.

Chemical	Company	Purity
Acetic acid	Sigma Aldrich	>99.5 %
Acetic anhydride	Sigma Aldrich	>98.0 %
Aniline	Sigma Aldrich	>99.5 %
3,3',4,4'-	ABCR	>97.0 %
Benzophenonetetracarboxylic dianhydride		
Bicyclo[2,2,2]oct-7-en-2,3,5,6-tetracarboxylic dianhydride	TCI	-
<i>m</i> -Cresol	Sigma Aldrich	99.8 %
Dichloromethane	Sigma Aldrich	99.9 %
Dimethylformamide	VWR Chemicals	>99.8 %
3,3',4,4'-	TCI	-
Diphenylsulfonetetracarboxyl dianhydride		
Ethanol	VWR Chemicals	>96 %
Hydrochloric Acid	Grüssing GmbH	-
4,4'-	Sigma Aldrich	99 %
Hexafluoroisopropylidene)diphthalic anhydride		
Hydrazine monohydrate	Sigma Aldrich	(N ₂ H ₄ , 64-65 %), 98 %
Isopentylnitride	Sigma Aldrich	96 %
Isoquinoline	Sigma Aldrich	97 %
Methanol	VWR Chemicals	-
4,4'-Oxydiphthalic dianhydride	TCI	>98.0%
Phosphinic acid	Sigma Aldrich	50 wt% in H ₂ O
Raney nickel	Sigma Aldrich	-
Tetrahydrofuran	VWR Chemicals	>99.9 %
Tritylchloride	Sigma Aldrich	97 %

2. Linker

2.1 Liquid NMR Spectra

2.1.1 ^1H -NMR

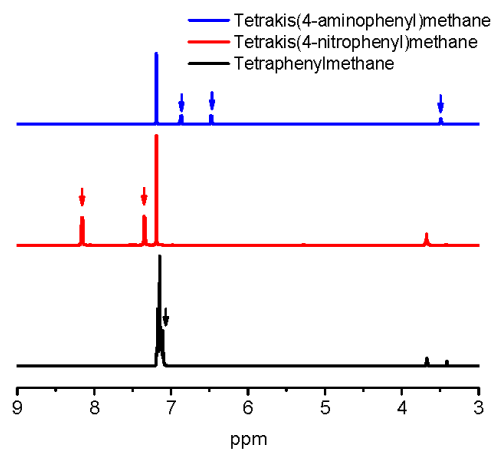


Figure S1: ^1H -NMR spectra of Tetrakis(4-aminophenyl)methane, Tetrakis(4-nitrophenyl)methane and Tetraphenylmethane. The arrows point towards the signals of the related monomers.

2.1.2 ^{13}C -NMR

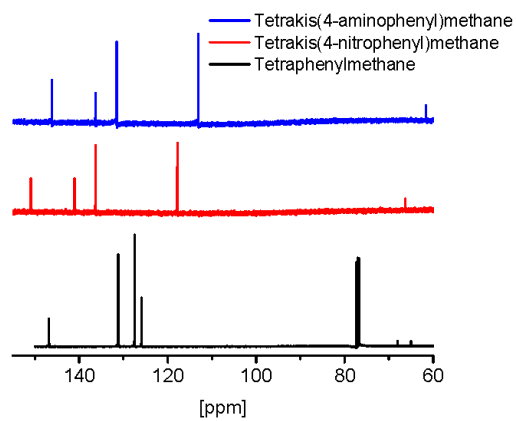


Figure S2: ^{13}C -NMR spectra of Tetrakis(4-aminophenyl)methane, Tetrakis(4-nitrophenyl)methane and Tetraphenylmethane.

2.2 IR-Spectra

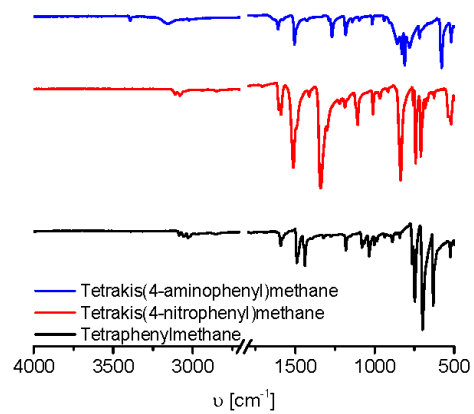


Figure S3: IR spectra of Tetrakis(4-aminophenyl)methane, Tetrakis(4-nitrophenyl)methane and Tetraphenylmethane.

3. Polyimides

3.1 NMR/IR Spectra

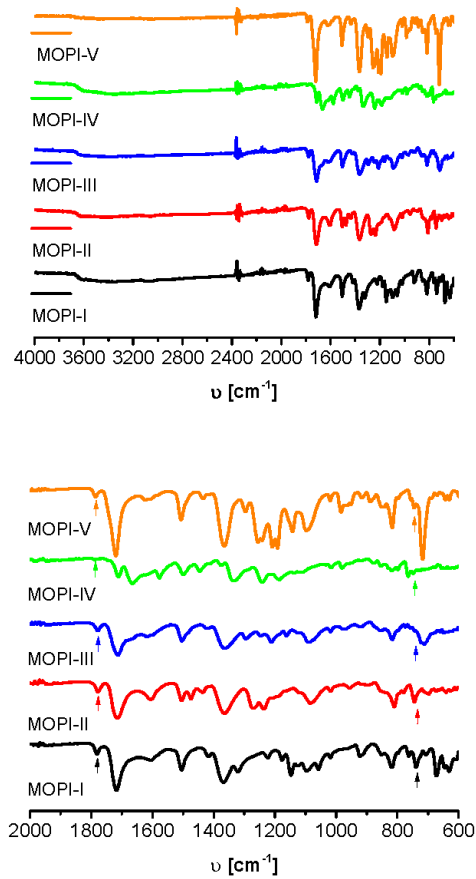


Figure S4: Infrared spectra of the MOPIs. The arrows point towards the characteristic signals for the imide bond formation.

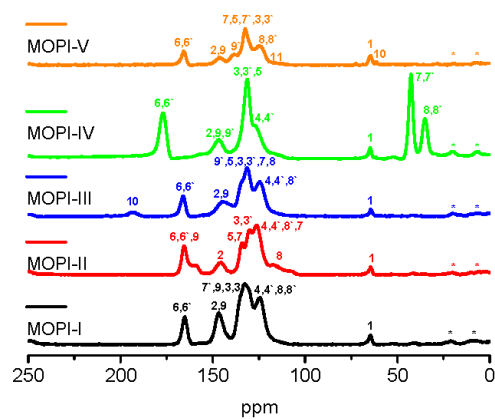


Figure S5: ^{13}C NMR spectra of MOPI-I-V.

Table S2: Assignment of ^{13}C NMR shifts. All values are given in ppm.

Polymer	1	2	3	4	5	6	7	8	9	10	
MOPI-I	65	146	133	124	133	165	133	124	146	-	-
MOPI-II	65	145	130	125	134	166	125	125	159	-	-
MOPI-III	65	145	132	124	132	166	132	132	145	193	-
MOPI-IV	65	147	131	124	131	177	43	35	147	-	-
MOPI-V	65	144	132	124	132	166	132	124	146	61	117

3.1.1 MOPI-I

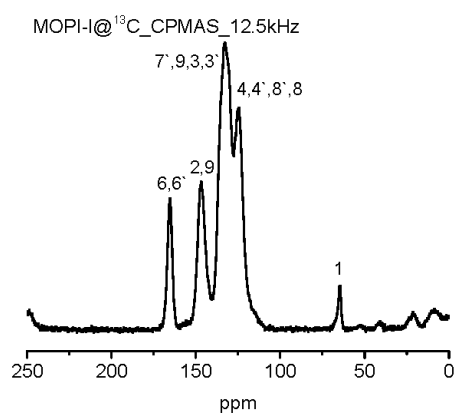
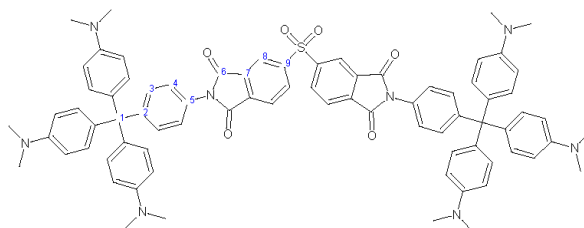


Figure S6: ¹³C-NMR spectra of MOPI-I.

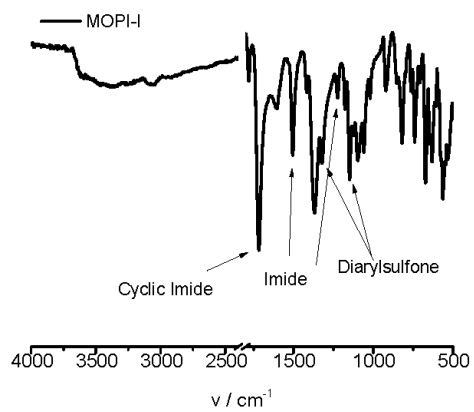


Figure S7: IR spectra of MOPI-I.

3.1.2 MOPI-II

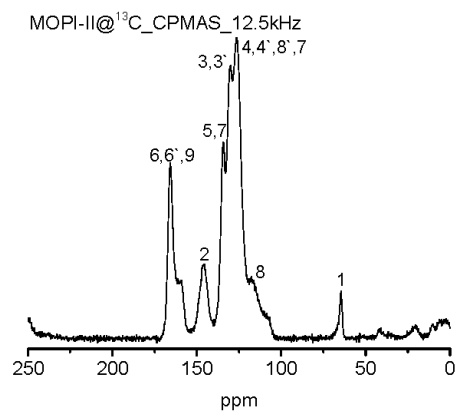
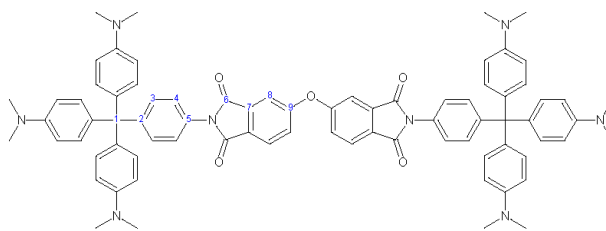


Figure S8: ¹³C of MOPI-II.

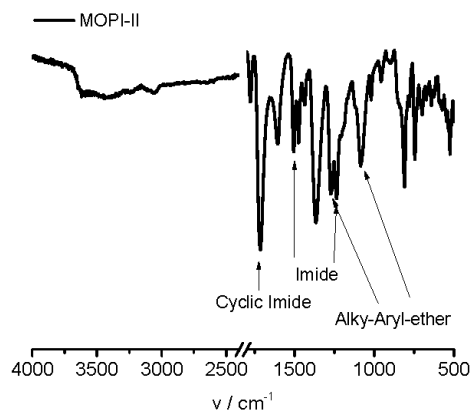


Figure S9: Ir-spectra of MOPI-II.

3.1.3 MOPI-III

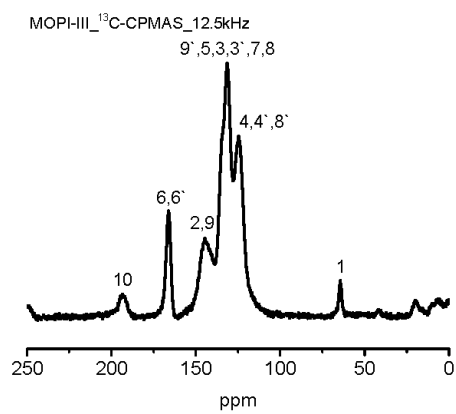
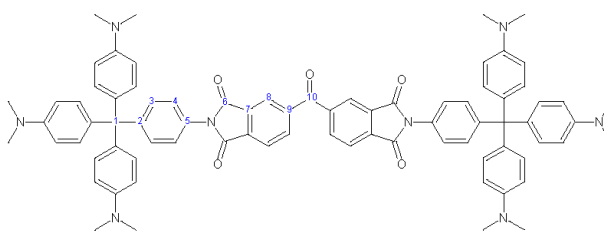


Figure S10: ^{13}C of MOPI-III.

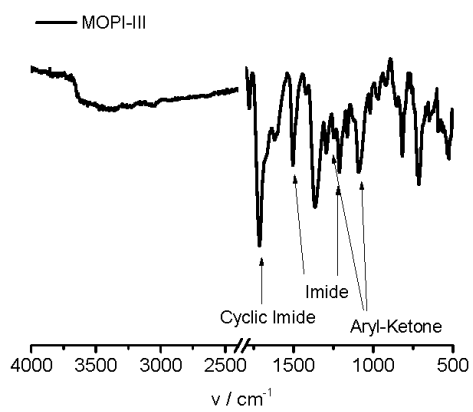


Figure S11: IR of MOPI-III.

3.1.4 MOPI-IV

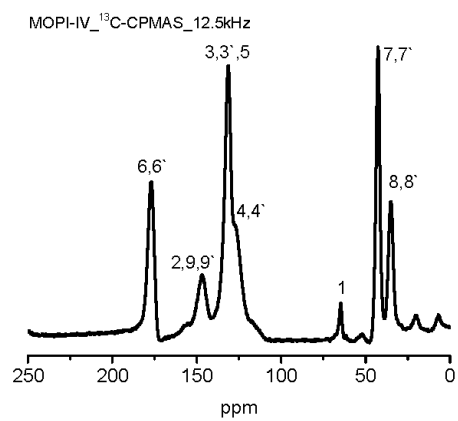
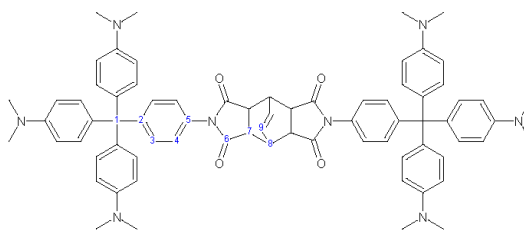


Figure S12: ¹³C of MOPI-IV.

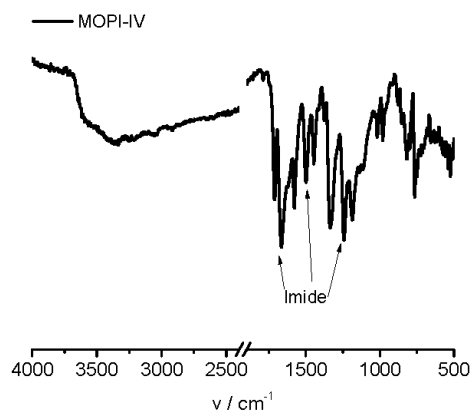


Figure S13: IR of MOPI-IV.

3.1.5 MOPI-V

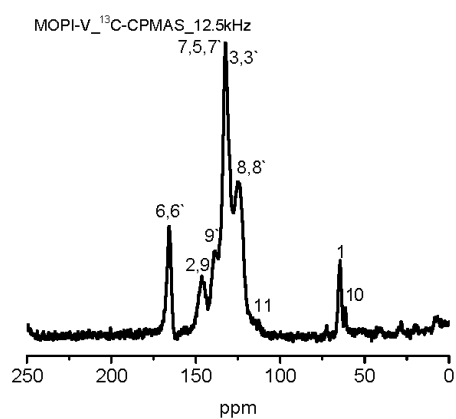
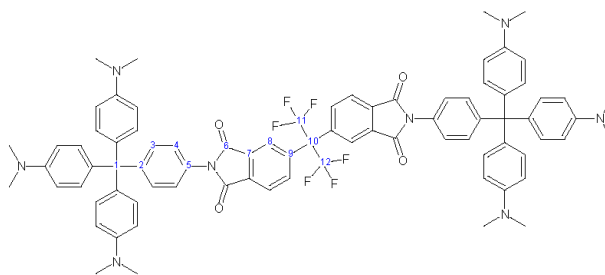


Figure S14: ¹³C spectra of MOPI-V.

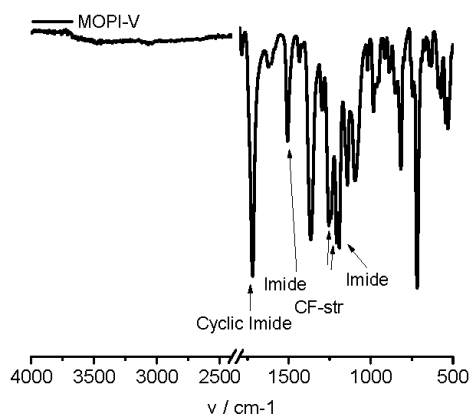


Figure S15: IR spectra of MOPI-V.

3.2 CHN analysis

3.2.1 MOPI-I

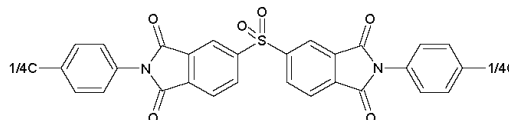


Table S3: Repeating unit used for CHN-Analysis of MOPI-I.

MOPI-I	C / %	H / %	N / %
Meas.	61.12	3.661	5.114
Calc.	66.79	2.75	6.26
Deviation	5.7 %	0.91 %	1.15 %

3.2.2 MOPI-II

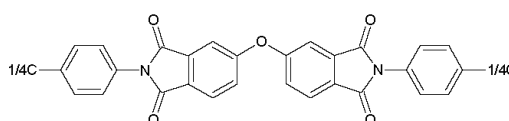


Table S4: Repeating unit used for CHN-Analysis of MOPI-II.

MOPI-II	C / %	H / %	N / %
Meas.	70.45	3.426	5.719
Calc.	73.71	3.04	6.03
Deviation	3.25	0.39	0.31

3.2.3 MOPI-III

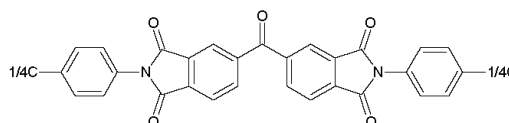


Table S5: Repeating unit used for CHN-Analysis of MOPI-III.

MOPI-III	C / %	H / %	N / %
Meas.	69.59	3.482	5.293
Calc.	74.36	2.97	5.88
Deviation	4.77 %	0.51 %	0.59 %

3.2.4 MOPI-IV

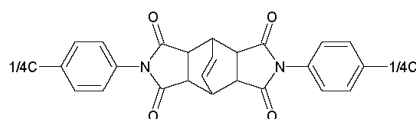


Table S6: Repeating unit used for CHN-Analysis of MOPI-IV.

MOPI-IV	C / %	H / %	N / %
Meas.	69.61	4.201	6.26
Calc.	73.14	4.01	6.96
Deviation	3.53 %	0.19 %	0.7 %

3.2.5 MOPI-V

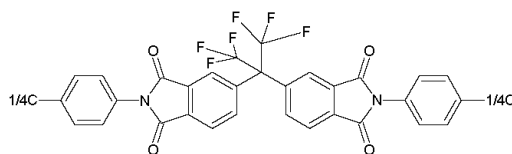


Table S7: Repeating unit used for CHN-Analysis of MOPI-V.

MOPI-V	C / %	H / %	N / %
Meas.	62.02	2.923	4.653
Calc.	63.22	2.36	5.62
Deviation	1.20	0.56	0.97

3.3 Powder x-ray diffractograms

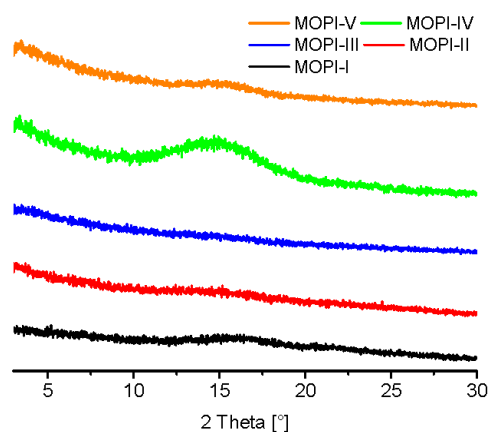


Figure S16: Powder diffraction pattern of MOPI-I to -V.

3.4 TGA patterns

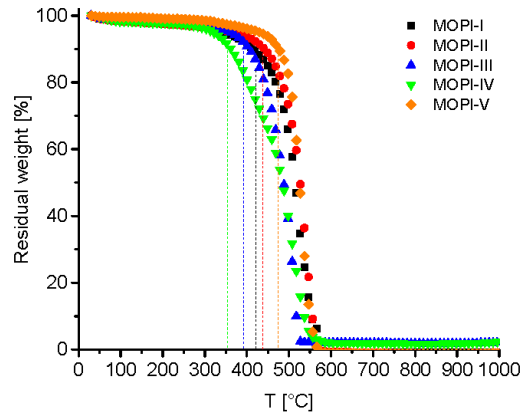


Figure S17: Thermogravimetric analysis of the polymer networks, measured under air.

4. Isotherms

4.1 Ar isotherms and pore size distributions

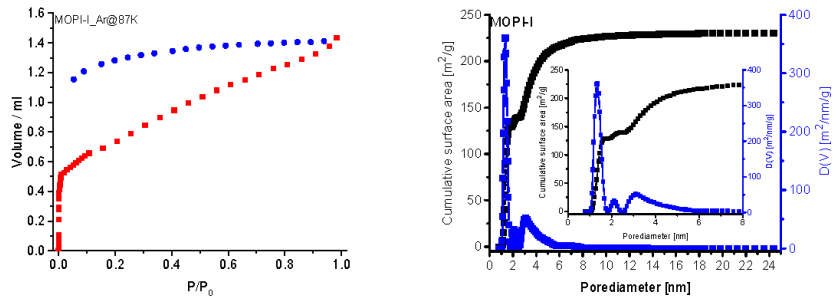


Figure S18: Ar isotherm and pore size distribution of MOPI-I.

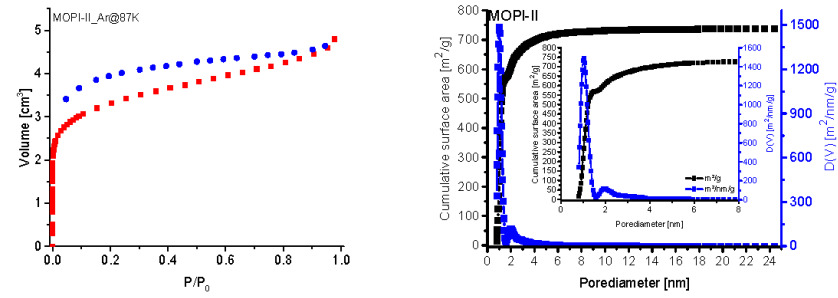


Figure 1: Ar isotherm and pore size distribution of MOPI-II.

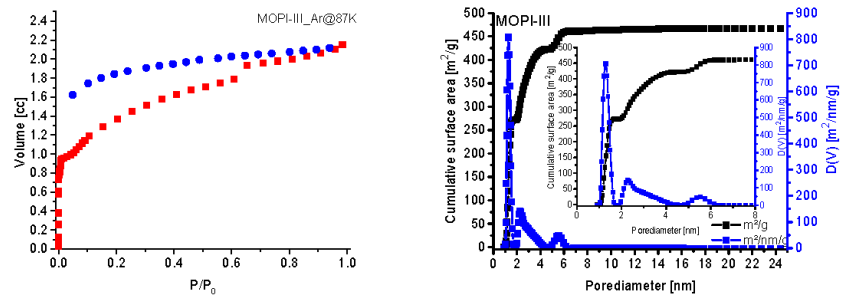


Figure 2: Ar isotherm and pore size distribution of MOPI-III.

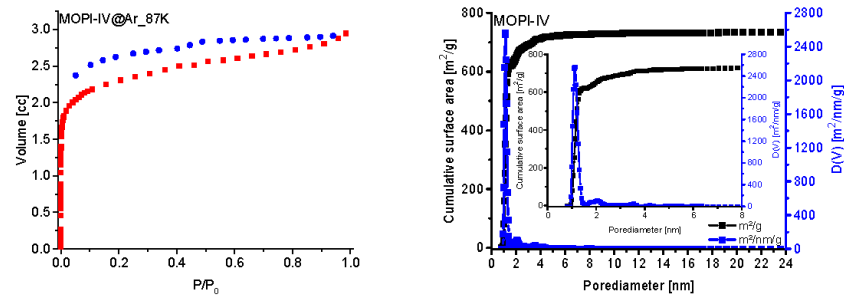


Figure 3: Ar isotherm and pore size distribution of MOPI-IV.

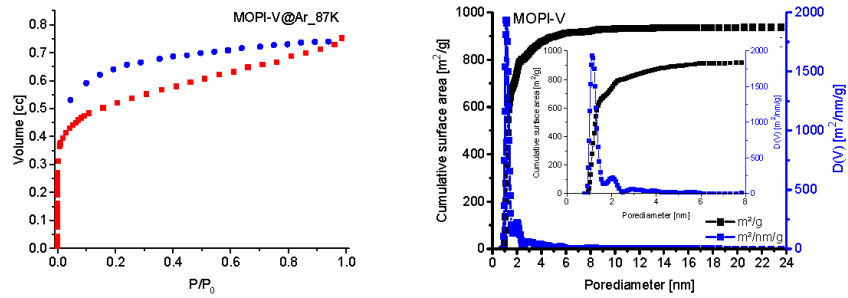


Figure 4: Ar isotherm and pore size distributions of MOPI-V.

4.2 CO₂ isotherms and pore size distributions

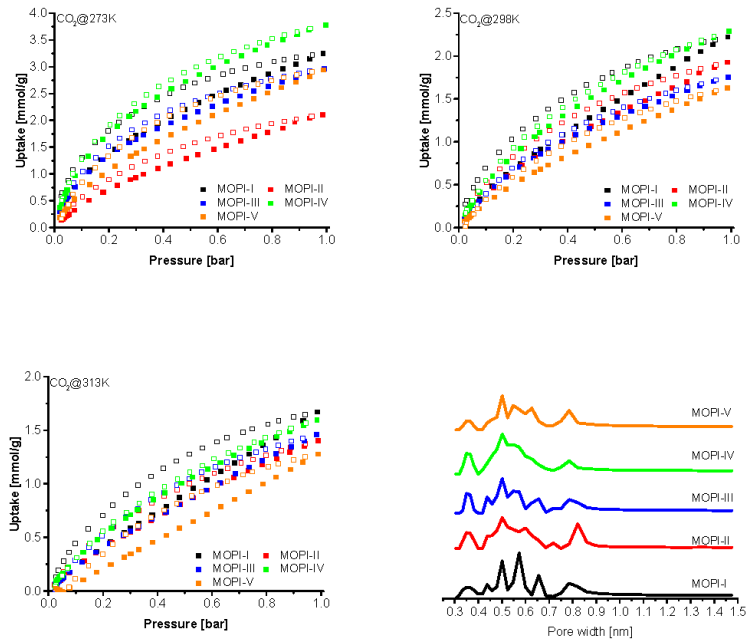


Figure S19: CO₂ uptake measured at 273, 298 and 313 K and pore size distribution measured at 273 K. Full symbols characterize adsorption isotherms, hollow symbols the corresponding desorption curve.

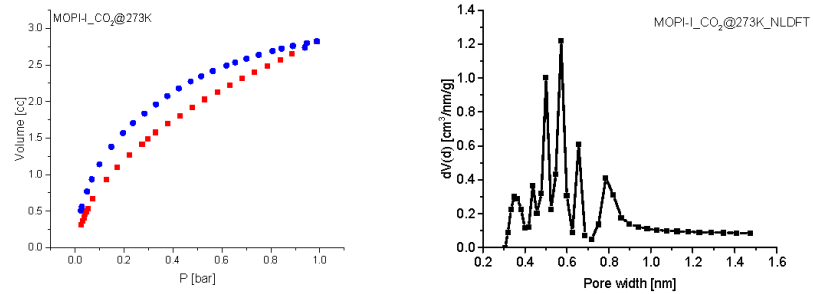


Figure S20: CO₂ isotherm and pore size distribution of MOPI-I.

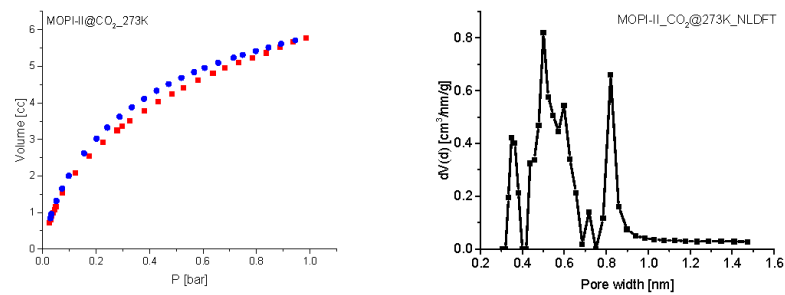


Figure S21: CO₂ isotherm and pore size distribution of MOPI-II.

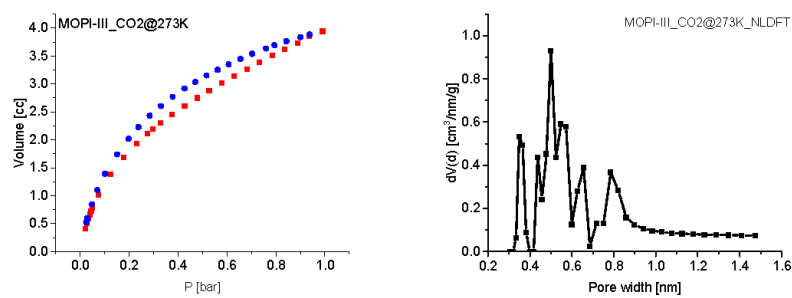


Figure S22: CO₂ isotherm and pore size distribution of MOPI-III.

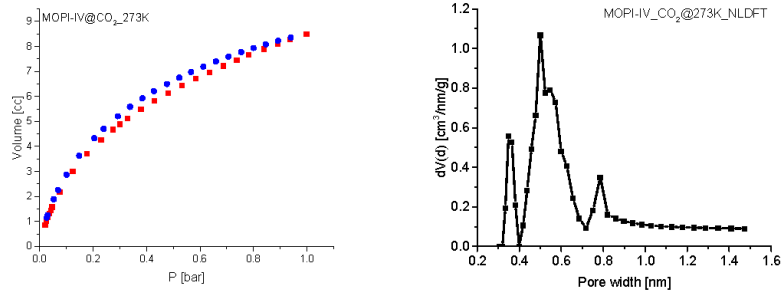


Figure S23: CO₂ isotherm and pore size distribution of MOPI-IV.

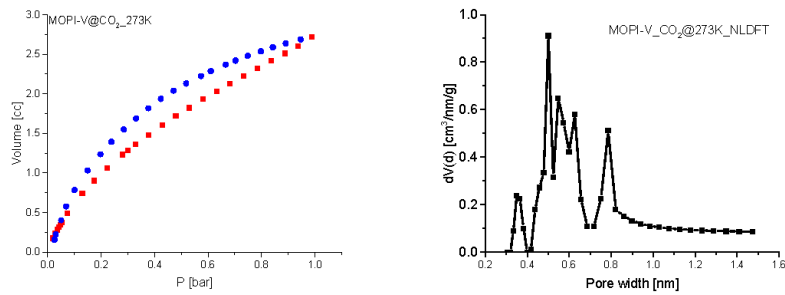


Figure S24: CO₂ isotherm and pore size distribution of MOPI-V.

4.3 CH₄ isotherms

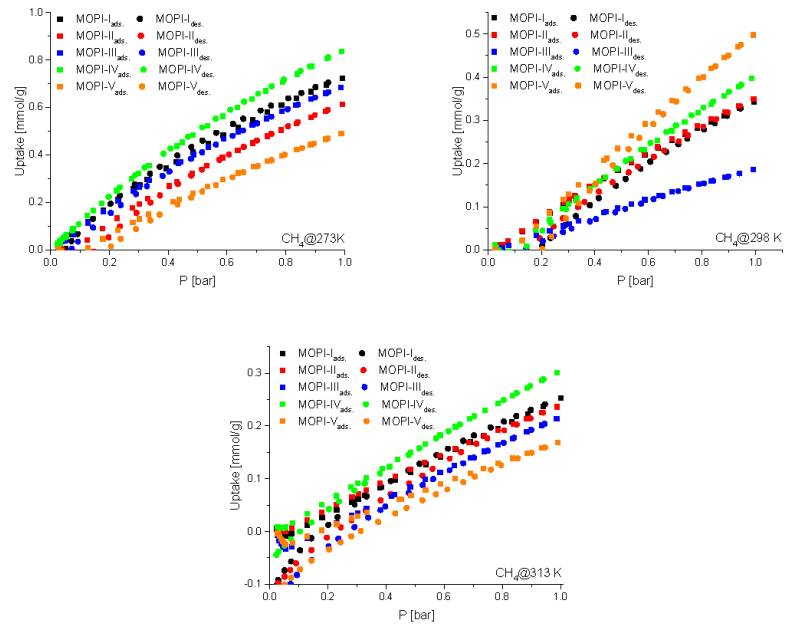


Figure S25: CH₄ adsorption of MOPIs at 273, 298 and 313 K.

5. Selectivities

5.1 CO₂/N₂

5.1.1 MOPI-I

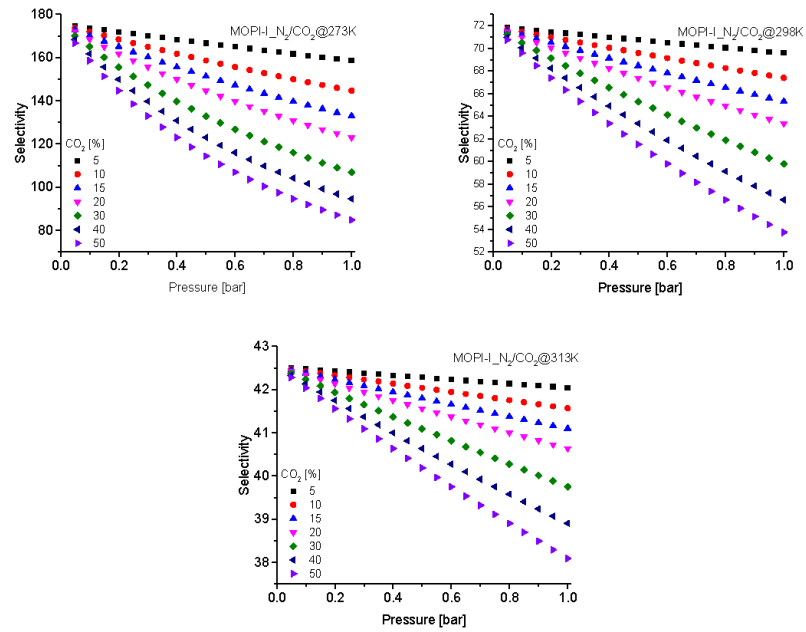
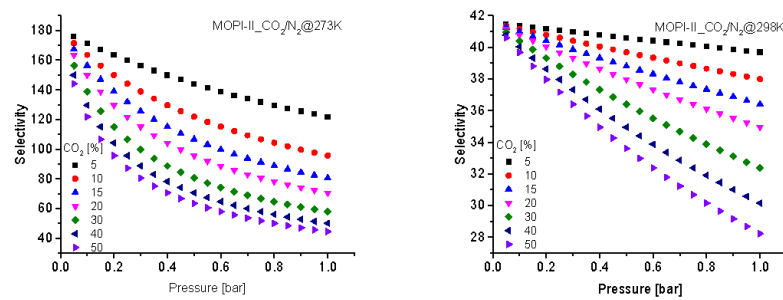


Figure S26: CO₂ over N₂ selectivities for MOPI-I at 273, 298 and 313 K.

5.1.2 MOPI-II



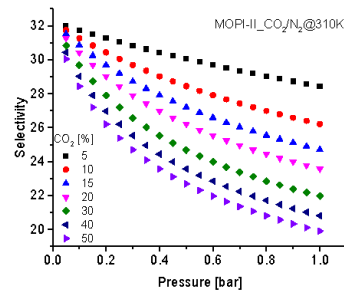


Figure S27: CO_2 over N_2 selectivities for MOFI-II at 273, 298 and 313 K.

5.1.3 MOFI-III

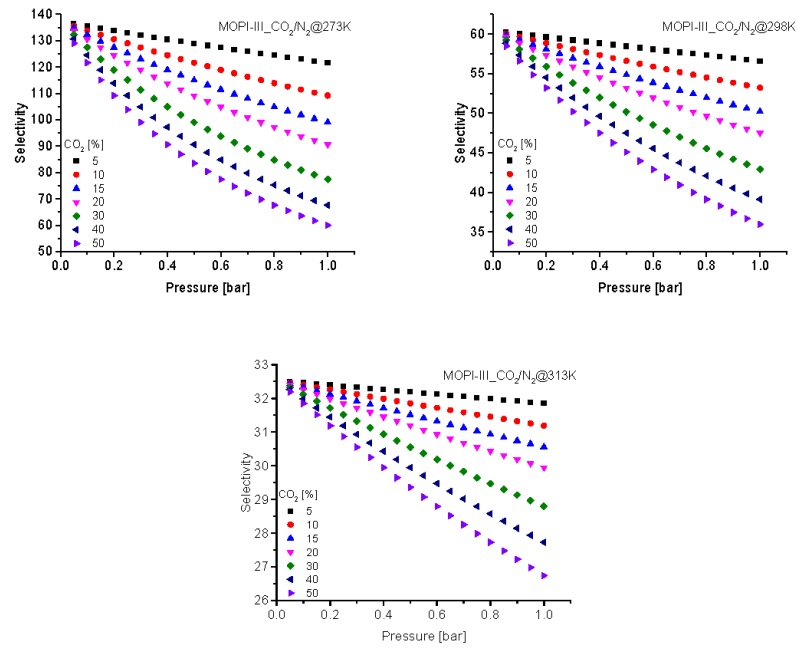


Figure S28: CO_2 over N_2 selectivities for MOFI-III at 273, 298 and 313 K.

5.1.4 MOPI-IV

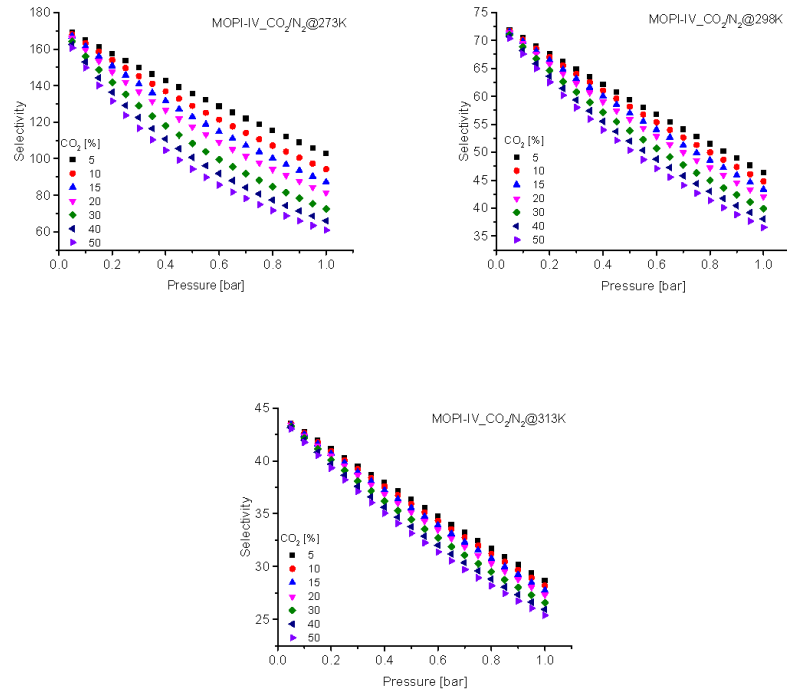
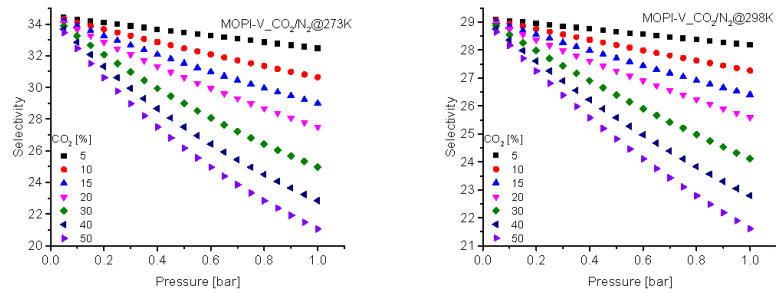


Figure S29: CO₂ over N₂ selectivities for MOPI-IV at 273, 298 and 313 K.

5.1.5 MOPI-V



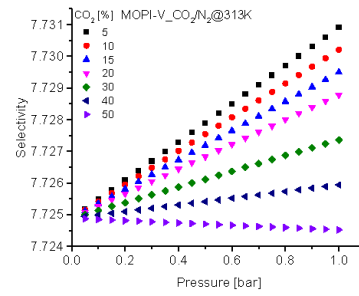


Figure S30: CO_2 over N_2 selectivities for MOPI-V at 273, 298 and 313 K.

5.2 CO_2/CH_4

5.2.1 MOPI-I

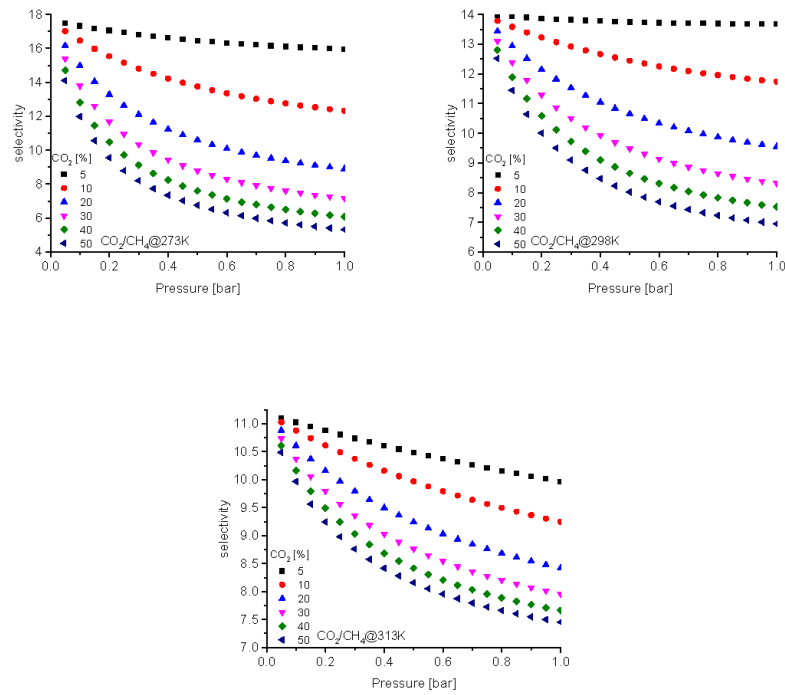


Figure S31: CO_2 over CH_4 selectivities for MOPI-I at 273, 298 and 313 K.

5.2.2 MOPI-II

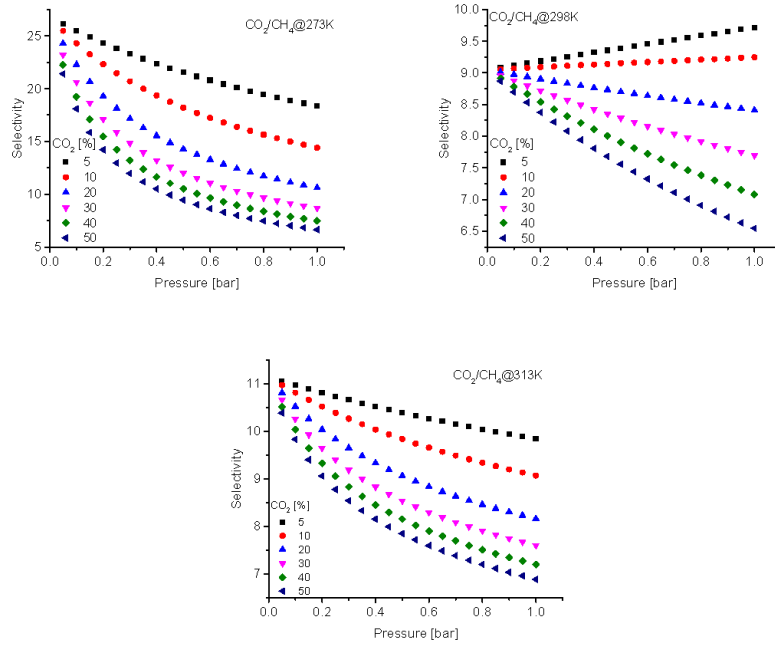
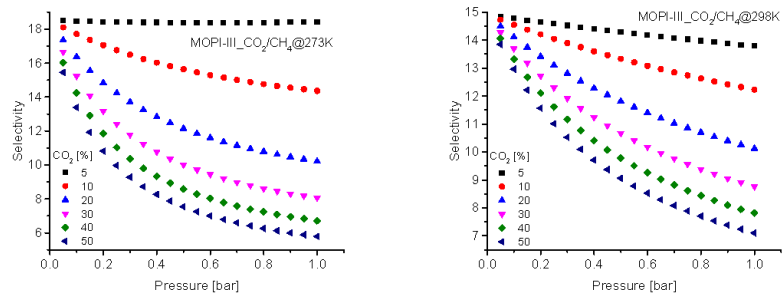


Figure S32: CO_2 over CH_4 selectivities for MOPI-II at 273, 298 and 313 K.

5.2.3 MOPI-III



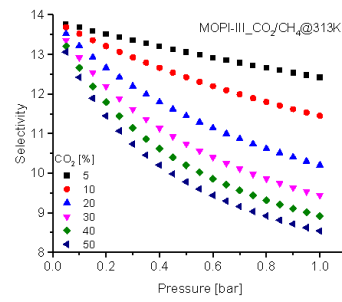


Figure S33: CO₂ over CH₄ selectivities for MOPI-III at 273, 298 and 313 K.

5.2.4 MOPI-IV

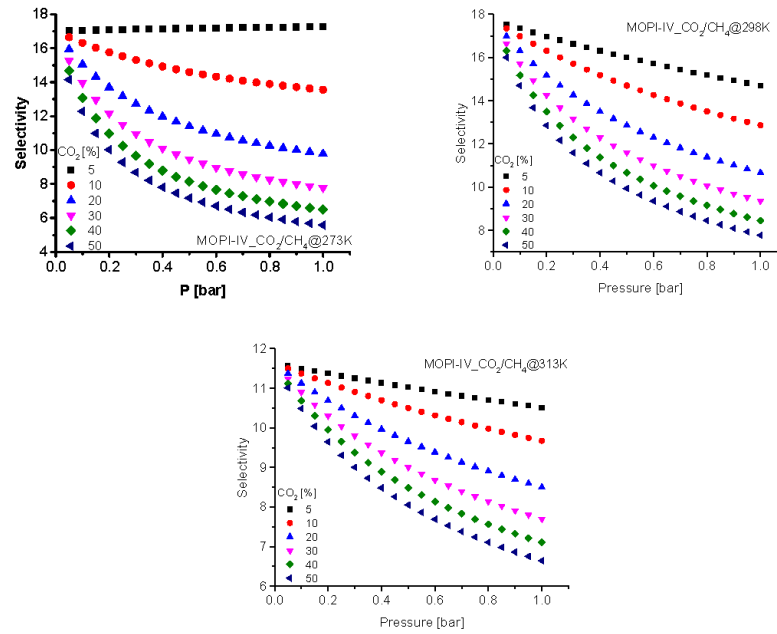


Figure S34: CO₂ over CH₄ selectivities for MOPI-IV at 273, 298 and 313 K.

5.2.5 MOPI-V

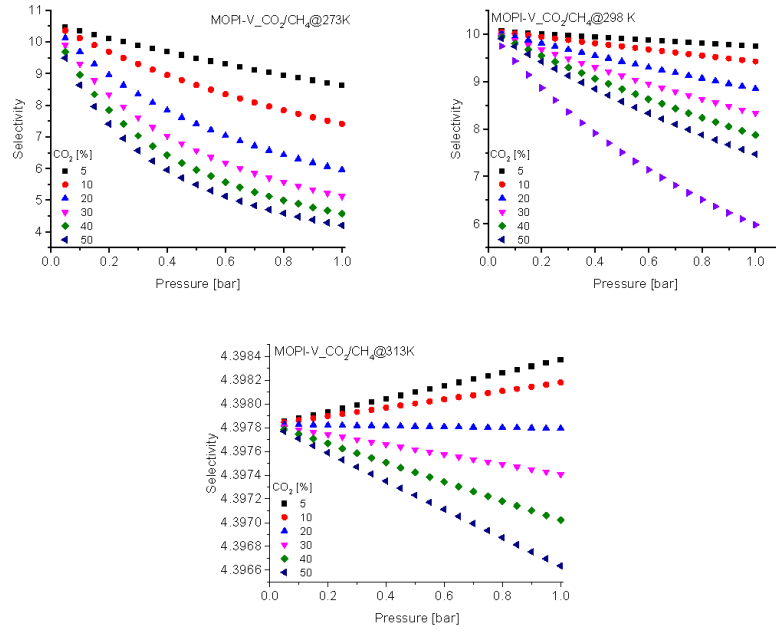


Figure S35: CO₂ over CH₄ selectivities for MOPI-V at 273, 298 and 313 K.

6. SEM images

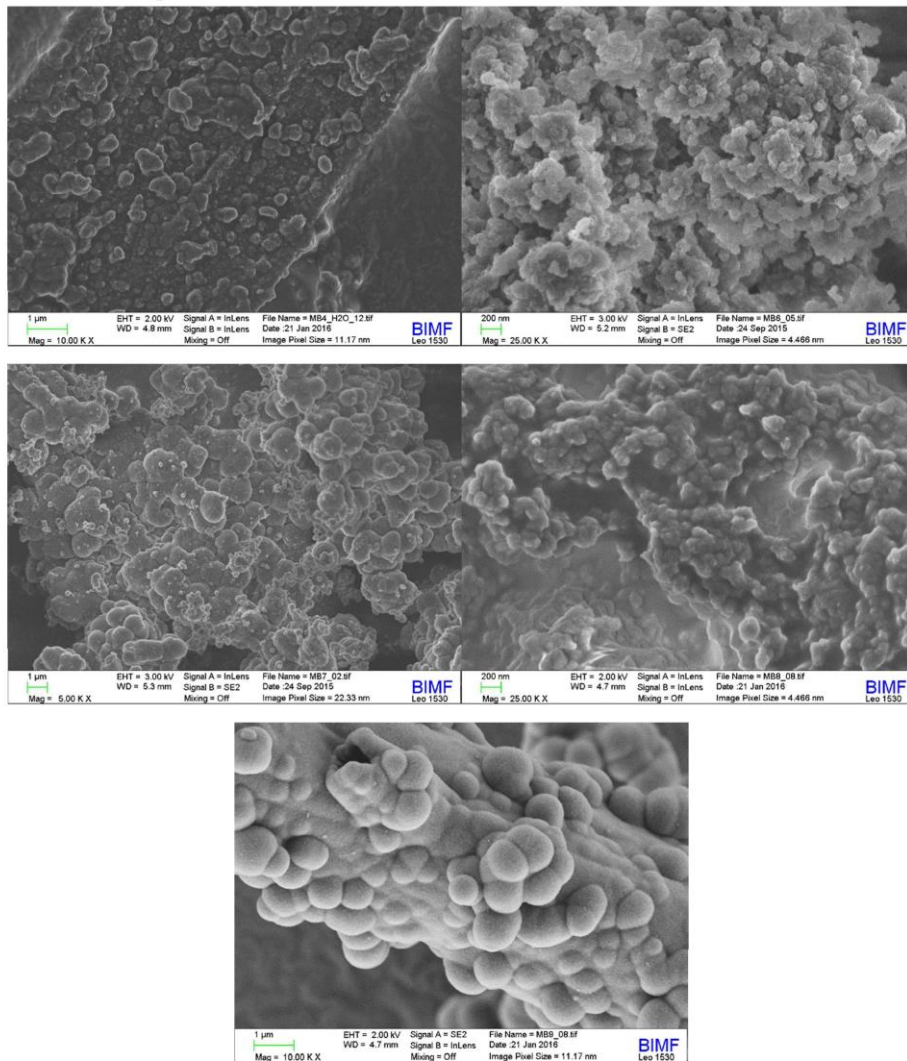


Figure S36: SEM images of the MOPIs. Starting with MOPI-I (top, left) followed by MOPI-II (top, right), MOPI-III (middle, left), MOPI-IV (middle, right), and MOPI V (bottom centered).

5.2 BILP-19 – An Ultramicroporous Organic Network with Exceptional Carbon Dioxide Uptake

Die Publikation wurde in Zusammenarbeit mit dem Lehrstuhl für Chemische Verfahrenstechnik der Universität Bayreuth, Prof. Dr. A. Jess, durchgeführt. Die Beiträge der Autoren sind wie folgt:

Christoph Klumpen

- ⇒ Projektplanung und Durchführung
- ⇒ Synthesen und Charakterisierung der Verbindungen
- ⇒ Durchführung und Auswertung der Gassorptionsanalytik
- ⇒ Auswertung des Gesamtdatensatzes
- ⇒ Planung und Aufsetzen des Manuskripts

Florian Radakovitsch, Andreas Jess


- ⇒ Durchführung der Wassersorptionsmessungen
- ⇒ Design des Manuskripts

Jürgen Senker

- ⇒ Projektplanung und Supervision
- ⇒ Planung und Aufsetzen des Manuskripts

Article

BILP-19—An Ultramicroporous Organic Network with Exceptional Carbon Dioxide Uptake

 Christoph Klumpen ¹, Florian Radakovitsch ², Andreas Jess ² and Jürgen Senker ^{1,*} 
¹ Inorganic Chemistry III, University of Bayreuth, Universitätsstraße 30, 95440 Bayreuth, Germany; christoph.klumpen@uni-bayreuth.de

² Chair of Chemical Engineering, University of Bayreuth, Universitätsstraße 30, 95440 Bayreuth, Germany; florian.radakovitsch@uni-bayreuth.de (F.R.); jess@uni-bayreuth.de (A.J.)

* Correspondence: juergen.senker@uni-bayreuth.de; Tel.: +49-(0)921-552532

Received: 16 July 2017; Accepted: 8 August 2017; Published: 12 August 2017

Abstract: Porous benzimidazole-based polymers (BILPs) have proven to be promising for carbon dioxide capture and storage. The polarity of their chemical structure in combination with an inherent porosity allows for adsorbing large amounts of carbon dioxide in combination with high selectivities over unpolar guest molecules such as methane and nitrogen. For this reason, among purely organic polymers, BILPs contain some of the most effective networks to date. Nevertheless, they are still outperformed by competitive materials such as metal-organic frameworks (MOFs) or metal doped porous polymers. Here, we report the synthesis of BILP-19 and its exceptional carbon dioxide uptake of up to 6 mmol·g⁻¹ at 273 K, making the network comparable to state-of-the-art materials. BILP-19 precipitates in a particulate structure with a strongly anisotropic growth into platelets, indicating a sheet-like structure for the network. It exhibits only a small microporous but a remarkable ultra-microporous surface area of 144 m²·g⁻¹ and 1325 m²·g⁻¹, respectively. We attribute the exceptional uptake of small guest molecules such as carbon dioxide and water to the distinct ultra-microporosity. Additionally, a pronounced hysteresis for both guests is observed, which in combination with the platelet character is probably caused by an expansion of the interparticle space, creating additional accessible ultra-microporous pore volume. For nitrogen and methane, this effect does not occur which explains their low affinity. In consequence, Henry selectivities of 123 for CO₂/N₂ at 298 K and 12 for CO₂/CH₄ at 273 K were determined. The network was carefully characterized with solid-state nuclear magnetic resonance (NMR) and infrared (IR) spectroscopy, thermal gravimetry (TG) and elemental analyses as well as physisorption experiments with Ar, N₂, CO₂, CH₄ and water.

Keywords: Benzimidazole linked polymers; gas-sorption; carbon dioxide adsorption; methane adsorption; water vapor sorption; carbon dioxide capture and storage; microporous organic polymers

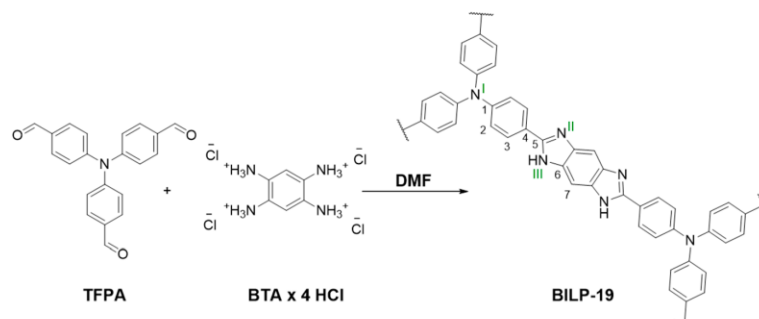
1. Introduction

The reduction of anthropogenic carbon dioxide emission as main contributor of global warming is a crucial task of today's society. Therefore, in 2015, within the Paris Agreement, 195 states agreed to reduce the risks and impacts of climate change [1]. According to this, short term technologies such as carbon capture and storage (CCS) are needed to ensure effective and cost efficient filtration of industrial flue gas emissions [2]. CCS technologies combine both the selective capture of CO₂ and its energetically beneficial storage. In this respect, adsorptive materials such as amines, alkalized alumina or carbonates already play a key role, especially in post- and precombustion filtration. However, the major drawback of those materials is their chemisorptive interaction with once captured carbon dioxide, which leads to high regeneration. In this respect, physisorptive materials have gained

attention, due to their applicability for highly efficient approaches such as thermal- or pressure swing adsorption [3]. Furthermore, easier access to the once captured gas is the key to subsequent carbon dioxide-based chemistry. Additionally, a high physical and chemical stability is often required to ensure long-term stability and utilizability upon operation. In this respect, microporous organic polymers (MOPs) have proven to be a promising class of materials for effective carbon dioxide adsorption [4,5]. Their lightweight morphology, quasi-unlimited diversity and high physicochemical stability are the main advantages of MOPs. Thus, many different types of networks with partially excellent performances have been investigated in the past decade, showing that for a high carbon dioxide uptake the content of ultra-micropores (<0.7 nm), the chemical nature and the postsynthetic functionalization of a framework are essential [6–9].

The inherent functionality of benzimidazole linked polymers (BILPs) and their ability to form narrow pores result in an enhanced interaction with polar guest molecules as well as high storage capacities. Thus, BILPs exhibit the highest uptakes of carbon dioxide in line with excellent selectivities compared to other flue gas participants such as nitrogen or methane, which rank them among the most promising networks for CCS applications. BILPs were first synthesized by Rabbani and El-Kaderi based on a template and catalyst-free condensation reaction of diamines with the respective aldehydes [10]. In this manner, peak carbon dioxide uptakes up to $5.34 \text{ mmol} \cdot \text{g}^{-1}$ (BILP-4 [11]) with a preference for CO_2 over N_2 of 79 and 10 for CO_2 over CH_4 at 273 K were observed. With a value of 113 for CO_2/N_2 and 17 for CO_2/CH_4 at 273 K, even higher selectivities were found for BILP-2 [11], although the peak uptake for carbon dioxide is only around $3.39 \text{ mmol} \cdot \text{g}^{-1}$, which is still remarkable in comparison to most porous polymers reported to date [11]. Consequently, further BILPs were investigated by varying the respective linker molecules to change both the morphology and the functionality of the network (Table S1, Figure S1) [12–17], making them comparable to state-of-the-art porous polymers such as PPN-6-deta [18], ALP-1 [19] or MOPI-IV [7] and metal organic frameworks such as mmen- $\text{Mg}_2(\text{dobpdc})$ [20], underlining the success of this polymer class.

Previous studies [7,21] suggest that a high uptake for carbon dioxide is closely linked to a distinct ultra-microporosity in combination with basic nitrogen containing functionalities [22,23]. Additionally we found that small, flexible linker molecules have the tendency to form narrow pore systems [22]. Therefore, we expect that the utilization of small linker molecules, which create the unique ambivalent functionality of benzimidazoles upon network formation, is promising for the synthesis of porous polymers with high affinities towards carbon dioxide [7,21]. In this respect, we report the synthesis of a new benzimidazole linked polymer (BILP-19) by a catalyst-free condensation reaction of triformylphenylamine and tetra-aminobenzene (Scheme 1). The network was fully characterized by nuclear magnetic resonance (NMR) spectroscopy (^{13}C , ^{15}N) and infrared spectroscopy (IR), as well as elemental (CHN) analysis, thermogravimetric analysis (TGA) and powder X-ray diffraction (PXRD). The surface area and porosity was determined from Ar and CO_2 isotherms to explore the full spectrum of potential pore sizes. Furthermore, the gas-sorption of CO_2 , CH_4 , N_2 and H_2O was investigated and respective selectivities for carbon dioxide within prominent gas mixtures such as CO_2/N_2 and CO_2/CH_4 are discussed.



Scheme 1. General polymerization reaction of tris(4-formylphenyl)amine (TFPA) and 1,2,4,5-benzenetetramine tetrahydrochloride (BTA·4 HCl) to BILP-19 and its simplified structure.

2. Results and Discussion

2.1. Synthesis and Characterization

BILP-19 was synthesized by a condensation reaction of tris(4-formylphenyl)amine (TFPA) and 1,2,4,5-benzenetetramine tetrahydrochloride (BTA·4 HCl) as brown solid in an overall yield of 99%, following a synthesis procedure published by Rabbani and El-Kaderi (Scheme 1) [10]. The resulting network was characterized by solid-state NMR and infrared spectroscopy. In the ^{13}C and ^{15}N cross polarization (CP) NMR spectra, the resonances at 152 ppm (^{13}C) as well as -149 and -241 ppm (^{15}N) are assigned to the carbon atom C-5 and the nitrogen atoms N-II and N-III, proving the formation of the benzimidazole bridging units (Figure 1). This is underlined by infrared spectroscopy, where characteristic bands for N-H (3383 cm^{-1}) and C=N (1600 cm^{-1}) stretching vibrations are present (Figure S2). Additionally, the absence of the aldehyde signal, expected around 190 ppm in the ^{13}C -NMR spectrum (Figure 1a) and the NH^{3+} resonances of the BTA linker in the ^{15}N NMR spectrum (Figure 1b) at around -330 ppm, hint to a complete conversion of both linker molecules, anticipating a high crosslinking degree [24]. This is in line with results of the CHN analysis of BILP-19, which showed only small deviations to the calculated values (C [4.60%], H [0.09%], N [1.19%]; Table S3). Furthermore, PXRD and TGA data measured under air revealed an amorphous network structure with a thermal stability up to $494\text{ }^\circ\text{C}$ (Figures S3 and S4). In the TG curve, the first 6% of weight loss are assigned to water evaporation (Figure S4). In spite of the amorphous character of BILP-19, SEM images reveal a platelet-like texture of the particles, indicating a sheet-like growth of the network (Figure S5).

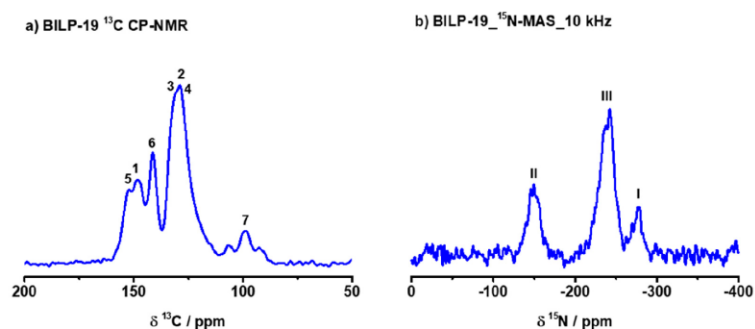


Figure 1. ^{13}C CP NMR (a) and ^{15}N MAS NMR (b) spectra of BILP-19 with assignment of the signals. The spectra were measured at 12.5 kHz and 10.0 kHz, respectively. Fully observed ranges are provided in Figures S6 and S7 (Supplementary Materials).

2.2. Surface Area and Porosity

The surface area of BILP-19 was calculated from Ar, N₂ and CO₂ adsorption isotherms measured at 87 K, 77 K and 273 K, respectively (Figures 2a, S11 and 2c). The Ar and N₂ sorption isotherms exhibit a type II shape, which is typical for non- or macroporous materials [25]. Nevertheless, the steep increase at low p/p_0 hints towards a small amount of micropores. This is in line with a type III hysteresis, typical for platelet-like particles and macropores. The *Brunauer-Emmett-Teller* (BET) surface area accessible for Ar and N₂ was calculated to 144 and 252 m²·g⁻¹ (Table S2). Based on a quenched solid density functional theory (QSDFT) kernel for cylindrical pores and carbon materials, the qualitative pore size distribution shows a primary mesoporous content (Figure 2b) with a small micropore contribution ($p_{V_{mic.}}/p_{V_{tot.}}$) of 4% and 9% (Table S2). According to the *t*-plot method, the latter is associated mainly with external surfaces (Figure S20) [26]. Due to the shape of the isotherm, we also expect the mesopores to be part of the external surface volume, created by dense packing of network platelets during sample preparation.

To probe the ultra-microporosity (pore diameter < 0.7 nm) of BILP-19, the use of carbon dioxide is advantageous due to its higher kinetic energy and thus eased penetration of narrow pores. A prerequisite is the physisorptive and reversible character of the host-guest interactions. Since no unreacted end groups like amines or aldehydes remain in the network and benzimidazole does not tend to chemical reactions with CO₂ [12,14,27], we expect that this condition is fulfilled. The carbon dioxide adsorption isotherm revealed a remarkable surface area of 1325 m²·g⁻¹ (Figure 2c, Table S1). Based on a nonlocal density functional theory (NLDFT) kernel for carbon materials, the calculated qualitative pore size distribution shows diameters <1 nm for the major part of the pores (Figure 2d). We expect the narrow pores to be a result of the small linker molecules, leading to short repeating units upon formation of the two-dimensional network.

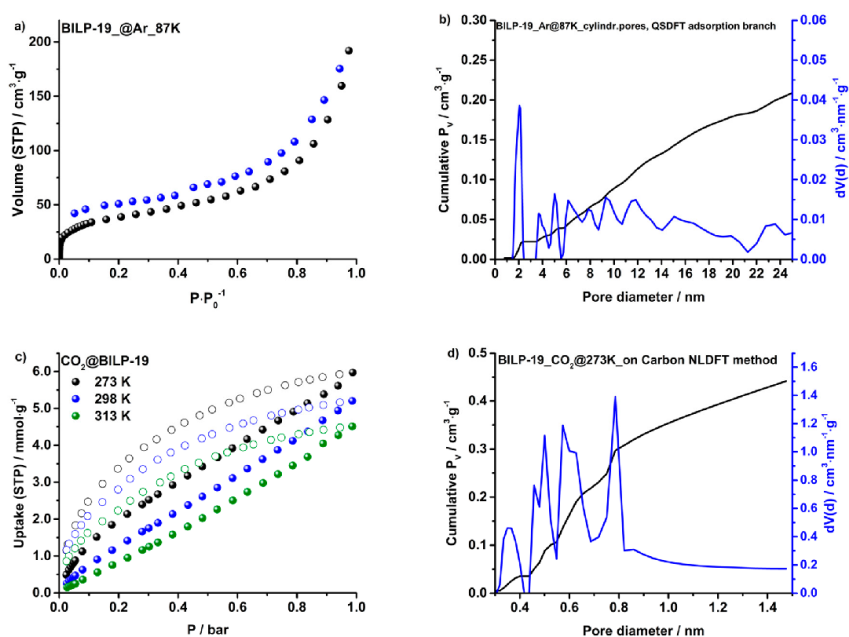


Figure 2. Ar adsorption isotherm (a) measured at 87 K and the respective, qualitative pore size distribution (b). CO₂ adsorption isotherms (c) measured at 273 K, 298 K and 313 K. Qualitative pore size distribution calculated from the CO₂ adsorption isotherm measured at 273 K (d). The gas volume and the uptake for the isotherms is given at standard temperature and pressure (STP).

2.3. Gas Adsorption of CO₂, N₂, CH₄ and H₂O

The large ultra-microporous region in combination with the poor accessibility for Ar hints to a favourable interaction with small polar guests like carbon dioxide or water. Indeed, the CO₂ isotherms measured at 273 K, 298 K and 313 K (Figure 2c) increase steeply towards higher pressures. The desorption branch is markedly shifted towards lower *p*-values resulting in a large desorption hysteresis. We attribute this to an expansion of the interparticle space of BILP-19, where with increasing pressure (~0.1 bar) the polymer sheets expand upon carbon dioxide uptake, creating additional pore space and, therefore, better access to the inner platelets (Figure 3a). The small cavities in combination with the homogeneously distributed amount of polar groups lead to a strong interaction with carbon dioxide as well as kinetic hindrance due to long diffusion pathways, explaining the large hysteresis. Since the hysteresis does not change upon the subsequent, temperature-dependent carbon dioxide measurements, this process seems to be reversible.

Calculating thereby the amount of CO₂, incorporated into the network at 0.95 bar and 273 K, revealed an overall uptake of 5.97 mmol·g⁻¹, which is among the highest values reported for physisorptive materials to date (Table 1). At higher temperatures, the adsorption of CO₂ is decreased towards 5.20 mmol·g⁻¹ and 4.51 mmol·g⁻¹ at 298 K and 313 K, respectively. Even at these temperatures and thus more relevant conditions, the obtained values outperform most materials [3]. We attribute the superior CO₂ affinity to be mediated by the exceptional ultra-microporosity in combination with the high density of functional groups. Both the central amino bridging-groups and the N-containing benzimidazole moieties provide preferred adsorption sites for small polar compounds like carbon dioxide or water, which are physisorptive by nature [12,14,27].

Table 1. Affinity of BILP-19 for CO₂, CH₄, N₂ and H₂O at 273 K, 298 K and 313 K taken from the respective isotherms at 0.95 bar.

T (K)	CO ₂ (mmol·g ⁻¹)	CH ₄ (mmol·g ⁻¹)	N ₂ (mmol·g ⁻¹)	H ₂ O (mmol·g ⁻¹)
273	5.97	0.88	-	-
298	5.20	0.51	0.11	18.17
313	4.51	0.38	-	-

The isosteric heat of adsorption, as indicator of the type of sorption interaction was calculated from the CO₂ isotherms at different temperatures. At zero pressure limit, values around 30 are found, which furthermore indicate a physisorptive interaction between the host material and the respective guests (Figure S8) [28]. We proposed a macroscopic swelling upon adsorption, which should change with temperature and will thus influence the isotherms. As a consequence, only the heat of adsorption for zero coverage will be reliable for our discussion [29].

For methane adsorption, however, a severely lowered uptake of 0.88 mmol·g⁻¹ at 273 K was observed, which hints to a minor affinity of BILP-19 for the respective guest molecules (Table 1). Again, the uptake decreases further to 0.51 mmol·g⁻¹ and 0.38 mmol·g⁻¹ at 298 K and 313 K, respectively (Table 1). The low uptake values found for methane in combination with the absence of a hysteresis are a result of its size and missing affinity to the network's functional groups, causing the disability of the molecule to penetrate the small ultra-micropores and thus to push the network layers apart (Figure 3a). In consequence, without expansion of the particles, even at higher pressures no breathing behavior is observed as for carbon dioxide and thus no additional pore space is accessible (Figure 3a). Combined with only weak interactions of the polar polymer backbone with the unpolar guests, methane could only be stored in the external interparticle voids, which contribute to only a small part of the total pore volume of BILP-19 (Table S2). Similar to methane, the affinity of the network towards nitrogen is also remarkably low, resulting in uptake values of 0.11 mmol·g⁻¹ at 298 K. Again, no hysteresis was found, indicating that no breathing behavior occurs. We found low nitrogen uptakes at 298 K to be typical for polar networks in earlier work [7,22,30].

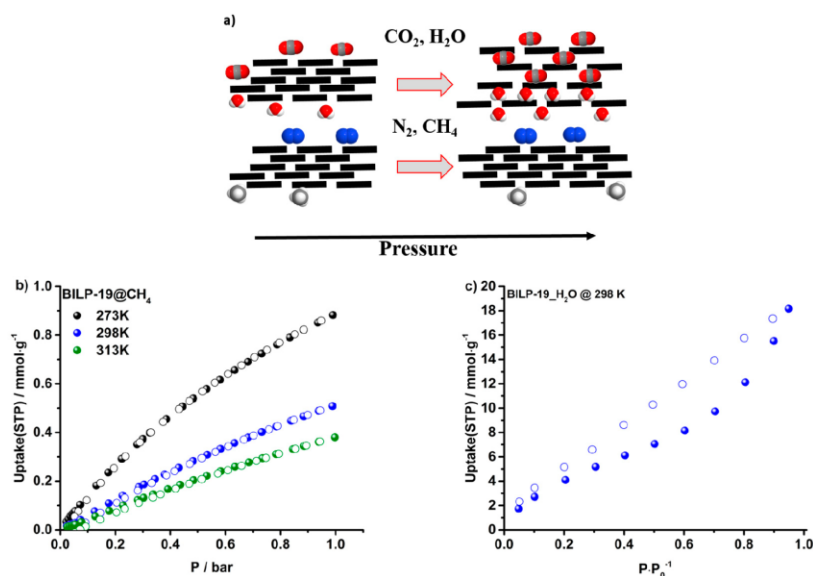


Figure 3. Schematic presentation of the postulated adsorption mechanism for BILP-19, where the black bars represent the polymer particles (a). Methane adsorption isotherms measured at 273 K, 298 K and 313 K, respectively (b) and a water sorption isotherm measured at 298 K (c). Adsorption branches are depicted by closed symbols, while open symbols represent desorption branches.

Water vapor sorption is an often neglected but important issue for the design of materials for CCS application. In this respect, especially postcombustional flue gas usually contains up to 20 vol % water vapor, which can susceptibly decrease a material's adsorption performance when not taken into account [4]. For BILP-19, a water vapor sorption revealed an uptake of $5.17 \text{ mmol}\cdot\text{g}^{-1}$ at 0.95 p/p_0 and $18.17 \text{ mmol}\cdot\text{g}^{-1}$ at 0.95 p/p_0 (Figure 3c). The comparison to literature-known materials such as MOPI-IV ($19.5 \text{ mmol}\cdot\text{g}^{-1}$) [7], AB-COF ($22.9 \text{ mmol}\cdot\text{g}^{-1}$) [31] or TpPA-148 ($24.5 \text{ mmol}\cdot\text{g}^{-1}$) [32] determines the network as highly hydrophilic. Based on the results of our earlier work, we once more attribute this to the high amount of ultra-micropores within the network [7]. Similar to carbon dioxide, the ultra-micropores are also penetrable for water molecules, which in combination with the polar backbone of BILP-19 leads to a high uptake. Furthermore, similar to the carbon dioxide sorption isotherms, a hysteresis occurs indicating once more a hindered desorption of polar guest molecules.

2.4. Selectivities over N₂ and CH₄

Flue gas as well as natural gas matrices are usually complex mixtures consistent of CO₂, CH₄, N₂, H₂O and other impurities such as H₂S or NO_x [4,33]. Thus, additionally to high uptake values for a specific type of gas, a distinct selectivity is required. The observed behavior of BILP-19 to adsorb only minor amounts of unpolar gases, while it expresses a great affinity towards polar molecules, indicates a high selectivity towards the latter. Here we present the selectivities of BILP-19 for CO₂ over N₂ and CH₄ within industrial relevant gas mixtures such as CO₂/N₂ (15/85) and CO₂/CH₄ (15/85) (Table 2). The selectivity values are calculated based on the ideal adsorbed solution theory IAST method for specific gas mixtures and initial slope of pure component-sorption isotherm calculations for a more general rating (Henry's method) [34,35].

In this respect, for carbon dioxide over nitrogen we calculated the Henry selectivity to 123 at 298 K (Table 2). The high performance of the network is a result of its well distributed polar groups and, therefore, very low affinity towards nitrogen, especially in the low-pressure region (Figure S11). Taking

the whole isotherm into account, IAST calculations for the industrial relevant gas mixture CO₂/N₂ (15/85) revealed a selectivity of 59, underlining its competitiveness in comparison to state-of-the-art networks (e.g. COP-1 (91) [36], MOPI-I (65) [7], TBILP-1 (62) [17], AB-COF (88) [31]). By increasing the part of carbon dioxide within the gas mixture the selectivity decreases towards 50 (Figure S21).

For carbon dioxide over methane, similar effects like for nitrogen are expected. We found a Henry selectivity of 12 at 273 K (Table 2). Interestingly, at higher temperatures the selectivity, estimated by initial slope of pure component isotherms remains similar. The same effect was found for the IAST calculations on a 15/85 CO₂/CH₄ mixture where the selectivity was calculated to be between 11 and 12 for 273 K, 298 K and 313 K, respectively (Supplementary Materials Section 3.2.2, Figures S22–S24). For both, nitrogen and methane, we assign the adsorption behavior primarily to a sieving effect, caused by the inaccessibility of the ultra-micropores for the respective guest. Thus, the influence of the temperature should be lowered in comparison with pure guest-functionality interactions.

Table 2. Henry and IAST selectivities of BILP-19 for CO₂ over CH₄ and N₂, respectively.

T/K	CO ₂ /CH ₄		CO ₂ /N ₂	
	Henry	IAST (15:85)	Henry	IAST (15:85)
273	12.0	11.9	-	-
298	14.0	12.3	123	59.1
313	10.3	11.3	-	-

3. Materials and Methods

3.1. General Information

Tris(4-formylphenyl)amine (TFPA) and 1,2,4,5-benzenetetramine tetrahydrochloride (BTA·4 HCl) were purchased from Sigma Aldrich (Steinheim, Germany). Dimethylformamide (DMF) was purchased from VWR Chemicals (Darmstadt, Germany), further dried over CaH₂ and freshly distilled before utilization.

3.2. Synthesis of BILP-19

Under argon atmosphere, 0.256 g BTA × 4 HCl (9.01×10^{-4} mol, 2 eq.) were dissolved in 50 mL dry DMF and cooled down to -30 °C in a dry-ice/acetone bath. Afterwards a solution of 0.150 g TFPA (4.55×10^{-4} mol, 1 eq.) dissolved in 50 mL dry DMF was added dropwise. The reaction mixture was allowed to reach room temperature and stirred for 19 h. After flushing with air for 10 min the reaction vessel was put into an oven at 130 °C for 3 days. The resulting solid was filtered and washed with DMF, acetone and H₂O. After soaking in 2 M HCl and 2 M NaOH for 5 min each, the material was washed again with H₂O and acetone prior to further purification in a Soxhlet-extractor with acetone/dichloromethane (1:1) for 2 days. The brown material was dried in vacuo at 100 °C. Yield: 0.255 g (5.35×10^{-4} mol, 99%). ¹³C-NMR (CP-MAS, 20.0 kHz): δ [ppm] = 152 (C-5), 148 (C-1), 141 (C-6), 128_{br} (C-2, C-3, C-4), 106 (C-7) (Figure 1). ¹⁵N-NMR (CP-MAS, 10 kHz) = -149 (N-II), -241 (N-III), -276 (N-I) (Figure 1). IR (ATR): ν [cm⁻¹] = 3383, 1600, 1478, 1361, 1264, 1178, 1104, 1015, 824, 739, 683 (Figure S2).

3.3. Experimental Details

Argon and nitrogen sorption measurements were carried out on a Quantachrome (Odelzhausen, Germany) Autosorb-1 pore analyzer at 87 K and 298 K, respectively. The data was analyzed using the Quantachrome ASIQ v 3.0 software package. For the Ar-based isotherms, the choice of the QSDFT adsorption branch kernel for cylindrical pores in carbon-based materials depended on the calculated fitting error. The polymer was degassed under vacuum (10^{-2} kPa) at 100 °C for 12 to 16 h before starting the adsorption experiments. Selectivities and adsorption parameters were calculated using

IAST and Henry methods according to the literature [34,37]. Specific surface areas, pore volumes and qualitative pore size distributions were calculated from CO₂ isotherms at 273 K using the nonlocal density functional theory (NLDFT) model for carbon materials. The isosteric heat of adsorption was calculated using the CO₂ adsorption isotherms at 273, 298, and 313 K. CO₂ and CH₄ adsorption isotherms were measured on a Quantachrome Nova surface analyzer at 273, 298, and 313 K, respectively. Water adsorption isotherms were derived from a Quantachrome Autosorb iQ at 298 K.

For infrared spectra (IR) a JASCO (Groß-Umstadt, Germany) FT/IR-6100 Fourier transform infrared spectrometer with an attenuated total reflectance (ATR) unit was used. CHN analysis was carried out at a Elementar (Langenselbold, Germany) vario EL-III with acetanilide as standard (Measured: C [65.7], H [4.2], N [17.9]. Calcd.: C [70.3], H [4.3], N [19.1]. For thermogravimetric analysis (TGA) a Mettler Toledo (Gießen, Germany) TGA/SDTA851^e was used. Powder X-ray diffraction (PXRD) measurements were performed on a PANalytical (Almelo, The Netherlands) X'Pert Pro diffractometer. The measurement included a region from 2 to 30° 2θ and was done with a 1/4 anti-scatter slit and Cu Kα radiation (nickel-filtered). Scanning electron microscopy (SEM) micrographs were measured with a scanning electron microscope, Zeiss (Oberkochen, Germany) LEO 1530 FESEM, equipped with a field emission cathode. All samples were drop-coated on a silicon wafer and sputtered with carbon. Energy dispersive X-ray scattering was performed with 20 kV.

All solid-state NMR MAS spectra were acquired on a Bruker (Leipzig, Germany) Avance-III HD spectrometer operating at a B₀ field of 9.4 T. ¹³C (δ = 100.6 MHz) and ¹⁵N (δ = 40.6 MHz). MAS spectra were obtained with ramped cross-polarization (CP) experiments where the nutation frequency ν_{nut} on the proton channel was varied linearly from 70–100%. The samples were spun at 12.5 kHz (¹³C) and 10.0 kHz (¹⁵N) in a 4 mm MAS double resonance probe (Bruker). The corresponding ν_{nut} on the ¹³C channel and the contact time were adjusted to 70 kHz and 3.0 ms, respectively. On the ¹⁵N channel, the corresponding ν_{nut} and the contact time were adjusted to 35 kHz and 5.0 ms, respectively. Proton broadband decoupling with spinal-64 and ν_{nut} = 12.5 kHz was applied during acquisition [38]. ¹³C spectra are referenced with respect to TMS (tetramethylsilane) using the secondary standard adamantane. ¹⁵N spectra are referenced with respect to CH₃NO₂ using the secondary standard glycine.

4. Conclusions

We showed the successful synthesis and careful characterization of a new benzimidazole linked polymer (BILP-19) with almost complete crosslinking via a condensation reaction of triformylphenylamine and tetraaminobenzene. Despite of a negligible micro- and mostly inter-particle surface area of 144 m²·g⁻¹ (Ar data), the network exhibits a high ultra-microporous surface area of 1325 m²·g⁻¹. Furthermore, CO₂ sorption isotherms revealed an exceptionally high CO₂ uptake up to 6 mmol·g⁻¹ at 273 K and water vapor sorption of 18.5 mmol·g⁻¹, which is among the highest values observed for porous polymers to date. Interestingly, both water and carbon dioxide isotherms reveal a pronounced hysteresis upon desorption, while for nitrogen and methane no formation of a hysteresis was observed. Furthermore, for the latter only low uptake values (N₂: 0.11 mmol·g⁻¹ at 298 K; CH₄: 0.88 mmol·g⁻¹ at 273 K) were found. The poor affinity towards methane and nitrogen results in excellent IAST selectivities of around 12 for CO₂/CH₄ at 273 K, 298 K and 313 K, respectively and 60 for CO₂/N₂ at 298 K. We attribute the excellent adsorption and selectivity performance to a sieving effect caused by the ultra-microporosity of the network as well as of the high and well distributed amount of polar groups, in combination with a reversible expansion of the interparticle space upon adsorption. Based on our earlier work, the results once more underline the importance of a network's ultra-microporosity on its performance of selective carbon dioxide capture. Moreover, based on its flexible packing, for BILP-19 a different way to create selectivity in two dimensional systems has been shown. Thus, the design and functionalization of ultra-microporous networks will be part of our future work.

Supplementary Materials: All the Supplementary Materials are available online.

Acknowledgments: The authors thank Renée Siegel and Beate Bojer for performing solid-state NMR spectroscopic measurements and Marko Schwarzmann for taking the SEM images at the Bavarian Polymer Institute (BPI) Keylab for Electron and Optical Microscopy. We gratefully thank Josef Breu for access to physisorption instruments and Rhett Kempe for access to CHN-analytics.

Author Contributions: C.K. performed all experiments unless mentioned otherwise in the acknowledgement. Analysis of the resulting data was done by C.K. The conceptual design of the study was performed by C.K. and J.S. Drafting of the manuscript was done by C.K. and J.S. F.R. performed water vapor sorption measurements.

Conflicts of Interest: The authors declare no conflict of interest.

References

1. UNFCCC. Conference of the Parties (COP). Adoption of the Paris Agreement. Proceedings of Paris Climate Change Conference. Paris, France, 2015. Available online: http://unfccc.int/meetings/paris_nov_2015/meeting/8926/php/view/decisions.php (accessed on 11 August 2017).
2. *The Global Status of CCS: 2016. Summary Report*; "Time To Accelerate"; Global CCS Institute: Docklands, Australia, 2016.
3. Dawson, R.; Cooper, A.I.; Adams, D.J. Chemical functionalization strategies for carbon dioxide capture in microporous organic polymers. *Polym. Int.* **2013**, *62*, 345–352. [[CrossRef](#)]
4. D'Alessandro, D.M.; Smit, B.; Long, J.R. Carbon Dioxide Capture: Prospects for New Materials. *Angew. Chem. Int. Ed.* **2010**, *49*, 6058–6082. [[CrossRef](#)] [[PubMed](#)]
5. Sakaushi, K.; Antonietti, M. Carbon- and Nitrogen-Based Organic Frameworks. *Acc. Chem. Res.* **2015**, *48*, 1591–1600. [[CrossRef](#)] [[PubMed](#)]
6. Zhu, G.; Ren, H. *Porous Organic Frameworks*; Springer: Berlin/Heidelberg, Germany, 2015.
7. Klumpen, C.; Breunig, M.; Homburg, T.; Stock, N.; Senker, J. Microporous Organic Polyimides for CO₂ and H₂O Capture and Separation from CH₄ and N₂ Mixtures: Interplay between Porosity and Chemical Function. *Chem. Mater.* **2016**, *28*, 5461–5470. [[CrossRef](#)]
8. Hao, S.; Liu, Y.; Shang, C.; Liang, Z.; Yu, J. CO₂ adsorption and catalytic application of imidazole ionic liquid functionalized porous organic polymers. *Polym. Chem* **2017**, *8*. [[CrossRef](#)]
9. Wang, J.; Sng, W.; Yi, G.; Zhang, Y. Imidazolium salt-modified porous hypercrosslinked polymers for synergistic CO₂ capture and conversion. *Chem. Commun.* **2015**, *51*, 12076–12079. [[CrossRef](#)] [[PubMed](#)]
10. Rabbani, M.G.; El-Kaderi, H.M. Template-Free Synthesis of a Highly Porous Benzimidazole-Linked Polymer for CO₂ Capture and H₂ Storage. *Chem. Mater.* **2011**, *23*, 1650–1653. [[CrossRef](#)]
11. Rabbani, M.G.; El-Kaderi, H.M. Synthesis and Characterization of Porous Benzimidazole-Linked Polymers and Their Performance in Small Gas Storage and Selective Uptake. *Chem. Mater.* **2012**, *24*, 1511–1517. [[CrossRef](#)]
12. Rabbani, M.G.; Reich, T.E.; Kassab, R.M.; Jackson, K.T.; El-Kaderi, H.M.; Zhang, W.; Lipkowski, J.; Guenther, J.; Blümel, J.; Krishna, R.; Li, Z.; Zhou, H.-C. High CO₂ uptake and selectivity by triptycene-derived benzimidazole-linked polymers. *Chem. Commun.* **2012**, *48*, 1141–1143. [[CrossRef](#)] [[PubMed](#)]
13. Sekizkardes, A.K.; İslamoğlu, T.; Kahveci, Z.; El-Kaderi, H.M. Application of pyrene-derived benzimidazole-linked polymers to CO₂ separation under pressure and vacuum swing adsorption settings. *J. Mater. Chem. A* **2014**, *2*, 12492. [[CrossRef](#)]
14. Sekizkardes, A.K.; Culp, J.T.; Islamoglu, T.; Marti, A.; Hopkinson, D.; Myers, C.; El-Kaderi, H.M.; Nulwala, H.B. An ultra-microporous organic polymer for high performance carbon dioxide capture and separation. *Chem. Commun. Chem. Commun* **2015**, *51*, 13393–13396. [[CrossRef](#)] [[PubMed](#)]
15. Altarawneh, S.; İslamoğlu, T.; Sekizkardes, A.K.; El-Kaderi, H.M. Effect of Acid-Catalyzed Formation Rates of Benzimidazole-Linked Polymers on Porosity and Selective CO₂ Capture from Gas Mixtures. *Environ. Sci. Technol.* **2015**, *49*, 4715–4723. [[CrossRef](#)] [[PubMed](#)]
16. Ashourirad, B.; Sekizkardes, A.K.; Altarawneh, S.; El-Kaderi, H.M. Exceptional Gas Adsorption Properties by Nitrogen-Doped Porous Carbons Derived from Benzimidazole-Linked Polymers. *Chem. Mater.* **2015**, *27*, 1349–1358. [[CrossRef](#)]
17. Sekizkardes, A.K.; Altarawneh, S.; Kahveci, Z.; İslamoğlu, T.; El-Kaderi, H.M. Highly selective CO₂ capture by triazine-based benzimidazole-linked polymers. *Macromolecules* **2014**, *47*, 8328–8334. [[CrossRef](#)]

18. Lu, W.; Sculley, J.P.; Yuan, D.; Krishna, R.; Wei, Z.; Zhou, H.-C. Polyamine-Tethered Porous Polymer Networks for Carbon Dioxide Capture from Flue Gas. *Angew. Chem. Int. Ed.* **2012**, *51*, 7480–7484. [[CrossRef](#)] [[PubMed](#)]
19. Arab, P.; Rabbani, M.G.; Sekizkardes, A.K.; İslamoğlu, T.; El-Kaderi, H.M. Copper(I)-Catalyzed Synthesis of Nanoporous Azo-Linked Polymers: Impact of Textural Properties on Gas Storage and Selective Carbon Dioxide Capture. *Chem. Mater.* **2014**, *26*, 1385–1392. [[CrossRef](#)]
20. McDonald, T.M.; Lee, W.R.; Mason, J.A.; Wiers, B.M.; Hong, C.S.; Long, J.R. Capture of carbon dioxide from air and flue gas in the alkylamine-appended metal-organic framework mmen-Mg₂(dobpdc). *J. Am. Chem. Soc.* **2012**, *134*, 7056–7065. [[CrossRef](#)] [[PubMed](#)]
21. Zhou, J.; Li, Z.; Xing, W.; Shen, H.; Bi, X.; Zhu, T.; Qiu, Z.; Zhuo, S. A New Approach to Tuning Carbon Ultramicropore Size at Sub-Angstrom Level for Maximizing Specific Capacitance and CO₂ Uptake. *Adv. Funct. Mater.* **2016**, *26*, 7955–7964. [[CrossRef](#)]
22. Liebl, M.R.; Senker, J. Microporous Functionalized Triazine-Based Polyimides with High CO₂ Capture Capacity. *Chem. Mater.* **2013**, *25*, 970–980. [[CrossRef](#)]
23. Seema, H.; Kemp, K.C.; Le, N.H.; Park, S.-W.; Chandra, V.; Lee, J.W.; Kim, K.S. Highly selective CO₂ capture by S-doped microporous carbon materials. *Carbon N. Y.* **2014**, *66*, 320–326. [[CrossRef](#)]
24. Hesse, M.; Meier, H.; Zeeh, B. *Spektroskopische Methoden in der Organischen Chemie*; Georg Thieme Verlag: Stuttgart, Germany, 2012.
25. Thommes, M.; Kaneko, K.; Neimark, A.V.; Olivier, J.P.; Rodriguez-Reinoso, F.; Rouquerol, J.; Sing, K.S.W. Physisorption of gases, with special reference to the evaluation of surface area and pore size distribution (IUPAC Technical Report). *Pure Appl. Chem.* **2015**, *87*, 1051–1069. [[CrossRef](#)]
26. Galarnau, A.; Villemot, F.; Rodriguez, J.; Fajula, F.; Coasne, B. Validity of the t-plot method to assess microporosity in hierarchical micro/mesoporous materials. *Langmuir* **2014**, *30*, 13266–13274. [[CrossRef](#)] [[PubMed](#)]
27. Islamoglu, T.; Behera, S.; Kahveci, Z.; Tessema, T.-D.; Jena, P.; El-Kaderi, H.M. Enhanced Carbon Dioxide Capture from Landfill Gas Using Bifunctionalized Benzimidazole-Linked Polymers. *ACS Appl. Mater. Interfaces* **2016**, *8*, 14648–14655. [[CrossRef](#)] [[PubMed](#)]
28. Mohr, R.; Rao, M.B. Isothermic Heat of Adsorption: Theory and Experiment. *J. Phys. Chem. B* **1999**, *103*, 6539–6546.
29. Lowell, S.; Shields, J.E.; Thomas, M.A.; Thommes, M. *Characterization of Porous Solids and Powders: Surface Area, Pore Size and Density*; Particle Technology Series; Springer: Dordrecht, The Netherlands, 2004; Volume 16.
30. Popp, N.; Homburg, T.; Stock, N.; Senker, J. Porous imine-based networks with protonated imine linkages for carbon dioxide separation from mixtures with nitrogen and methane. *J. Mater. Chem. A* **2015**, *3*, 18492–18504. [[CrossRef](#)]
31. Stegbauer, L.; Hahn, M.W.; Jentys, A.; Savasci, G.; Ochsenfeld, C.; Lercher, J.A.; Lotsch, B.V. Tunable Water and CO₂ Sorption Properties in Isostructural Azine-Based Covalent Organic Frameworks through Polarity Engineering. *Chem. Mater.* **2015**, *27*, 7874–7881. [[CrossRef](#)]
32. Biswal, B.P.; Kandambeth, S.; Chandra, S.; Shinde, D.B.; Bera, S.; Karak, S.; Garai, B.; Kharul, U.K.; Banerjee, R. Pore surface engineering in porous, chemically stable covalent organic frameworks for water adsorption. *J. Mater. Chem. A* **2015**, *3*, 23664–23669. [[CrossRef](#)]
33. Shimekit, B.; Mukhtar, H. Natural Gas Purification Technologies—Major Advances for CO₂ Separation and Future Directions. *Adv. Nat. Gas Technol.* **2012**, 235–270.
34. Landa, H.O.R.; Flockerzi, D.; Seidel-Morgenstern, A. A method for efficiently solving the IAST equations with an application to adsorber dynamics. *AIChE J.* **2013**, *59*, 1263–1277. [[CrossRef](#)]
35. Carroll, J.J. Henry's law revisited. *Chem. Eng. Prog.* **1999**, *95*, 49–56.
36. Xiang, Z.; Zhou, X.; Zhou, C.; Zhong, S.; He, X.; Qin, C.; Cao, D. Covalent-organic polymers for carbon dioxide capture. *J. Mater. Chem.* **2012**, *22*, 22663–22669. [[CrossRef](#)]
37. Dawson, R.; Stevens, L.A.; Drage, T.C.; Snape, C.E.; Smith, M.W.; Adams, D.J.; Cooper, A.I. Impact of water coadsorption for carbon dioxide capture in microporous polymer sorbents. *J. Am. Chem. Soc.* **2012**, *134*, 10741–10744. [[CrossRef](#)] [[PubMed](#)]
38. Fung, B.M.; Khitrin, A.K.; Ermolaev, K. An improved broadband decoupling sequence for liquid crystals and solids. *J. Magn. Reson.* **2000**, *142*, 97–101. [[CrossRef](#)] [[PubMed](#)]

Sample Availability: Samples of the compound BILP-19 are not available from the authors.



© 2017 by the authors. Licensee MDPI, Basel, Switzerland. This article is an open access article distributed under the terms and conditions of the Creative Commons Attribution (CC BY) license (<http://creativecommons.org/licenses/by/4.0/>).

Supplementary Information towards:

BILP-19— An Ultramicroporous Organic Network with Exceptional Carbon Dioxide UptakeChristoph Klumpen ¹, Florian Radakovitsch ², Andreas Jess ² and Jürgen Senker ^{1,*}¹ Inorganic Chemistry III, University of Bayreuth, Universitätsstraße 30, 95440 Bayreuth, Germany; christoph.klumpen@uni-bayreuth.de² Chair of Chemical Engineering, University of Bayreuth, Universitätsstraße 30, 95440 Bayreuth, Germany; florian.radakovitsch@uni-bayreuth.de (F.R.); jess@uni-bayreuth.de (A.J.)

* Correspondence: juergen.senker@uni-bayreuth.de; Tel.: +49-(0)921-552532

Table of Content

1. General Information	2
1.1 Literature on Benzimidazole linked Polymers (BILPs)	2
2. Characterization	4
2.1 Infrared Spectroscopy (IR)	4
2.2 Powder X-ray diffraction (PXRD)	4
2.3 Thermogravimetric analysis (TGA)	5
2.4 Scanning Electron Microscopy (SEM)	6
2.5 Nuclear Magnetic Resonance (NMR)	7
2.6 Surface area and porosity	7
3. Gas Sorption and Selectivity	8
3.1 Carbon dioxide	8
3.1.1 <i>Isosteric heat of adsorption</i>	8
3.1.1 <i>CO₂ Henry</i>	9
3.1.2 <i>CO₂ IAST</i>	10
3.2 Nitrogen	11
3.2.1 <i>Adsorption</i>	11
3.2.2 <i>N₂ Henry</i>	12
3.2.3 <i>N₂ IAST</i>	12
3.3 Methane	13
3.3.1 <i>Henry</i>	13
3.3.2 <i>IAST</i>	14
3.4 Argon	16
3.4.1 <i>T-Plot</i>	16
3.5 Selectivities based on IAST calculations	16
3.5.1 <i>Carbon dioxide over nitrogen</i>	16
3.5.2 <i>Carbon dioxide over methane</i>	17
4. Literature	18

1. General Information

1.1 Literature on Benzimidazole linked Polymers (BILPs)

Table S1: Key values of literature known porous polybenzimidazoles. For “?” assigned networks no literature could be found.

Network	S _A (BET) / m ² ·g ⁻¹	CO ₂ _273K / mmol·g ⁻¹	CO ₂ /N ₂ // 273K Henry	CO ₂ /CH ₄ // 273 K Henry
BILP-1[1]	1172 ^{Ar}	4.27	70	10
BILP-2[2]	708 ^{Ar}	3.39	113	17
BILP-3[3]	1306 ^{Ar}	5.11	59	8
BILP-4[2]	1135 ^{Ar}	5.34	79	10
BILP-5[2]	599 ^{Ar}	2.91	95	10
BILP-6[3]	1261 ^{Ar}	4.79	63	8
BILP-7[2]	1122 ^{Ar}	4.39	62	9
BILP-8 [?]	-	-	-	-
BILP-9 [?]	-	-	-	-
BILP-10[4]	787 ^{Ar}	4.02	111	14
BILP-11[4]	658 ^{Ar}	3.09	103	11
BILP-12[4]	1497 ^{Ar}	5.07	56	8
BILP-13[4]	677 ^{Ar}	2.57	103	9
BILP-14 [?]	-	-	-	-
BILP-15[5]	448 ^{Ar}	2.68	83	9
BILP-16[5]	435 ^{Ar}	2.70	53	10
BILP-15(AC) [5]	862 ^{Ar}	3.43	61	9
BILP-16(AC) [5]	643 ^{Ar}	3.45	49	9
BILP-17[6]	952 ^{Ar}	-	-	-
BILP-18[6]	947 ^{Ar}	-	-	-
BILP-101[7]	536 ^{N₂}	2.43 ^{298K}	80	-
PPN-101[8]	1096 ^{N₂}	5.14	199 IAST	-
TBILP-1[9]	330 ^{Ar}	117 mg/g	63	9
TBILP-2[9]	1080 ^{Ar}	228 mg/g	40	7

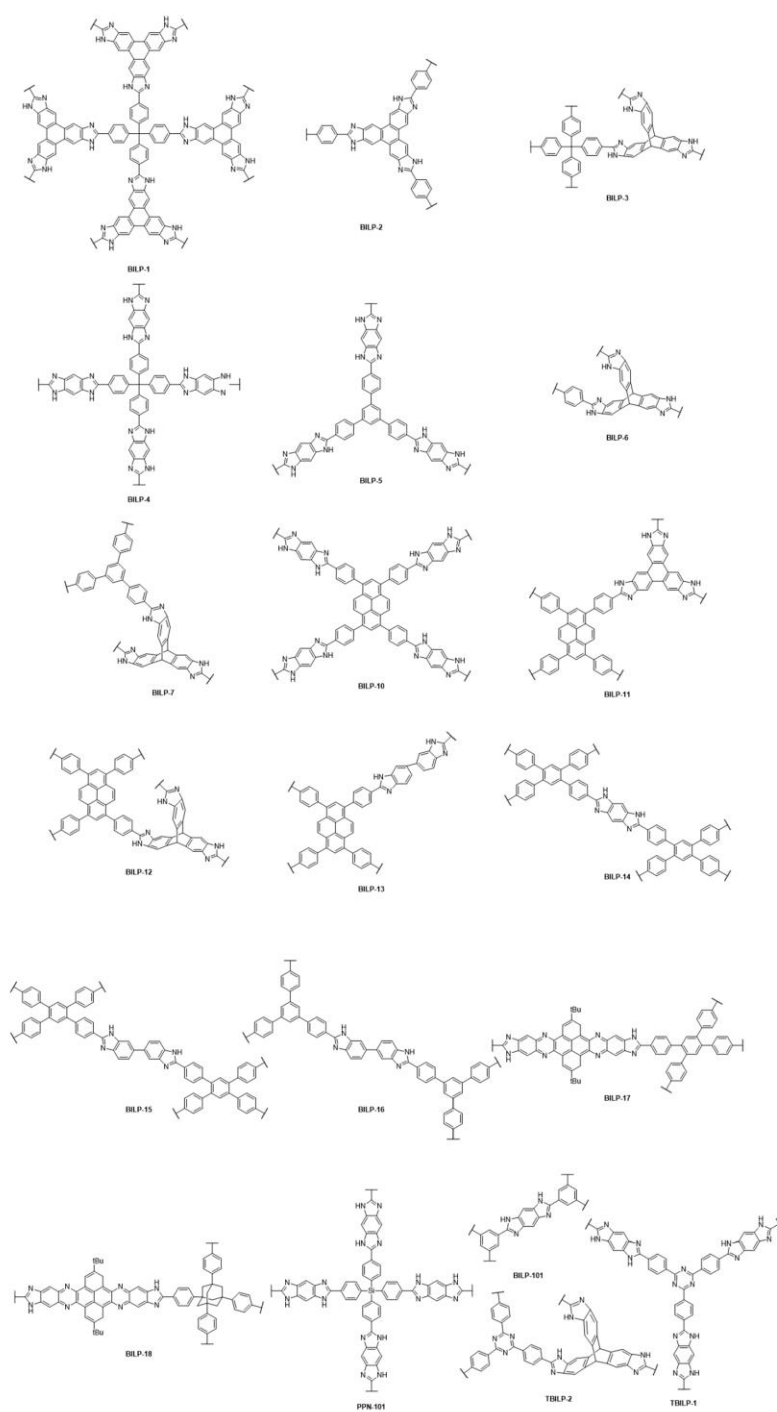


Figure S1: Schematic presentation of the benzimidazole based porous polymers compared in Table S1.

2. Characterization

2.1 Infrared Spectroscopy (IR)

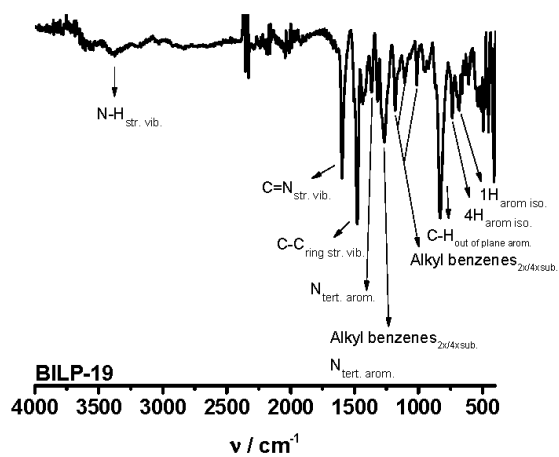


Figure S2: Infrared spectrum of BILP-19 and assignment of the most characteristic signals.

2.2 Powder X-ray diffraction (PXRD)

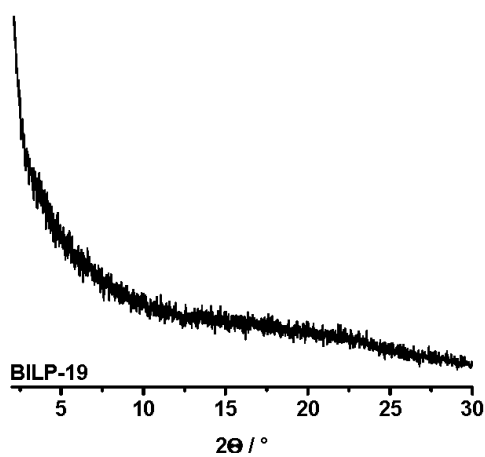


Figure S3: PXRD diffractogram of BILP-19.

2.3 Thermogravimetric analysis (TGA)

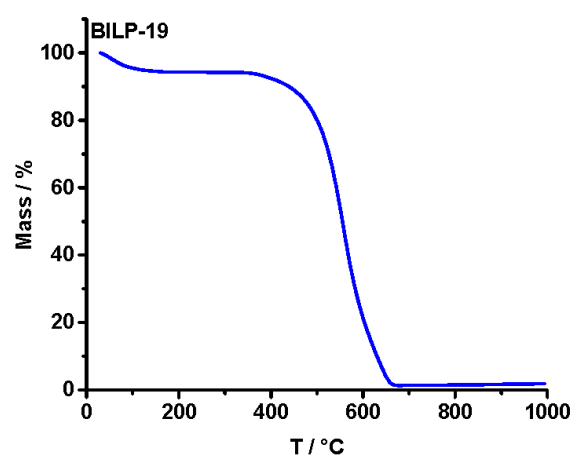


Figure S4: TGA curve of BILP-19 measured under air.

2.4 Scanning Electron Microscopy (SEM)

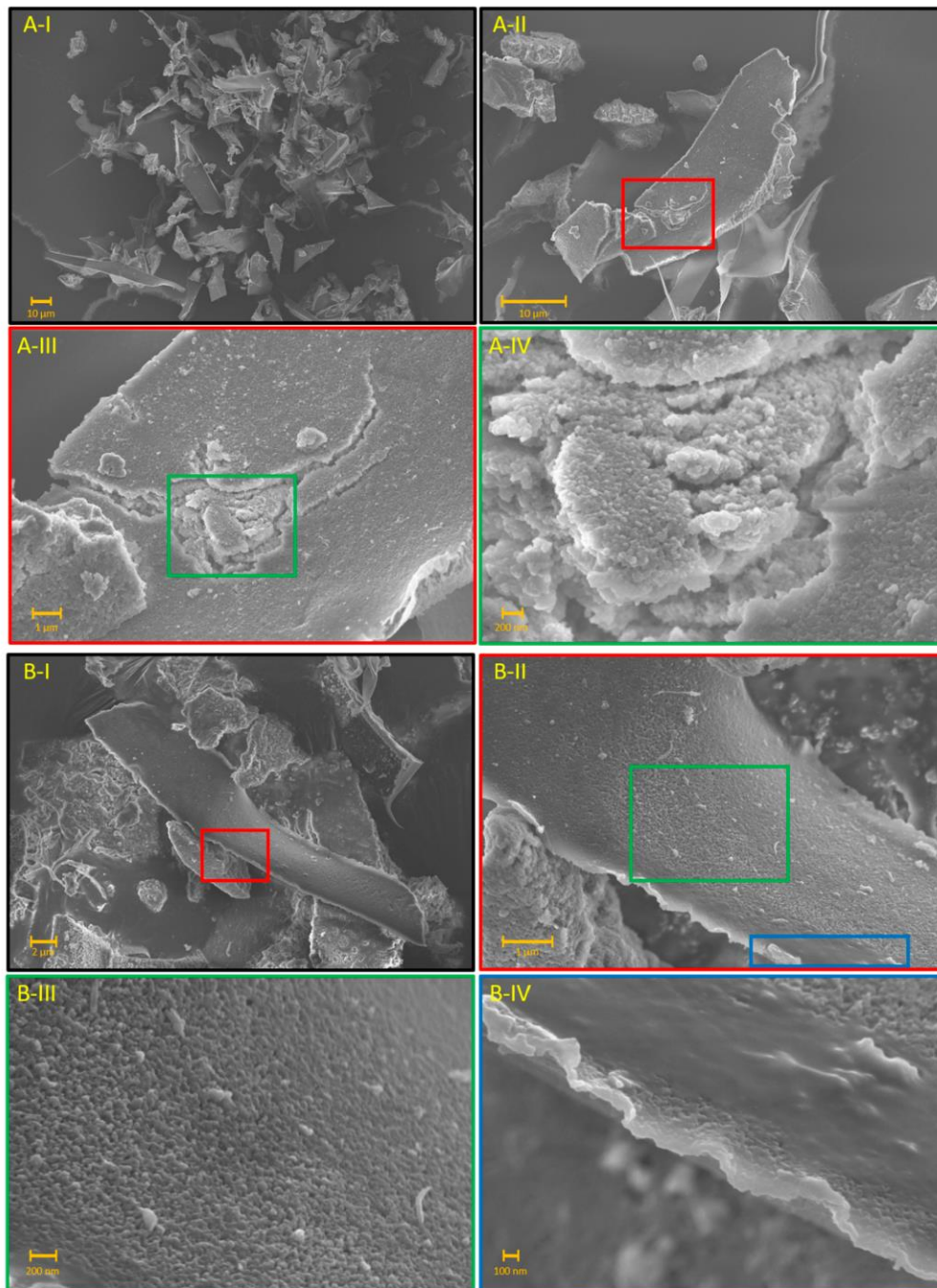
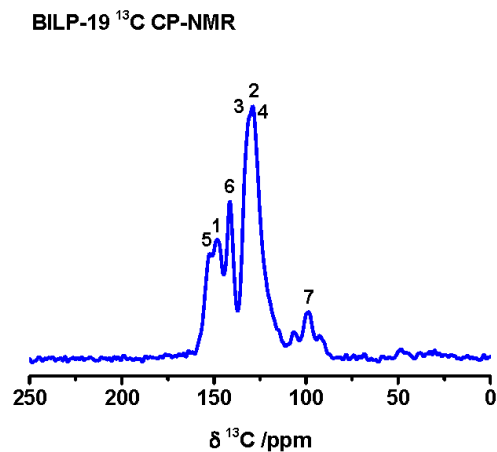
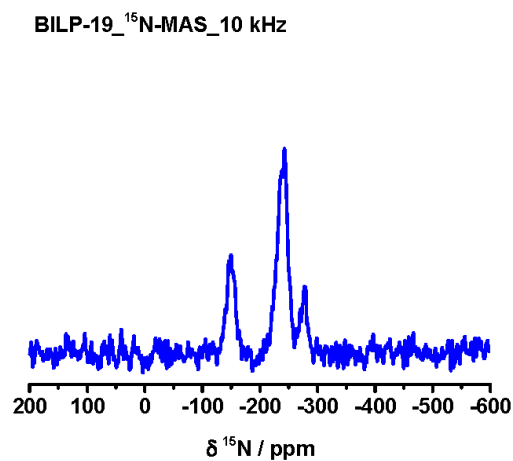


Figure S5: SEM Images of BILP-19, taken at to different positions (A, B).

2.5 Nuclear Magnetic Resonance (NMR)

Figure S6: Complete ^{13}C MAS CP NMR spectrum of BILP-19.Figure S7: Complete ^{15}N CP MAS NMR spectrum of BILP-19.

2.6 Surface area and porosity

Table S2: Surface area and porosity of BILP-19 estimated from Ar, N₂ and CO₂ sorption isotherms, respectively.

Adsorbive	$S_{A,BET} / \text{m}^2 \cdot \text{g}^{-1}$	$S_{A,DFT} / \text{m}^2 \cdot \text{g}^{-1}$	$P_{V,tot} / \text{cm}^3 \cdot \text{g}^{-1}$	$P_{V,mic} / \text{cm}^3 \cdot \text{g}^{-1}$	$P_{V,mic} / P_{V,tot}$
Ar	144	128	0.0232	0.013	0.04
N ₂	252	227	0.382	0.035	0.09
CO ₂	-	1325	0.442	-	-

2.7 CHN analysis

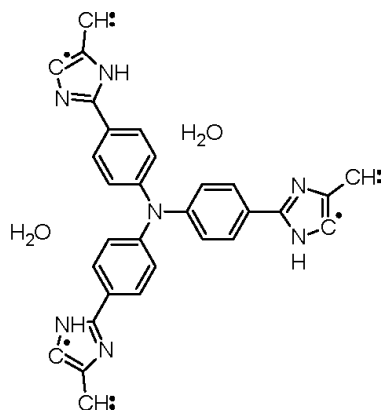


Table S3: Results of CHN analysis of BILP-19. Due to water content of 6 %, obtained by thermogravimetric analysis, two water molecules per linker were included in the theoretical calculations.

	C / %	H / %	N / %
BILP-19·2H₂O_{meas.}	65.67	4.24	17.94
BILP-19·2H₂O_{calc.}	70.30	4.33	19.13
Deviation	4.63	0.09	1.19

3. Gas Sorption and Selectivity

3.1 Carbon dioxide

3.1.1 Isosteric heat of adsorption

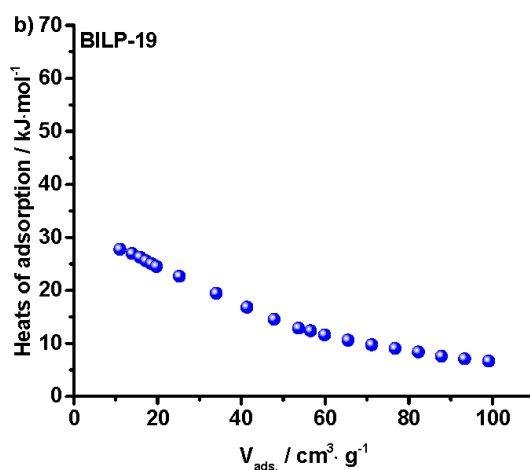


Figure S8: Isosteric heats of adsorption calculated from carbon dioxide adsorption isotherms measured at 273 K, 298 K and 313 K.

3.1.1 CO₂_Henry

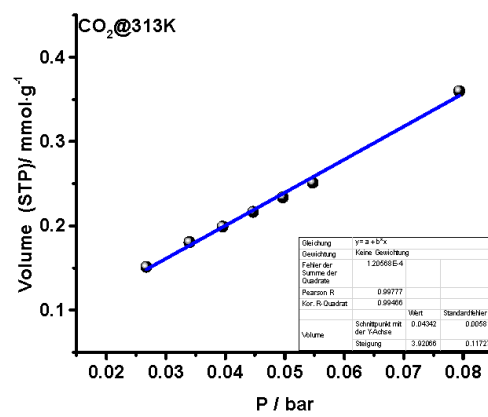
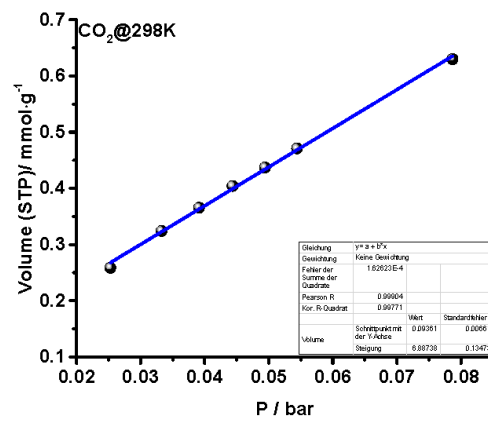
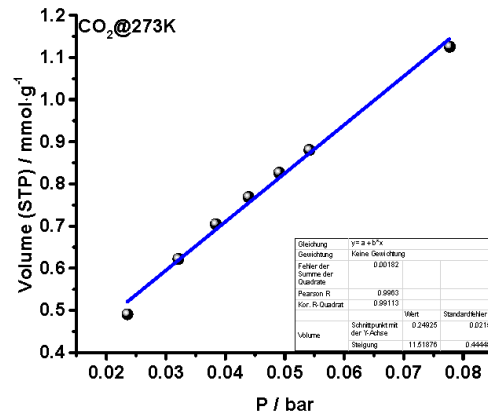


Figure S9: Fits for initial slope calculations (Henry method) of CO₂ isotherms measured at 273, 298 and 313 K.

3.1.2 CO₂_IAST

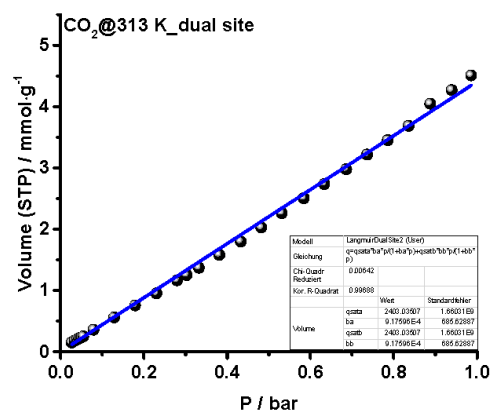
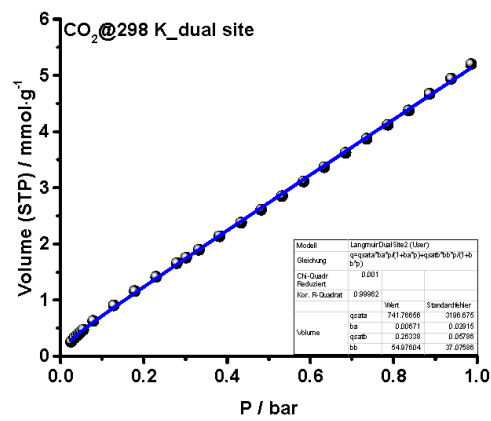
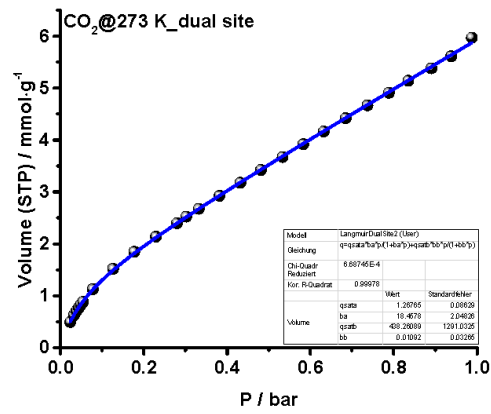


Figure S10: Langmuir dual site fits for CO₂ adsorption isotherms measured at 273, 298 and 313 K.

3.2 Nitrogen

3.2.1 Adsorption

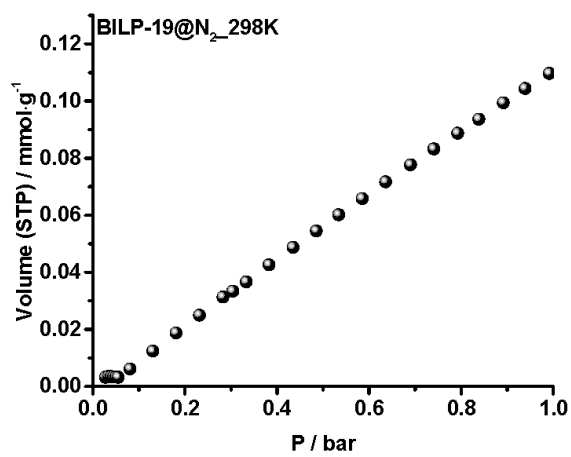
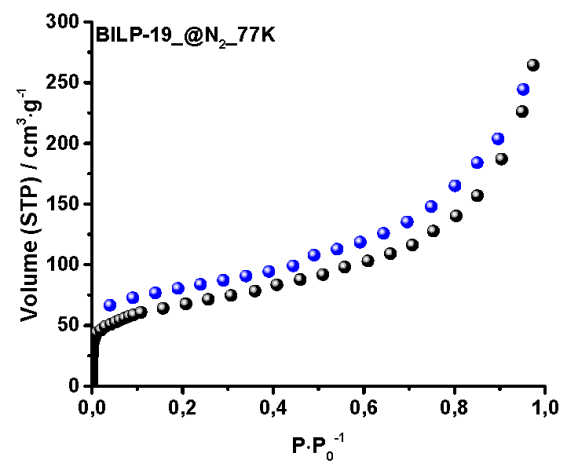


Figure S11: Nitrogen adsorption isotherm measured at 77K (top) and 298 K (bottom).

3.2.2 N₂ Henry

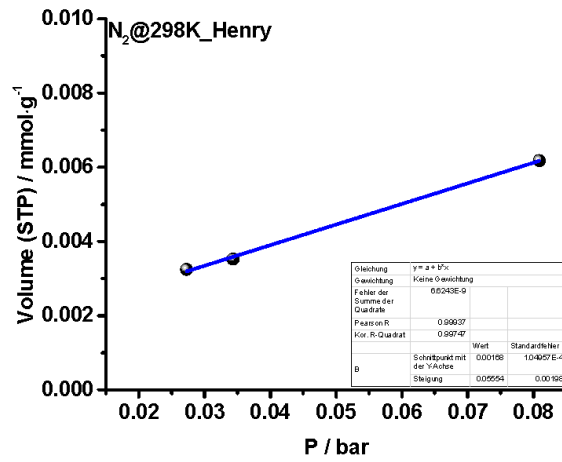


Figure S12: Initial slope of pure component fit for nitrogen adsorption at 298 K.

3.2.3 N₂ IAST

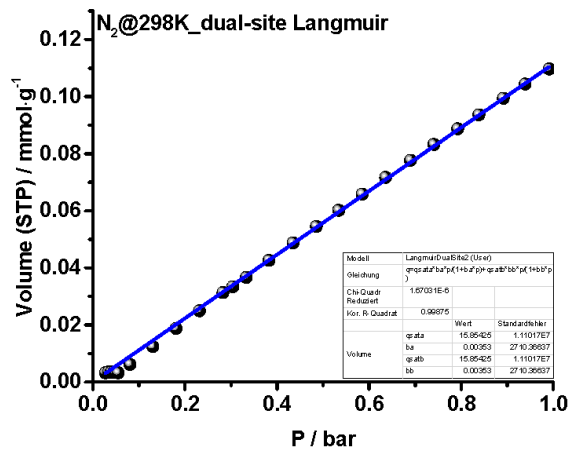


Figure S13: Langmuir dual site fit of N₂ sorption isotherms measured at 298 K.

3.3 Methane

3.3.1 Henry

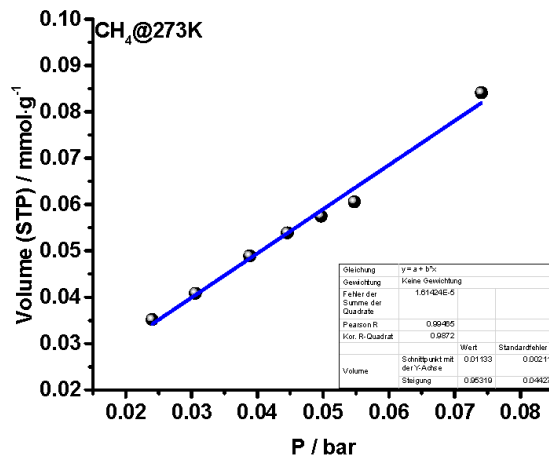


Figure S14: Initial slope of pure component adsorption fit for CH₄, measured at 273 K.

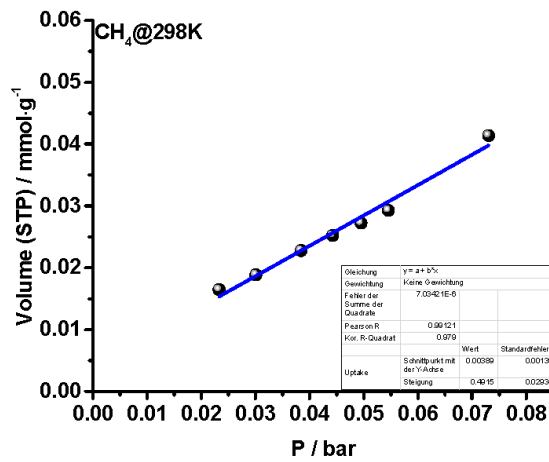


Figure S15: Initial slope of pure component adsorption fit for CH₄, measured at 298 K.

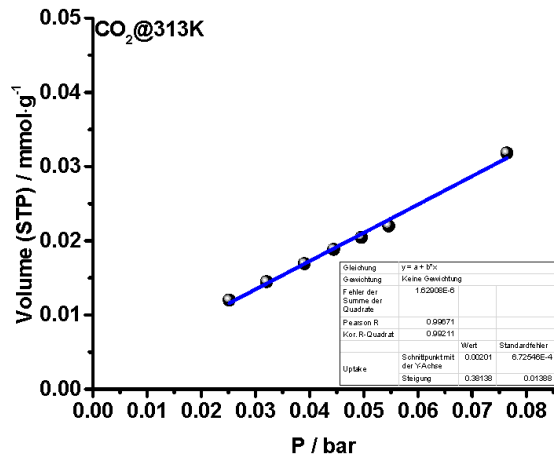


Figure S16: Initial slope of pure component adsorption fit for CH₄, measured at 313 K.

3.3.2 IAST

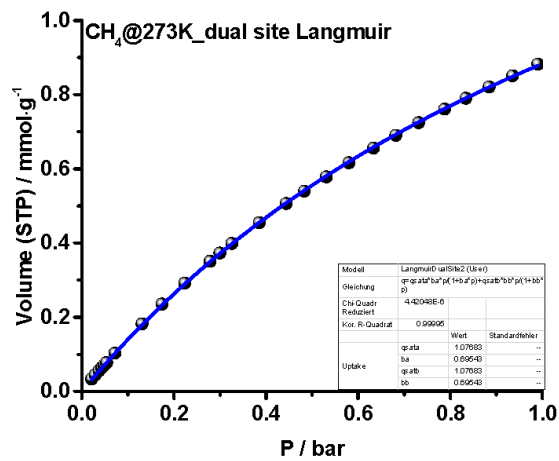


Figure S17: Langmuir dual site fit of CH₄ sorption isotherms measured at 298 K.

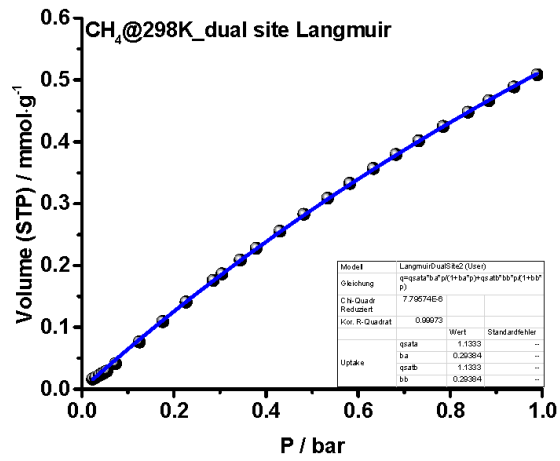


Figure S18: Langmuir dual site fit of CH₄ sorption isotherms measured at 298 K.

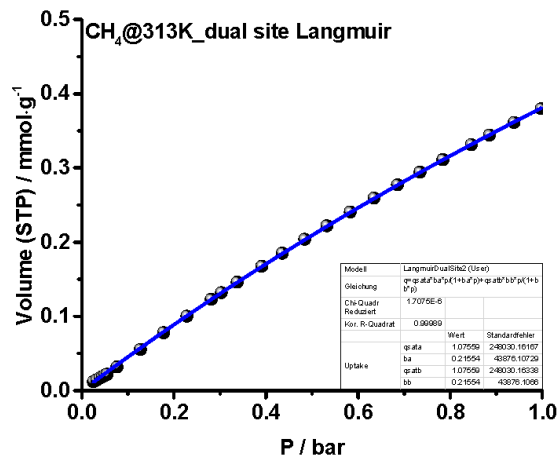


Figure S19: Langmuir dual site fit of CH₄ sorption isotherms measured at 313 K.

3.4 Argon

3.4.1 T-Plot

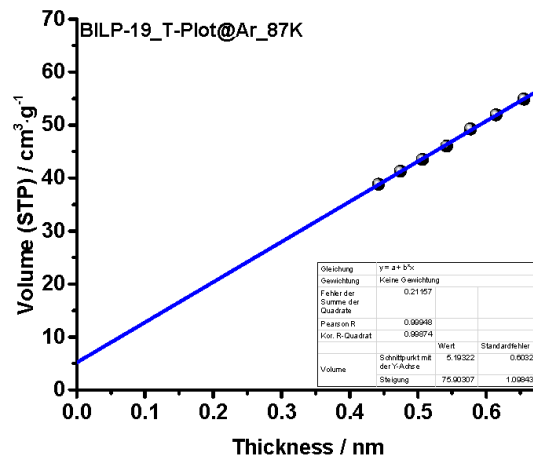


Figure S20: T-Plot applied on Ar isotherm measured at 87 K. The P/P_0 range was 0.2 - 0.5.

3.5 Selectivities based on IAST calculations

3.5.1 Carbon dioxide over nitrogen

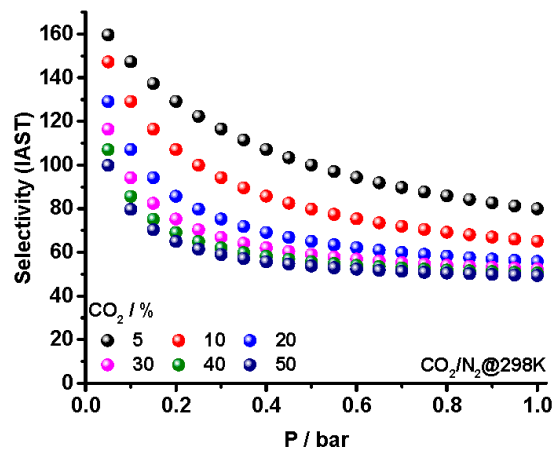


Figure S21: Selectivities of carbon dioxide over nitrogen, based on IAST calculations for different contents of carbon dioxide at 298 K.

3.5.2 Carbon dioxide over methane

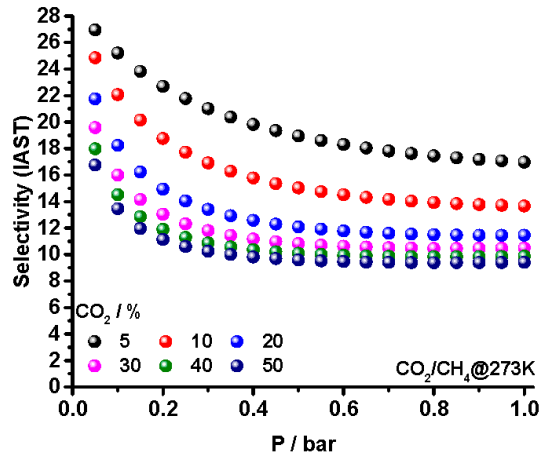


Figure S22: Selectivities of carbon dioxide over methane, based on IAST calculations for different contents of carbon dioxide at 273 K.

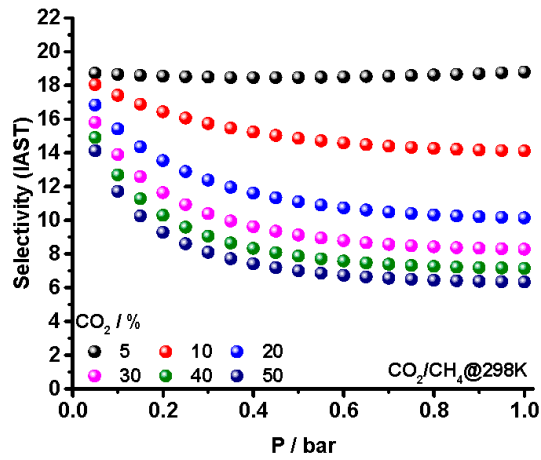


Figure S23: Selectivities of carbon dioxide over methane, based on IAST calculations for different contents of carbon dioxide at 298 K.

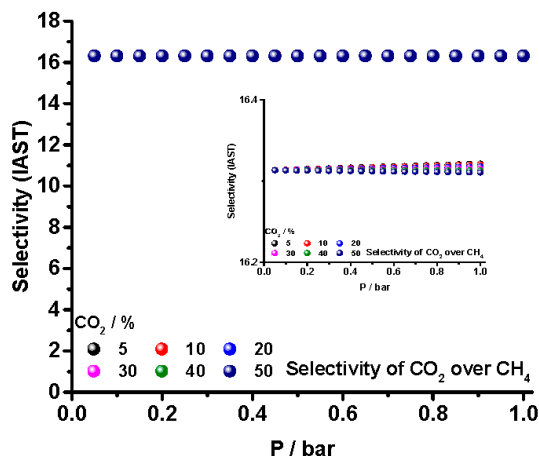


Figure S24: Selectivities of carbon dioxide over methane, based on IAST calculations for different contents of carbon dioxide at 313 K.

4. Literature

- Rabbani, M. G.; El-Kaderi, H. M. Template-Free Synthesis of a Highly Porous Benzimidazole-Linked Polymer for CO₂ Capture and H₂ Storage. *Chem. Mater.* **2011**, *23*, 1650–1653.
- Rabbani, M. G.; El-Kaderi, H. M. Synthesis and Characterization of Porous Benzimidazole-Linked Polymers and Their Performance in Small Gas Storage and Selective Uptake. *Chem. Mater.* **2012**, *24*, 1511–1517.
- Rabbani, M. G.; Reich, T. E.; Kassab, R. M.; Jackson, K. T.; El-Kaderi, H. M. High CO₂ uptake and selectivity by triptycene-derived benzimidazole-linked polymers. *Chem. Commun.* **2012**, *48*, 1141–1143.
- Sekizkardes, A. K.; İslamoğlu, T.; Kahveci, Z.; El-Kaderi, H. M. Application of pyrene-derived benzimidazole-linked polymers to CO₂ separation under pressure and vacuum swing adsorption settings. *J. Mater. Chem. A* **2014**, *2*, 12492.
- Altarawneh, S.; İslamoğlu, T.; Sekizkardes, A. K.; El-Kaderi, H. M. Effect of Acid-Catalyzed Formation Rates of Benzimidazole-Linked Polymers on Porosity and Selective CO₂ Capture from Gas Mixtures. *Environ. Sci. Technol.* **2015**, *49*, 4715–4723.
- Altarawneh, S.; Nahar, L.; Arachchige, I. U.; El-Ballouli, A. O.; Hallal, K. M.; Kaafarani, B. R.; Rabbani, M. G.; Arvapally, R. K.; El-Kaderi, H. M. Highly porous and photoluminescent pyrene-quinoxaline-derived benzimidazole-linked polymers. *J. Mater. Chem. A* **2015**, *3*, 3006–3010.
- Sekizkardes, A. K.; Culp, J. T.; Islamoglu, T.; Marti, A.; Hopkinson, D.; Myers, C.; El-Kaderi, H. M.; Nulwala, H. B. An ultra-microporous organic polymer for high performance carbon dioxide capture and separation. *Chem. Commun. Chem. Commun* **2015**, *51*, 13393–13396.
- Zhang, M.; Perry, Z.; Park, J.; Zhou, H.-C. Stable benzimidazole-incorporated porous polymer network for carbon capture with high efficiency and low cost. *Polymer (Guildf)*. **2014**, *55*, 335–339.
- Sekizkardes, A. K.; Altarawneh, S.; Kahveci, Z.; Islamoğlu, T.; El-Kaderi, H. M. Highly selective CO₂ capture by triazine-based benzimidazole-linked polymers. *Macromolecules* **2014**, *47*, 8328–8334.

5.3 Water mediated Proton Conduction in a Sulfonated Microporous Organic Polymer

Die Publikation wurde in Zusammenarbeit mit dem Lehrstuhl für Physikalische Chemie II der Universität Bayreuth, Prof. Dr. G. Papastavrou, durchgeführt. Die Beiträge der Autoren sind wie folgt:

Christoph Klumpen

- ⇒ Projektplanung und Durchführung
- ⇒ Synthesen und Charakterisierung der Verbindungen
- ⇒ Durchführung und Auswertung der Gassorptionsanalytik
- ⇒ Durchführung und Auswertung der impedanzspektroskopischen Analytik
- ⇒ Auswertung des Gesamtdatensatzes
- ⇒ Planung und Aufsetzen des Manuskripts

Sebastian Gödrich, Georg Papastavrou

- ⇒ Durchführung und Auswertung der AFM
- ⇒ Design des Manuskripts

Jürgen Senker

- ⇒ Projektplanung und Supervision
- ⇒ Planung und Aufsetzen des Manuskripts



Water mediated proton conduction in a sulfonated microporous organic polymer†

C. Klumpen,^a S. Gödrich,^b G. Papastavrou^{id}^b and J. Senker^{id}*^a

Cite this: *Chem. Commun.*, 2017, 53, 7592

Received 20th March 2017,
Accepted 2nd June 2017

DOI: 10.1039/c7cc02117h

rsc.li/chemcomm

Polymer membranes (PEMs) within fuel cells (FCs) act as separators and efficient proton conducting electrolytes. Established systems tend to microphase separation into hydrophilic and hydrophobic regions, making these materials prone to water loss at elevated temperatures. Therefore, recent approaches utilize porous materials, which promise stronger interactions between water molecules and the framework, while still providing efficient conductive pathways. Here we show, that the microporous polymer PAF-1 exhibits proton conductivities up to 10^{-1} S cm⁻¹ under hydrous conditions, after post-synthetic sulfonation. Gas phase sulfonation turned out to be the essential step for introducing a sufficiently large amount of -SO₃H groups and thus a high charge carrier concentration upon hydration. While the absolute conductivity of the sulfonated frameworks strongly depends on the water uptake, we found similar activation barriers for all relative humidities. Since water is homogeneously stored in micro- and mesoporous voids, the activation barrier of the inter-pore conductivity is decisive for the macroscopic properties.

To establish a power economy independent from fossil fuels, the development of new energy sources is of crucial importance in terms of environmental and economical requirements. Fuel cell systems provide a potential solution due to their clean energy production and flexibility.^{1,2} Nafion, developed by DuPont, is currently still the standard for PEMs. It consists of hydrophobic PFE-chains and hydrophilic sulfonic acid end groups.³ Upon hydration, macroscopic channels are formed due to microphase separation, allowing proton conduction through protonated bulk water.^{4,5} For Nafion, conductivities up to 10^{-1} S cm⁻¹ have been obtained at 60 °C and >99% relative humidity (rH). To date, this is challenged by only few materials.³

However, the limited working conditions (60–80 °C, 100% rH) and the cost intensive synthesis of Nafion inspires the development of substitutes with better performances.⁶

Directed proton transport through ordered pore systems is expected to provide high conductivities as well as a reduced water evaporation rate. Up to now, this concept is mostly explored for metal organic frameworks (MOFs), where continuously ordered and functionalizable pore structures act as alternative conduction pathways.^{7,8} The incorporation of acids and amphoteric molecules into the pore space allowed for high proton conductivities.⁹ *E.g.* after functionalizing UiO-66 with sulfonic acid groups, remarkable conductivities up to 8.4×10^{-2} S cm⁻¹ at 80 °C and 90% rH were achieved.¹⁰ However, most MOFs suffer from structural instabilities at harsher conditions, impeding a post-synthetic modification of the frameworks, *e.g.* through direct incorporation of strong acidic groups.¹¹

The principal idea of this study is to transfer this concept to porous organic polymers (POPs). As pure organic compounds, POPs exhibit high physicochemical stability due to covalent bonded network structures, and, therefore, allow for post-synthetic modification under harsh conditions, such as treating POPs with sulfonic acid. Due to their broad functionality and structural diversity POPs are widely used in the field of gas sorption and separation, as well as in catalysis and for light harvesting.^{12,13} For proton conduction, however, only few systems have been tested so far, which mainly concentrate on ion conduction *via* incorporation of amphoteric molecules into the respective pore structures.^{14–18} The first proton conducting POP was synthesized by Banerjee *et al.*¹⁴ They immobilized phosphoric acid in the crystalline network TP-Azo and observed moderate conductivities for both hydrous (9.9×10^{-4} S cm⁻¹ at 59 °C and 98% rH) and anhydrous conditions (6.7×10^{-5} S cm⁻¹ at 65 °C).

In order to achieve high conductivities, we aim at maximizing the charge carrier concentration as well as their mobility within the pore space. A promising approach is the introduction of strongly acidic groups, such as -SO₃H, in combination with adsorbed water. For this study, we concentrate on the highly resistant, adamantane porous aromatic framework (PAF-1),

^a University of Bayreuth, Inorganic Chemistry III, Universitätsstraße 30, 95447 Bayreuth, Germany. E-mail: juergen.senker@uni-bayreuth.de

^b University of Bayreuth, Physical Chemistry II, Universitätsstraße 30, 95447 Bayreuth, Germany

† Electronic supplementary information (ESI) available. See DOI: 10.1039/c7cc02117h

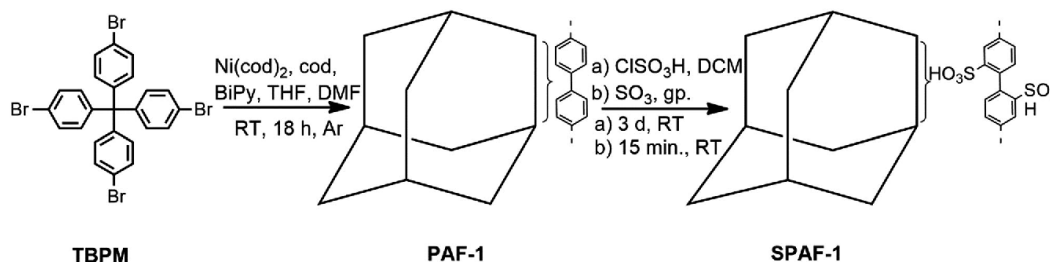


Fig. 1 Synthesis of sulfonated porous aromatic framework 1 (SPAF-1). Route (a) shows the solvent based reaction conditions towards SPAF-1(0.5), whereas route (b) shows the conditions for gas phase sulfonation of PAF-1 towards SPAF-1(1.25).

which was first reported by Ben *et al.* in 2009 (Fig. 1).¹⁹ PAF-1 exhibits a remarkable surface area up to $5600 \text{ m}^2 \text{ g}^{-1}$ and was already successfully explored for gas sorption and separation.^{19–24} Moreover, due to the adamantane building blocks, a locally ordered structure is expected, which is advantageous for the formation of efficient conduction pathways.

We synthesized PAF-1 by coupling triphenylmethyl chloride and aniline to obtain tetraphenylmethane, which was brominated afterwards using Br_2 . Applying a Yamamoto type homopolymerization on the resulting tetrakis(4-bromophenyl)methane, we obtained the respective network with an overall yield of 48% (Fig. 1).^{19,25} The network was characterized by IR and solid-state MAS NMR spectroscopy as well as by elemental analysis (Sections S2.2.1–S2.2.3, ESI†). The C-2 and C-5 intensity ratio of the quantitative ^{13}C MAS single-pulse NMR spectrum (Fig. S8, ESI†) indicates a crosslinking degree of about 80% (ref. to Section S2.2.1.1 for details, ESI†). The N_2 adsorption isotherm is typical for a mixed micro- and mesoporous system, showing a steep increase of the adsorption branch at low p/p_0 and a hysteresis for the desorption branch at higher p/p_0 . Based on a QSDFT kernel for cylindrical pore geometries and carbon materials,²⁶ an apparent surface area of $2040 \text{ m}^2 \text{ g}^{-1}$ ($S_{\text{A,BET}}$: $2625 \text{ m}^2 \text{ g}^{-1}$) and a total pore volume of $2.68 \text{ cm}^3 \text{ g}^{-1}$ was obtained (Section S1.1, ESI†). The pore volume consists of a mixture of micro- (33%) and mesopores (77%). The poresize distribution shows three well-defined maxima around 1, 5 and 7 nm (Section S2.2.4, ESI†). CO_2 adsorption isotherms revealed a surface area of $600 \text{ m}^2 \text{ g}^{-1}$, demonstrating a substantial amount of ultra-micropores with pore diameters between 0.5 and 0.8 nm (Section S2.2.5, ESI†).

For all sulfonation reactions the ^{13}C -NMR, IR and UV-VIS spectra support covalent binding of the $-\text{SO}_3\text{H}$ groups to the benzene rings (Fig. S9–S11 and S22, ESI†). Since both, benzene and biphenyl, remain colourless upon sulfonation, the observed colour change to violet is not a consequence of changes in the delocalized π system.²⁷ We attribute this effect to a charge transfer between the $-\text{SO}_3\text{H}$ groups and close by aromatic units, which occurs only in the dry solids. As such the colour change allows to follow the reactions' progress (Fig. S1 and S22, ESI†). The overall sulfonation degree was obtained from titration with NaOH and is consistent with results of the CHN analysis (Section S2.1.3, ESI†).²⁰ By using a solvent based sulfonating technique ($\text{ClSO}_3\text{H}/\text{DCM}$),

previously described by Zhou *et al.*, on average every second phenyl-ring was functionalized resulting in SPAF-1(0.5).²⁰ By contrast, for gas phase sulfonation (Fig. S1, ESI†), using oleum with 65% SO_3 , we were able to functionalize each aromatic ring on average with up to 1.25 $-\text{SO}_3\text{H}$ units (SPAF-1(1.25)), which are homogeneously distributed within the network as shown with EDX mapping (Fig. S26, ESI†). After post-synthetic modification, the N_2 - surface area for both SPAF-1(0.5) and SPAF-1(1.25) decreased to $670 \text{ m}^2 \text{ g}^{-1}$ and $115 \text{ m}^2 \text{ g}^{-1}$, respectively. This shift is accompanied by a decrease of the mesoporosity, most probably caused by a denser packing of the polymer particles after sulfonation. Nevertheless, the poresize distributions exhibit well defined maxima around 1, 2, 4 and 6 nm (Fig. S15 and S17, ESI†). The CO_2 surface area decreases for SPAF-1(1.25) from $600 \text{ m}^2 \text{ g}^{-1}$ to $392 \text{ m}^2 \text{ g}^{-1}$, while for SPAF-1(0.5) it remains nearly constant ($545 \text{ m}^2 \text{ g}^{-1}$). This indicates, that for liquid phase sulfonation, the ultramicropores are not accessible, probably leading to an inhomogeneous distribution of $-\text{SO}_3\text{H}$ groups. By contrast, for gas phase sulfonation the complete pore region takes part in the post-synthetic modification, leading to the observed homogeneous distribution (Fig. S26, ESI†).

For water mediated proton conduction, the performance of a material correlates with its ability of incorporating water molecules.^{28,29} Thus, the water uptake of SPAF-1(0.5) and SPAF-1(1.25) was measured by thermogravimetric analysis to calculate the amount of incorporated water molecules per sulfonic acid group (λ) (Fig. 2). λ increases with the rH up to 8 (SPAF-1(0.5)) and 13 (SPAF-1(1.25)) water molecules per sulfonic acid at 98% rH, which is a consequence of the stronger hygroscopicity with increasing sulfonation degree. Both values account for a specific volume of $0.64 \text{ cm}^3 \text{ g}^{-1}$ and $1.67 \text{ cm}^3 \text{ g}^{-1}$, respectively, assuming a density of liquid water. Those values exceed by far the pore volumes estimated from N_2 and CO_2 isotherms (Table S10, ESI†). However, for SPAF-1(0.5) significantly less water is incorporated within the voids and it is sufficient to reduce the rH below 90% to remove the interstitial water. By contrast, for SPAF-1(1.25) this turnover occurs only below 28% rH. This interpretation is based on the assumption that the pore volumes from both isotherms are approximately additive, since CO_2 is mostly sensitive to pores smaller than 1 nm (\emptyset), whereas N_2 detects pores larger than 0.8 nm (\emptyset).

ChemComm

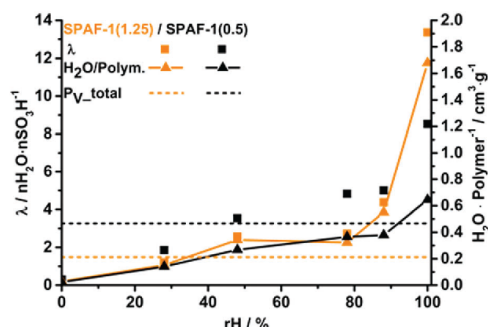


Fig. 2 Water uptake for SPAF-1(0.5) and SPAF-1(1.25) at 25 °C as function of relative humidities. It is given as amount of water molecules per sulfonic acid group (λ , triangles) and volumetric value, normalized on the polymer weight ($\text{cm}^3 \text{g}^{-1}$, triangles). Both are derived from thermogravimetric data and the assumption of a water density of 1 g cm^{-3} (liquid water) within the pores. The horizontal lines indicate the total pore volumes in $\text{cm}^3 \text{g}^{-1}$ ($V_{\text{N}_2} + V_{\text{CO}_2}$).

The absence of a melting/crystallization signature within the DSC measurement for SPAF-1(1.25) saturated at 30% rH down to -80°C (Fig. S24 top, ESI†) demonstrates that the water is exclusively adsorbed in microporous regions. Saturated at 98% rH, additionally 25% of the incorporated water is located in narrow mesopores, as indicated by a crystallization temperature as low as -25°C (Fig. S24 bottom, ESI†). The magnitude of the shift is consistent with the pore size distributions as derived from the N_2 sorption experiments (Fig. S13, S15 and S17, ESI†). The absence of an enthalpic signature around 0°C for both hydration states rules out the existence of bulk water, as found for systems with microphase separation.^{30,31} Additionally, an uniform distribution of sodium ions was found after ion exchange (Fig. S26, ESI†) as well as a homogeneous surface topology revealed by atomic force microscopy (Fig. S27, ESI†). In combination with the swelling of the spongiform particles (Fig. S25, ESI†) upon hydration, we expect that parts of the pore space observed for the original network PAF-1 are reactivated.

The proton conductivity of the networks was measured by electrochemical impedance spectroscopy as a function of rH (30–95%) and temperature (20–80 °C). The experimental data were modelled with an optimized Randles Cell as equivalent circuit (inset Fig. 3, top), which describes the behaviour of an ion conducting material placed between two blocking electrodes.³² Here R_1 and R_2 represent the electrode/pellet interface and the bulk resistance, respectively. The constant phase element (CPE) is used to describe the capacitive part of the system adapted to influences of surface roughness and system heterogeneity.^{32,33} The conductivity κ is calculated from R_2 by $\kappa = l \cdot (R_2 \cdot A)^{-1}$, taking the thickness l and surface area A of the pelletized sample into account.

For the conductivities κ of SPAF-1(0.5) and SPAF-1(1.25) we observed two main trends: first, κ is strongly dependent on the rH, leading to a steep increase by roughly four orders of magnitudes from $10^{-6} \text{ S cm}^{-1}$ at 39% rH up to $10^{-1} \text{ S cm}^{-1}$

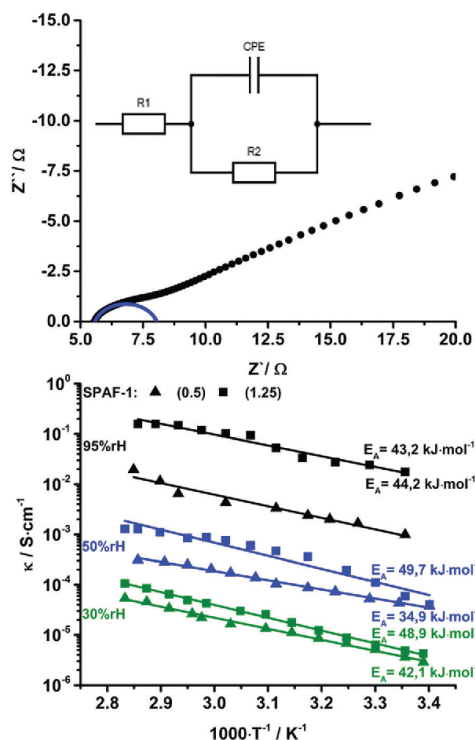


Fig. 3 Top: Nyquist plot for SPAF-1(1.25) at 80 °C and 95% rH fitted with the depicted equivalent circuit. Bottom: Conductivities of SPAF-1(0.5) and SPAF-1(1.25) at 30, 50 and 100% rH in a temperature range from 20 to 80 °C. E_A represent the respective activation energies.

at 95% rH. Notably, for the lowest rH of 30%, κ is similar for both materials, while for 95% rH SPAF-1(1.25) outperforms SPAF-1(0.5) by one order of magnitude. Notably, the conductivity of SPAF-1(1.25) exceeds the one for SPAF-1(0.5) for all rH, which we attribute to the higher degree of sulfonation and thus higher charge carrier density. For SPAF-1(1.25), we obtained conductivities up to $1.6 \times 10^{-1} \text{ S cm}^{-1}$ at 80 °C and 95% rH.

Second, κ roughly doubles for both sulfonation degrees between 20 and 80 °C and all rH. This corresponds to an activation barrier between 35 and 50 kJ mol^{-1} . As mentioned before, for the lowest rH, we expect that only the micropores are filled with water molecules while at 95% rH, water is also stored in mesopores reactivated by the swelling. The fact, that κ strongly depends on the water uptake but at the same time the activation energy E_A , as calculated from the Arrhenius plots (Fig. 3, bottom), remains similar, is in line with the above mentioned results from EDX and DSC experiments, ruling out microphase separation. In case of a continuous porosity with distributed micro- and mesopores filled with water upon hydration, the limiting process for the proton conduction is the transport through the micropores for which we expect a vehicle mechanism due to the relatively large activation barrier.

In summary, we showed that for the adamantane structured porous aromatic framework (PAF-1), the gas phase sulfonation (SPAF-1(1.25)) is superior to conventional liquid phase sulfonation (SPAF-1(0.5)). The former process allows to sulfonate every aromatic ring, thereby increasing the number of covalently bonded $\text{-SO}_3\text{H}$ groups by more than a factor of two. Both networks are highly hydrophilic with λ values of 8 and 13 for SPAF-1(0.5) and SPAF-1(1.25) at 95% rH, respectively. Depending on the rH the water molecules are either incorporated solely within the micropores (<50%) of the frameworks or in the reactivated mesoporous voids. Based on the protonation of water molecules by the acidic polymer backbone, a high charge carrier density was obtained, making both systems good proton conductors. The gas-phase sulfonated polymer with the higher charge carrier density exhibits conductivities κ as high as $1.6 \times 10^{-1} \text{ S cm}^{-1}$ at 80 °C and 95% rH, leading to a performance comparable to state of the art materials like Nafion. κ strongly depends on the water uptake, while E_A (30–50 kJ mol^{-1}) remains nearly constant, independent of where the water is adsorbed – either in the micropores or the mesopores. This is possible only, if the micro- and mesoporous regions are distributed homogeneously within the network, and the proton conduction is mediated through both. Our results show that already at low hydration states, where only the micropores are filled with water, SPAF-1 is a good proton conductor. Due to the stronger host-guest interactions compared to water in microphase regions like in Nafion, SPAF-1 might be used at even higher temperatures than 80 °C, which will make it very attractive for fuel cell applications. Further studies, to determine the upper temperature limit and the respective conductivity are currently underway.

We gratefully acknowledge financial support from the German Research Foundation for the projects SE 1417/7-1 and SFB840. The authors thank Dr Renée Siegel and Beate Bojer for performing solid-state NMR spectroscopic measurements and Dr Ulrike Lacher for performing mass spectrometry experiments. We gratefully thank Prof. Josef Brey for access to physisorption instruments and Prof. Rhett Kempe for access to CHN-analytics. Also we thank Dr Beate Förster from Bavarian Polymer Institute (BPI) Keylab for Electron and Optical Microscopy for SEM images and EDS measurements.

References

- 1 A. Alaswad, A. Baroutaji, H. Achour, J. Carton, A. Al Makky and A. G. Olabi, *Int. J. Hydrogen Energy*, 2016, **41**, 16499–16508.
- 2 J.-H. Wee, *Renewable Sustainable Energy Rev.*, 2007, **11**, 1720–1738.
- 3 K. A. Mauritz and R. B. Moore, *Chem. Rev.*, 2004, **104**, 4535–4586.
- 4 C. H. Park, C. H. Lee, J.-Y. Sohn, H. B. Park, M. D. Guiver and Y. M. Lee, *J. Phys. Chem. B*, 2010, **114**, 12036–12045.
- 5 Z. Taherkhani, M. Abdollahi and A. Sharif, *J. Electrochem. Soc.*, 2015, **162**, F1096–F1100.
- 6 S. J. Paddison, *Annu. Rev. Mater. Res.*, 2003, **33**, 289–319.
- 7 P. Ramaswamy, N. E. Wong and G. K. H. Shimizu, *Chem. Soc. Rev.*, 2014, **43**, 5913–5932.
- 8 S. Horike, D. Umeyama and S. Kitagawa, *Acc. Chem. Res.*, 2013, **46**, 2376–2384.
- 9 M. Sadakiyo, T. Yamada and H. Kitagawa, *Chempluschem*, 2016, **81**, 691–701.
- 10 W. J. Phang, H. Jo, W. R. Lee, J. H. Song, K. Yoo, B. Kim and C. S. Hong, *Angew. Chem., Int. Ed.*, 2015, **54**, 5142–5146.
- 11 K. Kreuer, *Solid State Ionics*, 1997, **97**, 1–15.
- 12 G. Zhu and H. Ren, *Porous Organic Frameworks*, Springer Berlin Heidelberg, Berlin, Heidelberg, 2015.
- 13 S. Das, P. Heasman, T. Ben and S. Qiu, *Chem. Rev.*, 2017, **117**, 1515–1563.
- 14 S. Chandra, T. Kundu, S. Kandambeth, R. Babarao, Y. Marathe, S. M. Kunjir and R. Banerjee, *J. Am. Chem. Soc.*, 2014, **136**, 6570–6573.
- 15 R. Banerjee, D. B. Shinde, H. B. Aiyappa, M. Bhadra, B. Biswal, S. Kandambeth, B. Garai, T. Kundu, P. N. Wadge and S. Kurungot, *J. Mater. Chem. A*, 2016, **4**, 2682–2690.
- 16 F.-M. Zhang, L.-Z. Dong, J.-S. Qin, W. Guan, J. Liu, S.-L. Li, M. Lu, Y.-Q. Lan, Z.-M. Su and H.-C. Zhou, *J. Am. Chem. Soc.*, 2017, **139**, 6183–6189.
- 17 H. Xu, S. Tao and D. Jiang, *Nat. Mater.*, 2016, **15**, 722–726.
- 18 Y. Ye, L. Zhang, Q. Peng, G.-E. Wang, Y. Shen, Z. Li, L. Wang, X. Ma, Q.-H. Chen, Z. Zhang and S. Xiang, *J. Am. Chem. Soc.*, 2015, **137**, 913–918.
- 19 T. Ben, H. Ren, S. Ma, D. Cao, J. Lan, X. Jing, W. Wang, J. Xu, F. Deng, J. M. Simmons, S. Qiu and G. Zhu, *Angew. Chem., Int. Ed.*, 2009, **48**, 9457–9460.
- 20 W. Lu, D. Yuan, J. Sculley, D. Zhao, R. Krishna and H.-C. Zhou, *J. Am. Chem. Soc.*, 2011, **133**, 18126–18129.
- 21 W. Lu, W. M. Verdegaal, J. Yu, P. B. Balbuena, H.-K. Jeong and H.-C. Zhou, *Energy Environ. Sci.*, 2013, **6**, 3559.
- 22 W. Lu, J. P. Sculley, D. Yuan, R. Krishna and H.-C. Zhou, *J. Phys. Chem. C*, 2013, **117**, 4057–4061.
- 23 S. Lee, G. Barin, C. M. Ackerman, A. Muchenditsi, J. Xu, J. A. Reimer, S. Lutsenko, J. R. Long and C. J. Chang, *J. Am. Chem. Soc.*, 2016, **138**, 7603–7609.
- 24 Z.-H. Hei, M.-H. Huang, Y. Luo and Y. Wang, *Polym. Chem.*, 2016, **7**, 770–774.
- 25 W. Lu, D. Yuan, D. Zhao, C. I. Schilling, O. Plietzsch, T. Müller, S. Bräse, J. Guenther, J. Blümel, R. Krishna, Z. Li and H.-C. Zhou, *Chem. Mater.*, 2010, **22**, 5964–5972.
- 26 G. Y. Gor, M. Thommes, K. A. Cychosz and A. V. Neimark, *Carbon N. Y.*, 2012, **50**, 1583–1590.
- 27 Z. Wang, W. Xu, T. Song, Z. Guo, L. Liu, Y. Fan, A. Wang and Z. Zhang, *Arch. Pharm.*, 2017, **350**, e1600251.
- 28 A. Kusoglu, M. A. Modestino, A. Hexemer, R. A. Segalman and A. Z. Weber, *ACS Macro Lett.*, 2012, **1**, 33–36.
- 29 G. S. Hwang, M. Kaviany, J. T. Gostick, B. Kientz, A. Z. Weber and M. H. Kim, *Polym.*, 2011, **52**, 2584–2593.
- 30 S. Kittaka, S. Takahara, H. Matsumoto, Y. Wada, T. J. Satoh and T. Yamaguchi, *J. Chem. Phys.*, 2013, **138**, 204714.
- 31 N. Walsby, S. Hietala, S. L. Maunu, F. Sundholm, T. Kallio and G. Sundholm, *J. Appl. Polym. Sci.*, 2002, **86**, 33–42.
- 32 A. Lasia, *Electrochemical Impedance Spectroscopy and Its Applications*, Springer New York, New York, NY, 2014.
- 33 R. Yadav and P. S. Fedkiw, *J. Electrochem. Soc.*, 2012, **159**, B340.

Supporting Information towards:

**Water mediated Proton Conduction in a Sulfonated Microporous
Organic Polymer**

C. Klumpen^a, S. Gödrich^b, G. Papastavrou^b, J. Senker^{a*}

^aUniversity of Bayreuth, Inorganic Chemistry III, Universitätsstraße 30, 95447 Bayreuth, Germany

^bUniversity of Bayreuth, Physical Chemistry II, Universitätsstraße 30, 95447 Bayreuth, Germany

Tables of Content

1. Experimental Section	3
1.1 General Information	3
1.2 Synthesis	6
1.2.1 Chemicals	6
1.2.2 Tetraphenylmethane ^[2]	6
1.2.3 Tetrakis(4-bromophenyl)methane ^[3]	7
1.2.4 PAF-1 ^[4]	8
1.2.5 SPAF-1(0.5) ^[4]	8
1.2.6 SPAF-1(1.25).....	9
2. Analytical Section	10
2.1 Linker analytics	10
2.1.1 Liquid NMR.....	10
2.1.1.1 ¹ H Tetraphenylmethane	10
2.1.1.2 ¹³ C Tetraphenylmethane	10
2.1.1.3 ¹ H Tetrakis(4-bromophenyl)methane	11
2.1.1.4 ¹³ C Tetrakis(4-bromophenyl)methane.....	11
2.1.2 Infrared spectroscopy	12
2.1.3 CHN-Analysis.....	12
2.1.3.1 Tetraphenylmethane	12
2.1.3.2 Tetrakis(4-bromophenyl)methane.....	13
2.2 Polymer analytics.....	13
2.2.1 Solid state NMR.....	13
2.2.1.1 ¹³ C_PAF-1.....	13
2.2.1.2 ¹³ C_SPAF-10.5.....	15

2.2.1.3 ¹³ C_SPAF-1(1.25)	15
2.2.2 Infrared spectroscopy	16
2.2.3 CHN-Analysis.....	16
2.2.3.1 PAF-1	16
2.2.3.2 SPAF-1(0.5).....	17
2.2.3.3 SPAF-1(1.25).....	17
2.2.4 Gas adsorption analysis – N ₂ at 77K.....	17
2.2.4.1 PAF-1	17
2.2.4.2 SPAF-1(0.5).....	18
2.2.4.3 SPAF-1(1.25).....	19
2.2.5 Gas adsorption analysis – CO ₂ at 273 K	20
2.2.5.1 PAF-1	20
2.2.5.2 SPAF-1(0.5).....	21
2.2.5.3 SPAF-1(1.25).....	21
2.2.5.4 Summary of gas sorption analysis	21
2.2.6 TGA analysis	22
2.2.6.1 Stability.....	22
2.2.6.2 Water Uptake	22
2.2.7 UV-Vis spectroscopy	23
2.2.8 Powder X-ray diffraction.....	23
2.2.9 Impedance spectroscopy.....	24
2.2.9.1 PAF-1(0.5).....	24
50 % rH (K ₂ CO ₃):.....	24
30 % rH (H ₃ C ₂ OOK):	25
2.2.9.2 SPAF-1(1.25).....	26
50 % rH (K ₂ CO ₃):.....	26
30 % rH (H ₃ C ₂ OOK):	27
2.2.10 Differential scanning calorimetry	28
2.2.11 Energy dispersive X-ray spectroscopy.....	29
2.2.12 Atomic force microscopy	30
3. Literature	31

1. Experimental Section

1.1 General Information

Nitrogen sorption measurements were carried out on a Quantachrome Autosorb-1 pore analyzer at 77 K. The data were analyzed using the ASIQ v 3.0 software package. Pore size distributions were calculated with methods of quasistationary density functional theory (QSDFT). CO₂ adsorption isotherms were measured on a Quantachrome Nova surface analyzer at 273 K. Based on these, calculations of the specific surface area, pore volumes and pore size distributions were carried out using the nonlocal density functional theory (NLDFT) slit-pore model for carbon materials. For the N₂-based isotherms, the N₂ at 77 K on Carbon (slit/cylindr. pores QSDFT adsorption branch) kernel was used. All polymers were degassed at 150 °C for 12 h before starting the sorption experiments.

¹H and ¹³C liquid-NMR spectra of the linker molecules were collected on a Bruker 500 MHz spectrometer using DMSO as solvent. For infrared spectra (IR) a JASCO FT/IR-6100 Fourier transform infrared spectrometer with an attenuated total reflectance (ATR) unit was used. CHN analysis was carried out at a vario EL-III with acetanilide as standard (Measured: C [71.09], H [6.71], N [10.36]. Calcd: C [71.09], H [6.71], N [10.36]). Mass spectrometry (MS) was performed at a Finnigan MAT-8500-spectrometer with an ionization energy of 70 eV. Thermogravimetric analysis (TGA) was carried out on a Mettler Toledo TGA/SDTA851^e under air. Powder X-ray diffraction (PXRD) measurements were performed on a PANalytical X'Pert Pro diffractometer. Here, a region from 2 to 30° 2θ was measured with a 1/4 antiscatter slit and Cu K_α radiation (nickel filtered). For the titration experiments a *Mettler Toledo* pH meter has been used with an aqueous NaOH solution as reference. UV-Vis experiments were performed on a *Varian Cary 300 Scan* UV-Visible spectrometer using an Ulbricht sphere.

All solid-state NMR spectra were acquired on a Bruker Avance III HD spectrometer operating at a B₀ field of 9.4 T. ¹³C (δ = 100.6 MHz) MAS spectra were obtained with ramped cross-polarization (CP) experiments where the nutation frequency ν_{nut} on the proton channel was varied linearly from 70 – 100 %. The samples were spun at 12.5 kHz (¹³C) in a 4 mm MAS double resonance probe (Bruker). The corresponding ν_{nut} on the ¹³C channel and the contact time were adjusted to 70 kHz and 3.0 ms, respectively. Proton broadband decoupling with *spinal-64* and $\nu_{\text{nut}} = 12.5$ kHz was applied during acquisition.^[1] ¹³C spectra are referenced with respect to TMS (tetramethylsilane) using the secondary standard adamantane. Quantitative single pulse experiments were carried out with a 90° pulse with a length of 3.70 μs and a recycle delay of 120 s.

For EDX measurements the sample was prepared as is on a stub with double sided sticky carbon tape and then coated with 20 nm carbon using a Leica EM ACE600 carbon coater. The EDS analysis was performed in a FEI Quanta FEG 250 Scanning Electron Microscope (SEM) under low vacuum conditions (45 Pa) with a SDD detector from Thermo Fisher Scientific applying an accelerating voltage of 5 kV. (Images were taken with a Large Field Detector (LFD) for secondary electrons and a Concentric Back Scattered Detector (CBS) for backscattered electrons.) To exclude microphase separation within the polymers at high relative humidities, we exchanged the hydrogens of the $-\text{SO}_3\text{H}$ units with sodium. Therefore, the material was stirred in saturated NaCl solution for 24 h including an exchange of the salt solution. The material was then dried in vacuo at 100 °C for 12 h and sputtered with carbon before performing the EDX experiment. For a phase separating material we expected concentrated regions for sodium due to an eased access into the network.

The crystallization temperatures of the sample were determined using a Mettler Toledo DSC/SDTA 821e DSC with autosampler. The measurements were performed over a temperature range of -80 °C - 120 °C at a heating/cooling rate of 2 °C/min under nitrogen atmosphere. Prior measurements, SPAF-1(1.25) was saturated at 30 % and 100 % rH for 24 hours, respectively.

Atomic force microscopy measurements were performed on a SPAF-1(1.25)-pellet, which was prepared from moist SPAF-1(1.25)-powder using a hand-held pill press. The sample was directly measured on the copper block of the press, which was placed in a petri-dish filled with water in order to prevent the sample from drying. The sample was imaged using tapping mode in air on Dimension ICON (Bruker) with a OTESPA-R3 cantilever (Olympus). Height images (Figure S27 left) at different sample spots show a granular morphology of the compressed powder material.

Impedance spectroscopy was carried out on a Zahner (Z) Emium potentiostat with an applied perturbation voltage of 10 mV. An impedance data set was created measuring the frequency range from from 1 MHz to 100 mHz. To ensure the shape and size of the pellet remains equal during the whole measuring procedure, the material was placed into a cylindrical bordering. The resulting pellets were placed between two copper electrodes and stored under defined humidity, obtained by saturated salt solutions, at 20 °C for 24 h (Table S1). To ensure equilibration before the measurements, an equilibration time of 30 minutes was included into the measurement protocol. After performing the measurements the length (l) and radius (r)

($A=r^2 \cdot \pi$) of the pellet have been taken and the conductivity was calculated using following equation:

$$\kappa = \frac{l}{(A \cdot R2)}$$

Were the resistance (R) was taken from the high frequency semicircle in the appropriate Nyquist plot (Cole-Cole plot), which has been fitted with an optimized Randles-Cell (Figure 3, top) using Zview (Scribner).

Table S1: Saturated salt solutions to obtain a defined relative humidity during EIS and TGA analysis.

Salt	Relative Humidity / %
vacuum	0
$K^+(H_3C_2O_2)^-$	30
K_2CO_3	50
$NaNO_3$	70
KCl	80
H_2O	100

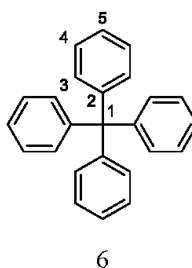
1.2 Synthesis

All chemicals were purchased at *Sigma-Aldrich Chemistry GmbH*, *VWR Chemicals*, *TCI* or *Grüssing* and, if not mentioned otherwise, were used without further purification (Tab. S2). All polymerizations were carried out under argon atmosphere in dry vessels. DMF and THF were purchased as technical reagents and purified via distillation.

1.2.1 Chemicals

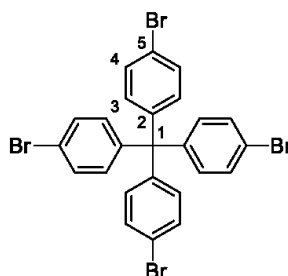
Table S2: List of chemicals used for this publication, their purities and distributor.

Chemical	Company	Purity
Aniline	Sigma Aldrich	>99.5 %
Brom	Sigma Aldrich	99.99 %
Chlorosulfonic acid	Merck-Millipore	-
2,5-Cyclooctadien	Sigma Aldrich	> 99 %
Dichloromethan	VWR-Chemicals	99.9 %
Dimethylformamide	VWR-Chemicals	>99.8 %
Ethanol	VWR-Chemicals	>96 %
Isopentylnitrite	Sigma Aldrich	96 %
Ni(cod) ₂	Sigma Aldrich	-
Phosphinic acid sol.	Sigma Aldrich	50 wt % in H ₂ O
Sulfuric acid fuming	Merck-Millipore	65 % SO ₃
Tetrahydrofuran	VWR-Chemicals	-
Triphenylchloromethane		
K ₂ CO ₃	Sigma Aldrich	97%
NaNO ₃	Sigma Aldrich	> 99 %
KCl	Sigma Aldrich	> 99 %
H ₃ C ₂ OOK	Sigma Aldrich	> 99 %
Sulfuric acid fuming	Merck-Millipore	65 % SO ₃

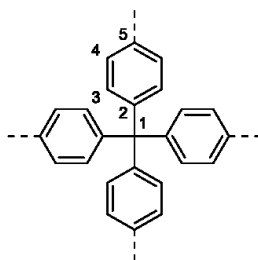
1.2.2 Tetraphenylmethane^[2]

15 g of trityl chloride (0.054 mol, 1 eq.) and 14.05 ml aniline (0.154 mol, 2.9 eq.) were heated up to 180 °C in a round flask with magnetic stirrer and condenser, until the reaction mixture turned into a violet solid. The heating process was extended for 10 more minutes. The solid was cooled down, crushed and resuspended in 75 ml MeOH and 75 ml 2 M HCl. The Suspension was refluxed for 30 min., filtered and washed with water. After resuspending in ethanol the reaction mixture was cooled down to -30 °C and 15.75 ml sulfuric acid and 9.44 g of isopentyl nitrite (0.081 mol, 1.5 eq.) were added under vigorous stirring. After stirring for 1 h at -10 °C, 26.9 ml of phosphinic acid (0.609 mol, 11 eq.) were added slowly and the reaction mixture was refluxed for 1.5 h. After cooling down, the solid was filtered, washed with DMF, H₂O and Ethanol and subsequently dried *in vacuo* to get a light brown powder. Further purification was not necessary but could be done by recrystallization in THF/methanol (1:1). Yield: 16.1 g (0.05 mol, 93 %). ¹H-NMR (500 MHz, DMSO-D₆): δ [ppm] = 7.30 (t, 1H, H-4), 7.21 (t, 1H, H-5), 7.15 (d, 1H, H-3) (Fig. S3). ¹³C-NMR (500 MHz, DMSO-D₆): δ [ppm] = 146.88 (C-2), 130.94 (C-3), 128.19 (C-4), 126.44 (C-5) (Fig. S4). EA [%]: C [91.25], H [6.54], N [0.18]; Calc.: C [93.71], H [6.29], N [0.00]. MS [M/z] = 243, 320, 165. IR (ATR): ν [cm⁻¹] = 1590, 1490, 1181, 1072, 1034, 767, 750, 696, 629, 491 (Fig. S7).

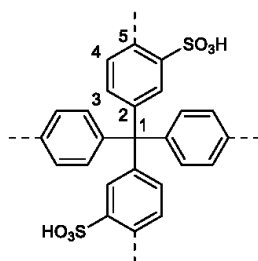
1.2.3 Tetrakis(4-bromophenyl)methane^[3]



In a three necked vessel with magnetic stirrer, thermometer and condenser 10 g tetraphenylmethane (31.2 mmol, 1 eq.) were cooled in an ice bath. Now 99.75 g Br₂ (624 mmol, 20 eq.) were added dropwise. After cooling towards -78 °C, 140 ethanol (4.5 ml/mmol) were applied and the mixture was allowed to reach room temperature overnight. Now sodiumdisulfide solution was added until the end of precipitation. The resulting solid was filtered, washed with H₂O and dried in an oven at 110 °C. Further purification was carried out performing recrystallization in a chloroform/ethanol mixture (1:1) to get a light brown solid. Yield: 12.9 g (20.28 mmol, 65 %). ¹H-NMR (500 MHz, DMSO-D₆): δ [ppm] = 7.53 (d, 2H, H-4), 7.06 (d, 2H, H-3) (Fig. S5). ¹³C-NMR (500 MHz, DMSO-D₆): δ [ppm] = 63.66 (C-1), 120.40 (C-5), 131.55 (C-3), 132.86 (C-4), 145.06 (C-2) (Fig. S6). EA [%]: C [46.09], H [2.13]; Calc.: C [47.21], H [2.54]. MS [M/z] = 279, 239, 636, 319, 555, 198. IR (ATR): ν [cm⁻¹] = 1569, 1486, 1393, 1181, 1072, 1005, 951, 908, 808, 750, 528, 507 (Fig. S7).

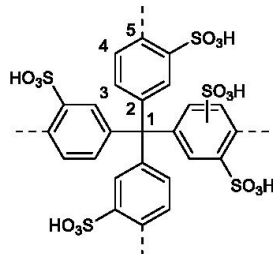
1.2.4 PAF-1^[4]

80 ml DMF_{dry} (21 ml/mmol), 1.14 g 2,2-bipyridiyl (7.29 mmol, 1 eq.), 2 g Ni(cod)₂ (7.27 mmol, 1 eq.), 0.8 ml cyclooctadiene (8.4 mmol, 1.2 eq.), 80 ml THF_{dry} (21 ml/mmol) and 1.16 g tetrakis(4-bromophenyl)methane (1.82 mmol, 0.22 eq.) were placed in a dry vessel under Ar and stirred for 9 h at room temperature. The mixture was cooled to 0 °C and 50 mL 6 M HCl were added dropwise and stirred overnight (13 h). The resulting solid was filtered, washed with MeOH. Further purification was done via a soxhlett apparatus with MeOH/THF (1:1) for 5 h. Yield: 0.458 g (1.45 mmol; 80 %). ¹³C NMR (CP-MAS, 12.5 kHz): δ [ppm] = 64.6 (C-1), 125.3 (C-3), 139, 34 (C-5), 145.9 (C-2) (Fig. S8). EA [%]: C [92.17], H [5.738], N [0.632]; Calc.: C [94.9], H [5.1], N [0.00]. IR (ATR): ν [cm⁻¹] = 3079, 3059, 3031, 1601, 1547, 1482, 1439, 1395, 1265, 1189, 1113, 1069, 1037, 1004, 961, 917, 839, 748, 701, 650, 630, 524 (Fig. S11).

1.2.5 SPAF-1(0.5)^[4]

100 mg ($3.16 \cdot 10^{-4}$ mol, 1 eq.) PAF-1 were suspended in 50 ml dichloromethane and cooled down to 0 °C. After dropwise addition of 0.11 ml ($1.58 \cdot 10^{-3}$ mol, 5 eq) chlorosulfonic acid, the suspension was stirred for 3 days at room temperature. The mixture was poured into ice and the solid was filtered, washed with H₂O and dried in vacuum to obtain a violet powder. Yield: 0.124 g ($2.60 \cdot 10^{-4}$ mol, >82 %). ¹³C NMR (CP-MAS, 12.5 kHz): δ [ppm] = 149-143 (2,5), 141-135 (3'), 132-126 (3,4,5'), 64 (1) (Fig. S9). EA [%]: C [65.47], H [4.45], N [0.47]; Calc.: C [63.01], H [3.38], N [0.00]. IR (ATR): ν [cm⁻¹] = 3500-2500, 3032, 2919, 2855, 1682, 1596, 1578, 1486, 1356, 1283, 1176, 1130, 1096, 1037, 1001, 898, 815, 745, 711, 606, 562, 539 (Fig. S11).

1.2.6 SPAF-1(1.25)



100 mg ($3.16 \cdot 10^{-4}$ mol, 1 eq.) of PAF-1 were activated at 150 °C in vacuum for 2 h. Now fuming sulfuric acid (65 % SO_3) was applied via gas phase for 10 minutes (Figure SNumber). The resulting solid was dried in vacuum at 150 °C for 1 h to yield a deep purple powder. Yield: 235 mg ($3.28 \cdot 10^{-4}$ mol, >99 %). ^{13}C NMR (CP-MAS, 12.5 kHz): δ [ppm] = 65.8 (C-1), 123.5 (C-6), 130, 3 (C-7), 147.8 (C-2/4) (Fig. S10). EA [%]: C [41.31], H [3.71], N [0.53]; Calc.: C [41.90], H [2.25], N [0.00]. IR (ATR): ν [cm^{-1}] = 3500-2500, 1687, 1589, 1489, 1468, 1468, 1354, 1291, 1266, 1169, 1127, 1090, 1039, 1001, 938, 888, 825, 750, 712, 556, 507, 457 (Fig. S11).

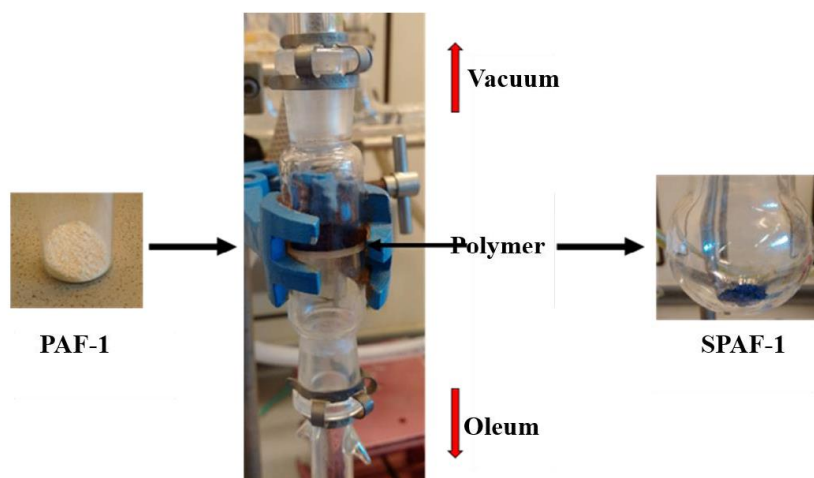


Figure S1: Schematic presentation of the gas phase sulfonation concept.

2. Analytical Section

2.1 Linker analytics

2.1.1 Liquid NMR

2.1.1.1 ^1H Tetraphenylmethane

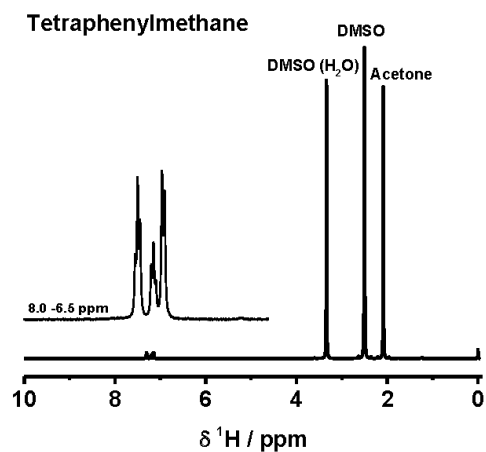


Figure S2: ^1H liquid NMR spectra of Tetraphenylmethane.

2.1.1.2 ^{13}C Tetraphenylmethane

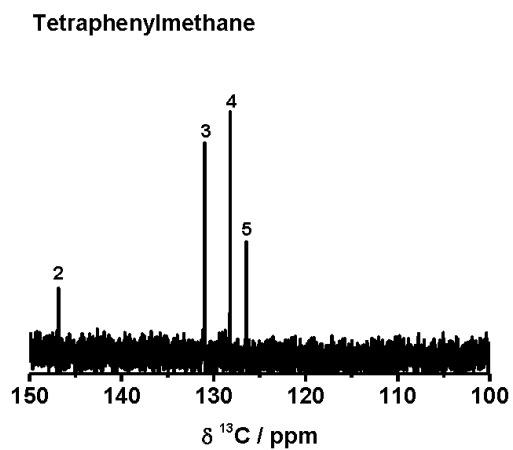


Figure S3: ^{13}C liquid NMR spectra of Tetraphenylmethane.

2.1.1.3 ^1H Tetrakis(4-bromophenyl)methane

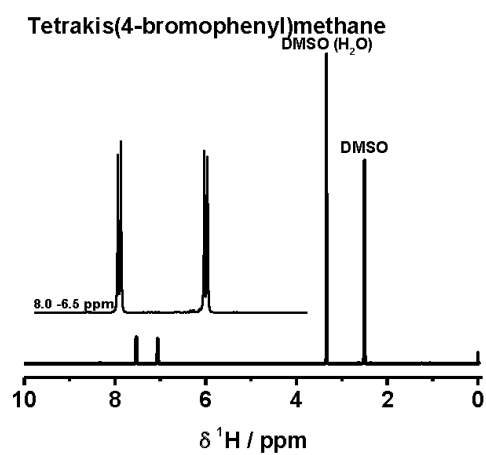


Figure S4: ^1H NMR spectra of Tetrakis(4-bromophenyl)methane.

2.1.1.4 ^{13}C Tetrakis(4-bromophenyl)methane

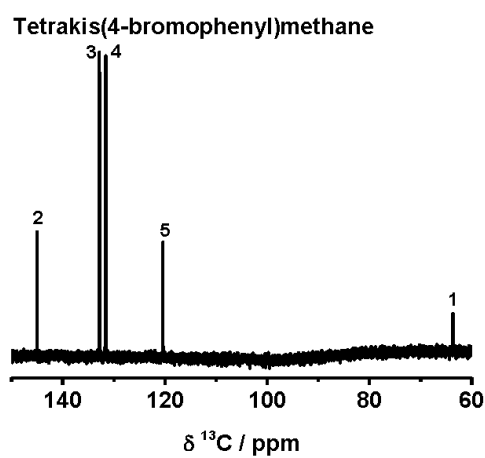


Figure S5: ^{13}C NMR spectrum of Tetrakis(4-bromophenyl)methane.

2.1.2 Infrared spectroscopy

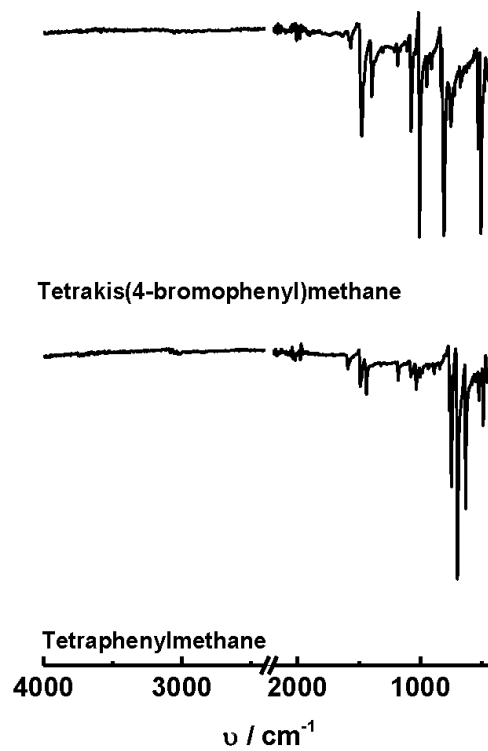


Figure S6: Infrared spectra of tetraphenylmethane and tetrakis(4-bromophenyl)methane.

2.1.3 CHN-Analysis

2.1.3.1 Tetraphenylmethane

Table S3: Results from CHN-analysis of tetraphenylmethane.

TPM	C [%]	H [%]	N [%]
Meas.	91.25	6.544	0.18
Calc.	93.71	6.29	0
Aberration	2.46	0.25	0.18

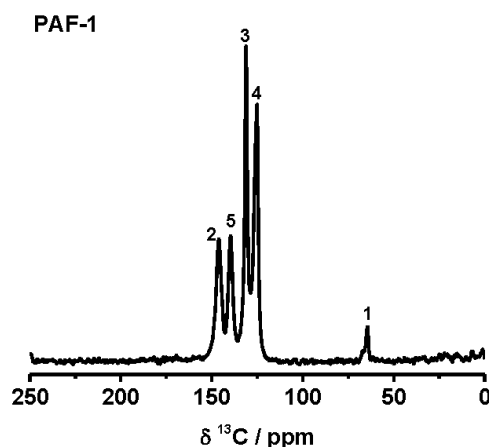
2.1.3.2 Tetrakis(4-bromophenyl)methane

Table S4: Results from CHN-analysis of tetrakis(4-bromophenyl)methane.

TBPM	C	H	N
Meas.	46.09	2	0.08
Calc.	47.21	2.54	0
Aberration	1.12	0.41	0.08

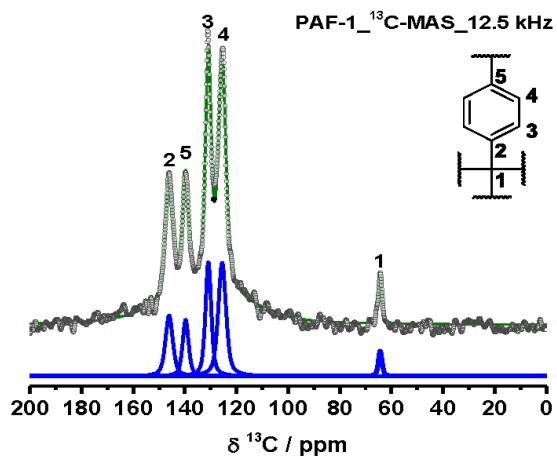
2.2 Polymer analytics

2.2.1 Solid state NMR

2.2.1.1 ^{13}C _PAF-1Figure S7: ^{13}C CP MAS NMR spectrum of PAF-1.

Calculation of the crosslinking degree for PAF-1

The resonances of a quantitative MAS single pulse ^{13}C spectrum (Figure S8) were deconvoluted using a pseudo-Voigt lineshape with a 1:1 ratio for the Gaussian and Lorentzian components. For 100 % crosslinking the intensity of C-5 (I(C-5)) should equal that of C2 (I(C-2)). Based on the reaction mechanism of the used Yamamoto coupling, in case of an incomplete turnover we expect either C-Br moieties (if no reaction occurred) or C-H moieties (if no CC coupling occurred). Both signals are predicted to have ^{13}C chemical shifts around 125 ppm (C-H) and 122 ppm (C-Br). Both resonances are thus superimposed with the signal for C4 and no additional signals are expected. As a consequence, while I(C-5) reduces, I(C-4) is increased. At the same time, I(C-2) should remain unaffected. Thus the intensity ratio I(C-5):I(C-2) estimated to 0.76(10) is a measure for the degree of crosslinking within the network.

Figure S8: ¹³C MAS onepulse NMR spectrum of PAF-1 for quantitative analysis.Table 5: Fit parameter derived from the Gauss/Lorentz model based deconvolution of the ¹³C MAS onepulse spectrum of PAF-1 with an overlap of 95.17 %.

Sites	2	5	3	4	1
$\delta(\text{iso}) / \text{ppm}$	146.19	139.8	130.9	125.7	64.5
LB / Hz	253.74	203.6	197.8	265.8	124.0
xG/(1-x)L	0.5	0.5	0.5	0.5	0.5
Integral	4.9	3.7	7.2	9.6	1

2.2.1.2 ^{13}C _SPAF-10.5

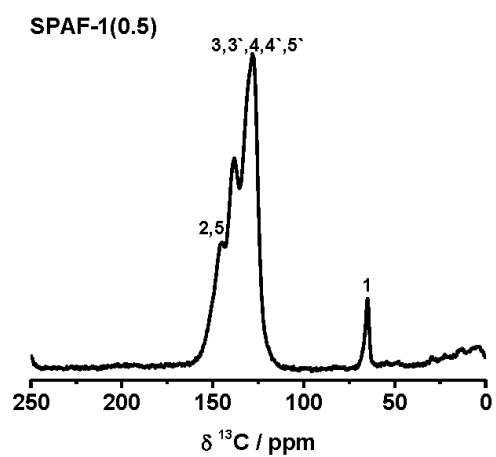


Figure S9: ^{13}C spectrum of SPAF-1(0.5).

2.2.1.3 ^{13}C _SPAF-1(1.25)

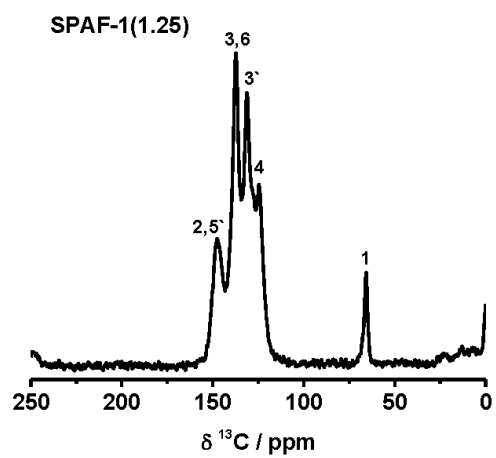


Figure S10: ^{13}C spectrum of SPAF-1(1.25).

2.2.2 Infrared spectroscopy

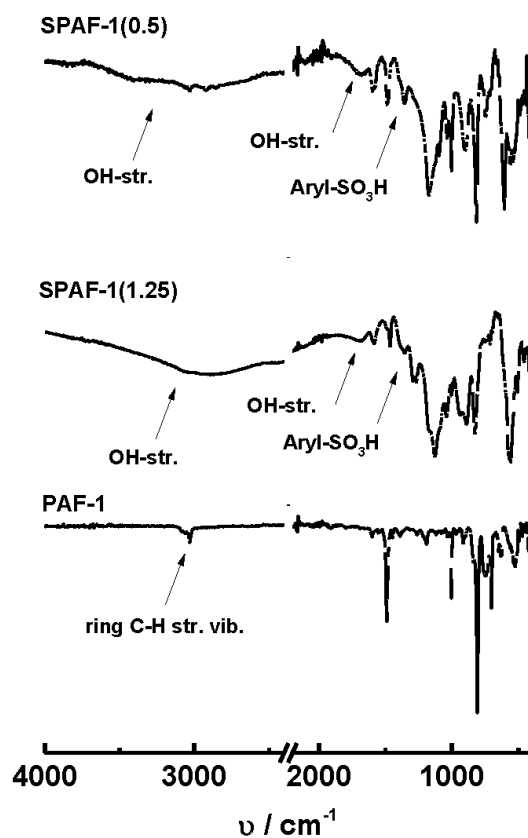


Figure S11: Infrared spectra of PAF-1, SPAF-1(0.5) and SPAF-1(1.25).

2.2.3 CHN-Analysis

2.2.3.1 PAF-1

Table S6: Results from CHN-analysis of PAF-1.

Polymer	C / %	H / %	N / %
PAF-1 _{calc.}	94.90	5.10	0.00
PAF-1 _{meas.}	92.17	5.74	0.63
Deviation	2.73	0.64	0.63

2.2.3.2 SPAF-1(0.5)

Table S7: Results from CHN-analysis of SPAF-1(0.5).

Polymer	C / %	H / %	N / %
SPAF-1(0.5) _{calc}	63.01	3.38	0.00
SPAF-1(0.5) _{meas}	65.47	4.45	0.47
Deviation	2.46	1.07	0.47

2.2.3.3 SPAF-1(1.25)

Table S8: Results from CHN-analysis of SPAF-1(1.25).

Polymer	C / %	H / %	N / %
SPAF-1(1.25) _{calc}	41.9	2.25	0.00
SPAF-1(1.25) _{meas}	41.31	3.71	0.53
Deviation	0.59	1.46	0.53

2.2.4 Gas adsorption analysis – N₂ at 77K

2.2.4.1 PAF-1

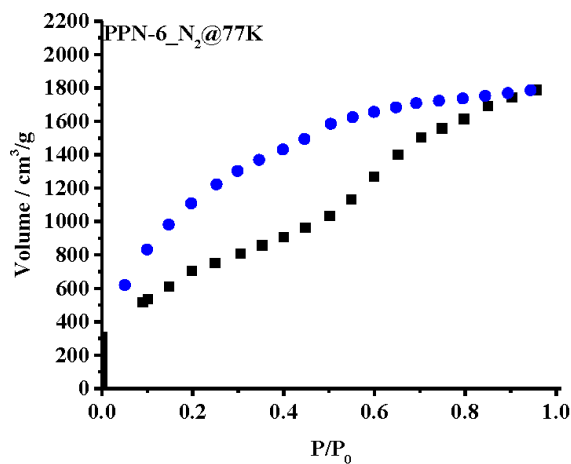


Figure S12: Adsorption isotherm of PAF-1 measured with N₂ at 77 K.

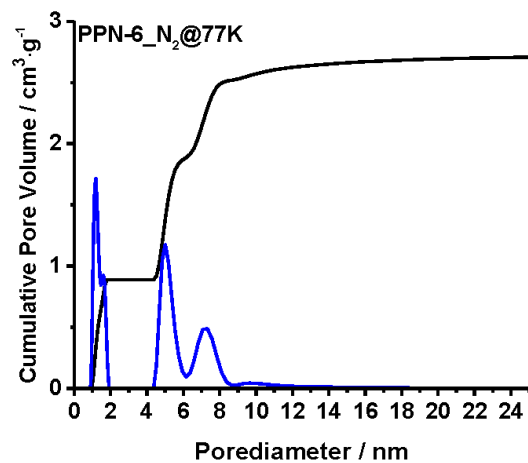


Figure S13: Pore size distribution of PAF-1, calculated from the N₂ at 77 K adsorption isotherm using slit/cylindrical pore QSDFT adsorption branch model.

2.2.4.2 SPAF-1(0.5)

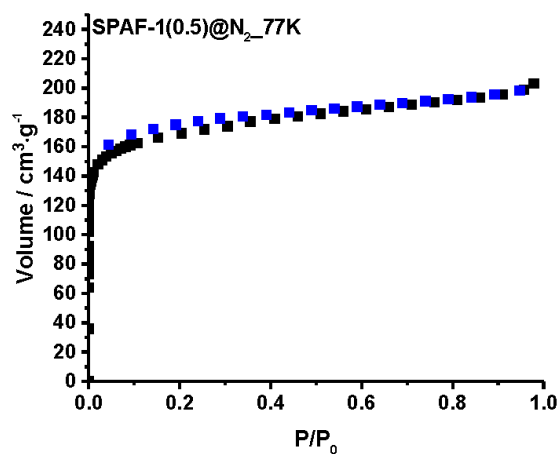


Figure S14: Adsorption isotherm of PAF-1-SO₃H_{solv} measured with N₂ at 77 K.

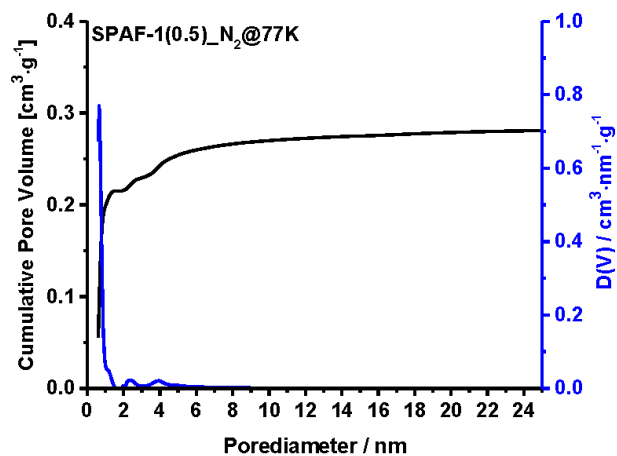


Figure S15: Pore size distribution of SPAF-1(0.5) calculated from the N₂ at 77 K adsorption isotherm using slit/cylindrical pore QSDFT adsorption branch model.

2.2.4.3 SPAF-1(1.25)

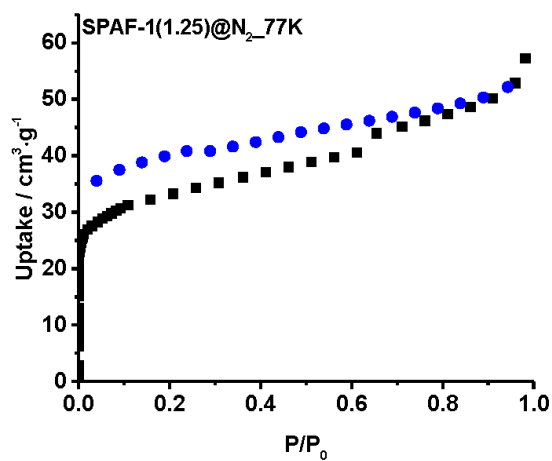


Figure S16: Adsorption isotherm of SPAF-1(1.25) measured with N₂ at 77 K.

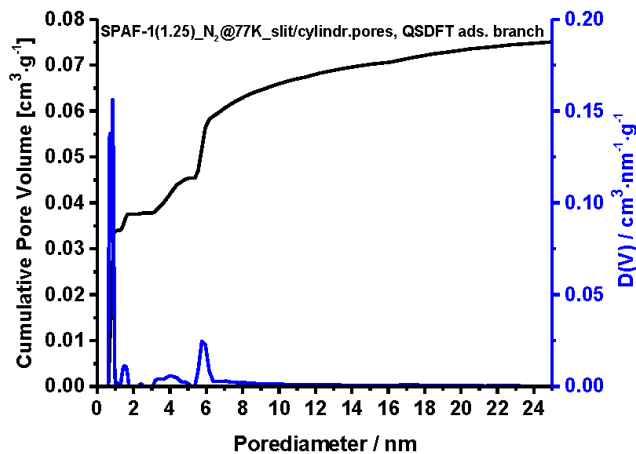


Figure S17: Pore size distribution of SPAF-1(1.25), calculated from the N₂ at 77 K adsorption isotherm using slit/cylindrical pore QSDFT adsorption branch model.

2.2.5 Gas adsorption analysis – CO₂ at 273 K

2.2.5.1 PAF-1

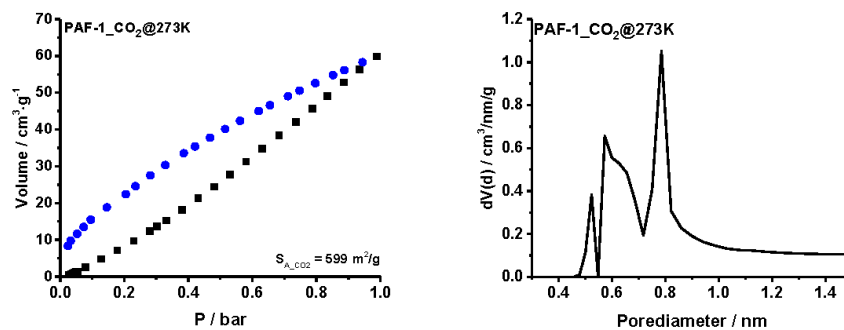


Figure S18: CO₂ Isotherm (left) and pore size distribution (right) of PAF-1. PSD was calculated using CO₂ at 273 K on Carbon NLDFT model.

2.2.5.2 SPAF-1(0.5)

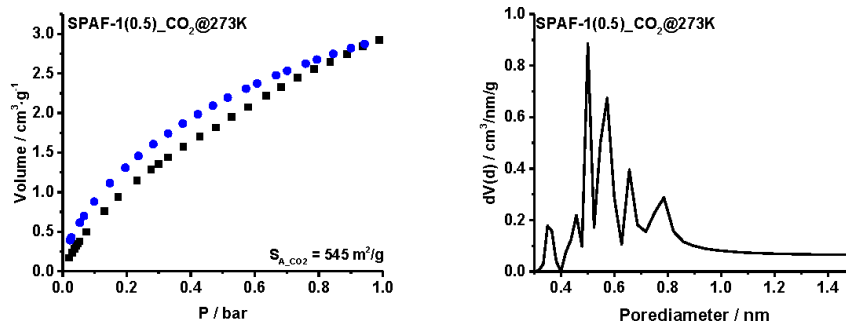


Figure S19: CO₂ Isotherm (left) and pore size distribution (right) of PAF-1-SO₃H_{sol}. PSD was calculated using CO₂ at 273 K on Carbon NLDFT model.

2.2.5.3 SPAF-1(1.25)

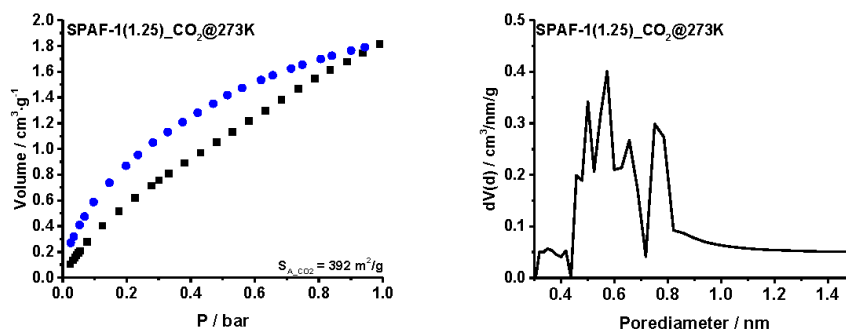


Figure S20: CO₂ Isotherm (left) and pore size distribution (right) of SPAF-1(1.25). PSD was calculated using CO₂ at 273 K on Carbon NLDFT model.

2.2.5.4 Summary of gas sorption analysis

Table S9: Data calculated from N₂ isotherms at 77 K and CO₂ isotherms at 273 K. For calculation the respective BET or DFT kernels were used.

Polymer	$S_{A,BET-N_2} / m^2 \cdot g^{-1}$	$S_{A,DFT-N_2} / m^2 \cdot g^{-1}$	$P_{V,N_2} / cm^3 \cdot g^{-1}$	$P_{V,mic} / P_{V,tot}$	$S_{A,DFT-CO_2} / m^2 \cdot g^{-1}$	$P_{V,CO_2} / cm^3 \cdot g^{-1}$
PAF-1	2625	2043	2.68	0.33	599	0.234
SPAF-1(0.5)	650	670	0.29	0.75	545	0.177
SPAF-1(1.25)	123	115	0.08	0.47	392	0.132

2.2.6 TGA analysis

2.2.6.1 Stability

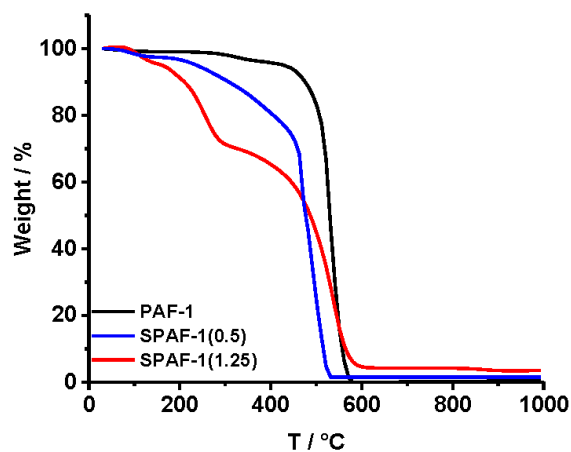


Figure S21: Thermogravimetric data from PAF-1, SPAF-1(1.25) and SPAF-1(0.5), respectively. All Curves were measured under air with a 10 °C / min temperature ramp.

2.2.6.2 Water Uptake

Table S10: Water uptake versus theoretical pore volume for SPAF-1(0.5) and SPAF-1(1.25).

Polymer	Uptake _{H₂O} @100%rH	P _{V_theoretical} ^{N₂}	Uptk. _{H₂O} /P _{V_theo.}
SPAF-1(0.5)	0.65 cm ³ ·g ⁻¹	0.47 cm ³ ·g ⁻¹	1.38
SPAF-1(1.25)	1.68 cm ³ ·g ⁻¹	0.21 cm ³ ·g ⁻¹	8

2.2.7 UV-Vis spectroscopy

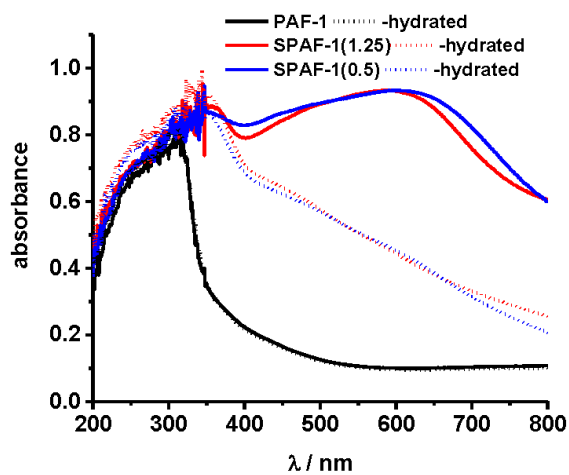


Figure S22: UV-VIS spectra of PAF-1, SPAF-1(1.25) and SPAF-1(0.5), respectively. Full lines show the absorbance of the polymers in the dry state, dashed lines stand for fully hydrated state.

2.2.8 Powder X-ray diffraction

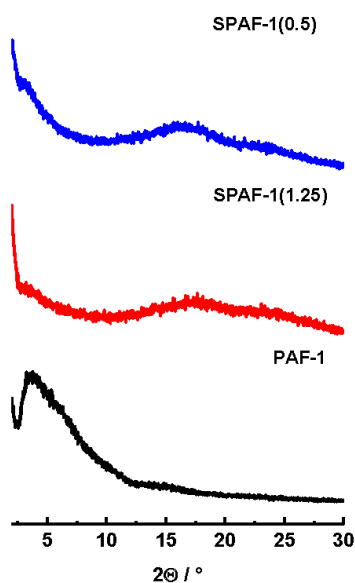


Figure S23: PXRDS of PAF-1, SPAF-1(1.25) and SPAF-1(0.5).

2.2.9 Impedance spectroscopy

2.2.9.1 PAF-1(0.5)

100% rH (H₂O):

Table S11: Temperature dependent resistance and conductivity values of SPAF-1(0.5) at 100 % rH taken from the related Nyquist plots. The data was calculated based on a pellet with $l = 0.25$ cm and $r = 0.4$ cm.

T / °C	T / K	R₂ / Ω	κ / S·cm⁻¹
25	298	505.1	0.00098
33	306	299.1	0.00166
38	311	248	0.00201
42	315	208.3	0.00239
48	321	149.4	0.00333
58	331	115	0.00433
68	341	76.82	0.00648
72	345	43.11	0.01154
78	351	25.42	0.01957

50 % rH (K₂CO₃):

Table S12: Temperature dependent resistance and conductivity values of SPAF-1(0.5) at 50 % rH taken from the related Nyquist plots. The data was calculated based on a pellet with $l = 0.19$ cm and $r = 0.4$ cm.

T / °C	T / K	R₂ / Ω	κ / S·cm⁻¹
22	295	10052	$3.76 \cdot 10^{-5}$
25	298	8707	$4.34 \cdot 10^{-5}$
32	305	7232	$5.23 \cdot 10^{-5}$
37	310	5191	$7.28 \cdot 10^{-5}$
42	315	4340	$8.71 \cdot 10^{-5}$
47	320	3635	$1.04 \cdot 10^{-4}$
52	325	2732	$1.38 \cdot 10^{-4}$
57	330	2198	$1.72 \cdot 10^{-4}$

60	333	1850	$2.04 \cdot 10^{-4}$
68	341	1513	$2.49 \cdot 10^{-4}$
71	344	1341	$2.82 \cdot 10^{-4}$
77	350	1214	$3.11 \cdot 10^{-4}$

30 % rH (H₃C₂OOK):

Table S13: Temperature dependent resistance and conductivity values of SPAF-1(0.5) at 30 % rH taken from the related Nyquist plots. The data was calculated based on a pellet with $l = 0.2$ cm and $r = 0.4$ cm.

T / °C	T / K	R₂ / Ω	κ / S·cm⁻¹
22	295	138830	$2.87 \cdot 10^{-6}$
25	298	110690	$3.59 \cdot 10^{-6}$
30	303	77582	$5.13 \cdot 10^{-6}$
35	308	58635	$6.79 \cdot 10^{-6}$
40	313	46654	$8.53 \cdot 10^{-6}$
45	318	35636	$1.12 \cdot 10^{-5}$
50	323	29521	$1.35 \cdot 10^{-5}$
57	330	24057	$1.65 \cdot 10^{-5}$
63	336	18073	$2.20 \cdot 10^{-5}$
65	338	14929	$2.67 \cdot 10^{-5}$
70	343	11757	$3.38 \cdot 10^{-5}$
75	348	8648	$4.60 \cdot 10^{-5}$
80	353	7375	$5.40 \cdot 10^{-5}$

2.2.9.2 SPAF-1(1.25)

100% rH (H₂O):

Table S14: Temperature dependent resistance and conductivity values of SPAF-1(1.25) taken from the related Nyquist plots. The data was calculated based on a pellet with $l = 0.2$ cm and $r = 0.4$ cm.

T / °C	T / K	R₂ / Ω	κ / S·cm⁻¹
25	298	16.9	0.018
31	304	12.3	0.024
37	310	10.8	0.028
43	316	8.9	0.034
48	321	5.6	0.053
53	326	4.3	0.094
58	331	3.9	0.103
63	336	3.4	0.118
68	341	2.7	0.148
73	346	2.5	0.157
77	350	2.5	0.157

50 % rH (K₂CO₃):

Table S15: Temperature dependent resistance and conductivity values of SPAF-1(0.5) at 50 % rH taken from the related Nyquist plots. The data was calculated based on a pellet with $l = 0.2$ cm and $r = 0.4$ cm.

T / °C	T / K	R₂ / Ω	κ / S·cm⁻¹
21	294	12269	$4.05 \cdot 10^{-5}$
25	298	8378	$5.94 \cdot 10^{-5}$
30	303	4473	$1.11 \cdot 10^{-4}$
35	308	2545	$1.95 \cdot 10^{-4}$
42	315	1384	$3.59 \cdot 10^{-4}$
48	321	1066	$4.67 \cdot 10^{-4}$
53	326	829	$5.99 \cdot 10^{-4}$

58	331	654	$7.60 \cdot 10^{-4}$
62	335	564	$8.82 \cdot 10^{-4}$
66	339	590	$8.43 \cdot 10^{-4}$
72	345	450	0.00111
77	350	389	0.00128
80	353	386	0.00129

30 % rH (H₃C₂OOK):

Table S16: Temperature dependent resistance and conductivity values of SPAF-1(0.5) at 30 % rH taken from the related Nyquist plots. The data was calculated based on a pellet with $l = 0.18$ cm and $r = 0.4$ cm.

T / °C	T / K	R₂ / Ω	κ / S·cm⁻¹
22	295	84342	$4.24 \cdot 10^{-6}$
25	298	73798	$4.85 \cdot 10^{-6}$
30	303	56344	$6.35 \cdot 10^{-6}$
35	308	40898	$8.77 \cdot 10^{-6}$
40	313	29112	$1.23 \cdot 10^{-5}$
45	318	20231	$1.77 \cdot 10^{-5}$
50	323	13869	$2.58 \cdot 10^{-5}$
55	328	11939	$2.99 \cdot 10^{-5}$
62	335	8364	$4.28 \cdot 10^{-5}$
66	339	7245	$4.94 \cdot 10^{-5}$
70	343	5509	$6.49 \cdot 10^{-5}$
75	348	4221	$8.48 \cdot 10^{-5}$
80	353	3366	$1.06 \cdot 10^{-4}$

2.2.10 Differential scanning calorimetry

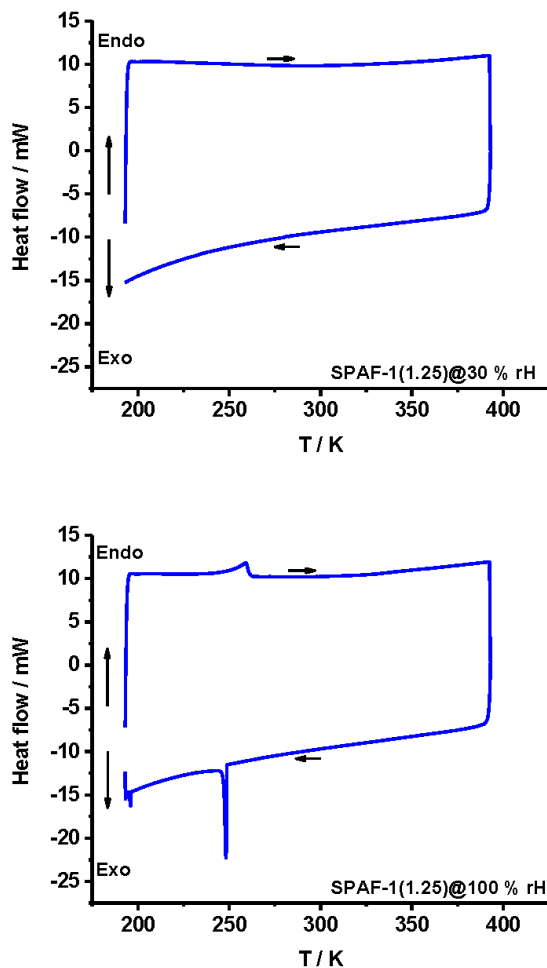


Figure S24: DSC curves for SPAF-1(1.25) hydrated at 30 % (top) and 100 % rH (bottom).

For SPAF-1(1.25) saturated for 100 %rH (Figure S24 bottom) an endothermic melting peak at around -25 °C with an area equivalent to 0.35 J was observed. With a melting enthalpy (ΔH_m) for water of 333.5 J/g, this corresponds to 0.06 mmol water. In contrast, TG measurements revealed a total amount of 0.23 mmol water to be adsorbed within the network. Thus, only 25 % of the incorporated water is stored in mesopores, while 85 % is located in micropores.

2.2.11 Energy dispersive X-ray spectroscopy

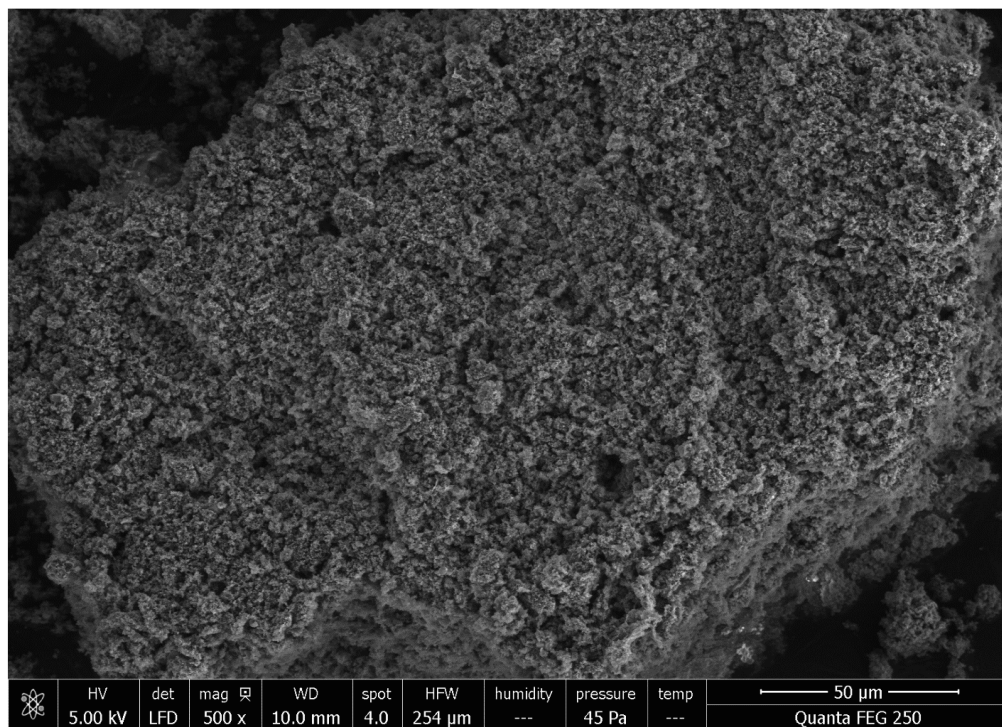


Figure S25: REM image of Na-SPAF-1(1.25).

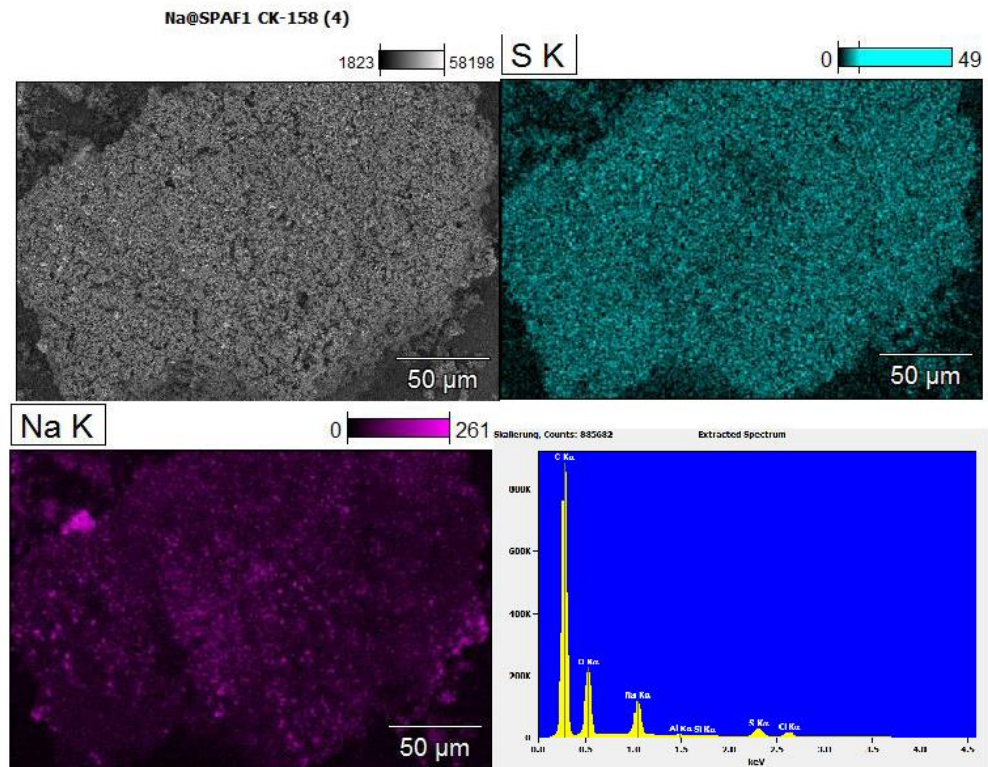
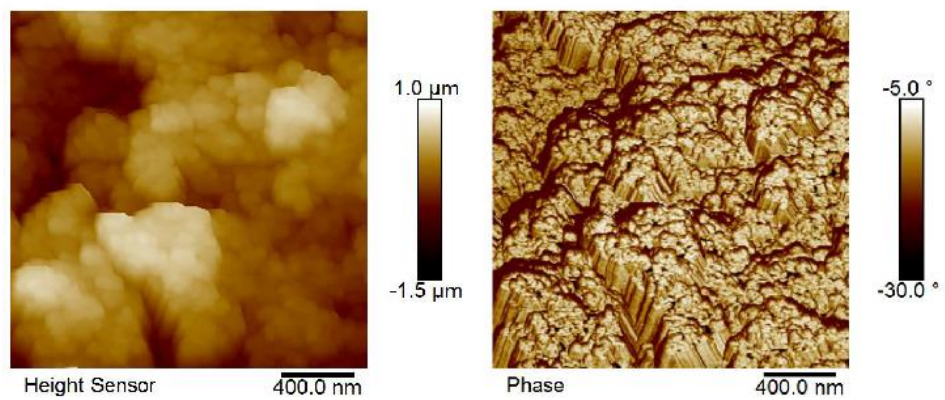


Figure S26: EDX spectra of Na-SPAF-1(1.25) without coloration, blue colored sulfur distribution, violet colored sodium distribution.

2.2.12 Atomic force microscopy



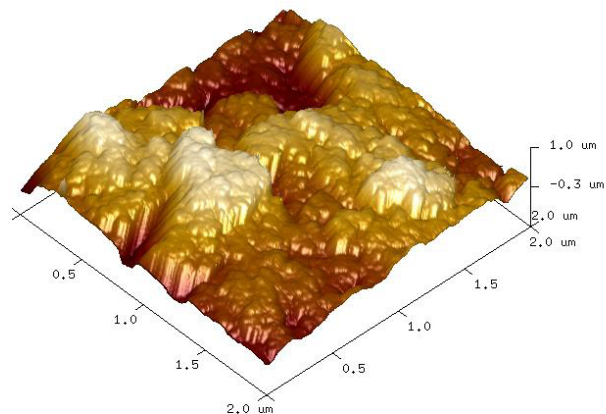


Figure S27: Height image (top, left) and corresponding phase image (top, right) as well as 3D surface mapping (bottom) of a pelletized (SPAF-1.25) sample, derived from AFM measurements.

3. Literature

- [1] B. M. Fung, A. K. Khitrin, K. Ermolaev, *J. Magn. Reson.* **2000**, *142*, 97–101.
- [2] W. Lu, D. Yuan, D. Zhao, C. I. Schilling, O. Plietzsch, T. Muller, S. Bräse, J. Guenther, J. Blümel, R. Krishna, et al., *Chem. Mater.* **2010**, *22*, 5964–5972.
- [3] Y. He, S. Xiang, B. Chen, *J. Am. Chem. Soc.* **2011**, *133*, 14570–3.
- [4] W. Lu, D. Yuan, J. Sculley, D. Zhao, R. Krishna, H.-C. Zhou, *J. Am. Chem. Soc.* **2011**, *133*, 18126–9.
- [5] S. Kittaka, S. Takahara, H. Matsumoto, Y. Wada, T. J. Satoh, T. Yamaguchi, *J. Chem. Phys.* **2013**, *138*, 204714.
- [6] N. Walsby, S. Hietala, S. L. Maunu, F. Sundholm, T. Kallio, G. Sundholm, *J. Appl. Polym. Sci.* **2002**, *86*, 33–42.

5.4 Anhydrous Proton Conduction in Porous Organic Networks

Das Manuskript wurde in Zusammenarbeit mit dem Lehrstuhl für Physikalische Chemie II der Universität Bayreuth, Prof. Dr. G. Papastavrou, durchgeführt. Die Veröffentlichung wurde bei der Fachzeitschrift *Journal of Materials Chemistry A* eingereicht und angenommen. Die Beiträge der Autoren sind wie folgt:

Christoph Klumpen

- ⇒ Projektplanung und Durchführung
- ⇒ Synthesen und Charakterisierung der Verbindungen
- ⇒ Durchführung und Auswertung der Gassorptionsanalytik
- ⇒ Durchführung und Auswertung der impedanzspektroskopischen Analytik
- ⇒ Auswertung des Gesamtdatensatzes
- ⇒ Planung und Aufsetzen des Manuskripts

Simon Winterstein

- ⇒ Synthese der Verbindungen

Georg Papastavrou

- ⇒ Design des Manuskripts

Jürgen Senker

- ⇒ Projektplanung und Supervision
- ⇒ Planung und Aufsetzen des Manuskripts



Journal Name

ARTICLE

Anhydrous proton conduction in porous organic networks

C. Klumpen,^a S. Winterstein,^a G. Papastavrou^b and J. Senker^{a,*}Received 00th January 20xx,
Accepted 00th January 20xx

DOI: 10.1039/x0xx00000x

www.rsc.org/

Solid electrolyte separators within fuel cells enable efficient charge transport and prevent mass bypass between the two half cells. Hydrated systems, like Nafion, reach unprecedented proton conductivities at ambient temperatures, but the demanding humidity management prevents their use beyond 80 °C, hence limiting the efficiency of nowadays polymer-based systems. As such, water free and chemically inert, solid materials with excellent conductivities between 100 °C and 200 °C, are of high interest. A promising approach is the incorporation of heavier amphoteric molecules into micro- and mesoporous frameworks. Stronger host-guest interactions allow for higher temperatures, while still maintaining sufficient mobility and efficient transport pathways. Here, we present a systematic study investigating the influence of porosity, framework topology and dimensionality as well as framework functionality and charge carrier uptake on the proton conductivity for six porous organic networks (PONs) loaded with imidazole via gas phase adsorption. The resulting materials were thoroughly characterized by multinuclear NMR and IR spectroscopy, physisorption as well as powder X-ray diffraction and DSC experiments, revealing a homogeneous distribution of the amphoteric guests within the pore structure. Electrochemical impedance spectroscopy up to 130 °C revealed remarkable conductivities of up to 10⁻³ S·cm⁻¹ under anhydrous conditions. We found 3D networks to favour high imidazole loading leading to high proton conductivities based on the Grotthuss mechanism. In contrast, 2D networks showed lower guest molecule uptake and thus lower proton conductivities, which were governed by vehicle transport. Additional acid/base functionalities within the frameworks seem to have a negative effect on the proton conduction.

Introduction

With respect to the challenges of global warming and an increasing world's population, fuel cell (FC) technology is among the most promising solution for future energy supply as it provides an efficient and environmentally friendly process.¹ By converting chemical energy into electricity, fuel cells operating on H₂ are detached from fossil fuels and thus avoid disadvantageous flue gas (e.g. CO₂, NO_x or SO_x) as well as sonic pollution.² The heart of a fuel cell setup is the membrane-electrode-assembly (MEA), which consists of an electro-catalyst and an electrolyte membrane. While the catalyst is responsible for the chemical reactions occurring at the anode and cathode of the system, the membrane acts as electrode separator and proton conductor.² Due to the harsh electrochemical environment within a FC system and a broad range of potential applications, special requirements, like physicochemical or electrochemical stability, are required for the development of novel membrane materials.³

Despite of its nearly 40-year-old history, the perfluorosulfonic acid Nafion® is still state of the art for FC membranes and one of the few materials, which were utilized in commercial products. Nafion

provides excellent proton conductivity and exhibits a long lifetime upon operational conditions. However, the high costs of Nafion (~700 USD/m²), its demanding humidity management and the problematical waste disposal of fluorinated polymers instigate the development of new materials.^{2,4} Besides, the still rare materials with intrinsic proton conductivity⁷ a promising approach towards anhydrous proton conduction is the substitution of water with other solvents like concentrated acids and amphoteric heterocycles. While these, provide properties like autoprotolysis and creation of long range hydrogen bond networks, they are prone to early evaporation.⁵ For both cases, operating temperatures beyond 100 °C will increase the ion mobility, decouple the system from a complex water management, and preserve the catalysts from CO-poisoning.^{3,8,9} However, to comply with this special condition, materials of high electrochemical and thermal stability are needed. Among all the possible candidates, porous organic networks (PONs) are a promising, yet hardly considered class of materials. Recently, PONs have been of major interest for gas sorption and separation technology as well as for photo- and electrocatalysis due to their high physicochemical stability, diverse structures and permanent porosity.¹⁰⁻¹⁴ The potential to entrap conductive species in the pores of such frameworks, using physisorptive interactions with the pore walls would prevent the leakage of the incorporated guests, ensure a long term persistence and thus a permanent conductivity.

^a University of Bayreuth, Inorganic Chemistry III, Universitätsstraße 30, 95440 Bayreuth, Germany.

^b University of Bayreuth, Physical Chemistry II, Universitätsstraße 30, 95440 Bayreuth, Germany.

† Footnotes relating to the title and/or authors should appear here.

Electronic Supplementary Information (ESI) available: [details of any supplementary information available should be included here]. See DOI: 10.1039/x0xx00000x

Please do not adjust margins

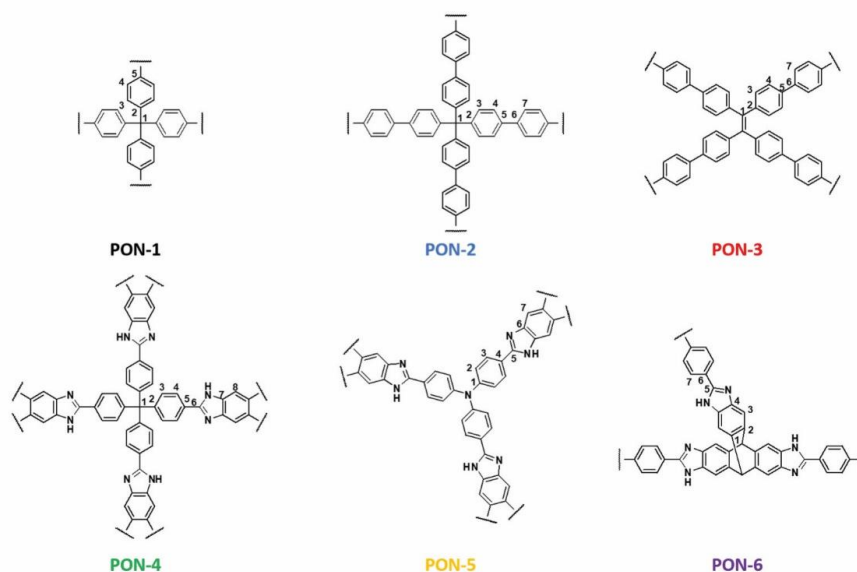


Fig. 1: Schematic presentation of the utilized porous organic networks. The assignments correspond to the ones in the ^{13}C and ^{15}N NMR spectra.

In recent publications the incorporation of amphoteric molecules like imidazole^{15,16} and triazole¹⁵ into the pores of a framework proved to be a successful approach towards anhydrous proton conduction in PONs. In this respect, Jiang and coworkers presented proton conductivities of $4.73 \cdot 10^{-3} \text{ S} \cdot \text{cm}^{-1}$ and $1.1 \cdot 10^{-3} \text{ S} \cdot \text{cm}^{-1}$ at 130°C under nitrogen by incorporating imidazole and triazole in the covalent organic framework TPB-TMTP.³ In another study, Xiang *et al.* incorporated imidazole in the mesoporous polyimides Td-PNDI 1 and Td-PPI, and found reasonable conductivities in a temperature range from -40 to 90°C with top values of $9.04 \cdot 10^{-5} \text{ S} \cdot \text{cm}^{-1}$ and $3.49 \cdot 10^{-4} \text{ S} \cdot \text{cm}^{-1}$ at 90°C and anhydrous conditions, respectively.¹⁶ Here, we report the synthesis and proton conductivity of six different porous organic networks (Fig. 1) and their post-synthetic modification by incorporation of imidazole. Although, the structures have been described previously, to our knowledge, they never have been investigated systematically with respect to their proton conductivity. We probed the conductivity as function of composition and topology for purely carbon-hydrogen networks and benzimidazole based polymers^{9,17} and thus were able to vary morphology, porosity and functionality of the networks. The networks were thoroughly characterized by ^{13}C and ^{15}N nuclear magnetic resonance (NMR) spectroscopy, infrared (IR) spectroscopy, powder X-ray diffraction (PXRD), thermogravimetric analysis (TGA) as well as argon physisorption. After incorporation of imidazole, the proton conductivity was investigated by electrochemical impedance spectroscopy in a temperature range from 90 to 130°C under nitrogen atmosphere.

Experimental

General Information

Argon sorption measurements were carried out on a Quantachrome Autosorb-1 pore analyzer at 87.3 K . The data were analyzed using the ASIQ v 3.0 software package. Surface areas were estimated by BET-method, while for pore sizes the *Gurvich* method was used. Pore size distributions were calculated with methods of quasistationary density functional theory (QSDFT). With respect to the network morphology, we used either a QSDFT kernel for cylindrical/sphere pores (3D polymers) or a QSDFT kernel for cylindrical pores (2D polymers) to estimate the pore size distribution of the respective materials. All polymers were degassed at 150°C for 12 h before starting the sorption experiments.

^1H and ^{13}C liquid-NMR spectra of the linker molecules were collected on a Bruker 500 MHz spectrometer using DMSO-d_6 as solvent. For infrared spectra (IR) a JASCO FT/IR-6100 Fourier transform infrared spectrometer with an attenuated total reflectance (ATR) unit was used. Thermogravimetric analysis (TGA) was carried out on a Mettler Toledo TGA/SDTA851^e under air. Powder X-ray diffraction (PXRD) measurements were performed on a PANalytical X'Pert Pro diffractometer. Here, a region from 2 to $30^\circ 2\theta$ was measured with a $1/4$ anticatter slit and $\text{Cu K}\alpha$ radiation (nickel filtered).

All solid-state NMR spectra were acquired on a Bruker Avance III HD spectrometer operating at a B_0 field of 9.4 T . ^{13}C ($\nu_0 = 100.6 \text{ MHz}$) MAS spectra were obtained with ramped cross-polarization (CP) experiments where the nutation frequency ν_{nut} on the proton channel was varied linearly from $70 - 100\%$. The samples were spun at 12.5 kHz (^{13}C) and 10.0 kHz (^{15}N) in a 4 mm MAS double resonance

Please do not adjust margins

probe (Bruker). The corresponding v_{nut} of the $^{13}\text{C}/^{15}\text{N}$ channels and the contact times were adjusted to 70/35 kHz and 3.0/5.0 ms, respectively. In all cases proton broadband decoupling with spinal-64 and $v_{\text{nut}} = 75$ kHz was applied during acquisition. ^{13}C spectra are referenced with respect to TMS (tetramethylsilane) using the secondary standard adamantane. ^{15}N spectra are referenced with respect to CH_3NO_2 using the secondary standard glycine. Differential Scanning microscopy was performed on a Mettler Toledo DSC/SDTA 821e DSC with an auto sampler. The measurements were performed over a temperature range from 25 °C to 200 °C at a heating/cooling rate of 5 °C/min under nitrogen atmosphere. The measuring routine was cycled three times to ensure the samples persistence.

Impedance spectroscopy was carried out on a Zahner (Z)Ennium potentiostat with an applied perturbation voltage of 50 mV with respect to the preserved response signal. Impedance data sets were acquired by measuring the frequency range from 1 MHz to 1 Hz at a temperature range of 90 °C to 130 °C. To ensure the shape and size of the pellet remained constant throughout the whole measuring process, the material was placed into a cylindrical glass encasement with an inner diameter of 8 mm between the two copper electrodes. The powder was then compressed by screwing the upper electrode tightly against the lower electrode with a force of 0.7 kN corresponding to a pressure of about 130 bar during the experiments. The thickness resulting pellets was determined after the measurements and is given in Tabs. S2-S7 in the supporting information. The loaded cell was handled under dry nitrogen atmosphere. To ensure equilibration before the measurements, an equilibration time of 30 minutes for each temperature step was included into the data acquisition protocol. After performing the measurements, length (l) and radius (r) ($A=r^2\pi$) of the pellet were used to calculate the conductivity using the following equation:

$$\kappa = \frac{l}{(A \cdot R1)}$$

Where the resistance ($R1$) was taken from the high frequency semicircle in the appropriate Nyquist plot (Cole-Cole plot), which has been fitted with an equivalence circuit using the Zview software package (Scribner).

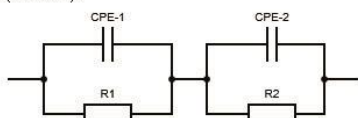


Fig. 2: Equivalent circuit used to fit the obtained results pictured in the respective Nyquist plots.

Experimental Section

All chemicals were purchased from either Sigma-Aldrich Chemistry GmbH, VWR Chemicals, TCI, or Grüssing GmbH and were, if not mentioned otherwise, used without further purification. The organic solvents were dried by distillation in accordance with standard procedure. All synthetic procedures as well as the apparatus for imidazole loading via the gas phase (Fig. S25) are given in the supplementary information.

Results and Discussion

Synthesis and Characterization

All polymers and linker molecules were synthesized by literature known procedures, which are provided in the electronic supplementary information (ESI). Both synthesis and characterisation were done repeatedly to ensure the reproducibility of the results. We observed only minor variations for recorded materials properties. PON-1 – PON-3, originally synthesized by the groups of Ben¹⁹, Kaskel²⁰ and Han²¹, were derived using metal-organic coupling procedures of the Yamamoto and Suzuki type, respectively. PON-4 – PON-6, first reported by the groups of El-Kaderi^{22,23} and Senker²⁴, were synthesized using a condensation reaction of diamines and aldehydes to the respective benzimidazole linked compounds.²⁵ Structural characterisation of the networks was done by solid-state NMR- and IR spectroscopy, as well as PXRD, CHN and TG analysis. The assignments for the respective resonances is given in Fig. 3. In the ^{13}C solid-state CP MAS NMR spectra, for PON-1, PON-2 and PON-4 the tetrahedral carbon signal at 65 ppm (C-1) is most characteristic (Fig. 3a). For PON-4 – PON-6, the ^{13}C signals around 100 ppm as well as the ^{15}N signals at -147 ppm and -238 ppm indicate the formation of the benzimidazole bridging unit. For PON-5 an additional signal at -278 ppm was found in the ^{15}N NMR spectrum, which was assigned to the central amino group of the aldehyde linker.²⁴ The absence of $\text{C}_{\text{ar}}\text{-Br}$ (PON-1, PON-2, PON-3) signals expected at 119 ppm and R-CHO (PON-4, PON-5, PON-6) signals expected at 194 ppm in the ^{13}C spectrum as well as the one for NH_3^+ (PON-4, PON-5, PON-6) at -330 ppm in the ^{15}N spectrum indicate a full conversion of the linker molecules and, therefore, a high crosslinking degree for all polymers (Fig. 3). The results are supported by infrared spectroscopy, which revealed for PON-1 – PON-3 vibrational bands at 3030 cm^{-1} (C-H_{str.vib.}), 1066 cm^{-1} (C-C_{vib.}) and 800 cm^{-1} (1,4 subst. benzenes) (Fig. S27). For PON-4, PON-5 and PON-6, the formation of the benzimidazole bridging units results in stretching vibrations around 3380 cm^{-1} (N-H) and 1595 cm^{-1} (C=N), respectively (Fig. S27). The value of the CHN analysis further determines the structural integrity, as they fit well to the calculated ones (ESI). However, for PON-2 and PON-3, some deviations occurred, which we attribute to remaining impurities of the catalyst. Morphology and thermal stability were characterized by PXRD and TGA measurements under air, respectively. The former indicated that all polymers were amorphous (Fig. S31). The latter proved the polymers to be temperature stable up to temperatures between 430 °C (PON-3) and 525 °C (PON-2) (Fig. S29). The consistently high thermal stabilities are attributed to the carbon and carbon-nitrogen based polymer backbones, which form strong and persistent networks. Notably, for the benzimidazole containing polymers a small weight loss around 100 °C was observed. Given that the networks are hydrophilic due to their inherent functionality, we attribute this to an incorporation of water molecules upon sample preparation.²⁴

The surface area and porosity of the networks was determined from argon physisorption isotherms measured at 87 K. The surface area was calculated using the optimized BET equation for microporous compounds.²⁶ The pore volumes were estimated by the Gurvich method.²⁷ Further information about pore size and distribution was calculated based on QSDFT adsorption branch kernels for carbon materials, which for three dimensional networks account to mixed pores of cylindrical and spherical shape (Fig. 4). For two dimensional networks, however, we used a kernel which accounts solely to

Please do not adjust margins

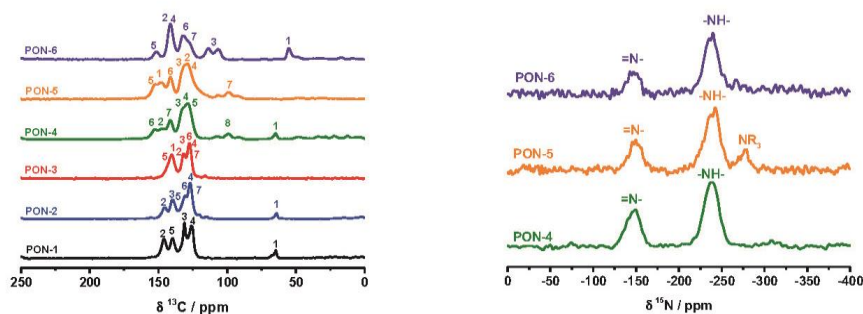


Fig. 3: ^{13}C CP MAS spectra of PON-1 - PON-6 with respective assignment (left) and ^{15}N CP MAS spectra of the correspondent benzimidazole derived polymers. The labelling is according to Fig. 1.

cylindrical pores. Since all networks are amorphous, the given kernels are not suitable to reflect a perfect image of the real porous environment and were, therefore, used to derive an estimate only. In accordance with the literature²⁸, the highest BET surface area was found for PON-1 with about $5000\text{ m}^2\cdot\text{g}^{-1}$ (Table 1). This network showed a type IV isotherm, typical for primarily mesoporous compounds (Fig. 4). For PON-2 and PON-4, which also reveal a three dimensional morphology, BET surface areas of $700\text{ m}^2\cdot\text{g}^{-1}$ and $1270\text{ m}^2\cdot\text{g}^{-1}$ were found, respectively. Both networks exhibit type I isotherms, correlated to primary microporous materials (Fig. 4).²⁹ The high surface areas of PON-1 and PON-4 are the result of their linker morphology, leading to an inherent porosity upon polymer formation. With respect to their similar buildup, we estimated their pore volume and pore size distribution using the *Gurvich* method and the QSDFT adsorption branch kernel for carbon materials with mixed spherical and cylindrical-pores. In accordance with the calculated surface areas the three-dimensional networks showed large pore volumes of $4.73\text{ cm}^3\cdot\text{g}^{-1}$, $0.34\text{ cm}^3\cdot\text{g}^{-1}$ and $0.54\text{ cm}^3\cdot\text{g}^{-1}$ for PON-1, PON-2 and PON-4, respectively (Table 1). The pore size distribution revealed a primarily mesoscopic pore environment for PON-1 (0.20), while PON-2 (0.6) and PON-4 (0.7) both showed a major microporous network morphology (Fig. 4).

Due to their seemingly two-dimensional structures, the porosity of PON-3, PON-5 and PON-6 is attributed to a stacking behaviour of the respective polymer sheets, probably driven by π - π interactions.²⁴ These networks revealed surface areas of $750\text{ m}^2\cdot\text{g}^{-1}$ (PON-6), $590\text{ m}^2\cdot\text{g}^{-1}$ (PON-5) and $490\text{ m}^2\cdot\text{g}^{-1}$ (PON-3), respectively, and type I isotherms (Fig. 4). With respect to the shape of the polymers, we used QSDFT adsorption branch kernel for carbon materials with cylindrical pores, since the expression of spherical pores in a two dimensional network is not reasonable. The pore volumes were estimated to be $0.37\text{ cm}^3\cdot\text{g}^{-1}$ (PON-3), $0.29\text{ cm}^3\cdot\text{g}^{-1}$ (PON-5) and $0.34\text{ cm}^3\cdot\text{g}^{-1}$ (PON-6) (Table 1). In accordance to the shape of their isotherms, the pore size distribution showed for PON-5 and PON-6 a primary microporous structure. PON-3, however, seems to consist mostly of small mesopores (Table 1 and Fig. 4 bottom).

Incorporation of imidazole

The substitution of water with nitrogen containing, amphoteric heterocycles such as imidazole already proved to be a promising approach for proton conduction in COFs and PONs.^{16,30} Since the nitrogen bearing functionalities are strong proton mediators, the formation of protonic charge carriers ($\text{C}_3\text{H}_3\text{N}_2\text{H}_2^+$), driven by self-dissociation, leads to extensive hydrogen bond interactions and thus creates proton conduction pathways.^{8,31,32} The high melting point and stability of imidazole allows temperatures beyond $100\text{ }^\circ\text{C}$ and is, therefore, favourable in terms of ion mobility and catalyst

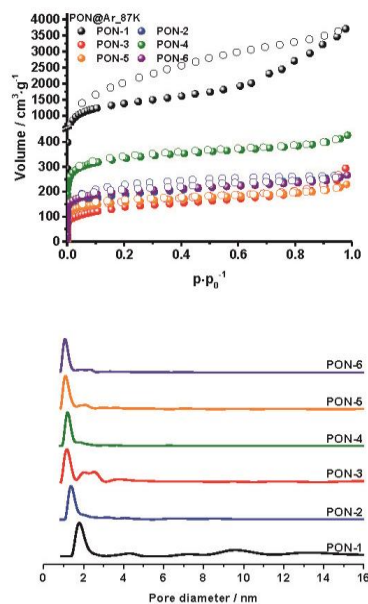


Fig. 4: Argon adsorption isotherms of PONs measured at 87 K (top). Pore size distribution (PSD) estimated by QSDFT kernels for cylindrical (PON-3, PON-5, PON-6) and cylindrical/sphere pores (PON-1, PON-2, PON-4) (bottom). For full PSD see Fig. S26.

Please do not adjust margins

Table 1: Surface areas and pore volumes taken from Ar adsorption isotherms measured at 87 K estimated by BET and DFT kernels for carbon materials.

Polymer	S _{A,BET} / m ² ·g ⁻¹	S _{A,DFT} / m ² ·g ⁻¹	P _{V,tot} / cm ³ ·g ⁻¹	P _{V,mic} / P _{V,tot}
PON-1 ^a	5043	4165	4.73 (4.49)	0.2
PON-2 ^a	700	647	0.34 (0.33)	0.6
PON-3 ^b	490	487	0.37 (0.35)	0.3
PON-4 ^a	1271	1376	0.54 (0.52)	0.7
PON-5 ^b	593	649	0.29 (0.28)	0.6
PON-6 ^b	753	855	0.34 (0.33)	0.7

^a P_{V,tot} estimated by the Gurvich method. ^b Estimated by a cylindrical/sphere pore QSDFT kernel. ^c Estimated by a cylindrical pore QSDFT kernel.

resistibility. Various procedures for the incorporation of imidazole into porous structures have been reported in the literature, e.g. through solvent, via condensation¹⁶ or through gas phase.³³ We found, that among all reported methods, gas phase incorporation provides the most reliable data, since only single molecules are incorporated into the pores of a network, which supports an effective pore filling and minimize condensation as well as crystallisation of imidazole upon the polymer particle surfaces. Thereby, we were able to incorporate imidazole into the voids of the respective networks. The success of the imidazole incorporation was monitored gravimetrically and by infrared spectroscopy. For the latter characteristic bands at 2650 cm⁻¹ and 1615 cm⁻¹ were assigned to the N-H-N and C-N vibrations of imidazole (Fig. S28). The absence of any Bragg reflections within the PXRD patterns (Fig. S32) corroborates that the frameworks are still amorphous and that imidazole is not crystallizing in the inter-particle voids but fills up the micropores. This finding is supported by DSC data, which indicate an absence of crystallisation and melting peaks (Fig. S33).

The amount of incorporated imidazole was determined by thermogravimetric analysis performed in air, where the weight loss between 150 °C and 200 °C signals the removal of imidazole (Fig. S30). We found the highest uptake for imidazole in PON-1 (1.08 g g⁻¹), which is due to its extended mesoporosity and high pore volume. Interestingly, by comparing the volume of incorporated imidazole (for which we used its liquid density as an estimate) with the theoretically available pore volume, there still remains a major part of free space (Fig. 5). We state this to pore blocking effects due to microporous parts of the interconnecting pore system. PON-2 and PON-5 revealed similar uptakes of 0.77 g g⁻¹ and 0.75 g g⁻¹. For both polymers, the amount of incorporated imidazole exceeds the respective pore volume, which might result from the breathing behaviour of the flexible networks.²⁴ With 0.6 g g⁻¹ and 0.43 g g⁻¹ the amount of incorporated imidazole exceeds the pore volumina of PON-4 and PON-6, however, only marginally. We state the latter finding to an additional filling of microporous interparticle voids.

PON-3 (0.23 g g⁻¹) has the lowest uptake value, as well as an incomplete pore filling. In order to estimate the influence of the benzimidazole backbone of PON-4, PON-5 and PON-6 on the proton conduction performance, we calculated the ratio of incorporated imidazole per functional group. While for PON-5 1.8 imidazole molecules per functional group were incorporated, PON-4 and

Table 2: Proton conductivities measured at 130 °C under nitrogen atmosphere and activation energies of the polymers, calculated from the respective Arrhenius plots.

Network	PON-1	PON-2	PON-3	PON-4	PON-5	PON-6
κ _{130 °C} / S·cm ⁻¹	5.2·10 ⁻⁴	7.3·10 ⁻⁵	2.1·10 ⁻⁷	9.7·10 ⁻⁶	2.0·10 ⁻⁵	4.9·10 ⁻⁶
E _A / kJ·mol ⁻¹	39	39	53	58	35	44

PON-6 revealed ratios of only 1.4 and 1.0, respectively.

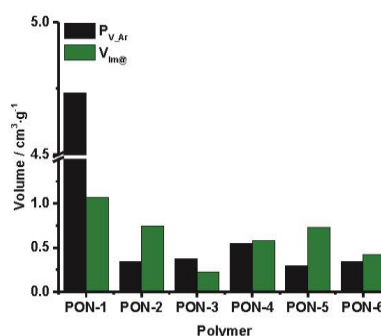


Fig. 5: Imidazole uptake in comparison to the available pore volume of the respective polymers.

Proton Conduction

The proton conductivity of the different networks has been determined as a function of temperature (90 °C - 130 °C) under static nitrogen atmosphere. The data were obtained by electrochemical impedance spectroscopy in a two electrode setup. They have been fitted to an equivalent circuit as shown in Fig. 2 and optimized to comply with the shape of the obtained semicircles in the respective Nyquist plots (Fig. 2, Figs. S36 – S41).³⁴ The circuit describes two semicircles in the impedance plots, which we assign to charge transfer resistance, for the high frequency circle, and additional boundary effects due to the measuring setup for the one at low frequencies (electrode contacting, two electrode setup etc.)³⁴ (Fig. 6). The constant phase elements (CPE-1, -2) are used to describe capacitive parts of the system adapted to influences of surface roughness and system heterogeneity.^{35,36} Interestingly, for the three dimensional polymers, two semicircles are well separated, while for the two-dimensional polymers, the semicircles separate to a lesser extent and showed an additional spur at low frequencies (Fig. 6, top and middle). We attribute this behaviour to the sheet-like morphology of the network, which, in comparison to the more

Please do not adjust margins

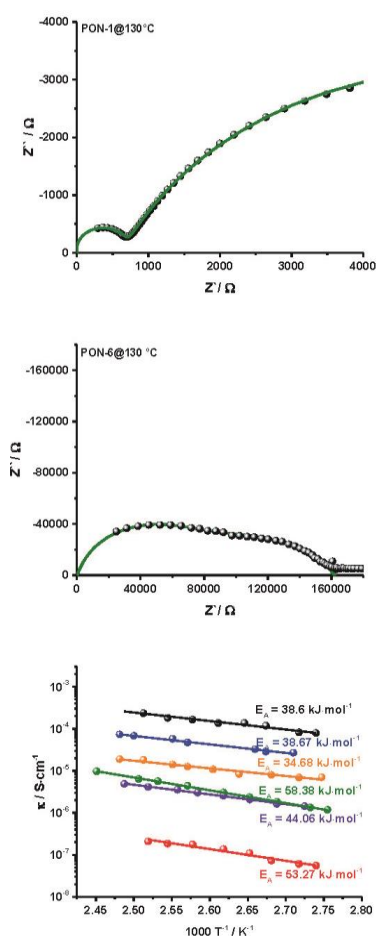


Fig. 6: Exemplary Nyquist plots of PON-1 (top) and PON-6 (middle), measured at 130 °C under N_2 atmosphere, fitted with the equivalent circuit pictured in the experimental section. Arrhenius Plot of PON-1 - PON-6 obtained from high frequency resistance data measured in a temperature range between 90 °C and 130 °C under N_2 atmosphere (bottom). The colour code is similar to the one in Fig. 1.

granular formed three-dimensional polymers, results in a different contact to the electrodes.³⁴

The proton conductivity of the polymers was estimated from the high frequency resistance R_1 , depicted by the first semicircle in the respective Nyquist plots (Fig. 6, Table 2 and Figs. S34 – S39). All samples were preheated towards 90 °C to ensure a full equilibration of the system before starting the measurement routine. Interestingly, although all networks rely on imidazole based proton transport, the conduction performance differs markedly (Fig. 6, bottom). While for PON-3, -4 and -6 only low conductivities in the

range from 10^{-6} to 10^{-7} $S \cdot cm^{-1}$ were observed, PON-5 and PON-2 exhibit conductivities around 10^{-5} $S \cdot cm^{-1}$. The best values were found for PON-1 ($5.2 \cdot 10^{-4}$ $S \cdot cm^{-1}$), making this network comparable to state of the art porous polymers like Im@TPB-DMTP-COF¹⁵ ($4.37 \cdot 10^{-5}$ $S \cdot cm^{-1}$, 130 °C), H_3PO_4 @TP-Azo³⁷ ($9.9 \cdot 10^{-4}$ $S \cdot cm^{-1}$, 70 °C) and Im@Td-PPI¹⁶ ($3.49 \cdot 10^{-4}$ $S \cdot cm^{-1}$, 90 °C). The comparison of the estimated proton conductivity with the amount of incorporated imidazole shows, that a high amount of proton mediators is favourable for an excellent performance.

Besides the varying conductivities, different activation energies for the polymers were obtained from the respective Arrhenius plots, which are indicative for the conduction mechanism (Fig. 6).^{38,39} For the Grotthuss mechanism (structure diffusion) activation barriers between 0.1 and 0.4 eV (9.6-38.6 $kJ \cdot mol^{-1}$) are postulated, while for the vehicle type mechanism activation energies (E_A) between 0.5 and 0.9 eV (48.2-86.8 $kJ \cdot mol^{-1}$) are reported.⁴⁰ For PON-1, PON-2 and PON-4 the activation barrier was calculated to be 39 $kJ \cdot mol^{-1}$ and 35 $kJ \cdot mol^{-1}$, respectively, which is within the range typical for Grotthuss mechanism (Fig. 6).⁴¹ We attribute this to the high amount of incorporated imidazole molecules within the networks, which leads to a homogeneous charge carrier distribution, and therefore interconnected proton conduction pathways. E_A for the networks PON-6, PON-3 and PON-4 are with 44, 53 and 58 $kJ \cdot mol^{-1}$ significantly larger indicating a vehicle type conduction mechanism (Fig. 6) in these cases. This might be due to the lower amount of guest molecules and, therefore, an inhomogeneous charge carrier distribution, which forces a charge transport via diffusion of protonated imidazole molecules.

However, the data seem to indicate a direct correlation between observed proton conductivity and the amount of incorporated imidazole (Fig. 7). Interestingly the level of pore filling seems to be subordinated, as PON-1 exhibits the highest conductivity with only 20 % pore filling, while PON-6 shows a minor conductivity, despite its excessive pore filling. In this respect, pore geometry also seems to have only minor effects, since there is just a slight difference between the two-dimensional PON-5 and three-dimensional PON-2 in states of imidazole incorporation and proton conductivity (Fig. 7). However, three dimensional polymers seem to be more promising as they tend to express a more rigid porous environment which is favourable for the incorporation of proton conductive species. This statement is based on PON-1 and PON-2, both based on rigid tetrahedral building units, showed the best performance in this study.

Furthermore, the presence of benzimidazole units in the polymer backbone like in PON-4, PON-5 and PON-6 seems to have a negative effect, as the imidazole affixation at the respective functional group is increased. While at lower imidazole to functional group ratios this might impede the carrier movement, due to a hindered diffusion, at high ratios the interplay between guest and functional group might be supported. Among the benzimidazole based polymers, PON-5 exhibits the highest ratio of 1.8 imidazole molecules per functional group (PON-4: 1.4; PON-6: 1.0), which in combination with its small repeating unit is indicative for a dense charge carrier concentration. In consequence PON-5 exhibit a higher proton conduction performance than the competitive benzimidazoles, despite of its two-dimensional morphology. Since we expect the conductive imidazole units in PON-4 and PON-6 to be primary located at the networks functional groups, not only their conduction performance is lower, but with -58 $kJ \cdot mol^{-1}$ (PON-4) and -44 $kJ \cdot mol^{-1}$ (PON-6) also their energy of activation is much higher with respect to the one of PON-5 (-35 $kJ \cdot mol^{-1}$).

Please do not adjust margins

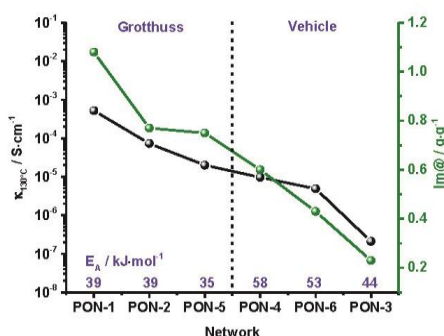


Fig. 7: Correlation between imidazole incorporation and proton conduction mechanism. The conductivity values were taken at 130 °C under nitrogen atmosphere.

Conclusions

We synthesized six different porous organic networks (PONs) based either on carbon-hydrogen (PON-1 - PON-3) or benzimidazole (PON-4 - PON-6) in order to study the influence of network morphology on anhydrous proton conduction. The polymers exhibit high crosslinking degrees as estimated by ¹³C and ¹⁵N solid-state NMR spectroscopy. The BET surface areas are between 490 m²·g⁻¹ (PON-3) and 5043 m²·g⁻¹ (PON-1) and they have a high thermal resistance up to 525 °C (PON-2). After post-synthetic incorporation of imidazole via the gas phase, which allowed to reach a maximal filling 1.1 g·g⁻¹ for PON-1, we investigated the proton conduction performance of these networks as function of the morphology, chemical functionality, and guest loading. The networks reveal conductivities between 10⁻⁷ S·cm⁻¹ and 10⁻⁴ S·cm⁻¹ at 130 °C under anhydrous conditions with maximum values for PON-1 (5.2·10⁻⁴ S·cm⁻¹ at 130 °C). The latter is comparable to state-of-the-art materials like Im@TPB-DMTP-COF¹⁵ (4.73·10⁻³ S·cm⁻¹ at 130 °C) or TD-PPI¹⁶ (3.49·10⁻⁴ S·cm⁻¹ at 90 °C). Moreover, we estimated the activation energy of the polymers to fall in the range of -39 kJ·mol⁻¹ to -58 kJ·mol⁻¹ and to correlate with the amount of incorporated guest molecules. In this respect, three-dimensional polymers, based on rigid tetrahedral building units seem to be favoured to provide more homogeneous charge carrier distributions. Interestingly, no further influence of pore geometry and degree of pore filling on the conduction performance were found. Furthermore, the presence of polybenzimidazole groups within the polymer backbone (PON-4 - PON-6) seemed to have an impeding effect on conduction, especially at low ratios of imidazole to functional groups. This might be due to a stronger binding of imidazole to the functional groups causing its immobilisation. In this respect, further investigations are part of our future work.

Conflicts of interest

There are no conflicts of interest to declare.

Acknowledgements

The authors thank Dr. Renee Siegel and Beate Bojer for performing the solid-state NMR spectroscopic measurements. We gratefully thank Prof. Josef Breu for access to physisorption instruments.

Notes and references

- R. F. Service, *Science*, 1999, **285**, 682–685.
- S. J. Peighambari, S. Rowshanzamir and M. Amjadi, 2010, **9**, 3–4.
- P. Ramaswamy, N. E. Wong and G. K. H. Shimizu, *Chem Soc Rev*, 2014, **43**, 5913–5932.
- C. Klumpen, S. Gödrich, G. Papastavrou and J. Senker, *Chem. Commun.*, 2017, **53**, 7592–7595.
- R. C. Woudenberg, O. Yavuzcetin, M. T. Tuominen and E. B. Coughlin, *Solid State Ionics*, 2007, **178**, 1135–1141.
- N. E. Wong, P. Ramaswamy, A. S. Lee, B. S. Gelfand, K. J. Bladec, J. M. Taylor, D. M. Spasyuk and G. K. H. Shimizu, *J. Am. Chem. Soc.*, 2017, **139**, 14676–14683.
- D. Umeyama, S. Horike, M. Inukai and S. Kitagawa, *J. Am. Chem. Soc.*, 2013, **135**, 11345–11350.
- M. F. H. Schuster and W. H. Meyer, *Annu. Rev. Mater. Res.*, 2003, **33**, 233–261.
- J. A. Asensio, E. M. Sánchez and P. Gómez-Romero, *Chem. Soc. Rev.*, 2010, **39**, 3210.
- G. Zhu and H. Ren, *Porous Organic Frameworks*, Springer Berlin Heidelberg, Berlin, Heidelberg, 2015.
- C. Klumpen, M. Breunig, T. Homburg, N. Stock and J. Senker, *Chem. Mater.*, 2016, **28**, 5461–5470.
- N. Popp, T. Homburg, N. Stock and J. Senker, *J. Mater. Chem. A*, 2015, **3**, 18492–18504.
- A. B. Soliman, M. H. Hassan, T. N. Huan, A. A. Abugable, W. A. Elmeahmeh, S. G. Karakalos, M. Tsotsalas, M. Heinle, M. Elbahri, M. Fontecave and M. H. Alkordi, *ACS Catal.*, 2017.
- R. S. Sprick, B. Bonillo, M. Sachs, R. Clowes, J. R. Durrant, D. J. Adams and A. I. Cooper, *Chem. Commun.*, 2016.
- H. Xu, S. Tao and D. Jiang, *Nat. Mater.*, 2016, **15**, 722–726.
- Y. Ye, L. Zhang, Q. Peng, G.-E. Wang, Y. Shen, Z. Li, L. Wang, X. Ma, Q.-H. Chen, Z. Zhang and S. Xiang, *J. Am. Chem. Soc.*, 2015, **137**, 913–918.
- J. C. Persson and P. Jannasch, *Chem. Mater.*, 2003, **15**, 3044–3045.
- B. M. Fung, A. K. Khitrin and K. Ermolaev, *J. Magn. Reson.*, 2000, **142**, 97–101.
- T. Ben, H. Ren, S. Ma, D. Cao, J. Lan, X. Jing, W. Wang, J. Xu, F. Deng, J. M. Simmons, S. Qiu and G. Zhu, *Angew. Chemie Int. Ed.*, 2009, **48**, 9457–9460.
- M. Rose, N. Klein, W. Böhlmann, B. Böhringer, S. Fichtner and S. Kaskel, *Soft Matter*, 2010, **6**, 3918.
- Q. Chen, J.-X. Wang, F. Yang, D. Zhou, N. Bian, X.-J. Zhang, C.-G. Yan and B.-H. Han, *J. Mater. Chem.*, 2011, **21**, 13554.
- M. G. Rabbani and H. M. El-Kaderi, *Chem. Mater.*, 2012, **24**, 1511–1517.
- M. G. Rabbani, T. E. Reich, R. M. Kassab, K. T. Jackson, H. M. El-Kaderi, W. Zhang, J. Lipkowsky, J. Guenther, J. Blümel, R. Krishna, Z. Li and H.-C. Zhou, *Chem. Commun.*, 2012, **48**, 1141–1143.
- C. Klumpen, F. Radakovitsch, A. Jess and J. Senker, *Molecules*, 2017, **22**, 1343.
- S. I. Alaqeel, *J. Saudi Chem. Soc.*, 2017, **21**, 229–237.

Please do not adjust margins

ARTICLE

Journal Name

- 26 K. S. Walton and R. Q. Snurr, *J. Am. Chem. Soc.*, 2007, **129**, 8552–8556.
- 27 S. Lowell, J. E. Shields, M. A. Thomas and M. Thommes, *Characterization of Porous Solids and Powders*, Springer Netherlands, Dordrecht, 2004.
- 28 S. Das, P. Heasman, T. Ben and S. Qiu, *Chem. Rev.*, 2017, **117**, 1515–1563.
- 29 M. Thommes, K. Kaneko, A. V. Neimark, J. P. Olivier, F. Rodriguez-Reinoso, J. Rouquerol and K. S. W. Sing, *Pure Appl. Chem.*, 2015, **87**, 1051–1069.
- 30 X. Meng, H.-N. Wang, S.-Y. Song, H.-J. Zhang, S. Kitagawa, G. K. H. Shimizu, H. Y. Zang, G. S. Zhu, N. Gadegaard, M. Mirza, D. Paul, J. Poblet, L. Cronin, K. D. Demadis and A. Cabeza, *Chem. Soc. Rev.*, 2017, **46**, 464–480.
- 31 K. D. D. Kreuer, A. Fuchs, M. Ise, M. Spaeth and J. Maier, *Electrochim. Acta*, 1998, **43**, 1281–1288.
- 32 B. S. Hickman, M. Mascal, J. J. Titman and I. G. Wood, *J. Am. Chem. Soc.*, 1999, **121**, 11486–11490.
- 33 S. Liu, Z. Yue and Y. Liu, *Dalt. Trans.*, 2015, **44**, 12976–12980.
- 34 Z. Xie, C. Song, B. Andraeus, T. Navessin, Z. Shi, J. Zhang and S. Holdcroft, *J. Electrochem. Soc.*, 2006, **153**, E173.
- 35 A. Lasia, *Electrochemical Impedance Spectroscopy and its Applications*, Springer New York, New York, NY, 2014.
- 36 R. Yadav and P. S. Fedkiw, *J. Electrochem. Soc.*, 2012, **159**, 340–346.
- 37 S. Chandra, T. Kundu, S. Kandambeth, R. Babarao, Y. Marathe, S. M. Kunjir and R. Banerjee, *J. Am. Chem. Soc.*, 2014, **136**, 6570–3.
- 38 M. F. H. Schuster, W. H. Meyer, M. Schuster and K. D. Kreuer, *Chem. Mater.*, 2004, **16**, 329–337.
- 39 W. Münch, K.-D. Kreuer, W. Silvestri, J. Maier and G. Seifert, *Solid State Ionics*, 2001, **145**, 437–443.
- 40 V. Zima, D. S. Patil, D. S. Raja, T.-G. Chang, C.-H. Lin, K. Shimakawa, T. Wagner, D. Senthil Raja, T.-G. Chang, C.-H. Lin, K. Shimakawa and T. Wagner, *J. Solid State Chem.*, 2014, **217**, 150–158.
- 41 W. Munch, K.-D. Kreuer, W. Silvestri, J. Maier and G. Seifert, *Solid State Ionics*, 2001, **145**, 437–443.

Please do not adjust margins

Supporting Information towards:

Anhydrous proton conduction in porous organic networks

C. Klumpen,^a S. Winterstein,^a G. Papastavrou^b and J. Senker^{a,*}

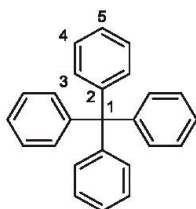
^aUniversity of Bayreuth, Inorganic Chemistry III, Universitaetsstraße 30, 95447 Bayreuth, Germany

^bUniversity of Bayreuth, Physical Chemistry II, Universitaetsstraße 30, 95447 Bayreuth, Germany

Table of content

Linker Synthesis	3
<i>Tetraphenylmethane</i> ²	3
¹ H NMR	4
¹³ C-NMR	4
IR	5
<i>Tetrakis(4-bromophenyl)methane</i> ³	6
¹ H NMR	6
¹³ C NMR	7
IR	7
<i>Tetrakis(4-formylphenyl)methane</i> ⁴	8
¹ H NMR	8
¹³ C NMR	9
IR	9
<i>1,1,2,2-Tetraphenylethylene</i> ⁵	10
¹ H-NMR	10
¹³ C-NMR	11
IR	11
<i>1,1,2,2-Tetrabromophenylethylene</i>	12
¹ H NMR	12
¹³ C NMR	13
IR	13
<i>Triptycene</i>	14
¹ H-NMR	14
¹³ C NMR	15
IR	15
<i>Hexanitrotriptycene</i> ⁶	16

^1H NMR.....	16
^{13}C NMR.....	17
IR.....	17
<i>Hexaaminotriptycene-hexachloride</i> ⁷	18
^1H -NMR.....	18
^{13}C - NMR.....	19
IR.....	19
Polymer Synthesis	20
<i>PON-1</i>	20
<i>PON-2</i>	20
<i>PON-3</i>	21
<i>PON-4</i>	22
<i>PON-5</i>	23
<i>PON-6</i>	24
Polymer Analytic	25
<i>Infrared Spectroscopy</i>	26
<i>Networks after loading with imidazole</i>	27
<i>Thermogravimetric analysis</i>	28
<i>Networks after loading with imidazole</i>	29
<i>Powder X-ray diffraction</i>	30
<i>Differential scanning calorimetry</i>	32
<i>Electrochemical impedance spectroscopy</i>	33
<i>Arrhenius Plot</i>	40

Linker Synthesis*Tetraphenylmethane*¹**Chemical Formula:** C₂₅H₂₀**Molecular Weight:** 320,43

15 g of trityl chloride (0.054 mol, 1 eq.) and 14.05 ml aniline (0.154 mol, 2.9 eq.) were heated up to 180 °C in a round flask with magnetic stirrer and condenser, until the reaction mixture turned into a violet solid. The heating process was extended for 10 more minutes. The solid was cooled down, crushed and resuspended in 75 ml MeOH and 75 ml 2 M HCl. The Suspension was refluxed for 30 min., filtered and washed with water. After resuspending in ethanol the reaction mixture was cooled down to -30 °C and 15.8 ml sulfuric acid and 9.44 g of isopentyl nitrite (0.081 mol, 1.5 eq.) were added under vigorous stirring. After stirring for 1 h at -10 °C, 26.9 ml of phosphinic acid (0.609 mol, 11 eq.) were added slowly and the reaction mixture was refluxed for 1.5 h. After cooling down, the solid was filtered, washed with DMF, H₂O and Ethanol and subsequently dried *in vacuo* to get a light brown powder. Further purification was not necessary but could be done by recrystallization in THF/methanol (1:1). Yield: 16.1 g (0.05 mol, 93 %). ¹H-NMR (500 MHz, DMSO-D₆): δ [ppm] = 7.30 (t, 1H, H-4), 7.21 (t, 1H, H-5), 7.15 (d, 1H, H-3) (Figure S1). ¹³C-NMR (500 MHz, DMSO-D₆): δ [ppm] = 146.88 (C-2), 130.94 (C-3), 128.19 (C-4), 126.44 (C-5) (Figure S2). IR (ATR): ν [cm⁻¹] = 3037, 1588, 1489, 1186, 1077, 1033, 990, 967, 631, 523 (Figure S3).

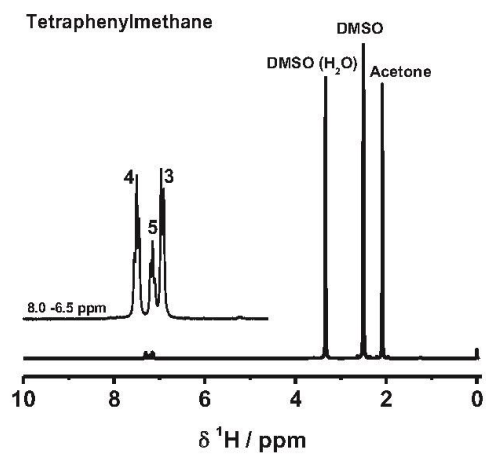
^1H -NMR

Figure S1: ^1H -NMR spectrum of tetraphenylmethane measured in DMSO-*d*₆.

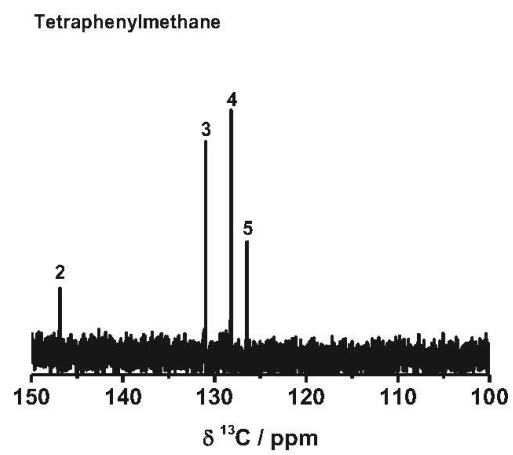
 ^{13}C -NMR

Figure S2: ^{13}C -NMR spectrum of tetraphenylmethane measured in DMSO-*d*₆.

IR

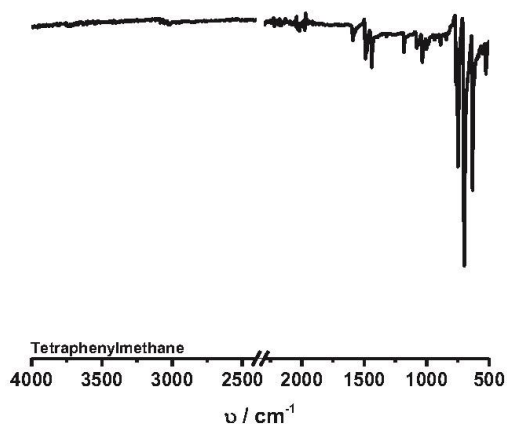
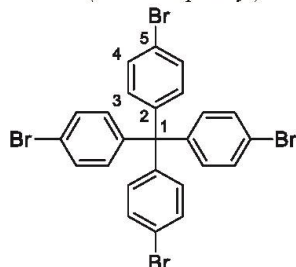


Figure S3: Infrared spectrum of tetraphenylmethane.

*Tetrakis(4-bromophenyl)methane*²

Chemical Formula: $C_{25}H_{16}Br_4$
Molecular Weight: 636,01

In a three necked vessel with magnetic stirrer, thermometer and condenser 10 g tetraphenylmethane (31.2 mmol, 1 eq.) were cooled in an ice bath. Now 99.8 g Br_2 (624 mmol, 20 eq.) were added dropwise. After cooling towards $-78\text{ }^\circ\text{C}$, 140 ml ethanol (4.5 ml/mmol) were poured in and the mixture was allowed to reach room temperature overnight. Now sodiumdisulfide solution was added until the end of precipitation. The resulting solid was filtered, washed with H_2O and dried in an oven at $110\text{ }^\circ\text{C}$. Further purification was carried out performing recrystallization in a chloroform/ethanol mixture (1:1) to get a light brown solid. Yield: 12.9 g (20.3 mmol, 65 %). 1H -NMR (500 MHz, DMSO- d_6): δ [ppm] = 7.53 (d, 2H, H-4), 7.06 (d, 2H, H-3) (Figure S4). ^{13}C -NMR (500 MHz, DMSO- d_6): δ [ppm] = 63.66 (C-1), 120.40 (C-5), 131.55 (C-3), 132.86 (C-4), 145.06 (C-2) (Figure S5). MS [M/z] = 279, 239, 636, 319, 555, 198. IR (ATR): ν [cm^{-1}] = 2960, 1569, 1486, 1393, 1181, 1072, 1005, 951, 908, 808, 750, 528, 507 (Figure S6).

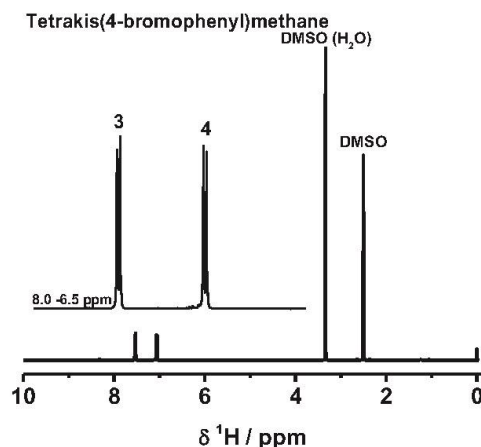
 1H NMR

Figure S4: 1H NMR spectrum of *Tetrakis(4-bromophenyl)methane* measured in DMSO.

^{13}C NMR

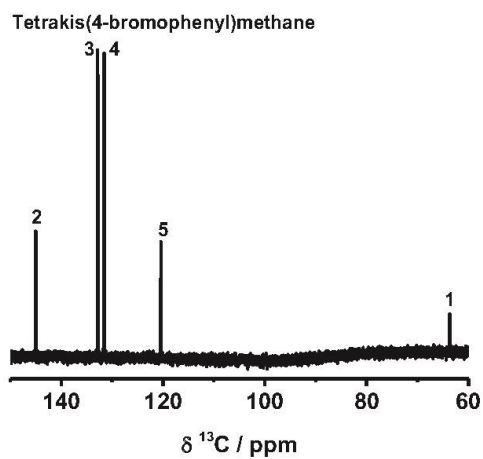


Figure S5: ^{13}C NMR spectrum of tetrakis(4-bromophenyl)methane measured in $\text{DMSO}-d_6$.

IR

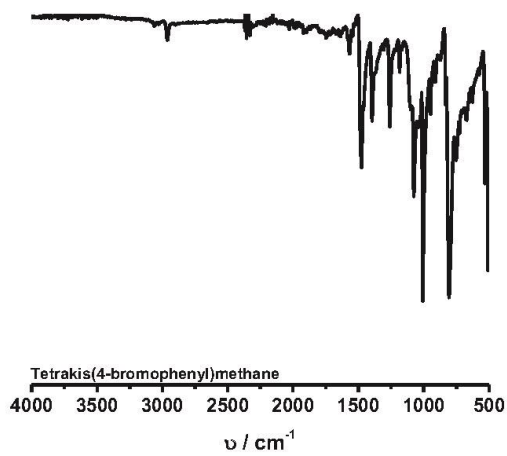
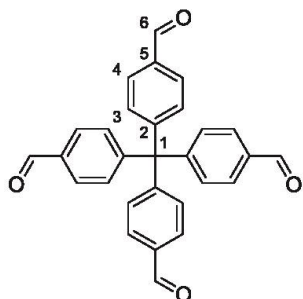


Figure S6: Infrared spectrum of tetrakis(4-bromophenyl)methane.

*Tetrakis(4-formylphenyl)methane*³

Chemical Formula: $C_{28}H_{20}O_4$
Molecular Weight: 432,47

Under argon atmosphere, 1.25 g of tetrakis(4-bromophenyl)methane ($1.97 \cdot 10^{-3}$ mol, 1 eq.) was dissolved in 75 ml dry tetrahydrofuran and cooled to -78 °C in a dry-ice/acetone bath. Now 10 ml *n*-BuLi (1.6 M in hexane, $1.6 \cdot 10^{-2}$ mol, 8 eq.) were added dropwise and the reaction mixture was stirred at -78 °C for further 7 h. Afterwards 5 ml dimethylformamide was added at -78 °C and the mixture was allowed to reach room temperature overnight. After addition of 1 M HCl, the mixture was extracted with dichloromethane (3x). The organic layers were combined, dried over $MgSO_4$, filtered and the solvent was evaporated. After performing flash column chromatographic with *n*-hexane/ethylacetate the product was obtained as white crystals. Yield: 0.246 g ($5.7 \cdot 10^{-4}$ mol, 29 %). 1H NMR (500 MHz, $CDCl_3$): δ [ppm] = 9.92 (s, 1H, H-6), 7.76 (d, 1H, H-4), 7.37 (d, 1H, H-3) (Figure S7). ^{13}C NMR (500 MHz, $CDCl_3$): δ [ppm] = 191.5 (C-6), 151.2 (C-2), 134.8 (C-5), 131.2 (C-4), 129.7 (C-3), 66.3 (C-1) (Figure S8). IR (ATR): ν [cm^{-1}] = 2947-2715_{mult.}, 1698, 1604, 1386, 1303, 1210, 1168, 1002, 795 (Figure S9).

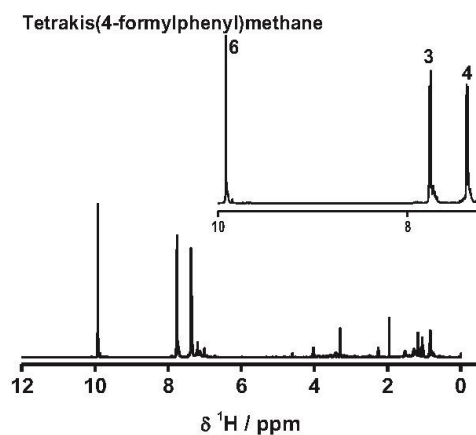
 1H NMR

Figure S7: 1H NMR Spectrum of tetrakis(4-formylphenyl)methane measured in $CDCl_3$.

^{13}C NMR

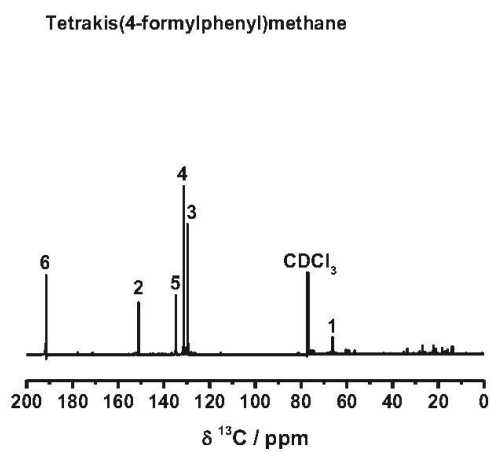


Figure S8: ^{13}C NMR spectrum of tetrakis(4-formylphenyl)methane measured in CDCl_3 .

IR

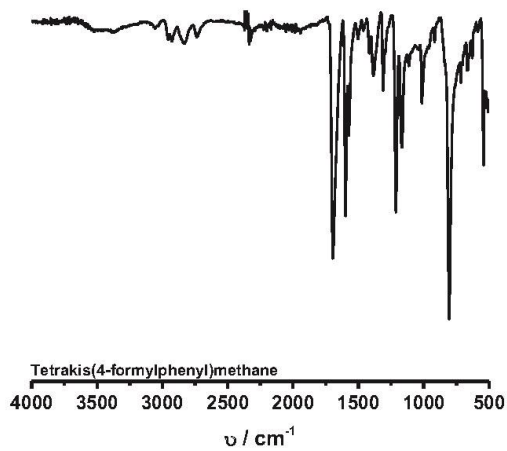
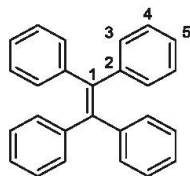


Figure S9: Infrared spectrum of tetrakis(4-formylphenyl)methane.

1,1,2,2-Tetraphenylethylene^A

Chemical Formula: C₂₆H₂₀
Molecular Weight: 332,44

In a dry vessel, 5 g of benzophenone (0.027 mol, 1 eq.) was placed under Ar. 4.24 g Zn powder (0.065 mol, 2.4 eq.) and 100 ml dry tetrahydrofuran were added. The mixture was cooled towards -78 °C in a dry-ice/acetone bath and 3.6 ml of TiCl₄ (0.032 mol, 1.2 eq.) were added dropwise. After stirring at -78 °C for 20 minutes the mixture was allowed to reach room temperature and then refluxed for 14 h. After cooling down, the reaction mixture was poured into water and extracted with dichloromethane (4 x 100 ml). The organic layer was washed with brine and water, dried over MgSO₄ and filtered. After solvent evaporation the product was recrystallized from dichloromethane to give an off white powder. Yield 2.6 g (7.83·10⁻³ mol, 58 %). ¹H NMR (500 MHz, DMSO-d₆): δ [ppm] = 7.45 (m, 1H, Ar-H), 7.12 (m, 1H, Ar-H), 6.96 (m, 1H, Ar-H) (Figure S10). ¹³C NMR (500 MHz, DMSO-d₆): δ [ppm] = 143.7 (C-2), 140.9 (C-1), 131.4 (C-3), 127.7 (C-4), 126.4 (C-5) (Figure S11). IR (ATR): ν [cm⁻¹] = 3023, 1598, 1493, 1443, 1167, 1076, 1021, 744, 690, 604, 564 (Figure S12).

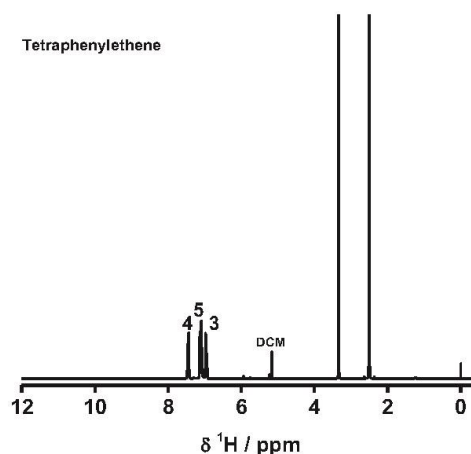
¹H-NMR

Figure S10: ¹H NMR spectrum of tetraphenylethylene measured in DMSO-d₆.

^{13}C -NMR

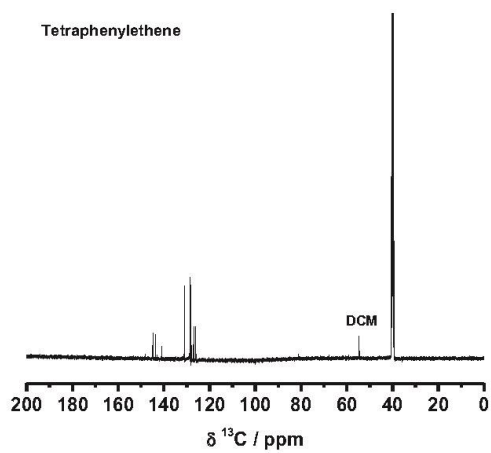


Figure S11: ^{13}C NMR spectrum of tetraphenylethene measured in $\text{DMSO-}d_6$.

IR

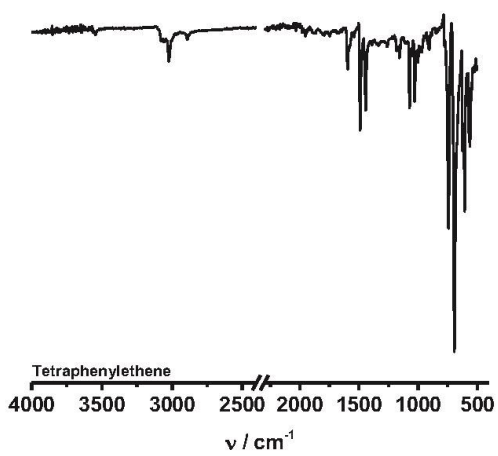
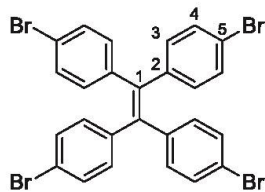


Figure S12: Infrared spectrum of tetraphenylethene.

1,1,2,2-Tetrabromophenylethylene

Chemical Formula: $C_{26}H_{16}Br_4$

Molecular Weight: 648,02

2 g of Tetraphenylethylene ($6.01 \cdot 10^{-3}$ mol, 1 eq.) was placed in a vessel which and cooled in an ice bath. Now 6.2 ml of bromine (0.12 mol, 20 eq.) were added slowly. The mixture was now cooled towards $-78\text{ }^{\circ}\text{C}$ in a dry-ice/acetone bath, followed by the addition of 30 ml ethanol. The mixture was allowed to rise to room temperature overnight (18 h) and sodium thiosulfate solution was added. The resulting precipitate was filtered, washed with water and dried in an oven at $130\text{ }^{\circ}\text{C}$. After recrystallization in chloroform/methanol a white solid was obtained. Yield: 3,36 g ($5.19 \cdot 10^{-3}$ mol, 86 %). ^1H NMR (500 MHz, DMSO- d_6): δ [ppm] = 7.4 (d, 1H, Ar-H), 6.9 (d, 1H, Ar-H) (Figure S13). ^{13}C NMR (500 MHz, DMSO- d_6): δ [ppm] = 140.8 (C-2), 138.7 (C-1), 132.2 (C-3), 130.5 (C-4), 119.8 (C-5) (Figure S14). IR (ATR): ν [cm^{-1}] = 1937, 1559, 1473, 1262, 1194, 1090, 896, 827, 586 (Figure S15)

 ^1H NMR

1,1,2,2-Tetrakis(4-bromophenyl)ethylene

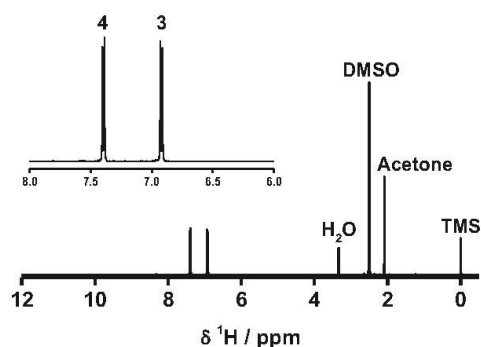


Figure S13: ^1H NMR spectrum of tetrakis(4-bromophenyl)ethen measured in DMSO- d_6 .

^{13}C NMR

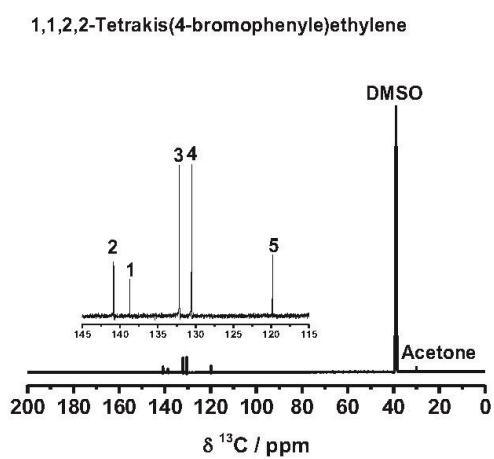


Figure S14: ^{13}C NMR spectrum of tetrakis(4-bromophenyl)ethene measured in DMSO- d_6 .

IR

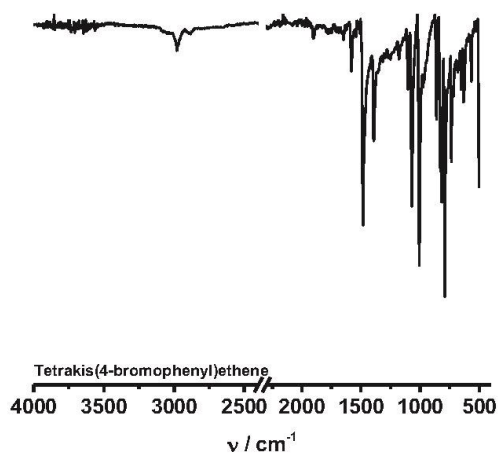
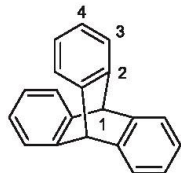


Figure S15: Infrared spectrum of tetrakis(4-bromophenyl)ethene.

Triptycene



Chemical Formula: $C_{20}H_{14}$

Molecular Weight: 254,33

Under dry conditions 10 g of anthracene (0.056 mol, 1 eq.) was refluxed in 200 ml chloroform. After addition of 9.1 ml amyl nitrite (0.067 mol, 1.2 eq.), 8.46 g anthranilic acid (0.062 mol, 1.1 eq.) in 100 ml dry tetrahydrofuran was added dropwise over a time frame of 1.5 h. Afterwards, the reaction mixture was stirred under reflux for further 45 minutes. Now the solvent was evaporated and 5.5 g maleic anhydride (0.056 mol, 1 eq.) and 50 ml dioxane were added. The mixture was again refluxed for 1 h. The resulting solution was given in an ice cooled mixture of 150 ml H_2O , 150 ml MeOH and 25 g KOH and stirred for 5 minutes. The precipitate was filtered and washed with MeOH and Water. The solid was solved in 75 ml hot butanone and filtered. The filtrate was given in 100 ml MeOH and was stored in a freezer overnight for crystallisation. The resulting precipitate was filtered, washed with cold MeOH and dried in an oven at 130 °C to yield the product as white crystals. Yield: 3.01 g (0.012 mol, 21 %). 1H NMR (500 MHz, DMSO- d_6): δ [ppm] = 7.4 (m, 1H, Ar-H), 6.9 (m, 1H, Ar-H), 5.6 (s, 1H, H-1) (Figure S16). ^{13}C NMR (500 MHz, DMSO- d_6): δ [ppm] = 146 (C-2), 125 (C-3), 124 (C-4), 53 (C-1) (Figure S17). IR (ATR): ν [cm^{-1}] = 3046, 2957, 1317, 1250, 1165, 1017, 794, 727, 618 (Figure S18).

 1H -NMR

Triptycene

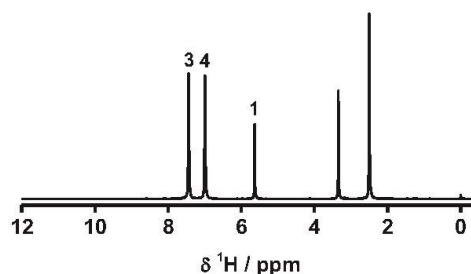


Figure S16: 1H NMR spectrum of triptycene measured in DMSO- d_6 .

^{13}C NMR

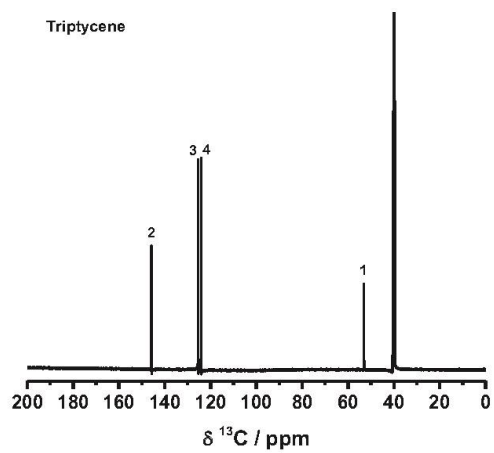


Figure S17: ^{13}C NMR spectrum of triptycene measured in DMSO- d_6 .

IR

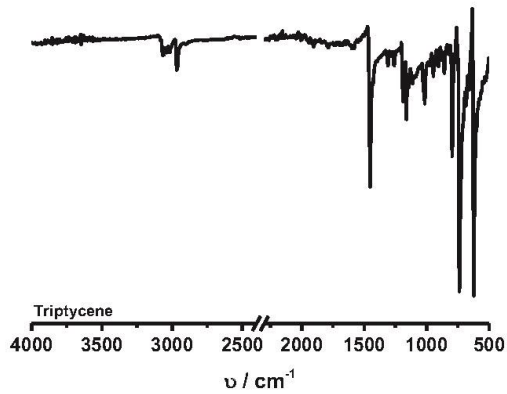
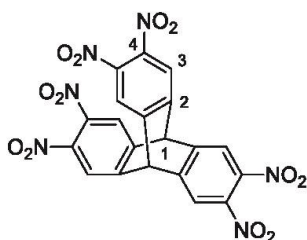


Figure S18: Infrared spectrum of triptycene.

*Hexanitrotriptycene*⁵

Chemical Formula: $C_{20}H_8N_6O_{12}$
Molecular Weight: 524,31

After combining 4.8 ml HNO_3 (100%) with 1.2 ml of sulfuric acid, 0.5 g triptycene ($1.97 \cdot 10^{-3}$ mol, 1 eq.) was added slowly. The resulting mixture was refluxed overnight at 85 °C. After cooling down, the reaction was quenched in 300 ml H_2O and stirred for further 10 min., causing the precipitation of a white solid, which was then filtered and dried in an oven at 130 °C. Recrystallization from hot acetone yielded the product as white crystals. Yield: 0.27 g ($5.1 \cdot 10^{-4}$ mol, 26 %). 1H NMR (500 MHz, $DMSO-d_6$): δ [ppm] = 8.4 (m, 1H, H-3), 6.7 (m, 1H, H-1) (Figure S19). ^{13}C NMR (500 MHz, $DMSO-d_6$): δ [ppm] = 148.1 (C-2), 140.6 (C-4), 124.0 (C-3), 51.1 (C-1) (Figure S20). IR (ATR): ν [cm^{-1}] = 3071, 1674, 1539, 1349, 1203, 902, 860, 778, 702, 522 (Figure S21).

 1H NMR

Hexanitrotriptycene

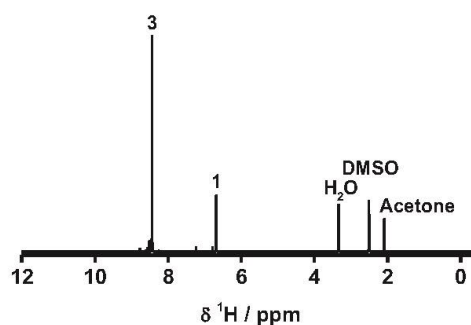


Figure S19: 1H NMR spectrum of hexanitrotriptycene measured in $DMSO-d_6$.

^{13}C NMR

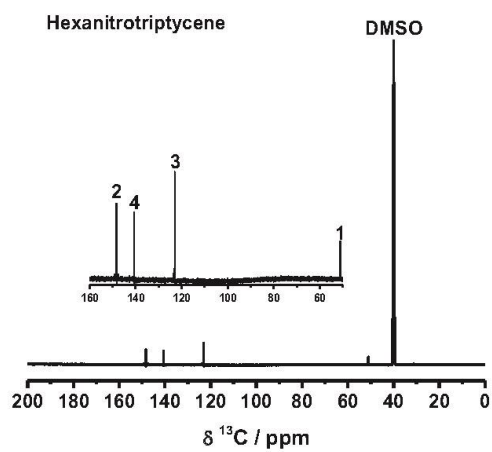


Figure S20: ^{13}C NMR spectrum of hexanitrotriptycene measured in DMSO-d_6 .

IR

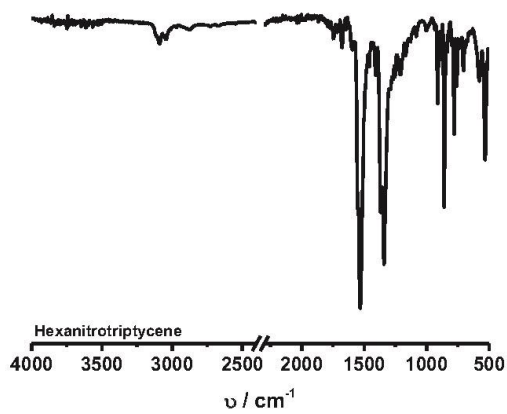
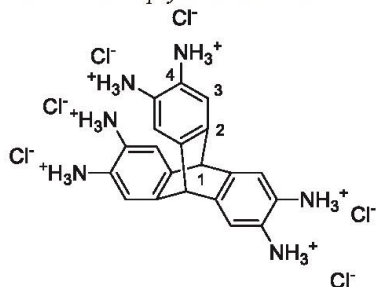


Figure S21: Infrared spectrum of hexanitrotriptycene.

*Hexaaminotriptycene-hexachloride*⁶

Chemical Formula: $C_{20}H_{26}Cl_6N_6$
Molecular Weight: 563,18

0.14 g of hexanitrotriptycene ($2.5 \cdot 10^{-4}$ mol, 1 eq.) and 1.86 g $SnCl_2 \cdot 2H_2O$ were suspended in 50 ml ethanol. After addition of 6.6 ml concentrated HCl (32 %) the mixture was refluxed for 24 h. The resulting solid was filtrated, washed with HCl and dried in an oven at 130 °C overnight to yield yellow platelets. Yield: 0.10 g ($1.8 \cdot 10^{-4}$ mol, 72 %). 1H NMR (500 MHz, D_2O): δ [ppm] = 7.14 (sbr, 1H, H-3), 5.4 (sbr, 1H, H-1) (Figure S22). ^{13}C NMR (500 MHz, D_2O): δ [ppm] = 141.6 (C-2), 125.3 (C-4), 117.2 (C-3), 50.2 (C-1) (Figure S23). IR (ATR): ν [cm^{-1}] = 2968, 1559, 1473, 1262, 1194, 1090, 896, 827, 586 (Figure S24).

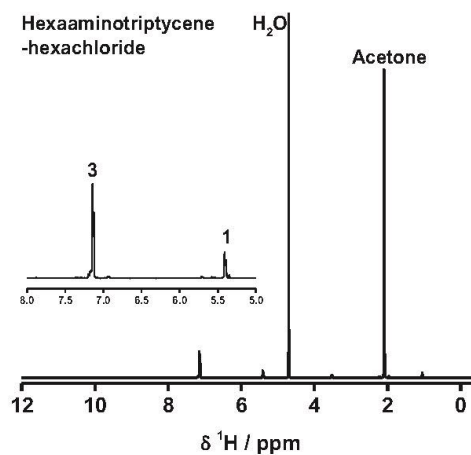
 1H -NMR

Figure S22: 1H NMR spectrum of hexaaminotriptycene hexachloride measured in D_2O .

^{13}C - NMR

Hexaaminotriptycene-hexachloride

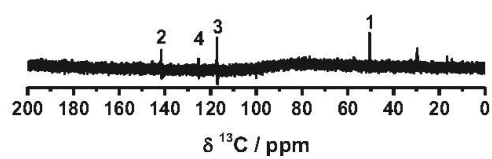


Figure S23: ^{13}C NMR spectrum of hexaaminotriptycene hexachloride measured in D_2O .

IR

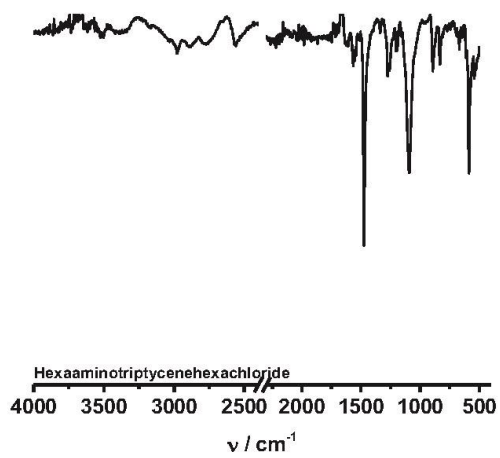
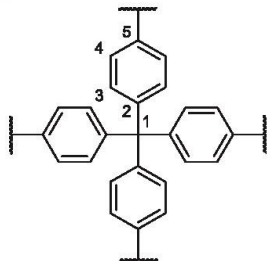
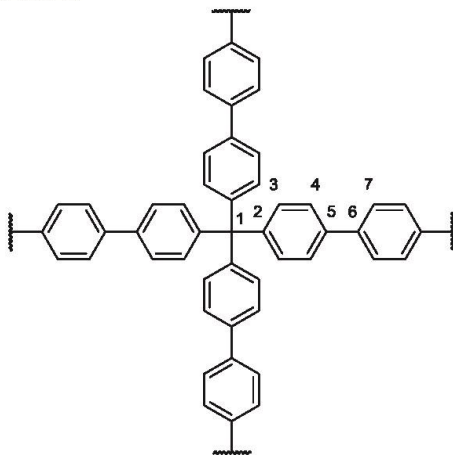


Figure S24: Infrared spectrum of hexaaminotriptycene hexachloride.

Polymer Synthesis*PON-1*

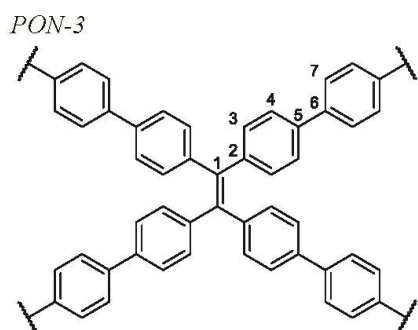
50 ml dry DMF (27 ml/mmol), 1.35 g 2,2-bipyridiyl (8.64 mmol, 1.2 eq.), 2 g Ni(cod)₂ (7.27 mmol, 1 eq.), 0.8 ml cyclooctadiene (8.4 mmol, 1.2 eq.), 50 ml dry THF (21 ml/mmol) and 1.16 g tetrakis(4-bromophenyl)methane (1.82 mmol, 0.22 eq.) were placed in a dry vessel under Ar and stirred for 22 h at room temperature. The mixture was cooled to 0 °C and 50 mL 6 M HCl were added dropwise and stirred overnight (8 h). The resulting solid was filtered, washed with MeOH. Further purification was done via a *Soxhlet* apparatus with MeOH/THF (1:1) for 16 h to yield the product as an off white powder. Yield: 0.59 g (1.85 mmol; 99 %). ¹³C NMR (CP-MAS, 12.5 kHz): δ [ppm] = 145.9 (C-2), 139, 34 (C-5), 131 (C-4), 125.3 (C-3), 64.6 (C-1) (Figure 2). CHN_{Found}: C [89.04], H [5.13], N [0.73]. CHN_{Calc.}: C [94.90], H [5.10], N [0.00]. IR (ATR): ν [cm⁻¹] = 3022, 1602, 1448, 1399, 1336, 1260, 1196, 1069, 1006, 917, 816 (Figure S27)

PON-2

A mixture of 45 ml THF and 5 ml 2 M aqueous K₂CO₃ were refluxed while purged with Ar for 45 min. After cooldown, the mixture was poured in a vessel with 0.41 g tetrakis(4-bromophenyl)methane (6.5·10⁻⁴ mol, 1 eq.), 0.216 g benzene-1,4-diboronic acid (1.3·10⁻³ mol, 2eq.), 0.008 g Pd(PPh₃)₄ (6.5·10⁻⁶ mol, 0.01 eq.), 0.006 g 1,1'-bis(diisopropyl-

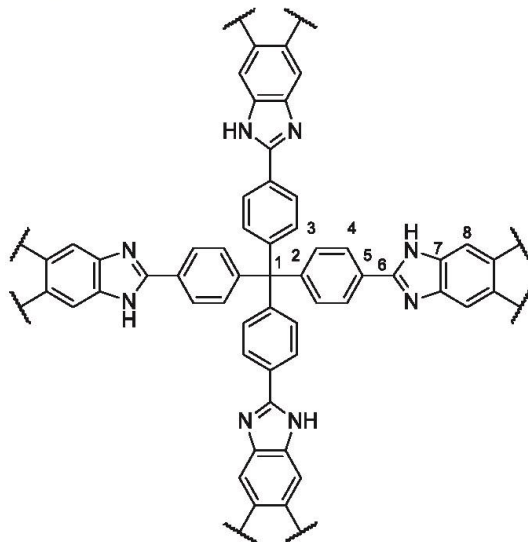
20

phosphino)ferrocene ($1.3 \cdot 10^{-5}$ mol, 0.02 eq.) under dry conditions. The reaction mixtures were refluxed at 100 °C under static Ar atmosphere for 19 h. After cooling down, the resulting solid was filtered, washed with acetone and dried in an oven. Further purification via *Soxhlet* extraction with tetrahydrofuran/methanol (1:1) gave a grey solid. Yield: 0.30 g ($6.54 \cdot 10^{-4}$ mol, 67 %). ^{13}C NMR (CP-MAS, 12.5 kHz): δ [ppm] = 146 (C-2), 139 (C-3, C-5), 131 (C-6), 127 (C-4, C-7), 64 (C-1) (Figure 2). $\text{CHN}_{\text{Found}}$: C [78.73], H [4.44], N [0.26]. $\text{CHN}_{\text{Calc.}}$: C [94.84], H [5.16], N [0.00]. IR (ATR): ν [cm^{-1}] = 3022, 1598, 1484, 1395, 1255, 1167, 1078, 1002, 799, 736 (Figure S27).



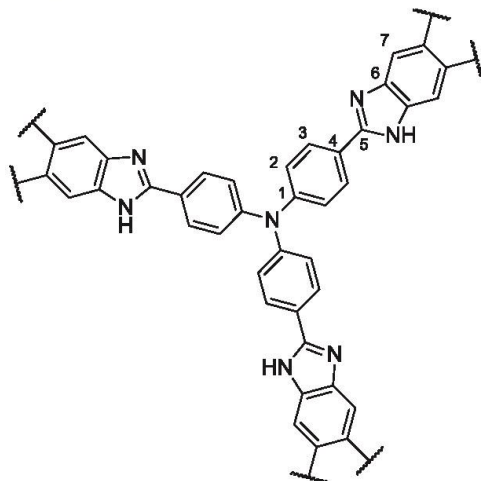
0.50 g of tetrakis(4-bromophenyl)ethene ($7.72 \cdot 10^{-4}$ mol, 1 eq.) and 0.26 g of benzene-1,4-diboronic acid were dissolved in a mixture of 135 ml dimethylformamide and 15 ml 1 M K_2CO_3 . The resulting solution was now degassed by freeze pump thaw cycles (4x). Now 0.120 g of $\text{Pd}(\text{PPh}_3)_4$ ($1.04 \cdot 10^{-4}$, 0.13 eq.) was added and the mixtures was stirred at 90 °C for 23 h under static Ar atmosphere. The resulting solid was filtered, washed with water, methanol and acetone and dried in an oven at 130 °C. Further purification via *Soxhlet*-extraction with tetrahydrofuran/methanol (1:1) gave a green solid. Yield: 0.359 g ($7.46 \cdot 10^{-4}$ mol, 65 %). ^{13}C NMR (CP-MAS, 12.5 kHz): δ [ppm] = 140_{br} (C-5; C-1; C-2), 132_{br} (C-3), 127_{br} (C-6, C-4, C-7) (Figure 2). $\text{CHN}_{\text{Found}}$: C [75.80], H [5.13], N [0.73]. $\text{CHN}_{\text{Calc.}}$: C [94.97], H [5.03], N [0.00]. IR (ATR): ν [cm^{-1}] = 3401, 1613, 1486, 1435, 1359, 1270, 1017, 814 (Figure S27).

PON-4



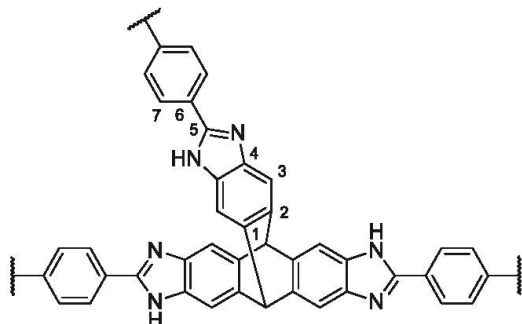
In a dry vessel 0.32 g of 1,2,4,5-benzenetetramine tetrahydrochloride ($1.1 \cdot 10^{-3}$ mol, 2 eq.) was dissolved in 40 ml dry DMF and cooled to -50 °C in a dry-ice/acetone bath. Now 0.24 g of tetrakis(4-formylphenyl)methane ($5.5 \cdot 10^{-4}$ mol, 1 eq.) in 20 ml dry DMF were added dropwise and the reaction mixture was slowly allowed to rise to room temperature. After stirring for 21 h under a static Ar atmosphere, the reaction mixture was flushed with air for 10 minutes, sealed and heated in an oven for 4 days. The resulting solid was filtered and washed with DMF, acetone, 1M HCl, 1M NaOH, H₂O and acetone, respectively. After Soxhlet extraction with DCM/acetone (1:1) for 22 h, the brown polymer was dried in vacuo at 120 °C. Yield: 0.274 g ($4.32 \cdot 10^{-4}$ mol, 79 %). ¹³C NMR (CP-MAS, 12.5 kHz): δ [ppm] = 152 (C-6), 147 (C-2), 142 (C-7), 128_{br} (C-3, C-4, C-5), 99 (C-8), 65 (C-1) (Figure 2). ¹⁵N NMR (CP-MAS, 5.0 kHz): δ [ppm] = -237 (-NH-), -148 (-N-) (Figure 2). CHN_{Found}: C [73.12], H [4.50], N [15.27]. CHN_{Calc.}: C [78.45], H [3.69], N [17.85]. IR (ATR): ν [cm⁻¹] = 3401, 1613, 1486, 1435, 1359, 1270, 1017, 814 (Figure S27).

PON-5



In a dry vessel 0.65 g of 1,2,4,5-Benzenetetramine tetrahydrochloride ($1.52 \cdot 10^{-3}$ mol, 1.5 eq.) was dissolved in 40 ml dry DMF and cooled to -60 °C in a dry ice/acetone bath. Now 0.5 g of tris(4-formylphenyl)amine ($1.52 \cdot 10^{-3}$ mol, 1 eq.) in 20 ml dry DMF were added dropwise and the reaction mixture was slowly allowed to rise to room temperature. After stirring for 16 h under a static Ar atmosphere, the reaction mixture was put under air for 10 minutes, sealed and heated in an oven for 5 days. The resulting solid was filtered and washed with DMF, acetone, 1M HCl, 1M NaOH, H₂O and acetone, respectively. After Soxhlet extraction with DCM/acetone (1:1) for 22 h, the black material was dried in vacuo at 120 °C. Yield: 0.884 g ($1.86 \cdot 10^{-3}$ mol, 99 %). ¹³C-NMR (CP-MAS, 20.0 kHz): δ [ppm] = 152 (C-5), 148 (C-1), 141 (C-6), 128_{br} (C-2, C-3, C-4), 106 (C-7) (Figure 2). ¹⁵N-NMR (CP-MAS, 10 kHz) = -149 (-N=), -241(-NH-), -276 (NR₃) (Figure 2). CHN_{found} [%] = 65.8 (C), 4.2 (H), 17.9 (N); CHN_{calc.} [%]: 70.3 (C), 4.3 (H), 19.3 (N). IR (ATR): ν [cm⁻¹] = 3393, 1593, 1479, 1276, 1188, 1098, 1022, 946, 832, 731 (Figure S27).

PON-6



In a dry vessel 0.1 g of 2,3,6,7,14,15-Hexaaminotriptycene hexachloride ($1.74 \cdot 10^{-4}$ mol, 1 eq.) was dissolved in 30 ml dry DMF and cooled to -40 °C in a dry-ice/acetone bath. Now 0.034 g of terephthalaldehyde ($2.5 \cdot 10^{-4}$ mol, 1.5 eq.) in 20 ml dry DMF were added dropwise and the reaction mixture was slowly warmed to room temperature. After stirring for 21 h under static Ar atmosphere, the reaction mixtures was flushed with air for 10 minutes, sealed and heated in an oven for 4 days. The resulting solid was filtered and washed with DMF, acetone, 1M HCl, 1M NaOH, H₂O and acetone, respectively. After Soxhlet extraction with DCM/acetone (1:1) for 22 h, the yellow polymer was dried in vacuo at 120 °C. Yield: 0.053 g ($1.098 \cdot 10^{-4}$ mol, 65 %). ¹³C NMR (CP-MAS, 12.5 kHz): δ [ppm] = 151 (C-5), 141 (C-2, C-4), 131 (C-6), 128 (C-7), 113 (C-3), 106 (C-3), 55 (C-1) (Figure 2). ¹⁵N NMR (CP-MAS, 10.0 kHz): δ [ppm] = -236 (-NH-), -146 (-N-)(Figure 2). CHN_{Found}: C [67.80], H [4.35], N [14.70]. CHN_{Calc.}: C [79.16], H [3.53], N [17.31]. IR (ATR): ν [cm⁻¹] = 3401, 1617, 1427, 1350, 1325, 1186, 1020, 843, 755, 602 (Figure S27).

Incorporation of Imidazol

For the incorporation of imidazole, the respective polymer was placed on a septum within a glas tube and primary dried for ca. 30 min. Afterwards imidazole was molten and introduced, by vacuum evaporation.



Figure S25: Apparatus for gas phase incorporation of imidazole.

Polymer Analytic

Pore size distribution

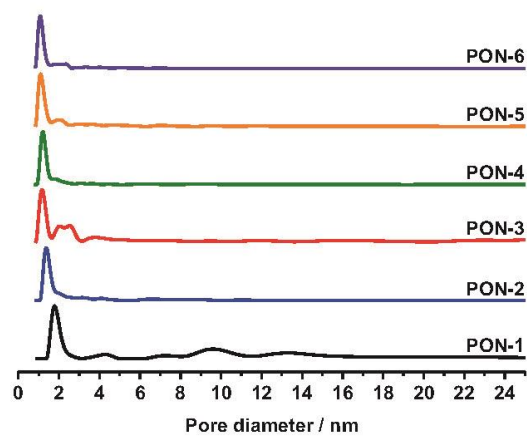


Figure S26: Pore size distribution estimated by argon physisorption isotherms at 87 K.

Infrared Spectroscopy

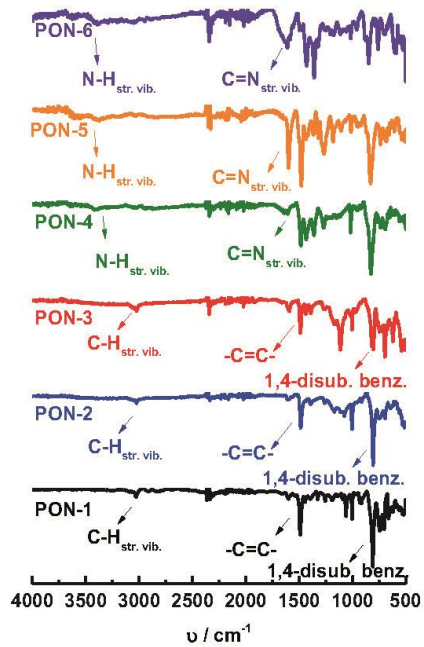


Figure S27: Infrared spectra of PON-1 – PON-6.

Networks after loading with imidazole

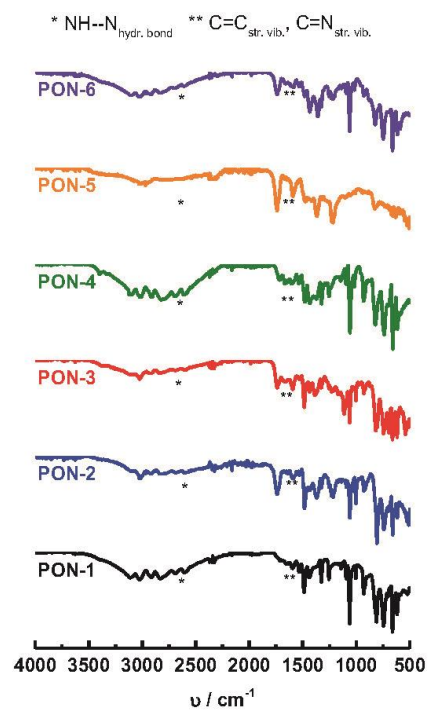


Figure S28: Infrared spectra of PON-1 - PON-6 after loading with imidazole.

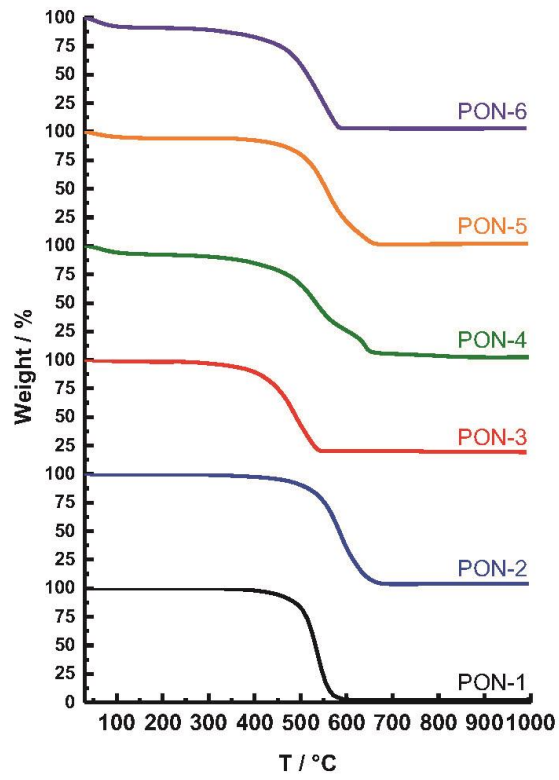
Thermogravimetric analysis

Figure S29: Decomposition curves taken from thermogravimetric analysis of PON-1 - PON-6.

Networks after loading with imidazole

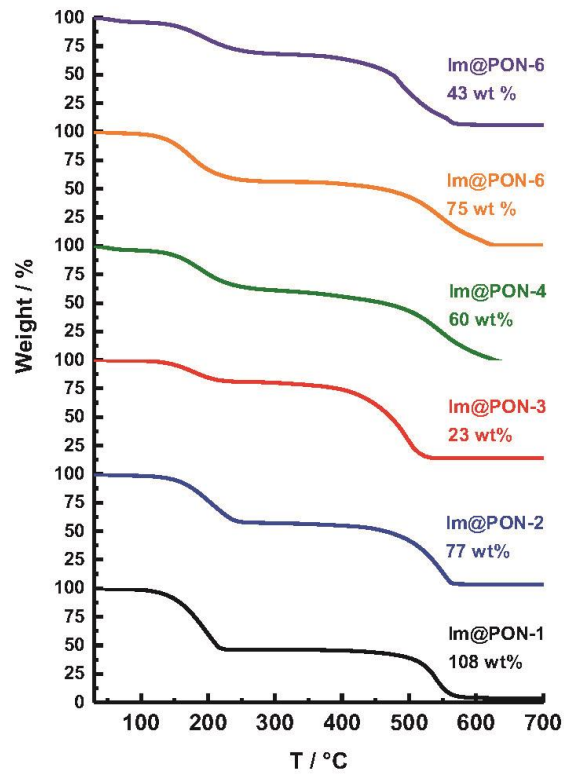
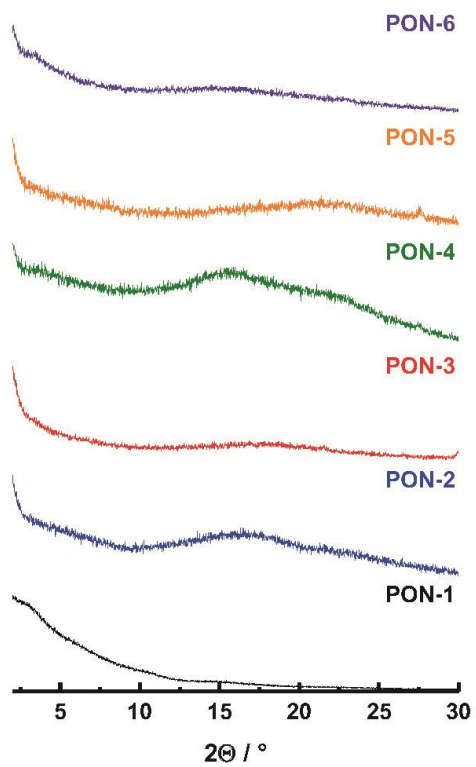


Figure S30: Decomposition curves from thermogravimetric analysis of PON-1 - PON-6, respectively, after loading with imidazole. The decrease of the curve around from 150 to 200 °C is assigned to the removal of imidazole.

Powder X-ray diffraction*Figure S31: Powder x-ray diffractograms of PON-1 - PON-6.*

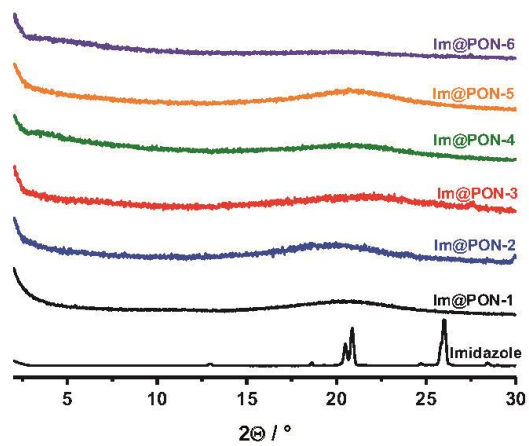


Figure S32: PXRDs of PON-1 - PON-6 after loading with imidazole.

Differential scanning calorimetry

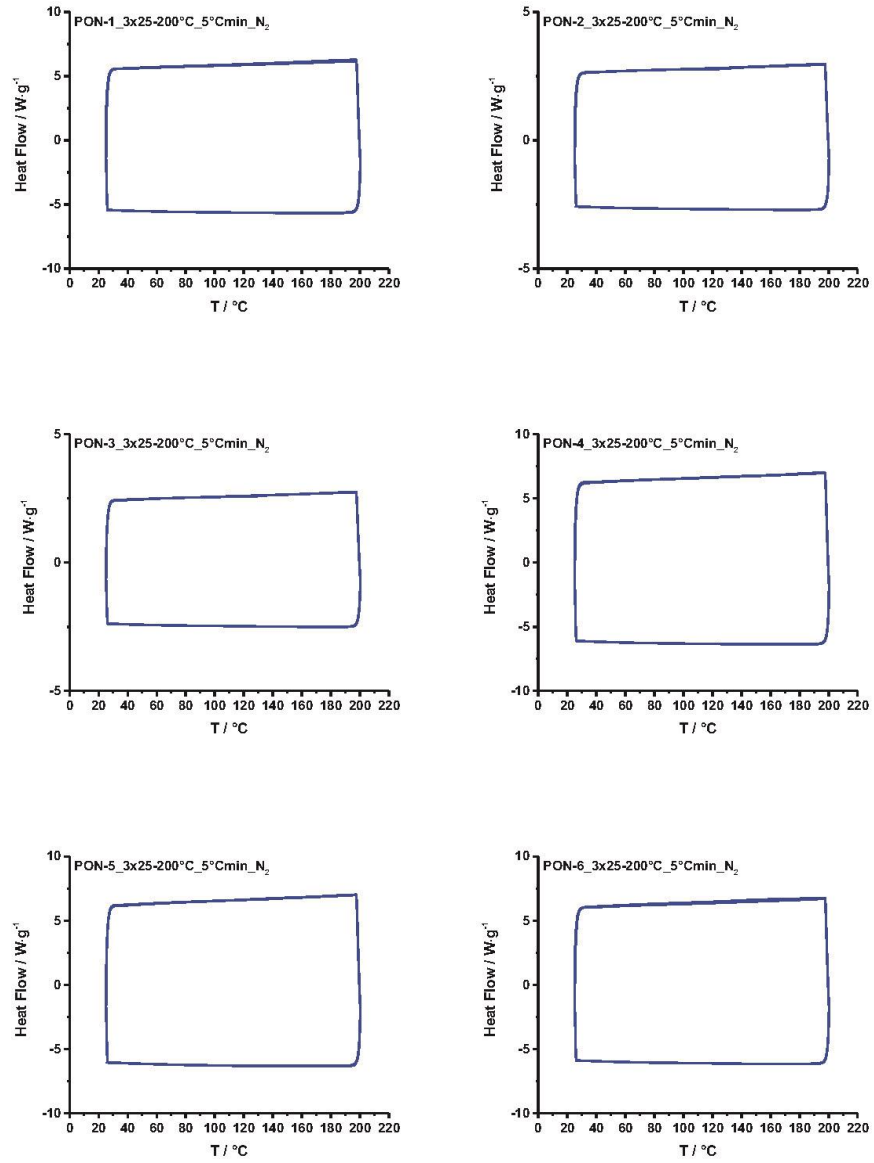


Figure S 33: DSC curves of PON-1 - PON-6 in a temperature range of 25 – 200 °C. The temperature range was cycled for three times to ensure the samples persistence.

Electrochemical impedance spectroscopy

Fitting procedure

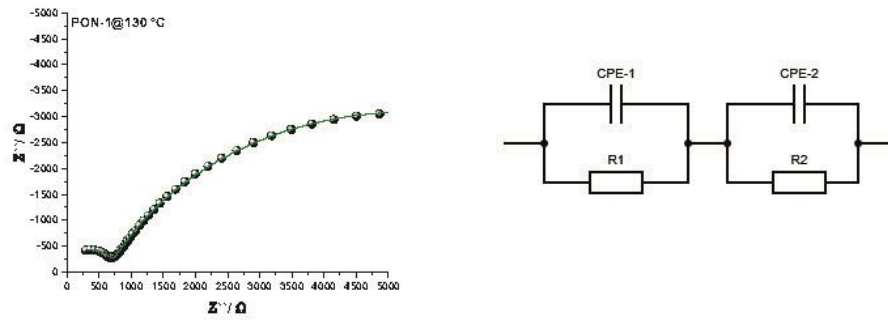


Figure S 34: Nyquist plot of PON-1 at 130 °C (left) fitted with the depicted equivalent circuit (right).

With:

Resistance (R): $Z = R$

Constant Phase Element (CPE): $Z = \frac{1}{T(i\omega)^P}$

Fit-Parameters CPE-T, CPE-P

Table S 1: Fitting parameters for PON-1 at 130 °C

Element	Value	Error	Error %
R2	9326	73.00	0.78
CPE2-T	6.43^{-8}	1.48^{-9}	2.45
CPE2-P	0.74	2.04^{-3}	0.27
R1	577	2.38	0.4
CPE1-T	9.26^{-12}	6.10^{-13}	6.59
CPE1-P	1,12	3.96^{-4}	0.35

With the resistance value (R) of the first semicircle and the pellet parameters (l = length, A=area) calculation of the relative conductivity is done as follows:

$$\kappa = \frac{l}{R \cdot A}$$

⇔

$$\kappa = \frac{0.15 \text{ cm}}{577 \Omega \cdot 0.5027 \text{ cm}^2}$$

⇔

$$\kappa = 5,17 \cdot 10^{-4} \text{ S} \cdot \text{cm}^{-1}$$

PON-1

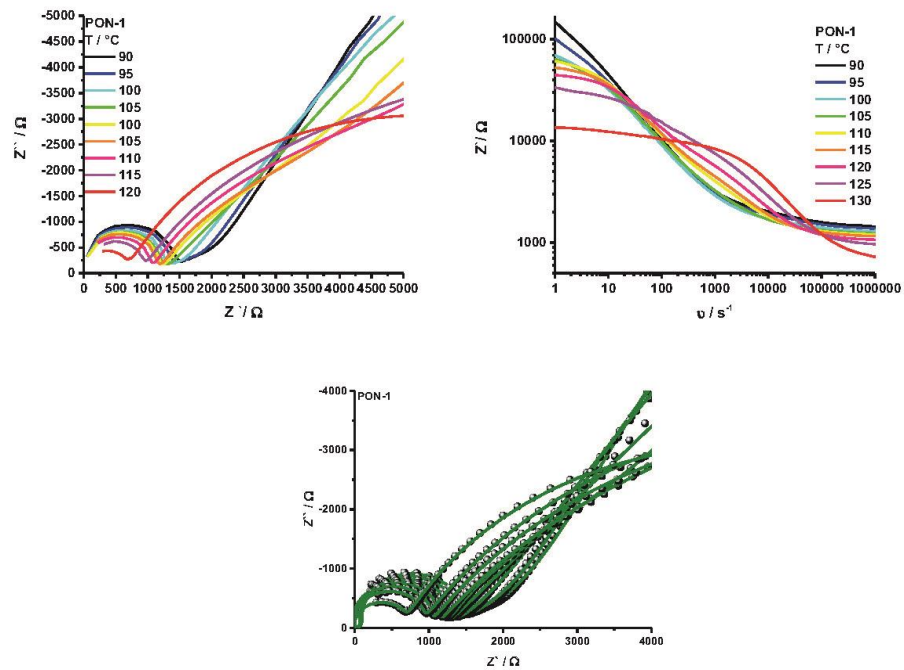


Figure S35: Nyquist (left) and Bode (right) plots of PON-1 measured on a temperature range between 90 °C and 130 °C with a perturbation signal of 20 mV. Nyquist plots with observed data (black circles) and corresponding fits (solid green lines) based on the described equivalent circuit (bottom).

Table S 2: Impedance values found for PON-1 and the respective conductivities (Pellet parameters: $A = 0.5027 \text{ cm}^2$, $l = 0.15 \text{ cm}$).

T / K	Z / Ohm	κ / $\text{S}\cdot\text{cm}^{-1}$
363	1560	$1.91\cdot 10^{-4}$
368	1440	$2.07\cdot 10^{-4}$
373	1301	$2.29\cdot 10^{-4}$
378	1181	$2.53\cdot 10^{-4}$
383	1060	$2.82\cdot 10^{-4}$
388	1075	$2.78\cdot 10^{-4}$
393	971	$3.07\cdot 10^{-4}$
398	857	$3.48\cdot 10^{-4}$
403	577	$5.17\cdot 10^{-4}$

PON-2

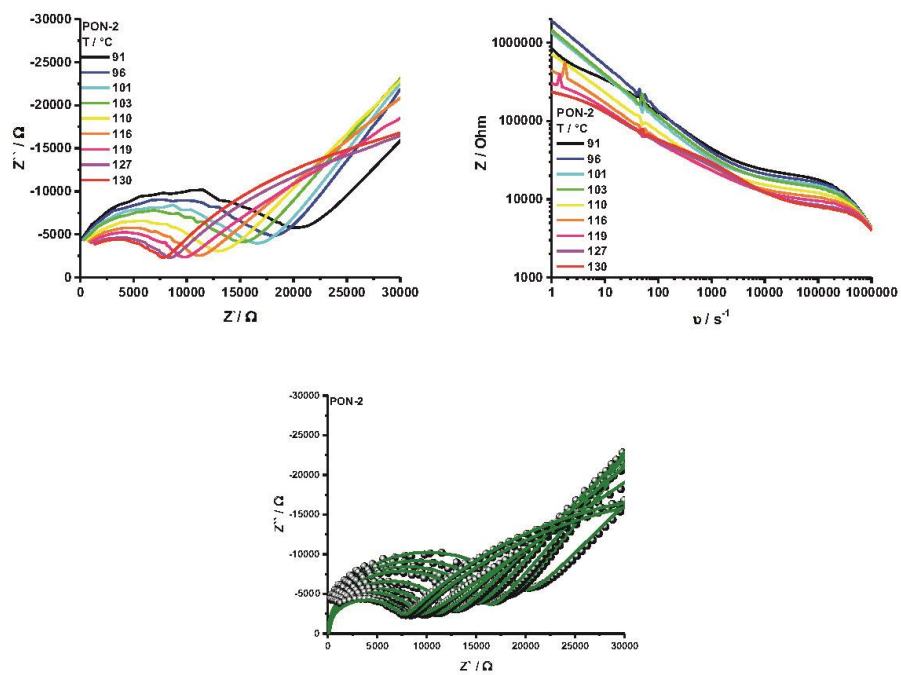


Figure S36: Nyquist (left) and Bode (right) plots of PON-2 measured on a temperature range between 90 °C and 130 °C with a perturbation signal of 10 mV. Nyquist plots with observed data (black circles) and corresponding fits (solid green lines) based on the described equivalent circuit (bottom).

Table S 3: Impedance values found for PON-2 and the respective conductivities (Pellet parameters: $A = 0.5027 \text{ cm}^2$, $l = 0.23 \text{ cm}$).

T / K	Z / Ohm	κ / $\text{S}\cdot\text{cm}^{-1}$
364	18995	$2.41\cdot 10^{-5}$
369	17011	$2.69\cdot 10^{-5}$
374	15888	$2.88\cdot 10^{-5}$
376	14069	$3.25\cdot 10^{-5}$
383	12107	$3.78\cdot 10^{-5}$
389	9665	$4.73\cdot 10^{-5}$
392	7941	$5.76\cdot 10^{-5}$
400	6741	$6.79\cdot 10^{-5}$

PON-3

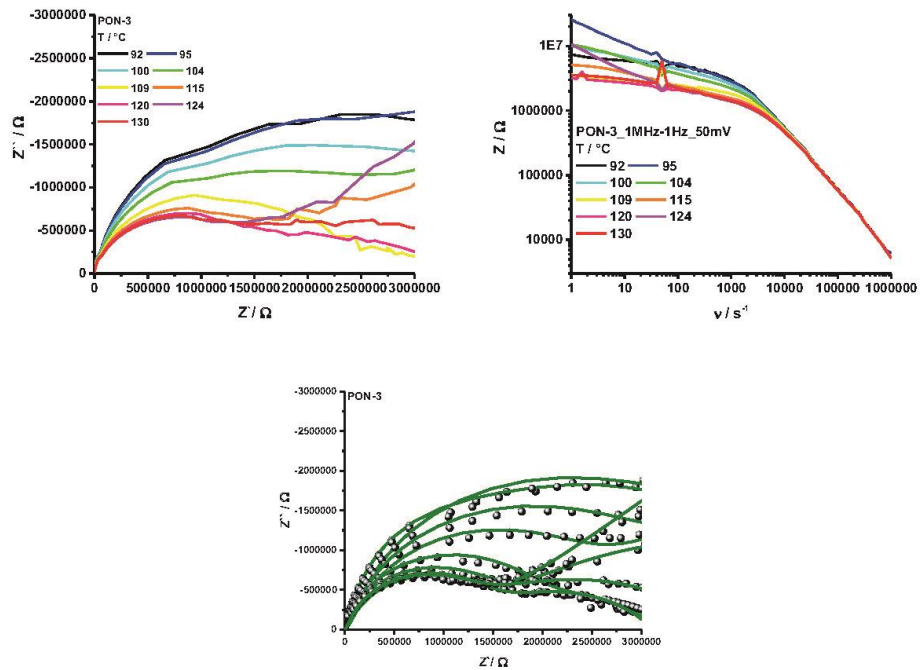


Figure S37: Nyquist (left) and Bode (right) plots of PON-3 measured on a temperature range between 90 °C and 130 °C with a perturbation signal of 50 mV. Nyquist plots with observed data (black circles) and corresponding fits (solid green lines) based on the described equivalent circuit (bottom).

Table S 4: Impedance values and the respective conductivities found for PON-3 (Pellet parameters: $A = 0.5027 \text{ cm}^2$, $l = 0.25 \text{ cm}$).

T / K	Z / Ohm	κ / $\text{S}\cdot\text{cm}^{-1}$
365	$4.51 \cdot 10^{-6}$	$5.54 \cdot 10^{-8}$
368	$4.12 \cdot 10^{-6}$	$6.06 \cdot 10^{-8}$
373	$3.41 \cdot 10^{-6}$	$7.33 \cdot 10^{-8}$
377	$2.29 \cdot 10^{-6}$	$1.09 \cdot 10^{-7}$
382	$1.83 \cdot 10^{-6}$	$1.37 \cdot 10^{-7}$
388	$1.42 \cdot 10^{-6}$	$1.76 \cdot 10^{-7}$
393	$1.36 \cdot 10^{-6}$	$1.84 \cdot 10^{-7}$
397	$1.20 \cdot 10^{-6}$	$2.08 \cdot 10^{-7}$

PON-4

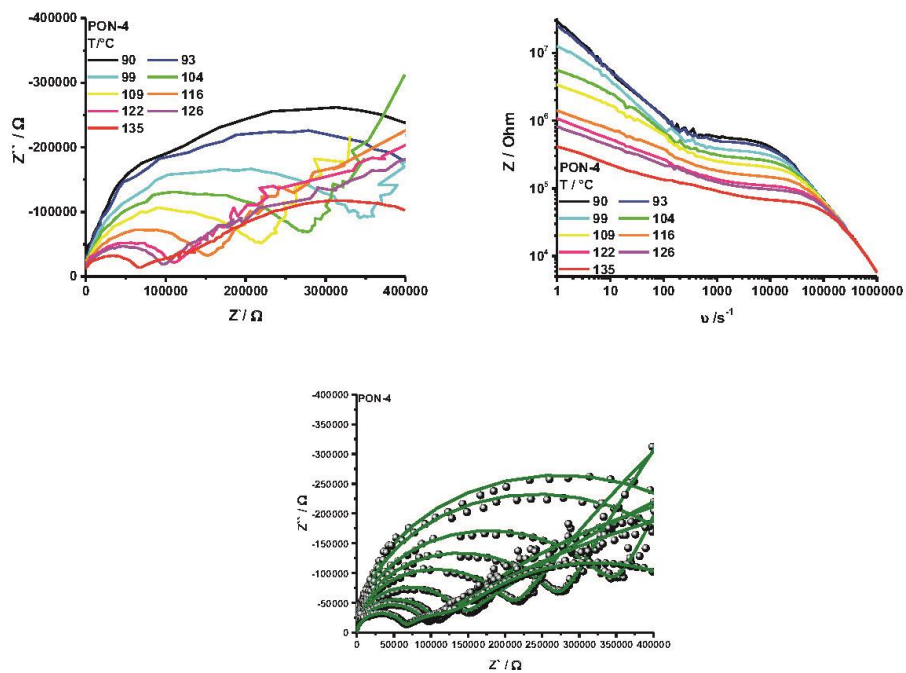


Figure S38: Nyquist (left) and Bode (right) plots of PON-4 measured on a temperature range between 90 °C and 130 °C with a perturbation signal of 10 mV. Nyquist plots with observed data (black circles) and corresponding fits (solid green lines) based on the described equivalent circuit (bottom).

Table S 5: Impedance values and the respective conductivities found for PON-4 (Pellet parameters: $A = 0.5027 \text{ cm}^2$, $l = 0.30 \text{ cm}$).

T / K	Z / Ohm	κ / $\text{S}\cdot\text{cm}^{-1}$
363	507840	$1.18\cdot 10^{-6}$
366	448110	$1.33\cdot 10^{-6}$
372	327400	$1.82\cdot 10^{-6}$
377	255510	$2.34\cdot 10^{-6}$
382	195750	$3.05\cdot 10^{-6}$
389	135960	$4.39\cdot 10^{-6}$
395	105300	$5.67\cdot 10^{-6}$
399	93489	$6.38\cdot 10^{-6}$
408	61432	$9.71\cdot 10^{-6}$

PON-5

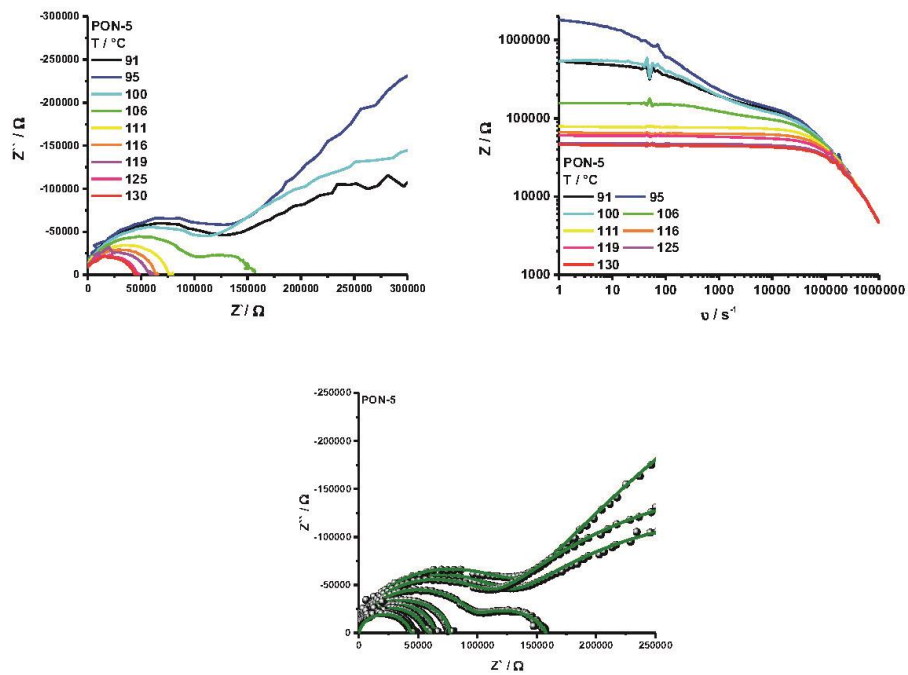


Figure S39: Nyquist (left) and Bode (right) plots of PON-5 measured on a temperature range between 90 °C and 130 °C with a perturbation signal of 10 mV. Nyquist plots with observed data (black circles) and corresponding fits (solid green lines) based on the described equivalent circuit (bottom).

Table S 6: Impedance values and the respective conductivities found for PON-5 (Pellet parameters: $A = 0.5027 \text{ cm}^2$, $l = 0.40 \text{ cm}$).

T / K	Z / Ohm	κ / $\text{S}\cdot\text{cm}^{-1}$
364	113300	$7.02\cdot 10^{-6}$
368	115540	$6.89\cdot 10^{-6}$
373	99957	$7.96\cdot 10^{-6}$
379	94459	$8.42\cdot 10^{-6}$
384	73708	$1.08\cdot 10^{-5}$
389	63409	$1.26\cdot 10^{-5}$
392	56429	$1.41\cdot 10^{-5}$
398	43897	$1.81\cdot 10^{-5}$
403	41940	$1.90\cdot 10^{-5}$

PON-6

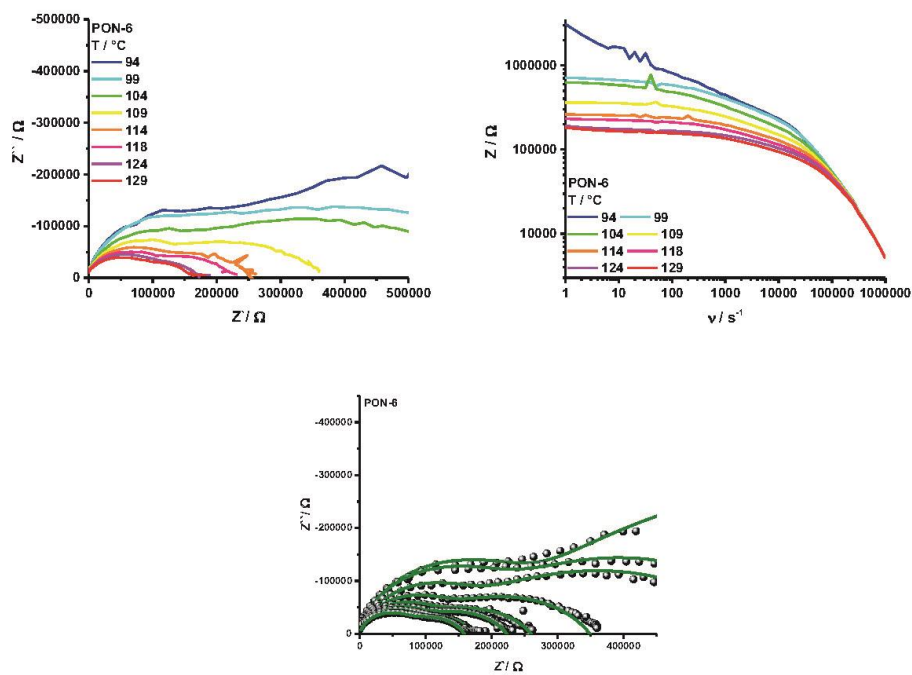


Figure S40: Nyquist (left) and Bode (right) plots of PON-6 measured on a temperature range between 90 °C and 130 °C with a perturbation signal of 10 mV. Nyquist plots with observed data (black circles) and corresponding fits (solid green lines) based on the described equivalent circuit (bottom).

Table S 7: Impedance values and the respective conductivities found for PON-5 (Pellet parameters: $A = 0.5027 \text{ cm}^2$, $l = 0.15 \text{ cm}$).

T / K	Z / Ohm	κ / $\text{S}\cdot\text{cm}^{-1}$
367	208180	$1.43 \cdot 10^{-6}$
372	183340	$1.63 \cdot 10^{-6}$
377	144060	$2.07 \cdot 10^{-6}$
382	116740	$2.56 \cdot 10^{-6}$
387	98770	$3.02 \cdot 10^{-6}$
391	84472	$3.53 \cdot 10^{-6}$
397	72242	$4.13 \cdot 10^{-6}$
402	61263	$4.87 \cdot 10^{-6}$

Arrhenius Plot

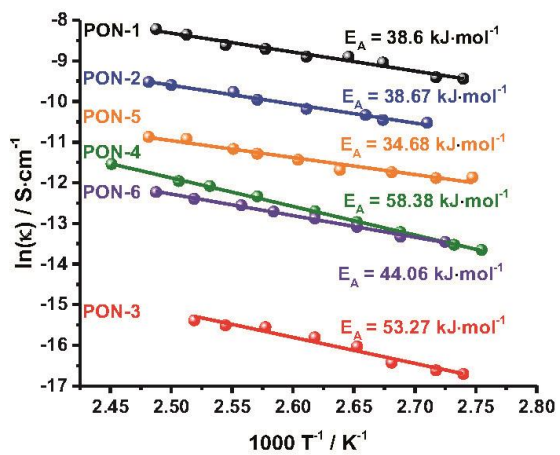


Figure S 41: Arrhenius Plots of all polymers.

Literatur

- 1 H. Qian, S. Li, J. Zheng and S. Zhang, *Langmuir*, 2012, **28**, 17803–17810.
- 2 Y. He, S. Xiang and B. Chen, *J. Am. Chem. Soc.*, 2011, **133**, 14570–3.
- 3 P. Wessig, M. Gerngroß, S. Pape, P. Bruhns and J. Weber, *RSC Adv.*, 2014, **4**, 31123–31129.
- 4 Z. Chang, Y. Jiang, B. He, J. Chen, Z. Yang, P. Lu, H. S. Kwok, Z. Zhao, H. Qiu, B. Z. Tang, I. D. et al., *Chem. Commun.*, 2012, **49**, 1–3.
- 5 N. G. White and M. J. MacLachlan, *J. Org. Chem.*, 2015, **80**, 8390–8397.
- 6 M. Mastalerz, S. Sieste, M. Cenić and I. M. Oappel, *J. Org. Chem.*, 2011, **76**, 6389–6393.

6. Anhang

Die folgenden Ausführungen sollen dem weiteren Verständnis der, die impedanzspektroskopischen Untersuchungen betreffenden, zugrundeliegenden Mechanismen dienen. Es sei erwähnt, dass es sich hierbei lediglich um eine Auswahl einiger für den Anwendungsalltag potentiell interessanter Hintergründe handelt. Für ein tiefergehendes Studium impedanzspektroskopischer Grundlagen seien die Werke von McDonald¹⁰⁴, Lasia¹⁰⁰ und Zhang et al.³⁷ empfohlen. Hinsichtlich grundlegender Untersuchungen der Ionenleitung haben sich die Arbeiten von D. Kreuer und W. H. Meyer als aufschlussreich erwiesen.^{105–112}

6.1 Frequenzabhängigkeit von Ionenleitern

Die Frequenzabhängigkeit von Ionenleitern kann durch das von K. Funke entwickelte Sprung-Relaxationsmodell beschrieben werden.^{113,114} Ausgangspunkt bildet ein bewegliches, geladenes Ion, welches durch eine äußere Kraft, z. B. das Anlegen einer Spannung, eine Dislokation, erfährt. Der induzierte Sprung des Teilchens auf eine neue Position führt zu einem Wechsel der Umgebungsbedingungen, welche auf dieses wirken, wie z.B. abstoßende Coulomb-Kräfte gleichgeladener Ionen. Im Folgenden sind nun zwei Szenarien möglich. Die abstoßenden Kräfte der neuen Umgebung induzieren einen Rücksprung in die energetisch günstigere Ursprungsposition, das System kehrt somit in den Ausgangszustand zurück. Ein Sprung des Ions mit anschließendem Rücksprung wird gemeinhin als „erfolglos“ bezeichnet. Alternativ kann sich die neue Umgebung des Teilchens an die veränderten Bedingungen anpassen, z.B. durch weitere Ionenbewegungen, und somit eine relaxationsbedingte Veränderung der Potentiallandschaft induzieren, was im Verbleib des Ions an der neuen Position resultiert. Ein derartiger Sprung ist somit als „erfolgreich“ zu bezeichnen.¹¹³

Die bei einer Messung angelegte Frequenz kann als inverses Zeitfenster der Abbildung ionischer Hüpfprozesse angesehen werden. Je höher also die angelegte Frequenz, desto kürzer das abgebildete Zeitfenster, in welchem etwaige Ionensprünge beobachtet werden. Im gleichen Maße nimmt somit auch die Wahrscheinlichkeit der Detektion vermeintlich „erfolgreicher“ Ionensprünge zu, da deren Rücksprung außerhalb eines begrenzten Zeitfensters liegt. In Folge dessen steigt die vermeintliche Leitfähigkeit eines Systems mit steigender Frequenz. Im Umkehrschluss nimmt bei abnehmender Frequenz das abgebildete Zeitfenster zu und somit auch die Wahrscheinlichkeit der Detektion wahrer „erfolgreicher“ Ionensprünge.

Bei der Impedanzspektroskopie lassen sich bei Auftragung des gemessenen Widerstands als Funktion der Frequenz (Bode-Auftragung) die beschriebenen Prozesse in die folgenden Bereiche gliedern (vergl. Abb. 18). Im Hochfrequenzbereich ($\omega \rightarrow \infty$, Abb. 18)) sind alle

Ionensprünge vermeintlich erfolgreich und tragen somit zur Leitfähigkeit bei. Es bildet sich ein sogenannter Hochfrequenzplateaubereich. Es sei erwähnt, dass das Erreichen des Hochfrequenzplateaus extrem hoher Frequenzen bedarf und somit meist außerhalb applikativer Bemühungen liegt. Aus der Abnahme der Frequenz resultiert im Folgenden ein Dispersionsbereich, da sich das Zeitfenster für Rücksprünge erhöht bis bei $\omega \rightarrow 0$ nur noch wahrhaft „erfolgreiche“ Sprünge abgebildet werden. Das hieraus resultierende Plateau wird als Gleichstromplateaubereich bezeichnet, welches nunmehr die wahre Leitfähigkeit eines Systems widerspiegelt.

6.2 Ersatzschaltkreise

Ein zwischen zwei Elektroden eingespanntes Material kann durch einen einfachen, parallelen Ersatzschaltkreis des RC-Typs beschrieben werden, in welchem R_∞ den Gesamtwiderstand (Bulk Widerstand) und C_∞ die geometrische Kapazität, welche aus der Probenmorphologie erwächst, wiedergibt (Abb. 18).¹⁰⁴

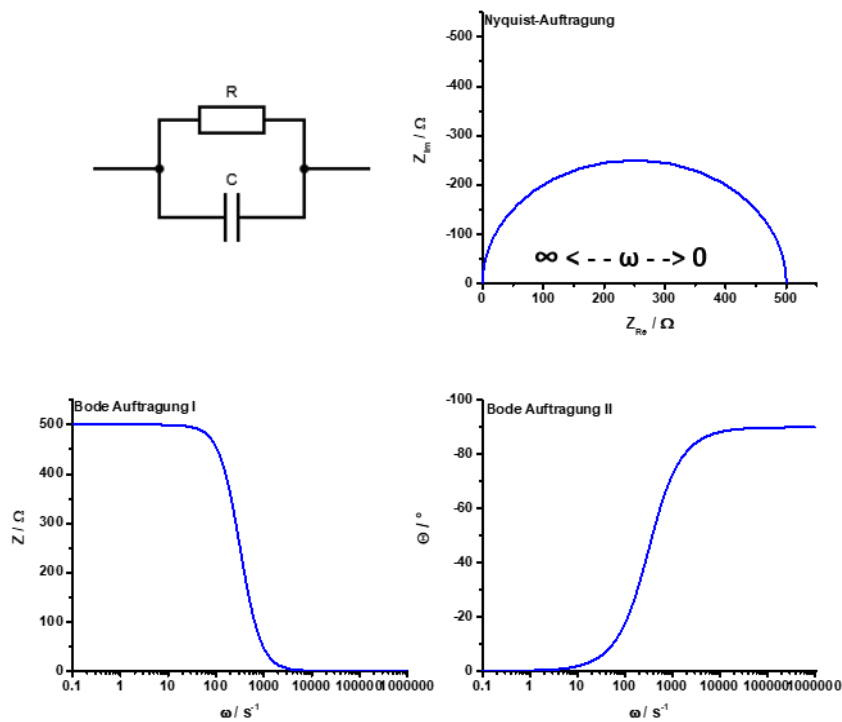


Abbildung 18: Einfacher RC Schaltkreis zur Darstellung eines vollständigen Impedanz Datensatzes mit Nyquist und Bode Auftragungen. Der Widerstand wurde mit 500 Ohm, die Kapazität mit 10^{-6} Farad gewählt. Der abgebildete Frequenzbereich beträgt 0.1 Hz – 1 MHz.

Aus dieser ergibt sich nach Gleichung (18)

$$\tau_D = R_\infty \cdot C_\infty \quad (18)$$

die dielektrische Relaxation τ_D eines Materials. Diese nimmt oft kleinste Werte ($< 10^{-7}$ s) an und kann somit nur teilweise mit dem gewählten Frequenzbereich abgebildet werden. Der typische Frequenzbereich bei impedanzspektroskopischen Untersuchungen liegt zwischen 10^{-1} s und 10^{-6} s. Die Folge sind somit unvollständige bzw. nur angedeutete Impedanzbögen in der Nyquist-Auftragung. Ein Lösungsansatz bildet hier die Herabsenkung der Temperatur, welche zu einer Erhöhung von τ_D führt und somit zu einer Verschiebung des Impedanzbogens in einen vollständig abbildbaren Bereich.

Oft werden neben dem *Bulk* Widerstand R_1 und geometrischer Kapazität C_1 auch heterogene Elektrodenreaktionen bei der Aufnahme eines impedanzspektroskopischen Datensatzes erfasst. Diese können durch einen weiteren Schaltkreis mit R_2 für den Reaktionswiderstand und C_2 für die diffuse Doppelschichtkapazität, welche sich am Material-Elektrodenübergang bildet, dargestellt werden. Ein Beispiel für einen derartigen Doppelschaltkreis ist in Abbildung 19 dargestellt.

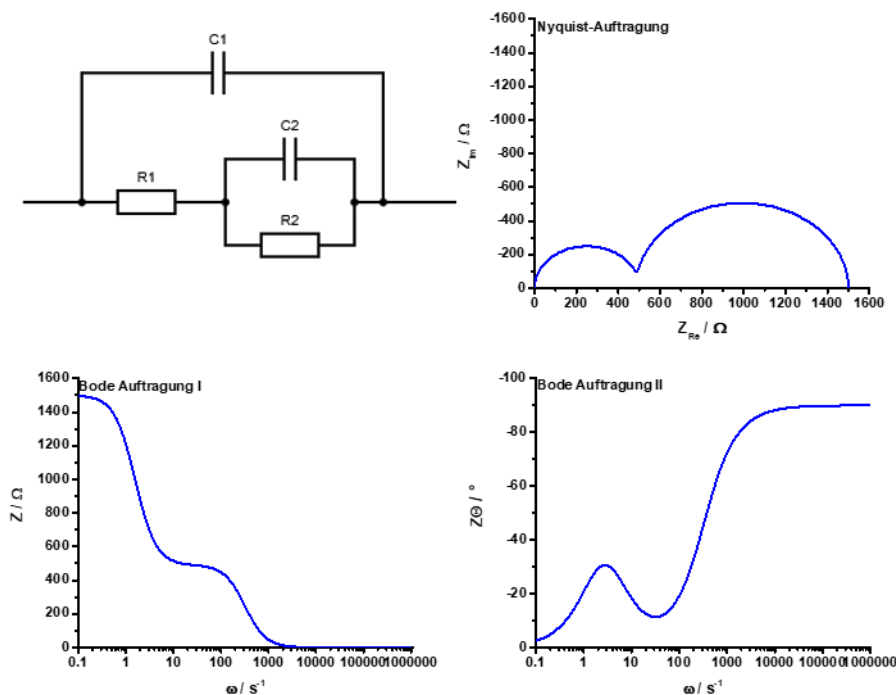


Abbildung 19: Ersatzschaltkreis nebst Nyquist und Bode-Auftragung für die Impedanz eines Bulk-Materials nebst heterogener Elektrodenreaktionen. Für letztere wurde R_2 mit 1000 Ohm und C_2 mit 10^{-4} Farad gewählt. Der abgebildete Frequenzbereich beträgt 0.1 Hz – 1 MHz.

Hier ist deutlich die Ausbildung zweier Halbkreise zu erkennen, aus welchen sich leicht die Widerstände der einzelnen Prozesse ableiten lassen. In der Bode Auftragung entsprechen diese den einzelnen Plateaus. Es sei erwähnt, dass für eine derartige Auflösung die Zeitkonstanten τ der einzelnen Prozesse, zu erkennen in der Bode Auftragung II, sich um mindestens zwei Größenordnungen unterscheiden müssen (Abb. 20). Wie bereits erwähnt, liegt die dielektrische Relaxationszeit des Bulkprozesses meist außerhalb des

betrachteten Zeitfensters, was zu einer unvollständigen Darstellung des entsprechenden Impedanzbogens führt. Dies kann mitunter zur ausschließlichen Darstellung des zweiten Bogens führen, sollten die Prozesse des $R_{\infty}C_{\infty}$ Kreises außerhalb des gewählten Frequenzbereichs liegen. Ein derartiger Fall ist in Abbildung 20 dargestellt.

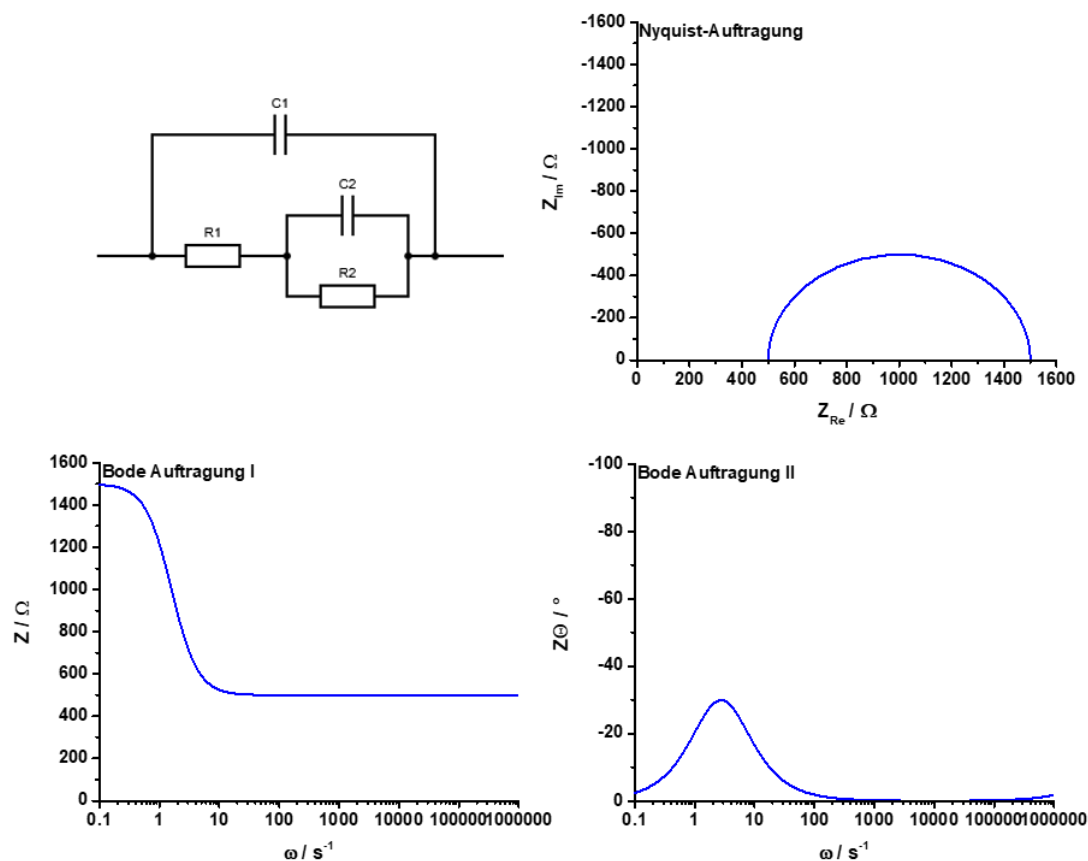


Abbildung 20: Darstellung eines Ersatzschaltkreises für Prozesse, welche teilweise außerhalb des Beobachtungsrahmens liegen. C_1 wurde mit 10^{-11} Farad gewählt, die übrigen Parameter gleichen den vorherigen. Der abgebildete Frequenzbereich beträgt $0,1 \text{ Hz} - 1 \text{ MHz}$.

6.3 Spezielle elektronische Elemente

Die oben dargestellten Ersatzschaltkreise stellen Beispiele bei idealisierten Bedingungen dar. Oft, bzw. gerade bei der Messung von porösen Oberflächen beziehungsweise Pulvermaterialien treten beispielsweise an den Übergangsschichten zwischen Elektroden und Material Effekte auf, die maßgeblichen Einfluss auf das Leitfähigkeitsverhalten zeigen können. Als solche sind beispielsweise Oberflächendefekte, Risse im Material, lokale Ladungsinhomogenitäten, adsorbierte Moleküle oder eine Variation in der chemischen Zusammensetzung zu nennen. Es sei an dieser Stelle erwähnt, dass die Impedanzspektroskopie nur das Verhalten des Gesamtmaterials widerspiegelt, man also einen gemittelten Effekt potentiell beeinflussender Effekte betrachtet.¹⁰⁴ In der Nyquist

Auftragung können sich derartige Effekte durch eine Veränderung des abgebildeten Ersatzschaltkreises darstellen (Tab. 1).¹⁰⁴

*Tabelle 1: Veränderungen des abgebildeten Impedanzbogens und deren mögliche Ursachen.*¹⁰⁴

Effekt	Mögliche Ursache
Verschiebung des Impedanzbogens auf der x-Achse (Realteil)	⇒ Relaxationszeiten vorgeschalteter Prozesse liegen außerhalb des beobachteten Frequenzbereichs ⇒ $R > 0$
Impedanzbogen ist gestaucht/gestreckt, das Zentrum des Halbkreises liegt unter/über der x-Achse	⇒ Vorhandensein weiterer spezifischer Eigenschaften/Prozesse, welche die Darstellung durch spezielle elektronische Elemente bedürfen.
Verzerrung des Impedanzbogens	⇒ Einfluss durch weitere Relaxationen mit ähnlichen Zeitkonstanten. Somit verlaufen mitunter zwei Bögen teilweise oder auch vollständig ineinander.

Da die Verschiebung des Impedanzbogens entlang der x-Achse sowie auf dessen Verzerrung durch Prozesse mit ähnlicher Zeitkonstante τ bereits im vorherigen Abschnitt behandelt wurden, sollen im Folgenden nur auf den Einfluss morphologischer bzw. diffusionsgetriebener Prozesse eingegangen werden.

Ist bei einem Elektroden-Material Aufbau die Kinetik des Ladungstransfer der limitierende Faktor, sprich also langsamer als die Diffusion der Ionen durch den Elektrolyten, spricht man von kinetischer Kontrolle. Die Folge ist der typische Impedanzbogen, welcher aus dem elektrochemischen Ladungstransfer an der Elektroden – Elektrolyt- Kontaktschicht erwächst. Steht ein System dagegen unter Diffusionskontrolle, sprich ist die Diffusion der Ionen durch den Elektrolyten langsamer als der Ladungstransfer an der Elektroden-Elektrolyt Oberfläche, zeigt sich ein Linearverhalten in Form einer 45° Linie in der Nyquist Abbildung. Der zugrundeliegende Prozess wird als Warburg Impedanz bezeichnet und lässt sich durch (19) darstellen,

$$W = \sigma\omega^{-0.5} - i\sigma\omega^{-0.5} \quad (19)$$

wobei ω der Frequenz entspricht und σ eine vom Diffusionspotential der beteiligten Ionen abhängige Konstante darstellt (20).^{37,104}

$$\sigma = \frac{RT}{n^2 F^2 \sqrt{2}} \left[\frac{\beta_0}{D_0^{0.5}} \right] - \left[\frac{\beta_R}{D_R^{0.5}} \right] \quad (20)$$

In Abbildung 21 ist die Einfluss des Warburg Elements leicht an der 45° Linie im Anschluss an den Impedanzbogen des Bulk Widerstandes R_∞ zu erkennen. Bei der hier gewählten Form läuft die Warburg Impedanz bei sehr niedrigen Frequenzen in einen endgültigen Widerstandswert, ein Verlauf der auch als *Finite Length Warburg Element* bezeichnet wird (Abb. 23).¹⁰⁰

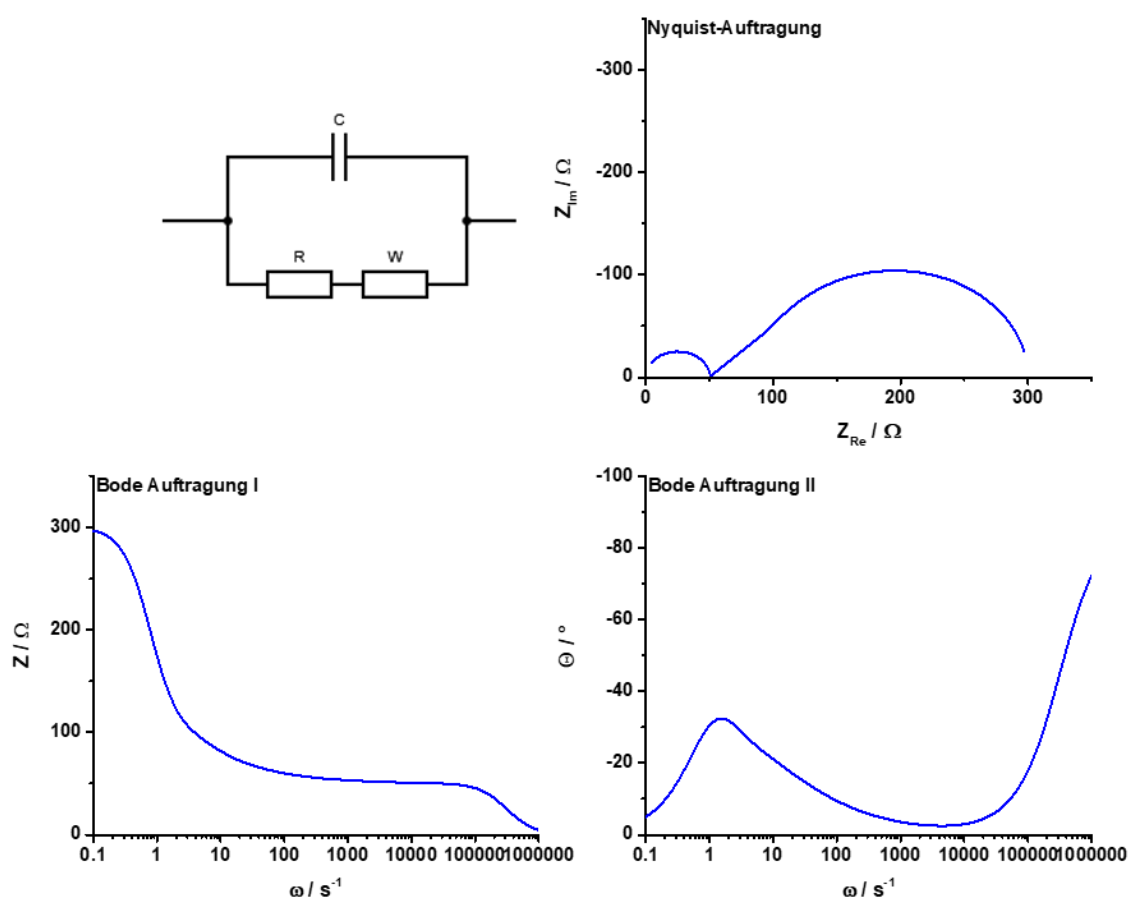


Abbildung 21: RC Ersatzschaltkreis mit implementierter Warburg Impedanz. R_∞ wurde mit 50 Ohm und C_∞ mit 10^{-8} Farad gewählt. Das Warburg Element besteht aus $W_R = 250$, $W_T = 0,5$ und $W_P = 0.5$ (s. ZView Software). Der abgebildete Frequenzbereich beträgt 0.1 Hz – 1 MHz.

Häufiger noch als ein Warburg Element, findet das so genannte *constant phase element* (CPE) Anwendung, mit dem sich beispielsweise Verzerrungen von Impedanzbögen, wie sie beispielsweise auf Grund von Inhomogenitäten des zu untersuchenden Materials auftreten, wiedergeben lassen. Tatsächlich handelt es sich hierbei um ein generalisiertes Element, welches durch Gleichung (21) beschrieben werden kann,

$$Z_{CPE}(\omega) = q^{-1} \cdot (i \cdot \omega)^{-n} \quad (21)$$

wobei q einen numerischen Proportionalitätsfaktor darstellt und n die Phasenverschiebung charakterisiert (Abb. 22). In Abhängigkeit des Faktors n kommt dem CPE unterschiedliche Bedeutung zu, sei es als Kapazität, Widerstand, Spule oder Warburg Element (Tab. 2).³⁷

Tabelle 2: Beschreibung verschiedener Einsatzbereiche für das constant phase element (CPE) in Abhängigkeit der Phasenverschiebung n .

n	Bereich (ε)	Zuordnung	Anwendung
$n = 1 - \varepsilon$	$0 < \varepsilon < 0.2$	Kapazität	Raue Elektrodenoberfläche, Ladungsträgerverteilung
$n = 0.5 \pm \varepsilon$	$0 < \varepsilon < 0.1$	Warburg Element	Diffusionsprozesse
$n = 0 \pm \varepsilon$	$0 < \varepsilon < 0.2$	Widerstand	Verzerrte Widerstände
$N < 0$	-	Spule	Induktive Energieakkumulation

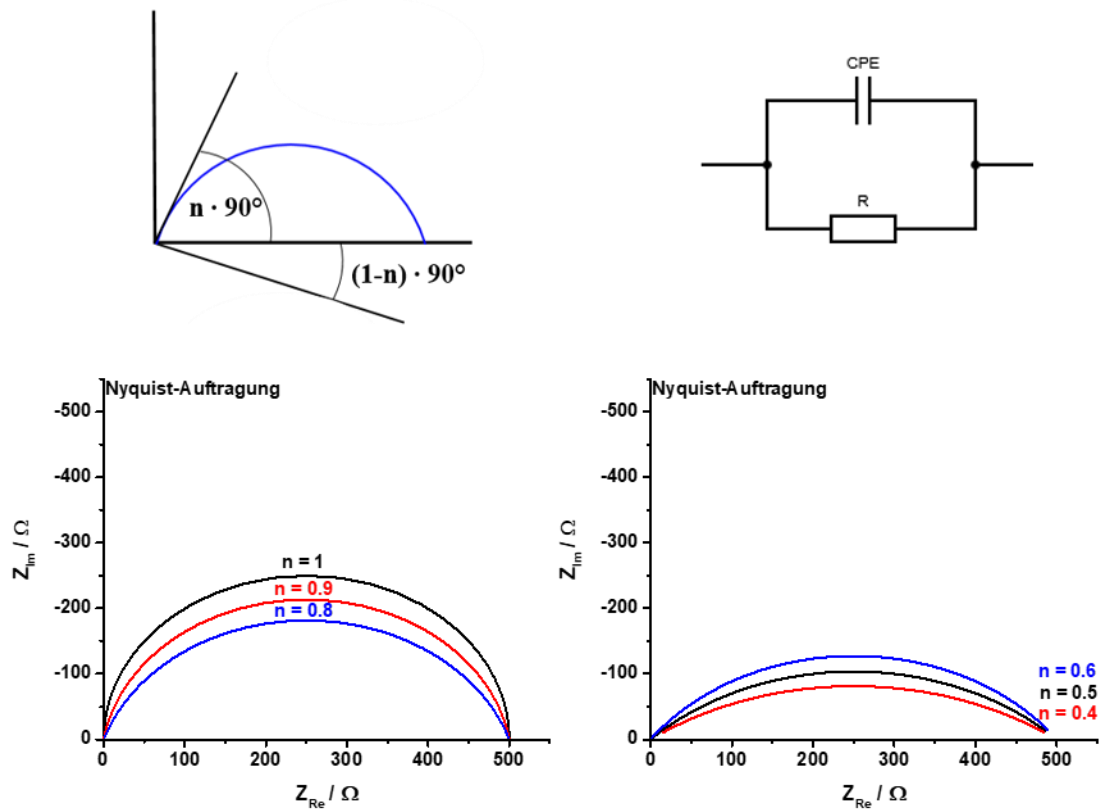


Abbildung 22: Die dem CPE zugrunde liegende Verschiebung des Impedanzbogens, nebst Ersatzschaltkreis. Nyquist Auftragung für des RCPE-Schaltkreise für das CPE als Kapazität (links, $R = 500, q = 10^{-6}, n = 1.0, 0.9, 0.8$) und Warburg Element (rechts, $R = 500, q = 10^{-4}, n = 0.6, 0.5, 0.4$), wobei der Einfluss des Exponent n hervorgehoben wurde.

Erklärung

Erklärung

Hiermit versichere ich eidesstattlich, dass die vorliegende Arbeit von mir selbst verfasst und für ihre Anfertigung keine anderen, als die angegebenen Quellen benutzt wurden (vgl. Art. 64 Abs. 1 Satz 6 BayHSchG) (§ 8 Satz 2 Nr. 3 PromO Fakultät).

Ferner versichere ich, dass diese Dissertation nicht bereits zur Erlangung eines akademischen Grades eingereicht und weder diese noch eine gleichartige Doktorprüfung endgültig nicht bestanden wurde (§ 8 Satz 2 Nr. 3 PromO Fakultät).

Die Hilfe von gewerblichen Promotionsberatern bzw. –vermittlern oder ähnlichen Dienstleistern wurden zu keiner Zeit in Anspruch genommen noch wird diese in Zukunft angenommen werden (§ 8 Satz 2 Nr. 4 PromO Fakultät).

Hiermit gebe ich mein Einverständnis, dass die elektronische Fassung der Dissertation unter Wahrung meiner Urheberrechte und des Datenschutzes einer gesonderten Überprüfung unterzogen werden kann (§ 8 Satz 2 Nr. 7 PromO Fakultät)

Ich erkläre mich hiermit ausdrücklich einverstanden, dass bei Verdacht wissenschaftlichen Fehlverhaltens Ermittlungen durch universitätsinterne Organe der wissenschaftlichen Selbstkontrolle stattfinden können (§ 8 Satz 2 Nr. 8 PromO Fakultät).

Christoph Klumpen

Bayreuth, den